Study of a visco-elastic model of the human lung and application to the High Frequency Chest Wall Oscillation

Michaël Brunengo

UNIVERSITÉ CÔTE D'AZUR

ÉCOLE DOCTORALE
SCIENCES FONDAMENTALES ET APPLIQUÉES

THÈSE DE DOCTORAT

Étude d'un modèle visco-élastique du poumon humain et application à l'oscillation haute fréquence extra-thoracique

Michaël Brunengo

Laboratoire Jean Alexandre Dieudonné

Présentée en vue de l'obtention du grade de docteur en Mathématiques **d'**Université Côte d'Azur

Dirigée par : *Benjamin MAUROY*

Soutenue le : 13 Octobre 2021

Devant le jury, composé de :
Céline Grandmont, DR, INRIA Paris
Philippe Poncet, Pr, Univ. Pau & pays de l'Adour
Laurent Monasse, CR, INRIA Sophia Antipolis
Plamen Bokov, MCU-PH, Hôpital Robert-Debré
Hélène Politano, DR, Université Côte d'Azur
Invité : Bernard Rousselet, Pr. Ém, Université Côte d'Azur
Barret R. Mitchell, CEO, RespInnovation SAS

resp Innovation

UNIVERSITÉ CÔTE D'AZUR
École Doctorale de Sciences Fondamentales et Appliquées

THÉSE
pour obtenir le titre de docteur de l'Université Côte d'Azur

Discipline : Mathématiques

presentée par
Michaël Brunengo

Study of a visco-elastic model of the human lung and application to the High Frequency Chest Wall Oscillation

-

Étude d'un modèle visco-élastique du poumon humain et application à l'oscillation haute fréquence extra-thoracique

Thèse dirigée par Benjamin Mauroy
soutenue le 13 Octobre 2021

devant le jury composé de

Rapporteurs

Céline Grandmont, Directrice de recherche, INRIA Paris
Philippe Poncet, Professeur, Université de Pau et des pays de l'Adour

Examinateurs

Laurent Monasse, Chargé de recherche, INRIA Sophia Antipolis
Plamen Bokov, MCU-PH, Hôpital Robert-Debré, Paris
Hélène Politano, Directrice de Recherche, CNRS
Benjamin Mauroy, Chargé de recherche, CNRS

Invités

Barret R. Mitchell, Directeur général, RespInnovation SAS, Seillans
Bernard Rousselet, Professeur émérite, Université Côte d'Azur

The human lung is a complex organ playing the role of interface for the vital gas exchanges (oxygen and carbon dioxide) between the ambient air and the blood. It is composed of two interconnected structures assuring the correct circulation of the air produced by the ventilation: the tracheo-bronchial tree and the lung's parenchyma, a porous medium where the gas exchanges between the air and the blood occur. Being reachable by external pollutants, the lung is protected among others by a specific secretion, also called the pulmonary mucus. The latter can accumulate and obstruct the airways in case of specific respiratory diseases. That can then alter and disturb the proper functioning of the lung. The use of therapeutic methods is then essential for the patient to maintain a good quality of life. The High Frequency Chest Wall Oscillation (HFCWO) is a respiratory technique, being part of the chest physiotherapy, that dispenses automated therapy which mobilizes the mucus and favors its expectoration. It is based on the application of small amplitude pressures at a relatively high frequency on the chest's patient. This mechanical treatment seems efficient but its use and effects on human lungs are based on empirical knowledge and are consequently not well understood as of today. The comprehension of this therapy rests on the study of the lung, complex system where specific behaviors occur. In that way, the mathematical modeling can be an useful tool. This thesis takes an interest in building and understanding a mathematical and numerical model of the lungs adapted to study the influences of the HFCWO on the human lungs. It is exploited to propose new insight on the use of this technique. Our work is based on the coupling between two idealised models : a 0D model of an airway tree that mimics the tracheo-bronchial tree and a multi-D homogeneous elastic medium that mimics the lung's parenchyma. The latter is used with its unidimensional formulation in most of this work. Our goal is to study the physics of the coupling between the air fluid dynamics in the airway tree and the deformation of the elastic medium, and to analyse the stresses felt by the mucus inside the tree. First, based on literature data, we show the efficiency of the model at mimicking ventilation at rest in healthy and non-healthy lungs. Meanwhile, we take an interest at understanding the role of its parameters. Then, with a dimensionless formulation of the model and comparative numerical simulations, we propose the use of a specific variable also known as the quality factor. Defined from the parameters of the lungs, this variable can suggest the capability of the lung to resonate with stimulations whose it is submitted. From the data observed in the literature, we suggest a range of frequencies that maximizes the effects of the HFCWO and potentially the displacement of the mucus in the tree. We show that this interval is directly linked to the fundamental natural frequency of the elastic material. The natural frequencies computed with our model are similar to the resonance frequencies deduced from clinical studies found in the literature. The end of the work propose prospects for improvement of the model such as the use of 3D lungs geometries constructed from CT-scan, the use of a splitting method to optimize the numerical time calculation or the establishment of a clinical study of the air flows at mouth induced by the HFCWO.

Keywords : Chest physiotherapy, HFCWO, Mathematical modelling, Fluid mechanics, Solid mechanics, Numerical simulation

Le poumon humain est un organe complexe jouant le rôle d'interface pour les échanges de gaz (oxygène et dioxide de carbone) entre l'air ambient et le sang. Il est composé de deux structures arborescentes interconnectées assurant la circulation de l'air générée par la ventilation : l'arbre trachéo-bronchique et le parenchyme pulmonaire, un matériau poreux où les échanges de gaz entre l'air et le sang se produisent. Etant accessible aux polluants extérieurs, le poumon est protégé entre autres grâce à une sécrétion spécifique, aussi appelée le mucus pulmonaire. Ce dernier peut s'accumuler et obstruer les voies aériennes lors de maladies respiratoires. Cela peut modifier et perturber le bon fonctionnement du poumon. L'utilisation de méthodes thérapeutiques est donc essentiel pour les patients afin de maintenir une bonne qualité de vie. L'Oscillation à Hautes Fréquences de la Cage Thoracique (HFCWO) est une technique respiratoire, appartenant à la kinésithérapie respiratoire, qui prodigue une thérapie automatisée permettant de mobiliser le mucus et de favoriser son expectoration. Elle est basée sur l'application de pressions à de relatives hautes fréquences et faibles amplitudes sur le thorax du patient. Ce traitement mécanique semble efficace mais son usage et ses effets sur le poumon humain sont basés sur des connaissances empiriques et sont donc peu compris de nos jours. La compréhension de cette thérapie repose sur l'étude du poumon, système complexe où interviennent des comportements spécifiques. Dans ce sens, la modélisation mathématique peut être un outil utile. Cette thèse s'intéresse à construire et à comprendre un modèle mathématique et numérique des poumons adapté à l'étude des influences de la HFCWO sur le poumon humain. Il est utilisé afin de proposer de nouvelles perspectives quant à l'utilisation de cette technique. Nos travaux sont basés sur le couplage entre deux modèles idéalisés : un modèle 0D d'arbre mimant l'arbre trachéo-bronchique et un modèle multi-D d'une matière élastique et homogène mimant le parenchyme pulmonaire. Ce dernier est utilisé sous sa formulation unidmensionelle dans une grande partie de ces travaux. Notre objectif est d'étudier la physique du couplage entre la dynamique de l'écoulement de l'air dans les voies aériennes et la déformation du matériau élastique, et d'analyser les contraintes ressenties par le mucus dans l'arbre. D'abord, en se basant sur des données de la litérature, nous montrons l'efficacité du modèle à mimer la ventilation de repos chez des poumons sains et malades. Dans un même temps, nous nous intéressons à comprendre le rôle de ses paramètres. Ensuite, avec une formulation adimensionnée du modèle et des simulations numériques comparatives, nous proposons l'utilisation d'une variable spécifique, aussi connue sous le nom de facteur de qualité. Définie à partir des propriétés du poumon, cette variable informe sur la capacité du poumon à résoner avec les stimulations dont il est soumis. A partir de données observées dans la litérature, nous suggérons une plage de fréquences qui optimise les effets de la HFCWO et potentiellement le déplacement du mucus dans l'arbre. Nous montrons que cet intervalle est directement lié à la fréquence propre fondamentale du matériau élastique. Les fréquences propres calculées à partir du modèle sont similaires aux fréquences de résonance déduites à partir d'études cliniques trouvées dans la litérature. Le contenu final de ces travaux propose des perspectives d'amélioration du modèle comme l'utilisation de géométries 3D des poumons construites à partir de CT-scan, l'utilisation d'une méthode de splitting pour optimiser les temps de calcul numérique ou la mise en place d'une étude clinique des flux d'air à la bouche induits par la HFCWO.

Mots clés : Kinésithérapie respiratoire, HFCWO, Modélisation mathématiques, Mécanique des fluides, Mécanique des solides, Simulation numérique

Remerciements

Je tiens tout d'abord à remercier Céline Grandmont et Philippe Poncet pour avoir rapporté ce travail de thèse. Je remercie également Laurent Monasse, Plamen Bokov et Hélène Politano d'avoir accepté de faire partie de mon jury de thèse.

Mes remerciements vont ensuite à Benjamin Mauroy, mon directeur de thèse. Benjamin, merci infiniment pour ton investissement, tes conseils et ta rigueur au travail. J'ai énormément appris grâce à toi et ton enseignement me suivra pour la suite. Cette thèse n'aurait pas été ce qu'elle est aujourd'hui sans toi, merci beaucoup.

Je dédie un remerciement particulier à Bernard Rousselet, professeur émérite qui m'a accompagné et conseillé pendant cette thèse. Je te remercie Bernard pour tous tes avis et remarques pertinents au sujet de mes travaux. J'espère pouvoir continuer notre collaboration.

Je remercie l'entreprise RespInnovation de m'avoir proposé cette aventure et de m'avoir suivi pendant ces années. Barry, merci pour ta vision industrielle de la recherche et pour toutes les perspectives d'études que tu m'as proposées. Sophie, merci pour tous ces échanges et ton investissement dans mes travaux. Brent, merci de m'avoir montré qu'allier la déconne à la rigueur peut amener, de manière intéressante, à des résultats parfaitement productifs. Je remercie particulièrement Sébastien avec qui j'ai partagé le bureau de RespInnovation pendant ces années. Séb, merci pour tout, tant professionellement qu'amicalement. Merci d'avoir pris le temps de me faire découvrir une partie du monde industriel et d'avoir eu la sympathie et la patience de m'écouter te raconter mes problèmes de recherches. Au plaisir de la prochaine session fractionnée en course à pied. Je remercie également Fausto et Céline ; et plus récemment Charles et Lilian pour m'avoir soutenu dans ces derniers mois en proposant une atmosphère autant sérieuse que plaisante. J'espère avoir de nouveau l'occasion de partager quelques balles avec vous sur un court de tennis. Enfin, je remercie Christophe pour son investissement sur les derniers mois.

Je remercie toute l'équipe de recherche du laboratoire J.A. Dieudonné autour du poumon. Merci pour tous ces échanges, ces cafés et ces réunions du lundi. Je remercie particulièrement Jonathan, partenaire de bureau. Jonathan, merci pour ta clairvoyance et ta persévérance qui m'ont toujours profondément inspiré. Merci également à André, Frédérique, Cyril, Thomas et Riccardo pour toutes ces discussions intéressantes et pour votre sympathie. Je remercie aussi Valentin pour son investissement dans les prémices de l'étude clinique ; j'espère pouvoir continuer cette collaboration.

Mes prochains remerciements s'adressent aux amis qui m'ont fait grandir pendant ma première et ma deuxième jeunesse. Pour cette deuxième jeunesse, je remercie tous les copains de la team Polytech - plus les amis par extension. Je m'adresse à vous tous directement sans vous nommer car vous êtes nombreux et je serai trop inquiet d'omettre un nom :-). Merci pour votre soutien et votre joie de vivre pendant tous ces voyages, ces soirées et ces sorties sportives. Ma première jeunesse a été partagé avec les copains d'enfance, Valentin, Victor et Mikael, à qui j'adresse un profond remerciement. Merci les gars pour avoir faconné la personne que je suis aujourd'hui. Les heures passées ensemble sont indénombrables et ont toutes été singulières et inspirantes pour moi.

Je tiens également à remercier celle avec qui je partage ma vie depuis maintenant plus de quatre années et qui m'a soutenu depuis le début de cette thèse. Laura, vivre à tes côtés a été pour moi une source d'inspirations et de motivations. Merci pour ta patience, ton écoute, tes conseils et pour tout cet amour que tu m'offres.

Mes derniers remerciements s'adressent à ma famille proche et "éloignée", qui m'ont soutenu et encouragé depuis toutes ces années. Merci les parents, le frère et sa petite famille, pour tout ce que vous m'avez apporté. Votre aide et amour sont inestimables à mes yeux.

Contents

Chapter 1

Background of the study and objectives

"Les poumons sont placés dans un sanctuaire sacré, dans un lieu tellement caché, qu'il semble que la nature se soit appliquée à abriter ces organes contre l'observation directe des yeux, l'intelligence et l'industrie des hommes."

John Mayow,
Traité deuxième de la respiration, 1668.

From *Traduction des oeuvres chimiques et physiologiques de Jean Mayow*, 1840, p.100.

Contents

1.1 Introduction

The oxygen is one of the essential elements needed by almost all the living multicellular organisms. It composes twenty percents of the ambient air in the form of dioxygen (O_2 : two atoms of oxygen). In specific cells, the dioxygen reacts with the glucose to produce carbon dioxide (CO_2), water and the Adenosine Triphosphate (ATP) molecule which stores the energy, a fundamental molecule of the metabolism. This reaction, called the cellular respiration, happens every second in the millions or billions of those cells that compose large and complex organisms, such as animals. Consequently, they have to maintain a necessary concentration of those reagents (O_2 and glucose) according to the energetic needs and in order to eliminate non-useful products (CO_2).

Focusing on human, two complex and intertwined structures of distribution act for that purpose : the blood network and the lung. The role of the blood network is to carry the oxygen and glucose toward the cells and to collect the carbon dioxide they produce, thanks to the heart that set the cadence of the blood circulation. The glucose is brought directly into the blood mainly by general nutrition (it is also produced by the liver in lower quantity). Meanwhile, the oxygen has to pass from the air to the blood and the carbon dioxide has to do the way around. This complex task is performed in the lungs while breathing.

The lung is an organ which is in direct contact with air. Consequently, it is a place easily accessible for bacteria, virus (recently : SARS-CoV-2∼COVID-19) or airborne pollutants. The lung has developed ways to protect itself, as for example cough with the mucus. The mucus is a secretion lining the interior of the lungs which catches such intruders. It is then evacuated to the outside of the lung by cough. However some pulmonary diseases alter the proper evacuation of the mucus. Hence therapeutic methods have been developed to overcome this dysfunction such as chest physiotherapy.

This thesis aims at studying the lung in the framework of a therapeutic technique of chest physiotherapy called High Frequency Chest Wall Oscillation. The main tools used for that purpose are mathematical modelling and numerical simulation. This thesis has been funded by RespInnovation SAS (Seillans, France) and the Enseignement supérieur, de la recherche et de l'Innovation by a CIFRE contract managed by the Association nationale de la recherche et de la technologie (ANRT). This work is a collaboration between RespInnovation SAS (Seillans, France) and the Laboratoire Jean Alexandre Dieudonné (Nice, France).

This chapter introduces the context of the study and the motivations. The human lungs, is detailed in section 1.2. The section 1.3 details how the structure of these organs has to be protected against any external pollutants to avoid infections and diseases. In the section 1.4, we explain the chest physiotherapy technique, used in the frame of obstructive respiratory diseases. Finally, the objectives of this thesis are presented in the section 1.5.

1.2 The human lungs

The main role of the lungs is to perform the exchange of gases between the blood and the ambient air. Millions of years of evolution have steered these organs toward maximizing the exchange surface in small volumes while minimizing the thickness of the interface, and the result is the tree-like structure of the lungs described in subsection 1.2.1. Then, the correct flows of gazes inside the tree is ensured by breathing , see subsection 1.2.2. As stated in [58, 76], we notice that the lungs have other functions as filter and reservoir of blood, metabolizer of some vasoactive substances or the phonation, which will not be discussed in this manuscript.

1.2.1 Anatomy and characteristics

Around the lungs. The lungs are composed of two parts, the left lung and the right lung that are respectively formed of two and three lobes. They are located inside the thorax[1], and

[1]Interestingly, the term *thorax* signifies "breastplate" in the ancient greek language, and contains the main important organs (lungs and heart) operating in the cardiovascular system (also called the circulation system).

share the space protected by the rib cage with, among others, the heart and the esophagus. Under them, a skeletal muscle separating the thorax from the abdomen, called the diaphragm, is tied to the lungs and participate in breathing. The rib cage consists of twelve pairs of ribs hinging on the spinal column and the sternum. With a partly cartilaginous constitution, it has a flexible structure that can easily follow all the thoracic movement during the lung ventilation. The intercostal space, between the ribs, contains essentially the intercostal muscles.

The external surface of the lungs and the internal part of the rib cage are covered with the pleura containing a cavity, called the pleural cavity, filled with a fluid at subatmospheric pressure (a negative pressure in comparison to the atmospheric pressure). The role of the pleura is to ensure the interconnected movements of the lungs and the rib cage during breathing. Sketches of the thorax is illustrated in the figure 1.1.

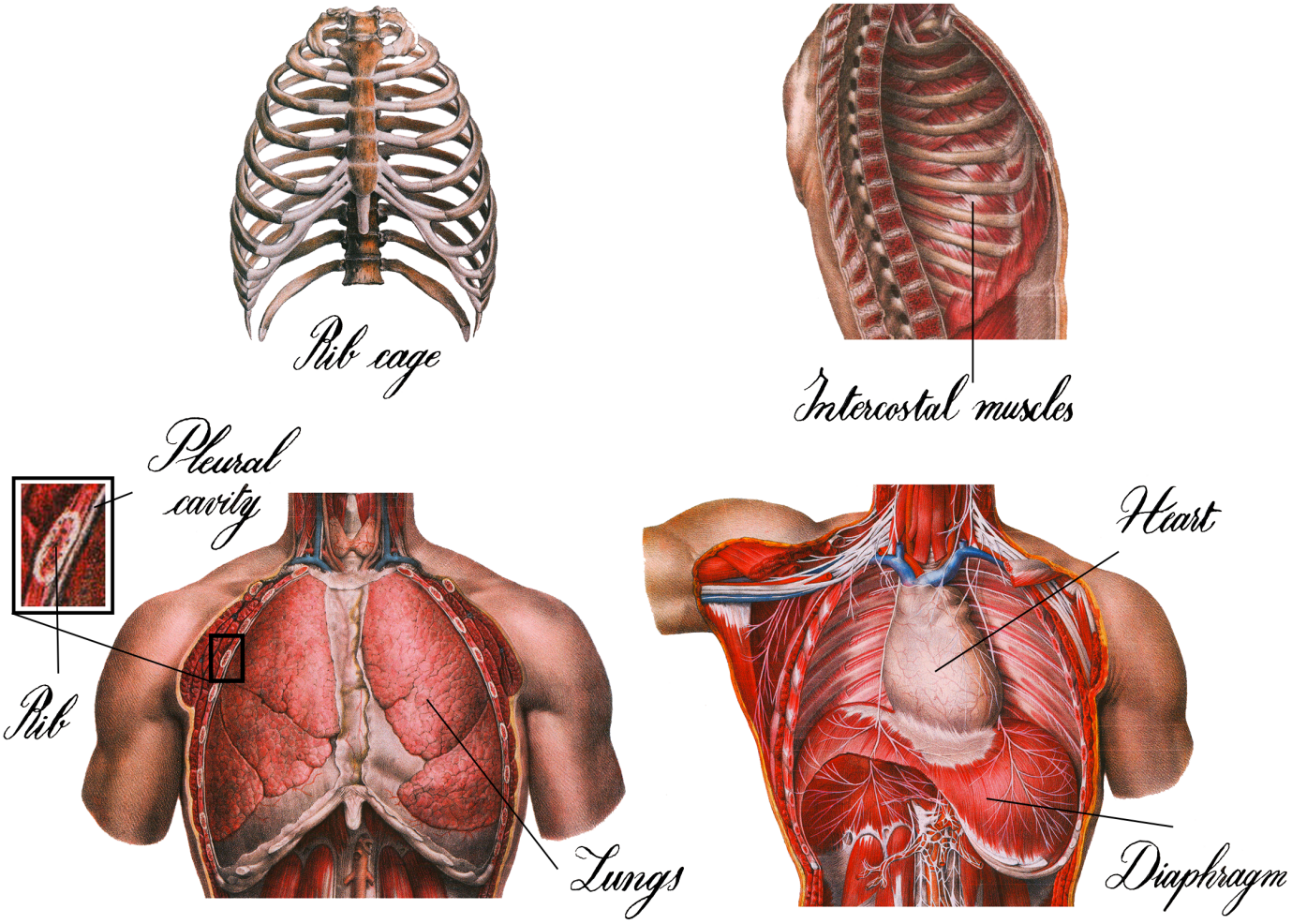

Figure 1.1: Illustrations of the thorax. **Top left:** Front view of the rib cage. **Top right:** Side view of the rib cage with the intercostal muscles. **Bottom left:** Front view of the external surface of the lungs surrounded by, among others, the pleural cavity, the rib cage and the intercostal muscles. The five lobes of the lungs are visible. **Bottom right:** Front view of the inside of the thorax without the lungs. Are mainly displayed the heart in its pericardial sac and the diaphragm. Adapted from [55], hand-written by [133].

In the interior of the lungs. The path of the dioxygen through the lungs, from the ambient air to the exchange surface with the blood, is winding. The journey of the dioxygen (opposite journey for the carbon dioxyde) begins at the mouth and the nose, and goes through pharynx and larynx to reach the trachea, a fibrous and cartilaginous pipe which is the entrance to the pulmonary airways. In the depth of the trachea, dioxygen is carried to one of two possible directions : to the left lung or to the right lung. There, the ducts are narrower than the trachea

and are called bronchi. No matter the way, the rest of the trip will bring the molecule to take one direction over two several times to reach the exchange surface with pathways becoming smaller and smaller as sinking in the tree. This illustrates the tree-like structure of the pulmonary tree which is detailed in the next paragraph. Following the tree-like of the human pulmonary tree to its depths, the bronchi become bronchioles, terminal bronchioles and finally respiratory bronchioles, which are the first branches of the acinar region. An acinus is the lung's element that acts as the gas exchanger. An acinus is composed of alveolar ducts leading to alveolar sacs. At the acinar level, the size of the airways[2] does not decrease much at bifurcations. Respiratory bronchioles are partially covered with alveoli whereas alveolar ducts and alveolar sacs are fully covered with it. The pulmonary alveoli, as its latin origin indicates[3], are small cloud-shape cavities whose membrane, surrounded by blood capillaries, is the exchange surface with blood. An alveolus is the unit base of gas exchange. The trachea is about 10cm long for barely 2 cm of diameter. The diameter of an alveolus is about 400μm for a length of 500μm [76], see the figure 1.2.

The pulmonary tree. The trachea is the root branch, or the mother branch, of the pulmonary network that branches globally in a way that can be seen as nearly dichotomous. In other words, two daughter branches with smaller size stem from the trachea and each of them divides into two smaller daughters branches and so on and so forth. The connection between the mother and the daughters branches is called a bifurcation. We call by *generation* all the branches resulting from a same number of bifurcations. The pulmonary airways do not branch symmetrically, i.e. two daughters can have different sizes. Hence, the number of bifurcations between different pathways from the trachea to the acini can be different. The total number of generations in the pulmonary tree vary from eighteen to thirty [40] ; this is mainly due to the physiological differences between the individuals. Nevertheless, commonly in the literature [135], it is estimated to be of about twenty-three. From that perspective, we can estimate that the pulmonary tree is being composed of about $2^{24} - 1$ branches (more than sixteen millions) including 2^{23} terminal branches at the last generation (more than eight millions).

Approximately, the part of the pulmonary tree from the generation one to the generation sixteen constitutes the bronchial tree or, by adding the trachea (at the generation zero), the tracheo-bronchial tree. Then the region consisting of the generation seventeen to twenty-three (more or less) is the respiratory zone, see the figure 1.2.

The bronchial tree. The main role of the bronchial tree is to conduct dioxygen and carbon dioxyde between the ambient air and the respiratory zone. It is called the conductive zone and the air inside is transported by convection and diffusion[4] [76, 58, 98]. In the proximal (close to the trachea) and central part of the bronchial tree, the main conducting transport is the convection. While sinking in the tree, the cumulative volume of the airways increases. Hence, the air velocity reduces progressively towards the distal part of the tree (far from the trachea) and a transition between convection and diffusion occurs. Typically, at a given point, the diffusion becomes the dominant transport phenomenon in front of the convection. Actually, this transition could occur either in the deepest part of the bronchial tree or in the respiratory zone. It relies on the morphology of the lung and on the ventilation intensity [99]. The bronchial tree does not participate in the gas exchanges. This remark leads to call the volume of all the bronchi and the bronchioles of this region, the dead space. The mean volume of the dead space is generally about 150 mL [76]; their value can differ between individuals [78]. All the airways in the bronchial tree are covered by smooth muscles. Although its main role is generally associated with the control of the opening of the airways, the physiological function of the smooth muscle remains not clear as of today [22, 8].

[2]In this work, the term *airway* is used to designate any anatomical element of the pulmonary tree such as the bronchus, the bronchioles, etc. It is a general duct in the tree structure of the lungs.

[3]In latin language, *alveolus* means "little cavity".

[4]The convection is the transport of a quantity due to the neighboring speed. The diffusion designates the capacity of an environment to homogenize its composition that lead to the motion of the particles.

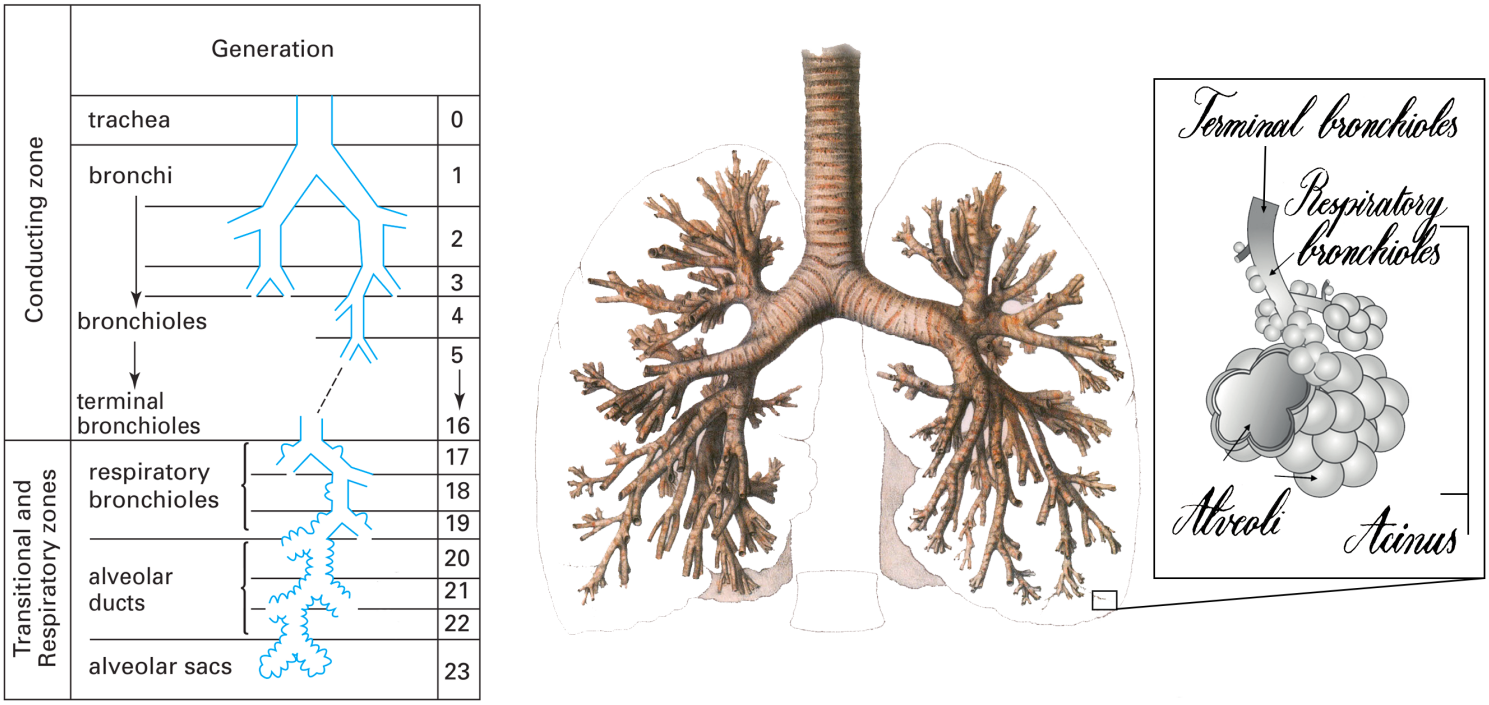

Figure 1.2: Schematic and illustrative representations of the dichotomous structure of the pulmonary tree. **Left:** Taken from [76]. **Right:** Painting of the first generations of the bronchial tree with a idealised zoom of an acinus. Adapted from [55, 127], hand-written by [133].

In the bronchial tree, the length and the diameter of the branches decrease as the generation index increases. Hence the way the branches size is decreasing acts on the shape and on the properties of the tree. The lungs tend to maximise the exchange surface in a finite volume while minimizing the resistance of the air flowing inside [136]. Thus, the branches reduction at bifurcations tends to be homothetic with an optimal reduction factor. The Hess-Murray law established in 1914 tells that to minimize the resistance of the flow of air inside a finite volume, the reduction factor through the generations has to be constant and equal to $h = (\frac{1}{2})^{\frac{1}{3}} \approx 0.79$ [80]. In reality, the bronchial tree is adapted to the available space around him and the airways rather branch asymmetrically. On average through the generations, the human lungs exhibit a homothetic coefficient slightly larger than h. Interestingly, this shift corresponds to a safety margin that might allow anatomical variations between individuals or that might compensate variations of the bronchi calibers during the life of an individual [80].

The use of idealized models of the lung simplifies the complexity of the organ structure and facilitates its modeling. The homogeneous model of bronchial tree proposed by Weibel [135], extensively used in the literature [123, 98], uses the optimal factor $h \approx 0.79$ and makes the assumption that the bronchial bifurcations are symmetrical. Thus the tree-like structure is considered perfectly dichotomous and symmetrical, i.e. the reduction factor does not vary through the generations and is the same at a given generation.

The respiratory zone. The respiratory zone is the part of the lungs involved directly in gaz exchanges. It contains all of the respiratory bronchioles, the alveolar ducts and the alveolar sacs. The bronchioles and the alveolar ducts also adopts a tree structure but their sizes does not change that much after bifurcation. There, the flow of air, brought by convection and diffusion through the bronchial tree, is very slow and, in general, the main phenomenon acting for that purpose is the diffusion [76, 58, 98]. Actually, in the respiratory zone, the diffusion is dominant toward the convection for low ventilated volume, as for ventilation at rest. The acini are contained in a viscoelastic medium called the lung parenchyma. A dense network of blood capillaries surround all the surface of the lung parenchyma which is the region where the dioxygen passes from the air to the blood. The opposite mechanism unfolds for the carbon

dioxide. The phenomenon ensuring the gaz transfer is also the diffusion. The alveolar–capillary barrier is the interface between the air and the blood, with a thickness of about 0.2 to 0.5 μm [76], namely at least 50 times thinner than the thickness of a sheet of paper. Thanks to the tree-like of the pulmonary airways, the surface of all the alveoli reaches around fifty to a hundred square meters. Those dimensions are necessary to fulfill the metabolic needs and to enable peaks of energy consumption during activities.

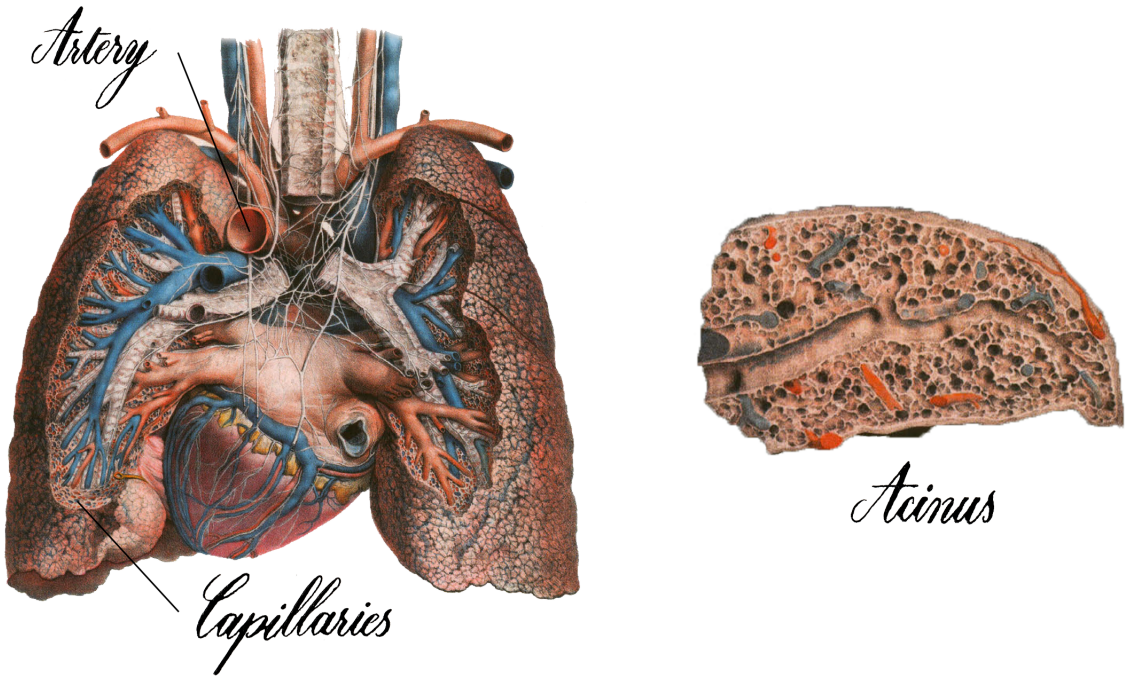

Figure 1.3: Illustrations of a semi-opened lungs (left) and a cut view of an acinus (right). It proposes a glimpse of the complex interconnection between the pulmonary and the blood networks. Adapted from [55], hand-written by [133].

We have described the anatomical elements composing the human lungs with some of their properties. The exchanges of oxygen and carbon dioxide have to be continuously assured to fulfill the metabolism energetic needs. The mechanism making this process possible is breathing, also named ventilation.

1.2.2 Mechanics of breathing

Breathing is the mechanism ensuring the transport of gas into and out of the pulmonary tree, necessary for a proper control of the concentration of oxygen and carbon dioxide in blood. The ventilation is often characterized by a flow rate in mL/s. At rest, the lungs ventilate about 500 mL per respiratory cycle, called the tidal volume [76]. By subtracting the dead space, which is not involved in the gas exchanges, the effective volume is about 350 mL.

Breathing relies on the principle that a difference of pressure between two connected environments leads the molecule of a Newtonian fluid to move from the higher pressure environment to the lower one. Hence, regarding the human lung, in order to create a movement of air (an air flow) from the ambient air to the exchange surface, the pressure inside the lungs has to be lower than the pressure of the ambient air (depression). Typically, it is performed by increasing the volume of the lungs. The opposite action of decreasing the volume of the lungs increases the pressure inside (overpression) and produces a flow of air from the lungs to the outside.

Mechanically speaking, different agents take part in the pulmonary ventilation and participate in the volume change of the lungs. One of the main actor is the diaphragm. Being attached at the bottom of the lungs and the rib cage, its contraction leads the lungs to stretch and to

increase its volume, thanks to the elastic properties of the pulmonary tissues. Then, the intercostal muscles help the action of the diaphragm to act on the outward displacement of the rib cage. The lungs, being connected to the rib cage by the pleura, follow the movement of the bones and also stretch sideways. Hence, the induced advection of air inside the lung, called the inspiration, is an active phenomenon because it is caused by controlled muscular efforts. At rest, the expiration (the evacuation, to the outside, of the air inside the pulmonary airways) is based on a different mechanism. The lungs, acting as an elastic medium, tend to return to their initial state (before inspiration) after having been stretched by inspiration. Hence, globally during tidal breathing, the different muscles involved during inspiration relax and release the lungs that go back to their resting state and, consequently, decrease back the pulmonary volume. Thus, at rest, the expiration is a passive phenomenon because it is not directly controlled by muscles. Nevertheless, the muscles involved in the inspiration may hold the lungs back during expiration to not let them go back too quickly [76]. During exercice[5], the main difference is that both inspiration and expiration are active phenomena. Specifically, the diaphragm and the intercostal muscles, also helped by the abdominal muscles, accompany the reduction of the pulmonary volume.

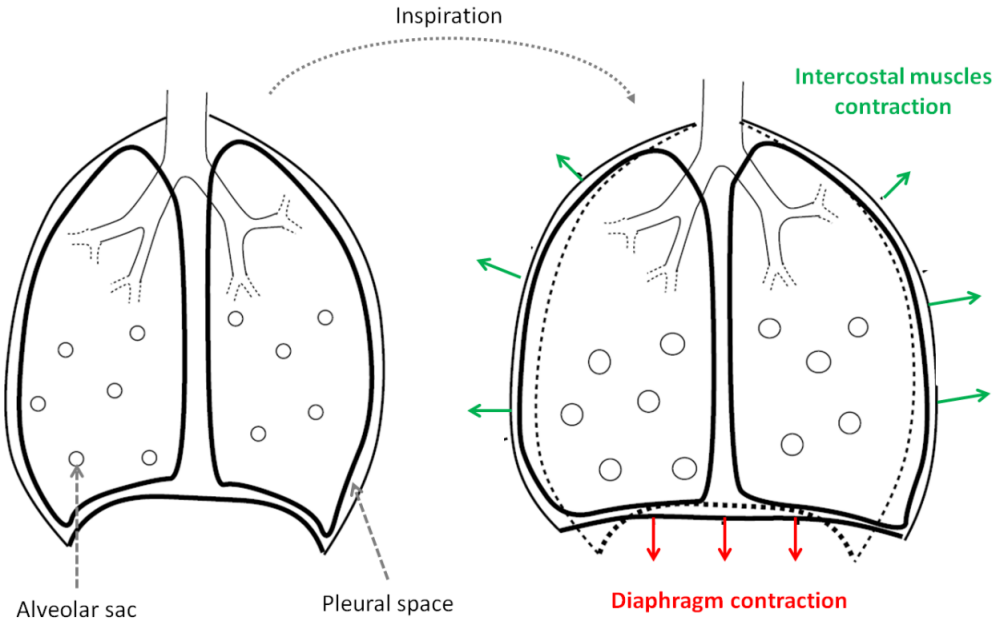

Figure 1.4: Graphic representations of the main bio-mechanical phenomena during inspiration. Taken from [109].

The pleura has a specific role during breathing [76]. Mainly, it links the motion between the lungs and the rib cage. The pleural liquid, the fluid in the pleural cavity, lubricates the two layers and consequently favours the sliding movement between the lungs and the rib cage. In addition, as mentioned in the previous subsection, the intrapleural pressure in the pleural cavity is negative, which allows to maintain a proper functioning of the ventilation[6]. The negative pressure maintains equal two pressures : the transpulmonary and the transthoracic pressures. The transpulmonary pressure is the pressure across the lungs wall, it is the difference between the alveolar pressure and the intrapleural pressure. The transthoracic pressure is the pressure across the chest wall, it is the difference between the intrapleural and atmospheric pressures. Moreover, the difference in pressure across an interface is called a transmural pressure. Going back to the topic, at the end of the expiration, the alveolar pressure is the same as the atmospheric pressure

[5]The human state designated by "exercice" indicates the state when the energetic needs are higher than at rest and they are relative to the effort intensity.

[6]If the pressure inside the pleural cavity is null (or positive), and for example if it is connected to the ambient air by an injury, the lungs would collapse and the rib cage would extend, due to the inward elastic recoil of the lungs and to the outward elastic recoil of the rib cage; this pathology is called pneumothorax.

that act on the thorax. As the intrapleural pressure is negative, the transpulmonary and the transthoracic pressures are acting on each other in opposite direction, the pressures balance each other out. The chest wall holds the alveoli open and the lungs hold the chest wall in. During inspiration, the muscles pull and tend to increase the volume of the thoracic cavity. The intrapleural pressure becomes more negative, the transmural pressure increases and the alveoli enlarge. The alveolar pressure becomes negative and establishes the needed pressure gradient for air to flow in. Several studies have shown that even the alveoli located in the center of the lungs are sensitive to the variation of the transmural pressure by their interdependence structure, i.e. their mechanical dependence due to their geometric shape [76].

Another essential element is the pulmonary surfactant [76]. If we take a look at the alveoli structure, we can observe that a liquid lines their surface and that their volume may differ. Consequently, due to the surface tension between the air inside and the liquid around them as well as the elastic property of their tisue, the smaller alveoli would collapse in favor of the bigger one which would expand. The pulmonary surfactant diminishes this tension and keeps opened all the alveoli during expiration by equalizing the different pressures inside. Moreover it helps the widening movement of the alveoli during inspiration and consequently reduces the work of breathing [62, 76]. Like the mucus, it is one of the pulmonary secretion which also participates to the protection of the body against pollutants and infections.

1.3 Protection against respiratory diseases

The previous sections show the complexity of the structure and the functioning of the lungs. We can understand already how a defective link in the chain of the pulmonary bio-mechanical mechanisms can be the cause of respiratory diseases. We have seen that the lungs have evolved to facilitate and to optimize the gases exchanges with the blood. However, the lungs form a direct interface with ambient air and is thus sensitive to aggression by airborne pollutants, bacteries, virus, etc.

1.3.1 Mucus : characteristics and role

The mucus, also produced in other organs as the vagina or in the gastrointestinal tract, is a gel-like substance lining the inner surface of the tracheo-bronchial tree. The mucus protects the lungs and the body by trapping all kind of foreign particles. It is present in most of the bronchial tree [56] as a thin layer of about 10 μm [59]. The mucus is a viscoelastic fluid whose main property is to exhibit a yield stress that has to be overcome for the mucus to flow. In broad terms, it behaves as a solid at low stress and as a liquid at high stress. The order of magnitude of the yield stress σ_0 for an healthy mucus is typically $\sigma_0 \simeq 0.1 - 1$ Pa [70, 83, 84]. The mucus is composed of more than 90% of water and 1 to 5% of mucins [102], a protein that forms a slimy polymeric substance when hydrated. The rest of the structure contains macromolecules. The mucus is continuously secreted by the lungs, and the secretion rate increases during the intrusion of non wanted particles or during exercice that stimulates the bronchi wall. Consequently, it has to be expelled from the bronchial tree to evacuate the pollutants and to avoid constriction of the pulmonary airways.

Two main natural mechanisms participate in the airway mucus clearance, i.e. the evacuation of the mucus : the mucociliary clearance (MCC) and cough. First, the cilia, a slender hair-like structure or organelle lining the inner surface of the bronchial airways, propels the mucus from the distal to the proximal airways by their rhythmic and synchronous beating. This beating motion carries the mucus to the larynx where it is usually swallowed or expelled by coughing. The ciliary beating is facilitated by an airway surface liquid that lubricates the inner sol layer of the respiratory tracts. The mucociliary clearance corresponds to the combination of the proper quality of the airway surface liquid and the ciliary beating [17]. The second mechanism is cough that induces strong air flows in the bronchi. Cough is the most efficient phenomenon to

expectorate the mucus from the proximal airways. However, those mechanisms[7] can be altered and impeded by some pulmonary diseases.

1.3.2 Respiratory diseases

The main symptom of the pulmonary diseases is breathlessness, for example in Chronic Obstructive Pulmonary Disease (COPD) or asthma [94, 15]. Typically, for those diseases, it comes from the obstruction of the airways due to the inflammation of the pulmonary tissue, to mucus hypersecretion, or to the contraction and the hypertrophy of the smooth muscle [117, 14, 94]. The COPD damages also the alveolar sacs by diminishing their elastic capacity, even to the point of making them no longer operational. It leads to parenchymal destruction and this is called the emphysema. Those factors causes limitations in the circulation of the air inside the airways, coughs, and wheezing. Wheezing symptom is also a typical sign of bronchiolitis in infants and young children. The etiology identifies different causes for those diseases. In most of the cases, bronchiolitis is due to viruses whereas smoking, generally, is the cause of COPD. For asthma, not well known and understood as of today, several origins are pointed out, tied to the environment and lifestyle, such as exercise, emotional stress, air pollutants, etc, as enumerated in [139]. Mutations in genes can also lead to an abnormal functioning of the lungs. For example, Cystic Fibrosis (CF) is a genetic disease that disturbs the hydration of the mucus inside the pulmonary airways making it too thick and sticky, and thus, hard to move. The Primary Ciliary Dyskinesia (PCD), also due to the mutation of a gene, disrupts the capacity of the pulmonary cilia to move the mucus. In both cases (CF and PCD), the disease allows the bacteria to remain in the respiratory tracts, and increases the risk of infections and reduces the bronchi lumen[8] area, hence altering the circulation of the air inside the bronchial tree.

None of the diseases cited above is easily curable. Treatments mainly help people affected by respiratory disease in their day-to-day life by reducing their symptoms. Several treatments are prescribed or advised, such as drugs[9], oxygen and ventilatory support, change in lifestyle habits[10], or manual therapy [103]. This manuscript focuses on one of those techniques, the chest physiotherapy, that is detailed in the next section.

1.4 The chest physiotherapy

The chest physiotherapy (CP) is a term referring to a large range of physical and mechanical therapeutic methods administered to patient with respiratory disorders [128]. CP favours the mobilization[11] and the removal of excess accumulation of pulmonary secretions in the tracheobronchial tree. It consists in changing the volume of the lungs to produce mechanical stresses and air flows in the respiratory airways that can, potentially, affects the secretions and move them. The methods can be identified by one of the two following groups or both groups : the one that mobilizes the secretions and/or the one that transports it [128, 21]. Depending on the pathology, they are also often combined together for optimal efficiency [128]. In addition, it might also bring the work of breathing closer to its healthy state, improving oxygenation and exercise tolerance [51].

Actually, CP is also named without clear distinction *respiratory physiotherapy*, *pulmonary physiotherapy* or most of the time *airway clearance technique* [68, 21, 100]. To the best of my knowledge, all terms are used and can be used similarly. It seems that *chest physiotherapy* was

[7] More specifically, the mucus clearance relates to the synchronisation of different factors : ion transport, water flow, mucin secretion, cilia action, and cough [18].

[8] Meaning 'light' or 'an opening' in the Latin language, the lumen, in biology, is the interior of tubular structures.

[9] We refer, for example, to bronchodilators or anti-inflammatory agents.

[10] It consists in identifying and reducing exposure to risk factors, such as smoking, allergens or even stress.

[11] The *mobilization* of the mucus refers to the different actions that act on setting the mucus in motion.

one of the first statement introduced in the 1960s in order to describe the conventional and traditional method, i.e. performed by a physiotherapist [128]. It may appear that the development of new mechanical devices performing automated CP has led to rather employ the term *airway clearance technique* [100]. Nevertheless, recent studies used both terms equivalently. Then, the distinction between the methods is emphasized by the use of adjectives such as *conventional*, *manual*, *self-administred* or *mechanical*.

The chest physiotherapy can be either performed autonomously by the patient, manually by a practitioner or automatically by specific mechanical devices. We can cite, as typical self-administered methods, the autogenic drainage [1] or huffing (also called forced expiratory technique when combined with breathing control) [4]. One of the main manual therapies involve chest percussion or vibration techniques and consist on applying either clapping pressures or vibrating pressures on the patient's chest with hands. However the two latters are not recommended anymore as showing a lack of efficiency [108]. Manual CP also refers to postural drainage or breathing control [128]. Those traditional techniques request either human and geographic dependencies or an active concentration from the patient, that can lead to the abandonment of the therapy [50, 68]. Hence, since a few decades, mechanical devices are often favored or used as a complement of other methods. Many of these devices apply pressures in or on the lung to help the draining of the mucus, such as the Positive Expiratory Pressure technique (PEP), the Intrapulmonary Percussive Ventilation (IPV), the high frequency chest compression (HFCC) or the High Frequency Chest Wall Oscillations (HFCWO), and seem to be quiet effective [65, 24, 50, 30, 96]. However, the democratization of these devices has led to the development of several new automated methods, but has animated the debate about the choice of the respiratory physiotherapy technique that is best adapted to the pathology or to the patient, with optimal functioning parameters. Indeed, there is, as of today, a lack of evidence regarding the efficiency of these mechanical devices since the knowledge of their therapeutic effects remains mainly empirical [89, 93, 29, 68, 97, 115]. However, as highlighted in [45], the absence of evidence does not necessarily mean an absence of benefit but further appropriate and methodological studies, along with validation and improvements, are needed to bring new clear insights.

In this work, we will particularly focus on the HFCWO technique. We define the HFCWO method as the technique that applies relatively small pressure at high frequency - about five to twenty-five Hertz - at localised spots on the thorax [96]. In the frame of the CIFRE contract, we had a full access to the HFCWO device of RespInnovation SAS called RespIn 11 (RespInnovation SAS, Seillans, France), see Figure 1.5. The jacket (blue), called the Wrap (RespInnovation SAS, Seillans, France), is worn by the patient during the therapy. The Wrap contains two lines of pistons at the front and three lines of pistons at the back. The main device (white and orange) is connected to the lines of pistons in the Wrap with five medical tubes, two for the front part of the Wrap and three for the back part of the Wrap. A strong blower in the main device feeds with air the pistons which inflate. The depression is made by rotating valves in the main device. By rotation, the valves connect successively the pistons with the ambient air, then the pistons with the blower, and so on. Consequently, the pistons inflate and deflate according to the frequency of the rotating valves. The pressures applied by the device come from the pistons inflation/deflation process. All the lines of pistons in the Wrap do not inflate/deflate synchronously. The back and the front parts are controlled independently by one valve. Then for each part, the lines inflate/deflate asynchronously.

1.5 Objectives of the thesis

The previous sections presented the need to study and understand the effects of mechanical devices of chest physiotherapy on the lungs. They also showed the complex tree-like structure of the lungs which highlights the intricate nature of its study. Several measurement tools can assess some lungs properties and are quite efficient [109]. For example, the ventilated flow and

Figure 1.5: Mechanical device of chest physiotherapy called RespIn 11 using High Frequency Chest Wall Oscillation technique. It is developed and commercialized by RespInnovation SAS, Seillans, France. **Left:** The jacket called Wrap (blue) with the controller device (orange and white). **Right:** Lines of pistons contained in the Wrap. The front part of the jacket contains two lines and the back part contains three lines. The pictures have been provided by RespInnovation SAS.

volume of air can be measured with spirometer, or a plethysmograph can measure resistance to air flow in the lungs. However, although being useful, such measuring instruments inform only on global properties of the lungs and not on local behaviors in the pulmonary tree. Moreover, as discussed previously, the results proposed by clinical studies (using such instruments) do not allow to infer on the efficiency of mechanical devices of chest physiotherapy. Hence, the use of mathematical modeling and of numerical simulations can be useful. Mathematical modelling allows to cut the complexity of a problem to favour its global comprehension. However, mathematical modelling is not the magic remedy. This science is based on hypotheses and, usually, it produces only estimations or predictions. Nevertheless, mathematical modelling has been often used in the framework of the lungs and has demonstrated its strength by the past.

Hence, a mathematical model is used in this thesis to bring new insights on the use of chest physiotherapy and particularly of High Frequency Chest Wall Oscillation (HFCWO) technique. For that purpose, we build a model of the lung inspired from the literature. In this work, this model has been studied, validated and applied to HFCWO. Ways to improve the model have also been investigated. It is following those steps that this thesis is written.

The chapter 2 presents the model of the lung and the way to solve it numerically. The model is based on the coupling between two models : a zero dimensional quasi-fractal tree mimicking the bronchial tree and a multi-dimensional linear and isotropic elastic medium mimicking the lung's parenchyma. The tree submits damping pressures at localized areas in the elastic medium, which affects the material deformation. In order to have a better comprehension of the model in three dimensions, we analyze thoroughly the model in one dimension which is more tractable. The model is first studied on idealized non-physiological cases. We analyze the effect of the tree on the deformation of the material. We show that the tree alters the natural modes of vibration of the material and consequently, the resonance of the material. Resonance relates on the capacity of a vibrating system at amplifying its motion according to the pulsation of a driving force. This phenomenon presents interesting features for HFCWO. The chapter introduces the resonance phenoman which is used in the chapter 3. The model is then applied to model the ventilation at rest for idealized healthy and non-healthy lungs. This application allows to validate the model. It allows also to tune the set of parameters to get model predictions compatible with

the physiology of the lungs. This configuration is then used to apply the model to HFCWO.

The chapter 3 presents the application of the model to the HFCWO. It also describes a dimensionless formulation of the equations of the model, which raises two dimensionless parameters. Those dimensionless parameters inform on the different interactions between the parameters of the model. This chapter also presents a simplified formulation of the model, which is based on the theory of harmonic oscillators. This formulation proposes a parameter known as the quality factor, which relates the intensity of the damping of the tree to the deformation of the elastic material. It informs particularly on the properties of resonance of the material. The model is then applied to an idealized HFCWO. The model suggests that a frequency can maximize the air flows in the tree induced by the deformation of the material during a HFCWO therapy. This frequency is related to the fundamental natural frequency of the material. We also show that this frequency, computed from lungs data taken in the literature, is in accordance with the resonance frequency of the respiratory system measured in the literature. Finally, we propose the use of HFCWO as an non-invasive tool to measure lungs resistance and compliance.

The chapter 4 proposes future perspectives of improvement of the model and shows preliminary results. It discusses the hypotheses of the model and proposes a splitting method to reduce computational time of the numerical simulations. It also presents the setup of a clinical study that aims at investigating the efficiency of a HFCWO device. Particularly, this study takes an interest on measuring the air flows at mouth induced by the HFCWO therapy isolated from the ventilation flows. Indeed our model suggests that a resonance frequency may exist for the lungs, and might be measured from the mouth air flows induced by HFCWO. This experimental setup aims at studying the theoretical results in a clinical framework.

Part of this work is the the topic of a scientific article, submitted :

Optimal efficiency of high frequency chest wall oscillations and links with resistance and compliance in a model of the lung - Michaël Brunengo, Barrett R. Mitchell, Antonello Nicolini, Bernard Rousselet, and Benjamin Mauroy. arXiv:2108.02437 [physics.med-ph]

Chapter 2

Modelling the lungs to simulate tidal breathing for healthy and non-healthy lungs

"Puisque l'air nous est si absolument necessaire, il étoit bon que nous pussions nous en fournir pour quelque temps, & cet avantage nous a été assés adroitement ménagé."

Jean Claude Adrien Helvetius,
Histoire de l'Académie royale des Sciences, 1718, p.14.

Contents

2.1 Introduction

As discussed in the first chapter of this manuscript, the HFCWO technique is a therapeutical method based mainly on empirical knowledge. During a HFCWO procedure, both ventilation and the action of the therapy act on and in the lungs. Hence, the comprehension of the global behavior of the lungs during HFCWO can be facilitated by studying separately each influence - ventilation and HFCWO. In this chapter, we take an interest first and foremost mimicking healthy and pathological lungs to which HFCWO is primarily dedicated to. For these different cases, we model the ventilation at rest. Prior to that, this chapter introduces the construction of the model of the lungs that we will use in this manuscript. We dedicate most of the chapter on the comprehension of the model and on the phenomenon that take part in it, and on its application through numerical simulations of non-physiological and physiological behaviors of the lungs. This chapter allows to prepare our model of the lungs, from the building to the calibration, to study the HFCWO.

We develop a mathematical and numerical model of the core biomechanical phenomena involved in HFCWO by linking the flow of the air into the bronchial tree with the HFCWO-induced displacement of the lung parenchyma. The number of airways in the lung is very large and prevents from an exhaustive modeling of these airways. Hence, as in [13, 111], we couple two distinct models: the air circulation in a model of the bronchial tree, and the deformation of a material that mimics the respiratory zone. Different frameworks have been used in the literature to model the bronchial tree, from the most complex, based on 3D geometries that are reconstructed from CT-scans (Computerized Tomography scan) of the lungs [129, 118], to idealised tree geometries. Idealised tree geometries allow to develop more tractable models. They are either generated by algorithms that mimic the statistics of the airways [63, 131] or by using data-based models, with different levels of complexity, going from fractal-like models (one or two parameters) [135, 80, 81] to more complex geometries where each level of bronchi is described independently [72, 85, 84, 125].

In this work, we use a one parameter model of the bronchial tree. The bronchial tree is represented using a symmetrical dyadic tree composed of a cascade of rigid cylinders [80, 83]. The deformation of the lung tissue is modeled using linear elasticity, considering the tissue as an isotropic and homogeneous material, as in [137, 110]. We use the theory of small strains which is well adapted to the relative low pressures induced by HFCWO on the thorax. To define the coupling between the two models, described in section 2.2, we assume that the lung tissue is incompressible. Hence, the rate of volume change of the material in a region of the lung is assumed to correspond to the amount of air flow that is exchanged with the airway that feeds that region, as in [13, 111].

Although defined for any space dimension, the model is used in only one dimension in order to understand the influence of the coupling on the deformation of the lungs. Particularly, we observe some similarities between the behaviors of the model and the ones of oscillator systems that suggests the interest of studying the phenomenon of resonance, see section 2.4. Moreover, the unidimensional formulation is used to understand the intrinsic effects of each parameter on the deformation of the lungs and on the induced air flows and pressures in the tree in the case of the rest ventilation of healthy and pathological lungs, see section 2.5.

The contents of the appendices describe mostly the details of the mathematical computations. It explains more precisely some hypothesis and properties of the model and the way the numerical method is computed. Moreover it gathers in the form of tables the different configurations of parameters for the numerical simulations that we use in this manuscript.

2.2 The model of the lungs

We assume that the lungs fill a thee-dimensional reference domain $\Omega \subset \mathbb{R}^3$ at rest. We consider the lungs as two regions with different physics that are interacting together [13, 111]. The first region, called the tree region, corresponds to the bronchial airways and the alveolar ducts. The

second region, called the tissue region, corresponds to the lung's parenchyma. Our model of the lungs consists in the coupling between two models idealizing the two regions. The tissue region is modelled as an homogeneous deformable medium. It is considered incompressible and any rate of change of the volume of the material is related to a flow of air to and from the respiratory zone. The tree region gathers the airflows getting in or out of the respiratory region and consists in a cascade of bifurcating cylinders mimicking the bifurcating bronchi. The airflow in the airways has to overcome viscous friction that is represented by the airway hydrodynamic resistance to the air flow. The hydrodynamics resistance participates to the mechanics of the respiratory region by inducing a volumetric pressure in the material. The two next sections are dedicated to detail respectively the models of the bronchial tree (subsection 2.2.1) and of the lung's parenchyma and their coupling (subsection 2.2.2). The equation of the model is then written with the weak formulation suited to the numerical simulations (subsection 2.2.3). Finally, we present a numerical method to solve the equations of our model (subsection 2.2.4).

2.2.1 Modelling the air flow in the tree region

2.2.1.1 The tree region

Three different levels of modelling are used to describe the tree region, see Figure 2.1. The three levels of modelling are connected to mimic the bronchial airways and alveolar tracts. All the airways are considered as rigid cylinders assembled into a bifurcating tree. The size of the cylinders is decreasing at each bifurcation with a specific ratio h. The generation index of a cylinder in the tree corresponds to the number of bifurcations between the root of the tree and that cylinder. The root of the tree mimics the trachea and corresponds to the first generation with index 0.

The first level of the tree corresponds to $n+1$ successive generations. Here, the homothetic ratio between the generations is constant and is denoted $h = h_b$. We use the value of h_b from Weibel's model, $h_b = \left(\frac{1}{2}\right)^{\frac{1}{3}} \simeq 0.79$ [135, 80]. In this tree level, all the branches in the same generation have the same geometrical properties, but their inner air fluid dynamics can be different. The total number of terminal branches is $N = 2^n$.

The number of generations for the first level is $n+1$ and it can be lower than the approximate average of 17 generations of the conductive airways [136]. Hence, the second modelling level mimics the $17 - (n+1)$ generations of conductive airways. This level corresponds to a set of virtual subtrees, connected by set of two at each terminal branches of the tree of the first modelling level. The subtrees geometry is similar to the geometry of the tree of the first level, namely the homothetic ratio through the generations is still constant and $h = h_b$. However, within one of these subtrees, we assume that the air physics is identical in all the airways with the same generation index. The total number of terminal branches of the second modelling level is 2^{16}.

Finally, the third modelling level mimics the acini. An acinus can be viewed as a 6 generations dichotomous subtree with rigid cylindrical branches. In the acinus, we can consider that the size of the branches remain the same at each bifurcation, i.e. the size reduction ratio between two successive generations is $h_{ac} = 1$ [40]. The third modelling level corresponds to two acinus models connected to each terminal branches of the second modelling level.

With this model of tree, we study the air fluid dynamics in the first airways level only. The second and third level of modelling are virtual and only contribute in adding additional resistances into the first level of modelling tree, see below.

2.2.1.2 Pressure–flow relationship

The air in the branches is considered as an incompressible Newtonian fluid with viscosity η. We assume that air flows according to the steady-state Poiseuille's regime, i.e. the flow is low, fully developed and axisymmetric, and the acceleration of the fluid is neglected. We also neglect the

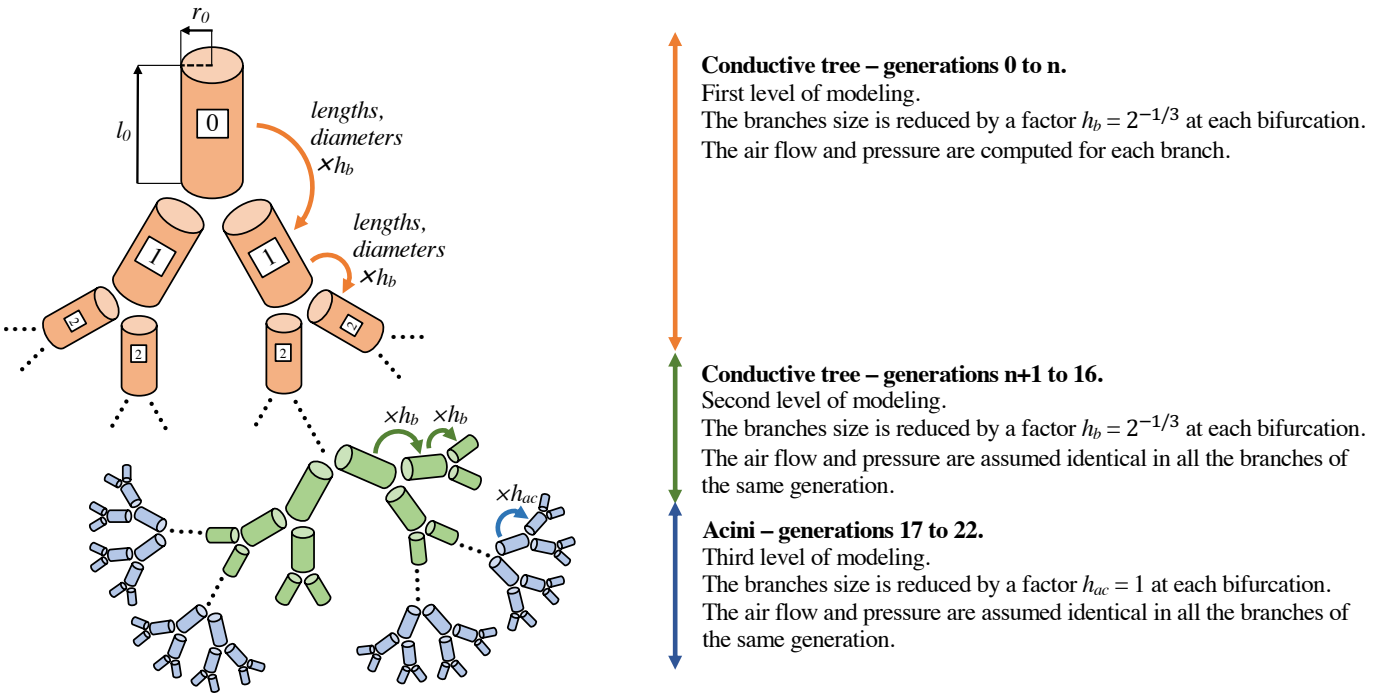

Figure 2.1: The airway tree is modelled as a cascade of bifurcating cylinders representing the bronchi and the alveolar ducts. At each bifurcation, the size of the branches is decreasing by an homothetic factor, fixed to $h_b = \left(\frac{1}{2}\right)^{\frac{1}{3}} \simeq 0.79$ in the conductive tree (17 first generations) [135, 80] and to $h_{ac} = 1$ in the acini (6 last generations) [136, 129]. The number written in the cylinders corresponds to the generation index of the branches, i.e. the number of bifurcations on the path between the root of the tree and the branch studied. The first generation corresponds the root of the tree that mimics the trachea, its index is 0. The airway tree model decomposes into three levels: the first level corresponds to the first $n+1$ generations where the air flows and pressures are determined in each airway; the second level corresponds to the next $17-(n+1)$ generations where the air flows and pressures are assumed identical in all the airways belonging to a same generation; the third level corresponds to the acini (last six generations) where the air flows and pressures are also assumed identical in all the airways belonging to the same generation.

influence of the bifurcations on the air flow and the pressure drop in the nasopharyngeal pathway [87]. We consider the pressures at the mouth and at the opening of the trachea equal, and the reference pressure (i.e. the zero pressure) is the atmospheric pressure [87]. We choose the sign of the volumetric flow rate to be positive if it exits the tree through the root. Poiseuille's flow corresponds to a linear regime and a linear relationship between pressure drops and flows can be derived [86]. If the pressure drop between the outlet and the inlet of the branch is $p_{in} - p_{out}$, then the flow F going through the cylinder checks

$$p_{in} - p_{out} = R\,F$$

where R is the hydrodynamic resistance of the cylinder. The hydrodynamic resistance depends on the geometry of the cylinder and on the properties of the fluid (i.e. the air),

$$R = \frac{8\eta l}{\pi r^4}$$

with r and l the respective radius and length of the cylinder.

In a quasi-fractal tree, radii and lengths of the branches in the generation i can be derived from the size of the root branch, whose radius is r_0 and length is l_0, and from the factor h: $r_i = h^i r_0$ and $l_i = h^i l_0$. Similarly, we can derive a scaling law on the hydrodynamic resistances, $R_i = \left(\frac{1}{h_b^3}\right)^i R_0$, with R_0 the hydrodynamic resistance of the trachea. Since $h_b = \left(\frac{1}{2}\right)^{\frac{1}{3}}$, we can

conclude that $R_i = 2^i R_0$. We underline here that the index 0 of the resistance R_0 corresponds to the first generation (the trachea). In parallel, the resistance R_i is associated to the resistance of the branches at the generation $i+1$, see Figure 2.2 for a simple case.

From the pressure–flow relationships in the cylinders, we can derive a linear relationship for the whole airway tree. We define the flows vector $F = (F_j)_{j=1,...,N}$, that represents the airflows at the terminal branches of the tree and the pressures vector $P = (p_j)_{j=1,...,N}$, that represents the air pressures at those same branches. The linear relationship between the pressures and flows vectors can be written using the resistance matrix $\mathcal{R}$ of the airway tree [37, 25],

$$P = \mathcal{R}F \tag{2.1}$$

The coefficients of the resistance matrix $\mathcal{R}$ are sums of the hydrodynamic resistances of the cylinders in the paths and the subpaths linking the root of the $n+1$ generations tree and the terminal branches of the $n+1$ generations tree. $\mathcal{R}$ is a symmetrical and positive definite matrix, thus invertible [25]. For example, the resistance matrix of a tree with three generations is

$$\mathcal{R} = \begin{pmatrix} R_0+R_1+R_2 & R_0+R_1 & R_0 & R_0 \\ R_0+R_1 & R_0+R_1+R_2 & R_0 & R_0 \\ R_0 & R_0 & R_0+R_1+R_2 & R_0+R_1 \\ R_0 & R_0 & R_0+R_1 & R_0+R_1+R_2 \end{pmatrix} \tag{2.2}$$

The equivalent resistance R_{eq} of the tree corresponds to the scalar that relates an identical pressure p applied at each terminal branch with the total amount of airflow in the tree F_0 (i.e. the air flow in the first generation): $p = R_{eq}F_0$. The pressures vector at terminal branches is then $P = pJ$ with $J =^t (1, ..., 1) \in \mathbb{R}^N$. The flows vector is then computed using the resistance matrix $P = \mathcal{R}F$. Then we can derive the scalar relationship, using $F_0 =^t JF$, $p = \frac{1}{{}^tJ\mathcal{R}^{-1}J}F_0$, and

$$R_{eq} = \frac{1}{{}^tJ\mathcal{R}^{-1}J}$$

In order to account for influence of the subtrees of the second and third modelling levels, the hydrodynamic resistances of the terminal branches of the tree of the first modelling levels are modified. Since the physics of air in the second and third modelling levels are assumed identical per generation of subtrees, the pressures at the terminal branches of a single subtree are all the same. Hence, each subtree hydrodynamic response is determined based on its equivalent hydrodynamic resistance only. The hydrodynamic resistance of one subtree of the second modelling level is $R_{st,n} = \frac{R_n}{h_b^3}\sum_{i=0}^{17-n-2}\left(\frac{1}{2h_b^3}\right)^i = (17-(n+1))\frac{R_n}{h_b^3}$ and for the third modelling level, it is $R_a = R_{16}\sum_{i=0}^{5}\left(\frac{1}{2h_{ac}^3}\right)^i$. To each terminal branch of the first modelling level of the tree are connected two subtrees of the second modelling level and $2^{17-(n+1)}$ subtrees of the third modelling level. Finally, the resistance R_{n+1} of the terminal branches of the tree of the first modelling level is replaced by the resistance $\tilde{R}_{n+1}$ that accounts for the subtrees,

$$\tilde{R}_n = R_n + \frac{R_{st,n}}{2} + \frac{R_a}{2^{17-(n+1)}} \tag{2.3}$$

see the appendix 2.A for more details. Hence, as an example, the resistance matrix of a three generations tree considering the three levels of modelling is different from (2.2) and is detailed in Figure 2.2.

2.2.1.3 Feeding the respiratory region with air

The domain Ω which reflects the spatial occupation of the lung's parenchyma is decomposed into $N = 2^n$ regions $(A_i)_{i=1..N}$. Each one of the A_i is fed (and feeds) with air by a single tree

branch among the terminal branches of the $n+1$ generations tree, as shown on Figure 2.2. We neglect the volume of the bronchial tree, which represents a small fraction of the volume of the lung, about 10% [136]. In order to mimic how the air is exchanged between the respiratory region and the tree region, we assume that the airflow that goes through the branch i is equal to the rate of volume change of the corresponding region A_i, see below.

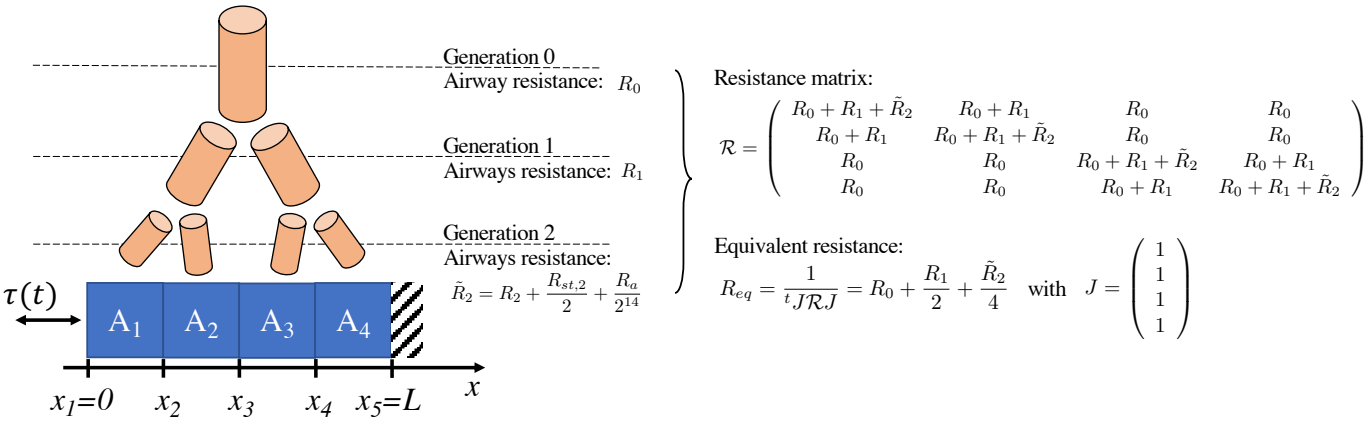

Figure 2.2: Unidimensional schematic of the coupling between the tree region and the tissue region describing the hypothesis of the tree. The airway tree is modelled as a cascade of bifurcating cylinders representing the bronchi and the alveolar ducts. At each bifurcation, the size of the branches is decreasing by an homothetic factor, fixed to $h_b = \left(\frac{1}{2}\right)^{\frac{1}{3}} \simeq 0.79$ in the conductive tree (17 first generations) [135, 80] and to $h_{ac} = 1$ in the acini (6 last generations) [136, 129]. The number written in the cylinders corresponds to the generation index of the branches, i.e. the number of bifurcations on the path between the root of the tree and the branch studied. The first generation corresponds the root of the tree that mimics the trachea, its index is 0. The airway tree model decomposes into three levels: the first level corresponds to the first $n+1$ generations where the air flows and pressures are determined in each airway; the second level corresponds to the next $17-(n+1)$ generations where the air flows and pressures are assumed identical in all the airways belonging to a same generation; the third level corresponds to the acini (last six generations) where the air flows and pressures are also assumed identical in all the airways belonging to the same generation.

2.2.2 Modelling the mechanics of the respiratory region

We model the lung tissue as an homogeneous elastic material [73] and use small strains theory. This choice is well adapted to HFCWO, since this technique applies small oscillating pressures on the thorax. This assumption has also been done in the literature for tidal ventilation modeling purposes and is considered valid since the tidal breathing frequency is low [109].

Lung's tissue displacesments at a location $x \in \Omega$ and at a time $t \in \mathbb{R}_+$ are represented by the variable $u(x,t) \in \mathbb{R}^3$, with 3 the spatial dimension considered. The displacements check the equation,

$$\rho \frac{\partial^2 u}{\partial t^2} - \mathrm{div}(\sigma(\mathrm{u})) = 0 \tag{2.4}$$

where ρ is the volumetric mass density and $\sigma(u)$ is the stress tensor describing the local stress of a material with the displacement u. The boundary $\partial\Omega$ of Ω is decomposed into two sub-boundaries: Γ_1 represents the part of the boundary where the stress is known, either due to the action of the respiratory muscles or to the action of the HFCWO device; and Γ_2 represents the zones where the displacement is known (typically zero). Then, the boundary conditions on $\partial\Omega$ and the initial conditions in Ω are

$$\begin{cases} \sigma(u).n = \tau(t) & \text{on } \Gamma_1 \\ u = u_b & \text{on } \Gamma_2 \\ u(x, t=0) = u_0(x) & \text{for } x \in \Omega \end{cases} \tag{2.5}$$

The applied force τ is assumed to be periodic in time unless specifically said. To cancel any rigid movement, the boundary Γ_2 is fixed ($u_b = 0$).

Stress-strain relationship. We assume the material to be isotropic and to follow linear elasticity. We denote the stress $\sigma_{elastic}(u)$, with u the local displacement. With I the identity matrix, we have

$$\sigma_{elastic}(u) = \lambda \text{ tr } (\epsilon(\text{u}))\, \text{I} + 2\mu\, \epsilon(\text{u}) \tag{2.6}$$

with the strain tensor $\epsilon(u) = \frac{1}{2}\left(\nabla u + {}^t\nabla u\right)$ and where λ and μ are the Lamé parameters, with λ the first Lamé coefficient and μ the shear modulus of the material. These coefficients can be related to the Young's modulus E and Poisson's ratio ν of the material: $\lambda = \frac{E\nu}{(1-2\nu)(1+\nu)}$ and $\mu = \frac{E}{2(1+\nu)}$.

The air flowing out of the respiratory region has to travel through the bronchial tree, so any change of the volume of the material is counteracted by the resistance to the air flow induced by the tree structure. This is reflected in the material stress–strain relationship by a supplementary local stress, actually a pressure, that depends on how the air is conveyed in the tree. Each terminal branch i induces a homogeneous pressure p_i in its corresponding region A_i in Ω. The pressures are determined by the rate of volume change of the A_i along time. In the case of small displacements, this rate, which corresponds to the air flow, can be approximated with

$$\mathcal{F}_i[\dot{u}] = \int_{A_i} -\text{div}(\dot{u})dx \quad [111]$$

with $\dot{u} = \frac{\partial u}{\partial t}$. Because of the pressures–flows relationship in the terminal branches expressed in the equation (2.1), the pressure p_i in one A_i depends on the air flows in all the tree terminal branches. Hence, denoting $\mathcal{F}[\dot{u}] = (\mathcal{F}_i[\dot{u}])_{1\leqslant i\leqslant N}$ and $P = (p_i)_{1\leqslant i\leqslant N}$, the pressure is a piecewise continuous function that depends on the hydrodynamic resistances of the airways tree:

$$p_{tree}(\mathcal{F}[\dot{u}]) = \sum_{i=1}^{N} p_i(\mathcal{F}[\dot{u}])\chi_i \tag{2.7}$$

$$\text{with } \chi_i(x) = \begin{cases} 1, & \text{if } x \in A_i \\ 0, & \text{otherwise} \end{cases}$$

and

$$P = (p_i(\mathcal{F}[\dot{u}]))_{1\leqslant i\leqslant N} = \mathcal{R}\mathcal{F}[\dot{u}] = \left(\sum_{j=1}^{N}\mathcal{R}_{ij}\mathcal{F}_j[\dot{u}]\right)_{1\leqslant i\leqslant N} = -\left(\sum_{j=1}^{N}\mathcal{R}_{ij}\int_{A_j}\text{div}(\frac{\partial u}{\partial t})dy\right)_{1\leqslant i\leqslant N}$$

Hence, the inner stress tensor induced by the tree is

$$\sigma_{tree}(\dot{u}) = -p_{tree}(\mathcal{F}[\dot{u}])I$$

Finally,

$$\sigma(u, \mathcal{F}[\dot{u}]) = \underbrace{\lambda\text{Tr}(\epsilon(\text{u}))\text{I} + 2\mu\epsilon(\text{u})}_{\sigma_{elastic}(u)}\ \underbrace{-p_{tree}(\mathcal{F}[\dot{u}])I}_{\sigma_{tree}(\dot{u})} \tag{2.8}$$

The resulting stress–strain relationships in equation (2.8) is that of a viscoelastic material, with a non-local viscous behavior.

2.2.3 Weak formulation of the system of equations

The model of the lung developed in the previous section consists in the equation of the mechanics for the respiratory zone (2.4), its boundary and initial conditions (2.5), the viscoelastic stress–strain relationship for the model of the respiratory zone (2.8), and the matrix pressures–flows relationship at the terminal branches of the bronchial tree model (2.1).

To compute an approximated solution, the system is solved numerically using its weak formulation and the finite element method. The weak formulation and the finite elements method are convenient for dealing with the divergence of piecewise constant functions, such as the pressures p_i. A detailed description of the method is given in the appendix 2.B.

Weak formulation of the system of equations. The stress tensor is not everywhere differentiable, hence equation (2.4) should be written using a principle of virtual work [11], or mathematically speaking, with the weak formulation, suited to the finite elements method. For any proper smooth test function $w : \Omega \to \mathbb{R}^3$, the weak formulation of the equation (2.4) is

$$\int_\Omega \left(\rho \frac{\partial^2 u}{\partial t^2} - div(\sigma(u)) \right) w dx = 0$$

or in other words with (2.8)

$$\int_\Omega \left(\rho \frac{\partial^2 u}{\partial t^2} - div(\sigma_{elastic}(u) + \sigma_{tree}(\dot{u})) \right) w dx = 0 \tag{2.9}$$

Using integration by parts and (2.7), the previous equation becomes

$$\int_\Omega \left(\rho \frac{\partial^2 u}{\partial t^2} w + \sigma_{elastic}(u) : \epsilon(w) \right) dx - \int_{\partial\Omega} \sigma(u).n \; w \; dS - \left(\int_\Omega \sum_{i=1}^{N} p_i(\mathcal{F}[\dot{u}]) \chi_i div(w) dx \right)_{1 \leqslant i \leqslant N} = 0 \tag{2.10}$$

with the colon denoting double contraction of two tensors of rank 2. Hence, the equation (2.10) writes

$$\int_\Omega \left(\rho \frac{\partial^2 u}{\partial t^2} w + \sigma_{elastic}(u) : \epsilon(w) \right) dx - \int_{\partial\Omega} \sigma(u).n \; w \; dS - \sum_{i=1}^{N} p_i(\mathcal{F}[\dot{u}]) \int_{A_i} div\,(w)\, dx = 0 \tag{2.11}$$

Finally, for any proper smooth test function $w : \Omega \to \mathbb{R}^3$, the weak formulation of (2.4) with boundary conditions gives the system :

$$\begin{cases} \int_\Omega \left(\rho \frac{\partial^2 u}{\partial t^2} w + \sigma_{elastic}(u) : \epsilon(w) \right) dx - \int_{\Gamma_1} \tau \; w \; dS - \sum_{i=1}^{N} p_i(\mathcal{F}[\dot{u}]) \int_{A_i} \mathrm{div}\,(w)\, dx = 0 & \text{on } \Omega \\ u(x, t = 0) = u_0(x) & \text{for } x \in \Omega \\ u = u_b \;\; \textbf{and} \;\; w = 0 & \text{on } \Gamma_2 \\ (p_i(\mathcal{F}[\dot{u}]))_{1 \leqslant i \leqslant N} = - \left(\sum_{j=1}^{N} \mathcal{R}_{ij} \int_{A_j} \mathrm{div}(\frac{\partial u}{\partial t}) dx \right)_{1 \leqslant i \leqslant N} & \end{cases} \tag{2.12}$$

This system holds for any smooth test function which cancels on Γ_2.

The solution of the system of equations (2.12) defines the three-dimensional displacement, for all points in space and for all time, of a visco-elastic material stimulated at boundaries. This mimicks the lung's parenchyma locally subjected to the dissipation of a network of connected pipes idealising the bronchial tree. In our model, the effects of the tree on the lung's tissue

arise as much from the deformation of the medium as from the different circulations of air inside the bronchus tracks. Hence, inside a 23 generations tree with millions of airways, at each time, different behaviors occur and act on different local regions of the elastic medium. In order to bring a better understanding of those phenomena and to suggest new insights on the physiology of the lungs, we will use numerical simulations with the finite element method.

We gather all the variables of the model in the following table 2.1 for a better distinction.

Model input parameters		
Physical quantity	**Parameter name**	**Unit**
Lung volumetric density	ρ	$\mathrm{kg.m^{-3}}$
Characteristic lungs size	L	m
Lamé parameters	$\lambda + 2\mu$	Pa
Tree root radius (trachea radius)	r_0	m
Tree root length (reduced trachea length)	l_0	m
Resistance matrix of the airway tree	$\mathcal{R}$	$\mathrm{cmH_2O.s.L^{-1}}$
Hydrodynamic resistance of the airway tree	R_{eq}	$\mathrm{cmH_2O.s.L^{-1}}$
Frequency of the applied pressure	f	Hz
Amplitude of the applied pressure	A	Pa

Table 2.1: Input parameters of the model.

2.2.4 Numerical method : the finite element method

The system of equations (2.12) has been defined for three dimensions. However, the system (2.12) is also valid for one or two dimensions. In this chapter and the next one, we focus the numerical study to one spatial dimension. This choice is explained in the next section. Nevertheless, we aim at applying and studying the model for multi-dimensions. Hence, the numerical method is introduced here for three dimensions and we send the reader to the chapter 4 for more details on the perspectives of its use. We will then study the unidimensional formulation of the model.

To solve the system of equations (2.12), we will use the finite element method. The Finite Element Method (FEM), very popular tools among engineers and researchers, is a numerical method approximating the solution of partial differential equations [11]. Every numerical method approximates solution of equations on a finite number of points in space, as the FEM. The FEM works with discrete systems based on the weak form of a partial differential equation with boundary conditions. Basically, a given structure, for example a beam, is represented as an assemblage of finite elements on which the solution is calculated, see below. The calculation details of the application of the method in our case is described in the appendix 2.B.

Using the finite element method, the continuous equation (2.10) is turned into a discrete one. Typically, the domain is splitted into a finite number n_e of identical elements, also called cells. The solution will be computed on specific points in the cells such as vertices, edges or faces. In three dimensions, the main element geometries are tetrahedron or hexahedron. The number of cell vertices (also called nodes) depends on the geometry of the element. Typically, while tetrahedron have four vertices, regular hexahedron (cube) have eight vertices. We denote

by n_v the number of vertices per cell. The goal, in our case, is to look for the displacement field. For that, it is expressed in the subspace spaned with the basis functions, denoted ϕ, which are polynomial with a specific order. The latter indicates the spatial points where the solution will be expressed on each cell. Those points are known as degrees of freedom. Hence, the more there are degrees of freedom, the more precise the approximated solution is. For example, if we use a 1^{st} order polynomial function, the degrees of freedom will be associated with the nodes of the mesh and we would have $n_e \times n_v$ degrees of freedom. Let's denote by n_d the number of degrees of freedom. For higher order elements, the degrees of freedom can be associated also to faces, edges, etc, and the number of degrees of freedom increases.

For any proper smooth test function $w : \Omega \to \mathbb{R}^m$, the weak formulation of the equation (2.4) is

$$\int_\Omega \left(\rho \frac{\partial^2 u}{\partial t^2} w + \sigma_{elastic}(u) : \epsilon(w) \right) dx - \int_{\partial\Omega} \sigma(u).n \; w \; dS + \sum_{i=1}^{N} p_i(\mathcal{F}[\dot{u}]) \int_{A_i} div\,(w)\, dx = 0 \quad (2.13)$$

The displacement field is approximated using the basis functions of the finite element $u(x,t) = \sum_{k=0}^{n_d} u_k(t)\phi_k(x)$ as well as the test function, $w = \sum_{l=0}^{n_d} w_l(t)\phi_l(x)$, with $x \in \mathbb{R}^3$, $t \in \mathbb{R}$. Injecting the approximated u and w in the equation (2.13) leads (2.13) to be written as a linear matrix-vector equation :

$$M\frac{d^2U(t)}{dt^2} \; + \; D\frac{dU(t)}{dt} \; + \; KU(t) \; = \; \tau(t)h \quad (2.14)$$

The vector $U(t) = (u_i(t))_{0 \leqslant i \leqslant n_d}$ is the unknown displacement vector containing the n_d displacement components u_i at the degree of freedom i for all time $t \in \mathbb{R}^+$. The matrices M and K are known as the mass and the stiffness matrix. The matrix D is the damping matrix arising from the coupling with the tree structure. It is defined as $D =^t G\mathcal{R}G$ whose terms are defined above. The vector h is the vector of loads. Finally the equation (2.18) has only a time dependency. With $x \in \mathbb{R}^3$, those objects are defined as

$$\begin{cases} M_{kl} = \int_\Omega \rho\phi_k(x)\phi_l(x)dx \\ K_{kl} = \int_\Omega \sigma_{elastic}(\phi_k(x)) : \epsilon(\phi_l(x))dx \\ h_l = \int_{\Gamma_1} \phi_l(x)dS \\ G_{ik} = \int_{A_i} \mathrm{div}(\phi_k)dx \end{cases} \quad (2.15)$$

More specifically, the components of the stiffness matrix are computed as

$$K_{kl} = \int_\Omega \left[\lambda \; \mathrm{div}(\phi_k(x))\mathrm{div}(\phi_l(x)) + \mu \; \epsilon(\phi_k(x)) : \epsilon(\phi_l(x))\right] dx$$

We recall that the calculation details are described in the appendix 2.B. Then, in order to solve the linear system (2.14), the time has to be discretized. However, for now, we refer the reader to the chapter 4. The numerical scheme is presented as well as the perspectives of the use of the multi-dimensional model.

In order to understand the physics hidden in the set of equations (2.12) in a tractable framework, we will focus, in most parts of this manuscript, on unidimensional cases and limit the spacial dimension to a single coordinate, say x_1. Actually, with one dimension, we will see that an analytical solution of the model equation can be computed in a particular case. In the next

section, we describe the unidimensional formulation of the model, the application of the FEM with one dimension and the way to compute the analytical solution.

2.3 The unidimensionnal formulation of the model of the lungs

The core of our application of the model is the understanding of the lungs, particularly during a HFCWO therapy. However, as the previous paragraphs have pointed out, the interaction between the tree and the tissue region, as well as the non negligible number of variables in the model, can lead to numerous different behaviors. In order to catch the essence of the coupling and of the influence of the parameters, we decide to study the model with simple cases. For that purpose, we restrict now the study to one spatial dimension. The unidimensional (1D) formulation allows us to analyze the behaviors involving in the coupling more easily. The reduction of the spatial dimension decreases the number of degrees of freedom and leads inevitably to a reduction of the complexity and of the calculation time of the solving numerical method. Validating the numerical method on simple case (1D) eases the implementation and the comprehension of more complex cases (3D). Additionally, we found out that an analytical solution of the strong formulation (2.4) in 1D can be calculated on a particular case. The analytical solution is used to reduce computational time and to validate the resolution of the 1D numerical method. We present in this section the unidimensional formulation of our model (subsection 2.3.1), the application of the numerical method with one dimension (subsection 2.3.2) and the way to compute the analytical solution (subsection 2.3.3).

2.3.1 Unidimensional formulation

The unidimensional geometry can be viewed in the three dimensional space as a cylinder that is the extrusion along the axis x_1 of a surface in the plane $(0, x_2, x_3)$. In terms of mechanics, we assume that the virtual displacement w_1 depends only on x_1 and that the displacements w_2 and w_3 are zero. We assume also that $\epsilon_{11}(u)$ is the single non zero term in the strain tensor. For the sake of simplicity, when using the unidimensional formulation, we will improperly drop most of the index 1 and use respectively x, u, w and τ instead of x_1, u_1, w_1 and τ_1 ; the rest of the manuscript will be careful to distincly highlight the use of this formulation.

In this case, the material spans on the domain $\Omega = [0, L]$ and $x \in \mathbb{R}$. We assume that the extruded surface is a square with side length L and surface area $S_L = L^2$. Then, the rate of volume change can be rewritten

$$\mathcal{F}_j[\dot{u}] = -\int_{A_j} \operatorname{div}(\frac{\partial u}{\partial t}) dx_1 dx_2 dx_3 = -S_L \int_{x_j}^{x_{j+1}} \frac{\partial}{\partial x}(\frac{\partial u}{\partial t}) dx$$

where the projection of A_j on the axis x_1 is the segment $[x_j, x_{j+1}]$. For the sake of simplification, we will now identify the set A_j with its projection on the x_1 axis, i.e. $A_j = [x_j, x_{j+1}]$. Then, the tree pressure in the stress–strain relationship reformulates as

$$\begin{aligned} p_{\text{tree}}(\mathcal{F}[\dot{u}]) &= (p_i(\mathcal{F}[\dot{u}]))_{1 \leqslant i \leqslant N} \\ &= -S_L \left(\sum_{j=1}^{N} \mathcal{R}_{ij} \int_{x_j}^{x_{j+1}} \frac{\partial}{\partial x}(\frac{\partial u}{\partial t}) dx \right)_{1 \leqslant i \leqslant N} \\ &= -S_L \left(\sum_{j=1}^{N} \mathcal{R}_{ij} \left(\frac{\partial u}{\partial t}(x_{j+1}, t) - \frac{\partial u}{\partial t}(x_j, t) \right) \right)_{1 \leqslant i \leqslant N} \end{aligned} \tag{2.16}$$

where $\mathcal{R}_{ij}$ is the i, j component of the matrix $\mathcal{R}$.

With the definition (2.8) of the stress tensor, $\sigma_{elastic}$ can be rewritten as $\sigma_{elastic}(u) = (\lambda + 2\mu)\frac{\partial u}{\partial x}$. The case studied here assumes an active constraint applied at $x = 0$ and no displacement

at $x = L$. Then, for any smooth function w such that $w(L) = 0$, the weak formulation of our model in one dimension with boundary conditions is

$$\begin{cases} \int_0^L \rho \frac{\partial^2 u}{\partial t^2} w + (\lambda + 2\mu) \frac{\partial u}{\partial x} \frac{\partial w}{\partial x} \, dx - \sum_{i=1}^{N} p_i(\mathcal{F}[\dot{u}]) \int_{A_i} \frac{\partial w}{\partial x} \, dx - \tau(t) w(t,0) = 0 \\ u(0,x) = u_0(x) \\ u(t,L) = u_b(L) \quad \textbf{and} \quad w(L) = 0 \\ p_i(F[\dot{u}]) = -S_L \left(\sum_{j=1}^{N} \mathcal{R}_{ij} \int_{A_j} \frac{\partial^2 u}{\partial x \partial t} dx \right) \quad i = 1, \dots N \end{cases} \tag{2.17}$$

In the next subsection, we adapt the finite element method described previously.

2.3.2 The finite element method and numerical scheme

Here, we present the application of the finite element with one dimension and the numerical scheme used to solve the unidimensional set of equations (2.17).

The finite element method

We apply the finite element method to the uni-dimensional set of equations (2.17), as explained previously in the subsection 2.2.4. We recall that a description of the method is detailed in the appendix 2.B. The unidimensional domain $\Omega = [0, L]$ is splited into n_x segments of two nodes, and we define $(x_i)_{0 \leqslant i \leqslant n_x}$, $x_i = i \times \delta x$, $\delta x = \frac{L}{n_x}$. Using the finite element method, and polynomial of order 1 as basis functions, the main equation of (2.17) is expressed as a linear matrix-vector relation :

$$M \frac{d^2}{dt^2} U(t) \; + \; D \frac{dU(t)}{dt} \; + \; KU(t) \; = \; \tau(t) h \tag{2.18}$$

where $U(t) = (u_i(t))_{0 \leqslant i \leqslant n_x}$ is the unknown displacement vector containing the $n_x + 1$ displacement elements u_i at point x_i for all time $t \in \mathbb{R}^+$. For one dimension, the matrices M, K and D as well as vector of load h are defined as

$$\begin{cases} M_{kl} = \int_0^L \rho \phi_k(x) \phi_l(x) dx \\ K_{kl} = \int_0^L (\lambda + 2\mu) \frac{\partial \phi_k(x)}{\partial x} \frac{\partial \phi_l(x)}{\partial x} dx \\ h_l = \phi_l(0) \delta_{l0} \\ G_{ik} = \int_{A_i} \frac{\partial \phi_k(x)}{\partial x} dx \end{cases} \tag{2.19}$$

As an example, the calculation of the mass matrix in one dimension can be found in the appendix 2.B.

Numerical scheme

The matrix-vector equation (2.19) is transformed into a system of two equations of order 1 by setting $V = \frac{dU}{dt}$. The numerical scheme is directly applied by the numerical tool we use. We use the solver ode15s of Octave [27] that uses variable order method based on backward difference formulas [20]. The system of two equations solved by ode15s is :

$$\begin{cases} V - \frac{dU}{dt} = 0 \\ M \frac{dV}{dt} = -KU \; - \; DV + \; \tau(t) h \end{cases} \tag{2.20}$$

Space and time discretization

In the unidimensional simulations of this manuscript, the maximal number of generations that

we consider for the tree structure is eight. Consequently the domain $\Omega = [0, L]$ is never splitted into more than $N = 2^7 = 128$ A_i sub-domains. In order to get a satisfying spatial precision, the space step is always lower than $L/128$. Specifically, for a eight generations tree, we choose 5 space steps per A_i sub-domain. The A_i sub-domains share $N - 1$ spatial points. Hence, the necessary number of points is $n_x + 1 = 5N - N = 4N = 512$. And consequently, the space step is $\delta x = L/511$. We set $\delta x = L/511$ for all unidimensional numerical simulations.

We denote by $T = 1/f$ the period of the periodic pressure τ applied on the boundary and by δt the time step. The time step is chosen experimentally. As we apply pressures with different frequencies, the time step is adapted to the case studied. We compare several solutions computed from several time steps : $\delta t = T/200$, $\delta t = T/250$ and $\delta t = T/300$. Globally, we observe that the computed solution is smoother with $\delta t = T/250$ than with $\delta t = T/200$. Moreover, the computed solution is similar with $\delta t = T/250$ and $\delta t = T/300$. Hence we set the time step to $\delta t = T/250$.

2.3.3 Analytical solution of the unidimensional model

We recall that we set $\Omega = [0, L] = \cup_{i=1}^{N} A_i$ and that the resistance matrix of the $n + 1$ tree is $\mathcal{R}$. To get the proper dimension for the air flows in 1D, we denote $\mathcal{R}_s = S_L \mathcal{R}$ with $S_L = L^2$ a surface area.

Here we denote by x_i and x_{i+1} the spatial coordinates of the boundaries of the A_i such as $A_i = [x_i, x_{i+1}]$. The equation of the lung model can be written on each A_i with boundary conditions at x_i and x_{i+1}. The solution of the equation on a A_i is denoted by u_i.

$$\rho \frac{\partial^2 u_i}{\partial t^2} - (\lambda + 2\mu) \frac{\partial^2 u_i}{\partial x^2} = 0 \qquad \text{on } A_i = [x_i, x_{i+1}] \ \forall i \tag{2.21}$$

$$(\lambda + 2\mu) \frac{\partial u_{i-1}}{\partial x}(t, x_i) - p_{i-1} = (\lambda + 2\mu) \frac{\partial u_i}{\partial x}(t, x_i) - p_i \qquad \text{for } i \geqslant 2 \tag{2.22}$$

$$(\lambda + 2\mu) \frac{\partial u_1}{\partial x}(t, x_1) - p_1 = A_1 \cos(c\kappa t) + A_2 \sin(c\kappa t) \qquad \text{for } i = 1 \tag{2.23}$$

$$u_i(t, x_{i+1}) = u_{i+1}(t, x_{i+1}) \qquad \text{for } i < N \tag{2.24}$$

$$u_N(t, x_{N+1}) = 0 \qquad \text{for } i = N \tag{2.25}$$

$$p = (p_i)_i = \mathcal{R}_s \times (F_i)_i \text{ with } F_i = \frac{\partial u_i}{\partial t}(t, x_i) - \frac{\partial u_i}{\partial t}(t, x_{i+1}) \tag{2.26}$$

Here, κ is in rad.m^{-1} and the time pulsation is $c\kappa$ which is in rad.s^{-1}.

We search a solution of the type

$$u_i(t, x) = (a_i \cos(\kappa x) + b_i \sin(\kappa x)) (c_i \cos(c\kappa t) + d_i \sin(c\kappa t))$$

with a_i, b_i, c_i, d_i four constants and $c = \sqrt{(\lambda + 2\mu)/\rho}$. It can be rewritten in the form

$$u_i(t, x) = \alpha_i \cos(\kappa x) \cos(c\kappa t) + \beta_i \cos(\kappa x) \sin(c\kappa t) + \gamma_i \sin(\kappa x) \cos(c\kappa t) + \delta_i \sin(\kappa x) \sin(c\kappa t)$$

with α_i, β_i, γ_i and δ_i four other constants. With this formulation, the equation (2.21) in A_i is always verified. We will now focus on the conditions at the boundaries of the A_i, i.e. at the $(x_i)_i$. We denote

$$\begin{aligned} C_{l,i} &= \cos(\kappa_i x_i) \text{ and } C_{r,i} = \cos(\kappa_i x_{i+1}) \\ S_{l,i} &= \sin(\kappa_i x_i) \text{ and } S_{r,i} = \sin(\kappa_i x_{i+1}) \end{aligned} \tag{2.27}$$

The boundary equations at the $(x_i)_i$ form a linear system on the α_i, β_i, γ_i and δ_i. Since the functions $t \to \sin(c\kappa t)$ and $t \to \cos(c\kappa t)$ are linearly independent, we obtain two equations for each boundary condition. Hence,

Equation (2.22), for $i \geqslant 2$:

On $\cos(c\kappa t)$: $(\lambda+2\mu)(-\alpha_{i-1}S_{r,i-1}+\gamma_{i-1}C_{r,i-1}) - c\left(\mathcal{R}_s\left(\beta_j(C_{l,j}-C_{r,j})+\delta_j(S_{l,j}-S_{r,j})\right)_j\right)_{|i-1}$
$= (\lambda+2\mu)(-\alpha_i S_{l,i}+\gamma_i C_{l,i}) - c\left(\mathcal{R}_s\left(\beta_j(C_{l,j}-C_{r,j})+\delta_j(S_{l,j}-S_{r,j})\right)_j\right)_{|i}$

On $\sin(c\kappa t)$: $(\lambda+2\mu)(-\beta_{i-1}S_{r,i-1}+\delta_{i-1}C_{r,i-1}) - c\left(\mathcal{R}_s\left(-\alpha_j(C_{l,j}-C_{r,j})-\gamma_j(S_{l,j}-S_{r,j})\right)_j\right)_{|i-1}$
$= (\lambda+2\mu)(-\beta_i S_{l,i}+\delta_i C_{l,i}) - c\left(\mathcal{R}_s\left(-\alpha_j(C_{l,j}-C_{r,j})-\gamma_j(S_{l,j}-S_{r,j})\right)_j\right)_{|i}$

Equation (2.23), $i = 1$:

On $\cos(c\kappa t)$: $(\lambda+2\mu)(-\alpha_1 S_{l,1}+\gamma_1 C_{l,1}) - c\left(\mathcal{R}_s\left(\beta_j(C_{l,j}-C_{r,j})+\delta_j(S_{l,j}-S_{r,j})\right)_j\right)_{|1} = A_1/\kappa$

On $\sin(c\kappa t)$: $(\lambda+2\mu)(-\beta_1 S_{l,1}+\delta_1 C_{l,1}) - c\left(\mathcal{R}_s\left(-\alpha_j(C_{l,j}-C_{r,j})-\gamma_j(S_{l,j}-S_{r,j})\right)_j\right)_{|1} = A_2/\kappa$

Equation (2.24), $i < N$:

On $\cos(c\kappa t)$: $\alpha_i C_{r,i}+\gamma_i S_{r,i} = \alpha_{i+1}C_{l,i+1}+\gamma_{i+1}S_{l,i+1}$

On $\sin(c\kappa t)$: $\beta_i C_{r,i}+\delta_i S_{r,i} = \beta_{i+1}C_{l,i+1}+\delta_{i+1}S_{l,i+1}$

Equation (2.25), $i = N$:

On $\cos(c\kappa t)$: $\alpha_N C_{r,N}+\gamma_N S_{r,N} = 0$

On $\sin(c\kappa t)$: $\beta_N C_{r,N}+\delta_N S_{r,N} = 0$

In order to solve the system, we reformulate the equations using a matricial formulation. We define the vectors $\alpha = (\alpha_i)_i$, $\beta = (\beta_i)_i$, $\gamma = (\gamma_i)_i$ and $\delta = (\delta_i)_i$.

First, we define the two diagonal matrices $C_{lr} = ((C_{l,j}-C_{r,j})\delta_{ij})_{ij}$ and $S_{lr} = ((S_{l,j}-S_{r,j})\delta_{ij})_{ij}$. With these matrices, we can express the flow terms that appear after the resistance matrix $\mathcal{R}_s$ in the linear version of the equations (2.22) and (2.23):

$$\left(\left(\beta_j(C_{l,j}-C_{r,j})+\delta_j(S_{l,j}-S_{r,j})\right)_j = C_{lr}\beta + S_{lr}\delta\right.$$

and

$$\left(\left(-\alpha_j(C_{l,j}-C_{r,j})-\gamma_j(S_{l,j}-S_{r,j})\right)_j = -C_{lr}\alpha - S_{lr}\gamma\right.$$

The linear versions of the two equations (2.22) and (2.23) can then be written using matrices:

$$S_l\alpha - C_l\gamma + \frac{c}{(\lambda+2\mu)}L\mathcal{R}_s\left(C_{lr}\beta+S_{lr}\delta\right) = v_1 \quad \text{with } v_1 = {}^t\left(\frac{A_1}{(\lambda+2\mu)\kappa},0,\ldots,0\right)$$

$$S_l\beta - C_l\delta - \frac{c}{(\lambda+2\mu)}L\mathcal{R}_s\left(C_{lr}\alpha+S_{lr}\gamma\right) = v_2 \quad \text{with } v_2 = {}^t\left(\frac{A_2}{(\lambda+2\mu)\kappa},0,\ldots,0\right)$$

with

$$S_l = \begin{pmatrix} S_{l,1} & 0 & 0 & \ldots & 0 & 0 \\ -S_{r,1} & S_{l,2} & 0 & \ldots & 0 & 0 \\ 0 & -S_{r,2} & S_{l,3} & \ldots & 0 & 0 \\ \ldots & \ldots & \ldots & \ldots & \ldots & \ldots \\ 0 & 0 & \ldots & -S_{r,N-2} & S_{l,N-1} & 0 \\ 0 & 0 & \ldots & 0 & -S_{r,N-1} & S_{l,N} \end{pmatrix}$$

$$C_l = \begin{pmatrix} C_{l,1} & 0 & 0 & \dots & 0 & 0 \\ -C_{r,1} & C_{l,2} & 0 & \dots & 0 & 0 \\ 0 & -C_{r,2} & C_{l,3} & \dots & 0 & 0 \\ \dots & \dots & \dots & \dots & \dots & \dots \\ 0 & 0 & \dots & -C_{r,N-2} & C_{l,N-1} & 0 \\ 0 & 0 & \dots & 0 & -C_{r,N-1} & C_{l,N} \end{pmatrix}$$

and

$$L = \begin{pmatrix} 1 & 0 & 0 & \dots & 0 & 0 \\ -1 & 1 & 0 & \dots & 0 & 0 \\ 0 & -1 & 1 & \dots & 0 & 0 \\ \dots & \dots & \dots & \dots & \dots & \dots \\ 0 & 0 & \dots & -1 & 1 & 0 \\ 0 & 0 & \dots & 0 & -1 & 1 \end{pmatrix}$$

The linear versions of the two equations (2.24) and (2.25) become

$$\begin{aligned} C_r\alpha + S_r\gamma = 0 &\longrightarrow \gamma = -S_r^{-1}C_r\alpha \\ C_r\beta + S_r\delta = 0 &\longrightarrow \delta = -S_r^{-1}C_r\beta \end{aligned}$$

with

$$S_r = \begin{pmatrix} S_{r,1} & -S_{l,2} & 0 & \dots & 0 & 0 \\ 0 & S_{r,2} & -S_{l,3} & \dots & 0 & 0 \\ 0 & 0 & S_{r,3} & \dots & 0 & 0 \\ \dots & \dots & \dots & \dots & \dots & \dots \\ 0 & 0 & \dots & 0 & S_{r,N-1} & -S_{l,N} \\ 0 & 0 & \dots & 0 & 0 & S_{r,N} \end{pmatrix}$$

and

$$C_r = \begin{pmatrix} C_{r,1} & -C_{l,2} & 0 & \dots & 0 & 0 \\ 0 & C_{r,2} & -C_{l,3} & \dots & 0 & 0 \\ 0 & 0 & C_{l,3} & \dots & 0 & 0 \\ \dots & \dots & \dots & \dots & \dots & \dots \\ 0 & 0 & \dots & 0 & C_{r,N-1} & -C_{l,N} \\ 0 & 0 & \dots & 0 & 0 & C_{r,N} \end{pmatrix}$$

Finally, mixing the matricial formulations leads to

$$S_l\beta - C_l\delta - \frac{c}{(\lambda+2\mu)}L\mathcal{R}_s\left(C_{lr}\alpha + S_{lr}\gamma\right) = v_2 \;\rightarrow\; \left(S_l + C_lS_r^{-1}C_r\right)\beta - \frac{c}{(\lambda+2\mu)}L\mathcal{R}_s\left(\left(C_{lr} - S_{lr}S_r^{-1}C_r\right)\alpha\right) = v_2$$

and

$$\beta = \left(S_l + C_lS_r^{-1}C_r\right)^{-1}\left(\frac{c}{(\lambda+2\mu)}L\mathcal{R}_s\left(\left(C_{lr} - S_{lr}S_r^{-1}C_r\right)\alpha\right) + v_2\right)$$

Then,

$$S_l\alpha - C_l\gamma + \frac{c}{(\lambda+2\mu)}L\mathcal{R}_s\left(C_{lr}\beta + S_{lr}\delta\right) = v_1 \;\rightarrow\; \left(S_l + C_lS_r^{-1}C_r\right)\alpha + \frac{c}{(\lambda+2\mu)}L\mathcal{R}_s\left(C_{lr} - S_{lr}S_r^{-1}C_r\right)\beta = v_1$$

and

$$\begin{aligned} &\left(S_l + C_lS_r^{-1}C_r + \frac{c}{(\lambda+2\mu)}L\mathcal{R}_s\left(C_{lr} - S_{lr}S_r^{-1}C_r\right)\left(S_l + C_lS_r^{-1}C_r\right)^{-1}\frac{c}{(\lambda+2\mu)}L\mathcal{R}_s\left(C_{lr} - S_{lr}S_r^{-1}C_r\right)\right)\alpha \\ &= -\frac{c}{(\lambda+2\mu)}L\mathcal{R}_s\left(C_{lr} - S_{lr}S_r^{-1}C_r\right)\left(S_l + C_lS_r^{-1}C_r\right)^{-1}v_2 + v_1 \end{aligned}$$

Finally, the linear system to solve in order to determine α, β, γ and δ is

$$\begin{cases} M\alpha = b \\ M = S_l + C_l S_r^{-1} C_r + \left(\frac{c}{(\lambda+2\mu)}\right)^2 L\mathcal{R}_s \left(C_{lr} - S_{lr} S_r^{-1} C_r\right) \left(S_l + C_l S_r^{-1} C_r\right)^{-1} L\mathcal{R}_s \left(C_{lr} - S_{lr} S_r^{-1} C_r\right) \\ b = -\frac{c}{(\lambda+2\mu)} L\mathcal{R}_s \left(C_{lr} - S_{lr} S_r^{-1} C_r\right) \left(S_l + C_l S_r^{-1} C_r\right)^{-1} v_2 + v_1 \\ \beta = \left(S_l + C_l S_r^{-1} C_r\right)^{-1} \left(\frac{c}{(\lambda+2\mu)} L\mathcal{R}_s \left(\left(C_{lr} - S_{lr} S_r^{-1} C_r\right)\alpha\right) + v_2\right) \\ \gamma = -S_r^{-1} C_r \alpha \\ \delta = -S_r^{-1} C_r \beta \end{cases}$$

Then for $x \in A_i$ and $t \in \mathbb{R}_+$,

$$u_i(t,x) = \alpha_i \cos(\kappa x)\cos(c\kappa t) + \beta_i \cos(\kappa x)\sin(c\kappa t) + \gamma_i \sin(\kappa x)\cos(c\kappa t) + \delta_i \sin(\kappa x)\sin(c\kappa t)$$

An analytical solution of the unidimensional equation of our model can then be computed. However, the solution is valid on the particular case where a Neumann boundary condition in the form of a sum of a sine and a cosine, is applied on one boundary. Nevertheless, with the unidimension formulation of the model, we will mostly use this boundary condition. Additionally, the analytical solution allows to validate the numerical resolution. In the next sections, we will use either the analytical solution or the numerical method depending on the case and on the computational time.

In order to numerically investigate how our model of the lungs behaves, we will apply our model to non-physiological cases. Particularly, we want to study the influence of the damping of the tree on the deformation of the elastic material.

2.4 Study of the coupling between the tree and the elastic material through non-physiological numerical simulations

Before numerically studying physiological cases of the lungs, here, we will apply our model to simple non-physiological cases with the unidimensional system of equations (2.17). Actually, from an unidimensional point of view, without the tree structure (namely $p_i = 0\ \forall i$), the strong formulation (2.4) is the linear elasticity equation for an isotropic and homogeneous material. From that perspective, we can already dig out some interesting information. It allows us to study, for materials of fixed size with homogeneous elastic properties, the propagation of the deformation wave and interestingly, the natural angular frequencies [114, 41, 69]. The natural angular frequencies[1] of an oscillatory system (such as an elastic material) are the pulsations at which the system oscillates in the absence of any external forces (driving or damping force) [120, 43]. Furthermore, if the oscillator is stimulated continuously by an external periodic force whose frequency is close to one of those natural frequencies, the motion of the oscillator amplifies through time more or less strongly depending on a potential damping. This is the phenomenon of resonance which we will investigate in this section. The resonance allows a potential amplification of the deformation of a material. For our study, this phenomenon could be interesting for the HFCWO. Hence, this section investigates the potential effect of the tree structure on the deformation (subsection 2.4.1) and the resonance of the material (subsection 2.4.2). The way the natural angular frequencies of the elastic material are computed is detailed in the appendix 2.C.

[1] Also named angular eigenfrequencies or natural pulsations. Equivalently, the frequency associated to a natural pulsation is named eigen frequency or natural frequency. The relation between a given frequency f and a given pulsation ω is $\omega = 2\pi$f.

2.4.1 Effect of the tree structure on the propagation of the wave deformation

With the tree structure, hence $p_i \neq 0\ \forall i$, we see in (2.16) that the effect of the tree structure act on the boundaries of the A_i regions but we do not know its general influence on the solution. Here, we study the influence of the tree on the propagation of the deformation wave by comparing the displacements of the material with or without the coupling with different tree structures. The cases studied here are not physiological. This analysis also allows to check the pertinence for the coupled case of the angular eigenfrequencies calculated in the absence of the tree, see the appendix 2.C. From the appendix 2.C, we also deduce the definition of the velocity of the wave propagation that is $c = \sqrt{\frac{(\lambda+2\mu)}{\rho}}$.

The domain is $\Omega = [0, L]$ with $L = 1$ m and corresponds to a homogeneous material coupled with a three generations tree structure, as shown in Figure 2.2. We consider first a tree structure with a very few numbers of generations in order to study in a tractable framework the influence of the hydrodynamic resistance on the material.

Boundary conditions. We chose the domain to be fixed (zero displacement) on one boundary and stimulated on the other. The pulsations ω_i denote the i^{th} angular eigenfrequency of the system without the tree, see the appendix 2.C. We set the Dirichlet condition $u(1, t) = 0$, and the Neumann condition $\tau(t) = A\sin(\omega_2 t)$ on $x = 0\ \forall t \in \mathbb{R}^+$.

We chose the pulsation of the boundary condition to be ω_2 for getting a visual point of comparison.

Initial conditions. A zero initial condition is imposed on displacement and velocity, the material is initially at rest.

Values of the physiological and physical parameters. We enforce the combination $(\lambda + 2\mu)$ and all the other parameters to be equal to 1 ; the velocity of the wave deformation is then $c = 1$ m.s^{-1}. As most of the variables are normalized to one, we also enforce the equivalent resistance of the resistance matrix to be equal to 1. For that purpose, we use the matrix $\mathcal{R}_{norm} = \frac{\mathcal{R}}{R_{eq}}$. The resistance matrix $\mathcal{R}$ is computed from the size of the first generation airway which is assumed of length $l_0 = 6$ cm and of radius $r_0 = 1$ cm. Since, the aspect ratio of the trachea is larger than the other airways, those values correspond to a reduced trachea. We do not attach equivalent resistance of the subtrees to the terminal branches. This configuration of parameters modeling non-physiological lungs is summed up in the appendix 2.E. We use it again in the next subsection.

Wave propagation and dissipation with a three generations tree

The numerical simulations are performed from $t = 0$ to $t = T_f$, with $T_f = 2/c = 2$ s, $c = \sqrt{\frac{(\lambda+2\mu)}{\rho}}$. The final time T_f is then the time needed for the wave to do a round trip between one boundary ($x = 0$) and the other ($x = L = 1$ m).

The black curves ($\triangle$-curves) in Figure 2.3 show the propagation of a wave in the absence of the tree, $p_i = 0\ \forall i$. As the final time is $T_f = 2$ s, the wave propagates through the material without any loss of energy, reaches $x = 1$ at time $t = 1$ s and comes back to $x = 0$ m at time $t = 2$ s, as expected.

The red curves (o-curves) in Figure 2.3 show the propagation of the wave in the presence of the tree structure. The wave is damped by the dissipation due to the viscosity of the air occurring in the tree. Moreover, several regions of the domain are deformed before the arrival of the deformation wave, see Figure 2.5. Actually, since we use Poiseuille's model for the air fluid mechanics in the tree, any change in pressures and airflows propagates instantaneously throughout the tree. Hence, all the material is instantaneously affected by the change of the air properties in the A_i.

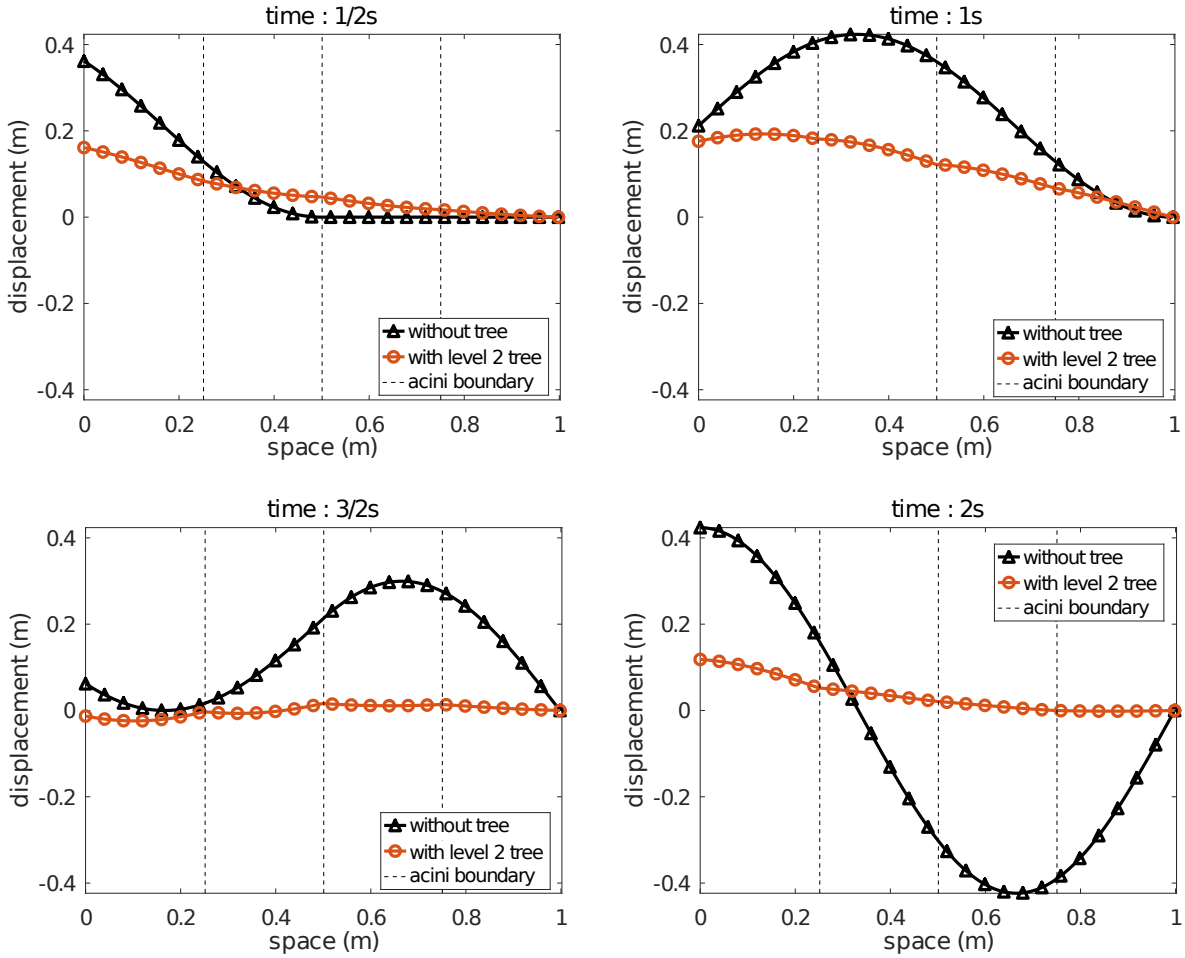

Figure 2.3: Propagation of the wave deformation with (o-red) and without ($\triangle$-black) tree structure constraint at time $t = \frac{T_f}{4} = \frac{1}{2}$ s, $t = \frac{T_f}{2} = 1$ s, $t = \frac{3T_f}{4} = \frac{3}{2}$ s and $t = T_f = 2$ s. The dash vertical lines show the boundaries of the $(A_i)_{1 \leqslant i \leqslant N}$.

The Figure 2.3 also shows that the wave propagation, stimulated at the second natural angular frequency of the material, is perturbed by the tree. In the absence of the tree, if the material is stimulated continuously by a periodic force with this pulsation its motion amplifies through time and the phenomenon of resonance occurs. According to the theory of linear elasticity, the vibration of the material would continuously amplify and the material would never break. This is what we can observe from the displacement computed without considering the tree if we extend the time of the simulation, see Figure 2.4. However, we observe that the displacement, computed with the tree consideration, does not amplify in the course of the time. Hence, it suggests that the tree affects the resonance phenomenon of the material. The subsection 2.4.2 studies specifically this behavior.

Influence of the number of generations on the wave propagation

As the tree affects the deformation of the material, the size of the tree affects the material displacement. Increasing the number of generations of the tree induces more terminal branches and smaller A_i, and the deformation of the overall domain of the material becomes smoother, see Figure 2.5 (left). This is due to smaller pressure shifts between two neighboring A_i, as seen in the figure 2.5 (right). Let us denote by p_s^i the pressure shift between A_i and A_{i+1}, $1 \leqslant i < N$. We compute the mean pressure shift between all pressure shifts p_s^i of a tree. We display, in the Figure 2.5, the mean pressure shift for the different trees. As expected, we observe that in average, the pressure shift between two neighboring A_i decreases as the generation in the tree increases. Finally, the figure 2.5 (left) tends to suggest that different numbers of generation in

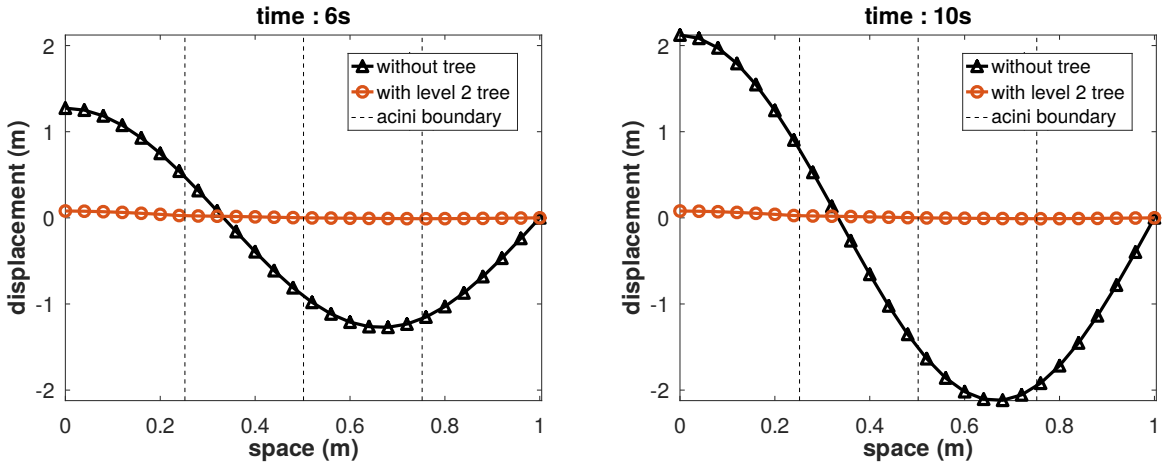

Figure 2.4: Propagation of the wave deformation with (o-red) and without ($\triangle$-black) tree structure constraint at time $t = 6$ s and $t = 10$ s. The dash vertical lines show the boundaries of the $(A_i)_{1 \leqslant i \leqslant N}$.

the tree induce different damping influences in the elastic material. However, the displacements are displayed for a small time, when the deformation wave has not propagated yet. Actually, after a small increment of time ($t = 1/3$ s), we can observe that for different tree sizes, the damping influence on the displacement amplitude is quite similar, see Figure 2.6. We recall that for this numerical simulation, the equivalent resistances of the different trees are equal. This suggests then that, for two symmetrical trees with same equivalent resistances, one with a small number of generations and the other one with a large number of generations, the induced damping influences on the displacement amplitude are quite similar.

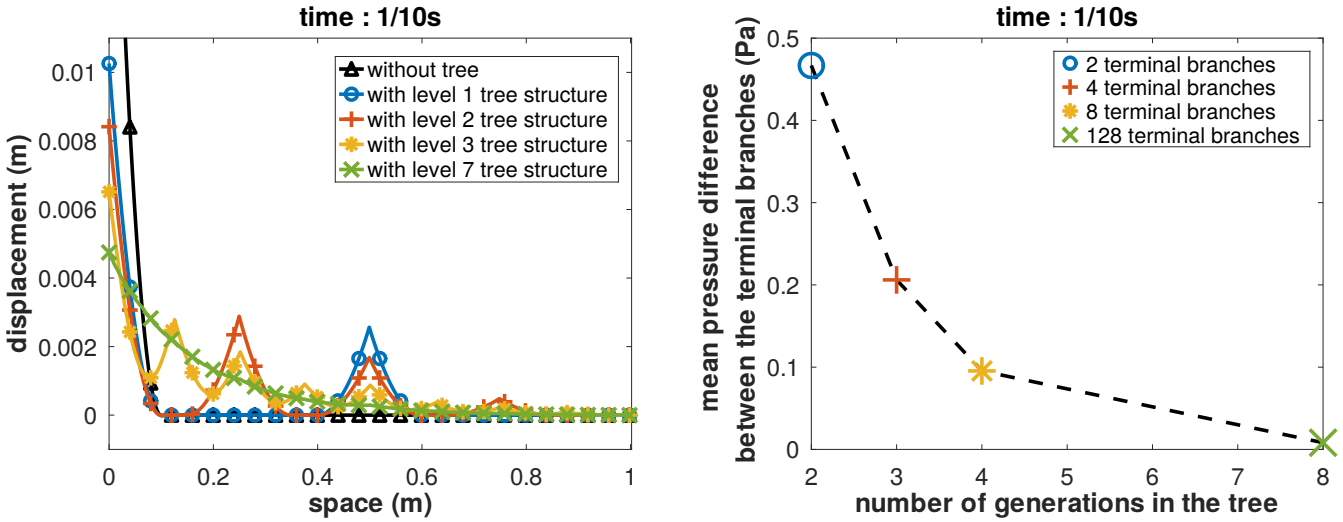

Figure 2.5: **Left:** Deformation of the material without tree structure ($\triangle$-black) and with tree structures of 2 (+-blue), 3 (o-red), 4 ($*$-purple) and 8 (+-green) generations at time $t = \frac{T_f}{20} = \frac{1}{10}$ s. The time t is intentionally small for a better visualization. Particularly, at this time, the wave has not propagated much. However we can observe displacements all along the domain at the A_i boundaries that depends of the size of the tree. Indeed, more regions in the material are affected if the number of generations of the tree is large. **Right:** Mean pressure difference between the terminal branches of a tree for different tree sizes. The pressure difference is computed from two neighboring A_i for all couples of terminal branches in a tree. Then the mean is computed for each tree. Four size of tree are considered : 2, 3, 4 and 8 generations tree.

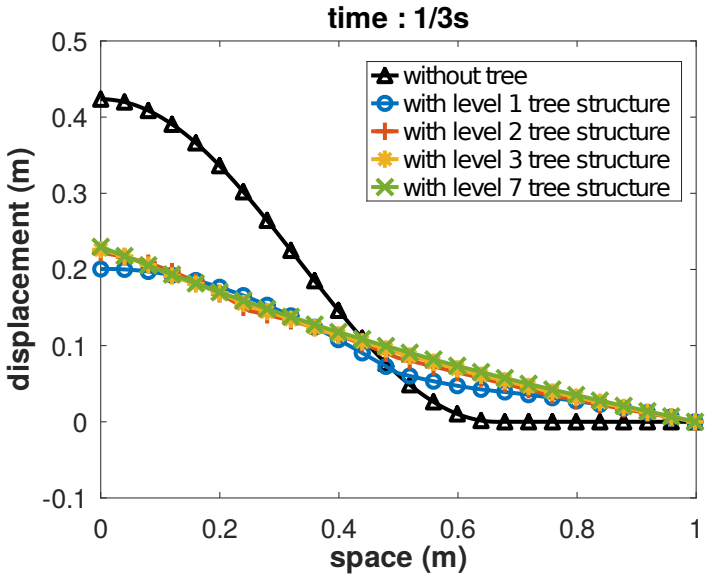

Figure 2.6: Deformation of the material without tree structure (△-black) and with tree structures of 2 (+-blue), 3 (o-red), 4 ($*$-purple) and 8 (+-green) generations at time $t = \frac{1}{3}$ s.

Wave propagation and dissipation with a level 2 tree with a local increase of resistance

If the hydrodynamic resistance of one terminal branch increases, the region A_i in the material fed by this branch would be less prone to deform. We arbitrarily increase by a factor 100 the resistance of a branch of the 3 generations tree associated to the region A_4, see (a) on the Figure 2.7. As we enforce no displacement at $x = L$, the material does not deform much in the region A_4, see (b) in the Figure 2.7. Note that the tree in this case is not anymore symmetrical.

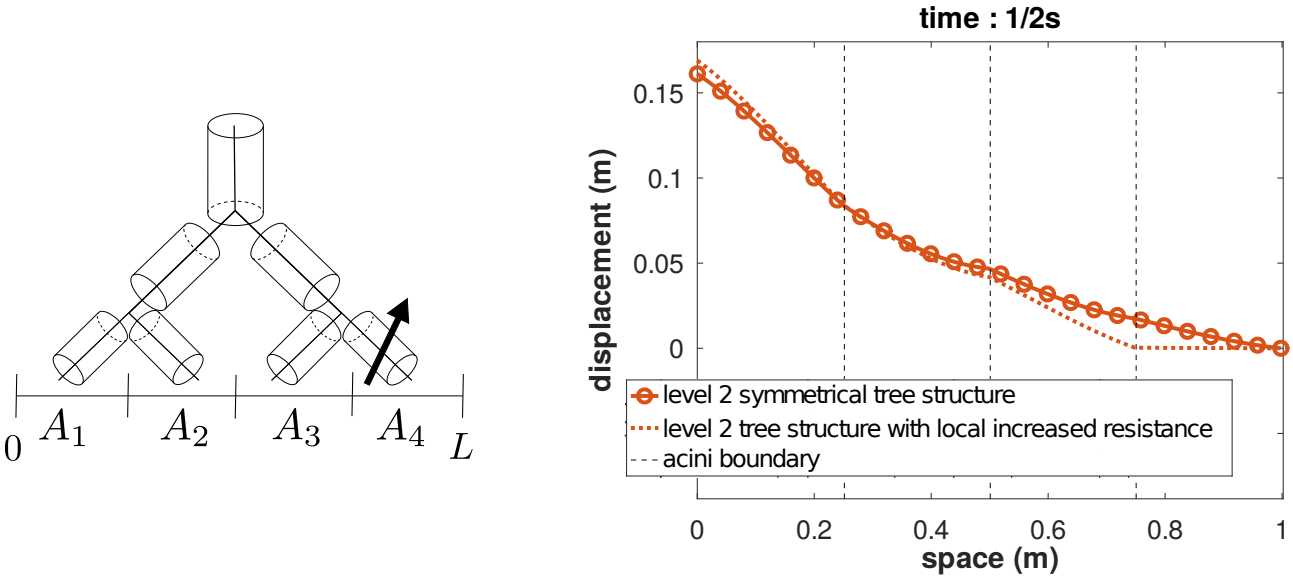

Figure 2.7: Comparison between the material displacements in the case of a three generations symmetrical tree and in the case of a three generations tree with a local increase of resistance. **Left:** A three generations tree. The resistance of the branch indicated by the arrow and feeding the region A_4 is increased. **Right:** Displacement at time $t = \frac{1}{2}$ s in the case of a three generations symmetrical tree and a three generations tree with a local increase of resistance (see left). The displacement associated to the region A_4 is close to zero, as expected. The dissipation of the tree feeding the regions A_4 becomes strong enough to prevent the deformation of the material.

2.4.2 The resonance phenomenon in the coupled model

The previous subsection shows the influence of the tree on the material displacement. Typically, the tree acts as a damping which decreases the amplitude of the material deformation. The effects of the tree are applied instantaneously at each time step and particularly at the A_i boundaries. It also shows the influence of the size of the tree. Finally, it suggests that the damping of the tree acts on the resonance of the material. The phenomenon of resonance of the elastic material can be interesting for our purposes. In our model, the deformation of the elastic material induces flow of air in the tree structure. This mimics the deformation of the lung's tissue and the induced flow of air inside the pulmonary tree. If the material resonates, its deformation is maximized as well as the induced air flow in the tree. Similarly, if the flow of air inside the pulmonary tree is maximised, this would favour the displacement of the secretions. The resonance of the material occurs around the natural pulsations of the material. The deformed shape of the material when the latter vibrates at one of its natural pulsations represents a natural mode [114]. Hence, first, the subsection studies the impact of the tree on the natural modes of vibration of the material.

The phenomenon of resonance arises in oscillatory systems [114]. A simple way to analyze such system is to study harmonic oscillators with one degree of freedom. With one degree of freedom, an harmonic oscillator describes, for example, the oscillations of a mass tied to a spring, of a pendulum or of an electronic circuit. The motion of such oscillator can be analytically computed and we can derive from it properties of resonance. Then, this subsection also studies, with numerical simulations, the impact of the tree on the resonance of the motion by comparison with harmonic oscillators with one degree of freedom. The configuration of parameters is the same as previously. We recall that, in this work, the degrees of freedom (DoF) are the positions where the unknown elements of a system are computed.

Impact of the tree on the natural modes

As described above, the natural modes of a vibrating system (such as an elastic solid) with several degrees of freedom are the deformed shape of the motion of the oscillator when vibrating at its natural pulsations [114]. The first natural mode corresponds to the motion of the oscillator vibrating at its first natural pulsation, the second natural mode is associated with the second natural pulsation and so on. The number of natural pulsations of a vibrating system is equal to the number of degrees of freedom of the vibrating system. Here we compare the four first natural modes of vibration of our elastic material with and without the damping tree.

In the absence of the tree, the unidimensional system of equations (2.17) with a zero displacement boundary condition at one boundary and a sinusoidal Neumann condition on the other boundary, can be assimilated to the deformation of an elastic bar fixed at one end and stimulated on the other end. Hence, as detailed in the appendix 2.C, the natural pulsations of the material can be computed and are the $\omega_k = \frac{(2k-1)c\pi}{2L}$ for $k \in [\![1, +\infty]\!]$, with c the velocity of the wave deformation and L the length of the 1D material. We compare the displacements of the material without and with the damping induced by the tree, using two different trees with three and eight generations. We use the same configuration as in the previous subsection.

As seen earlier, we can observe in the figures in Figure 2.8 the influence of the tree and of its size on the material displacements at the four first natural angular frequencies. As the number of generations of the tree increases, the damping influence of the tree is spread over the material. As seen previously, the deformation over the domain is smoother with the eight generations tree than with the three generations tree. Then, without the tree, we observe the four natural modes of vibrations of the material. With higher natural pulsation (ω_4), we observe that the frequency of the deformation wave is higher, as expected. However, with the tree, we see that the natural modes of vibration of the tree are altered. Moreover, we observe that the amplitude of the displacement is lower for higher natural pulsations than for lower ones. As the phenomenon of resonance occurs around the natural pulsations, this suggests that the damping effect of the tree, which is spread in several regions of the domain, tends to alter the phenomenon of resonance. To understand how the damping of the tree acts on the resonance of the material, we will describe somme properties of harmonic oscillatory system.

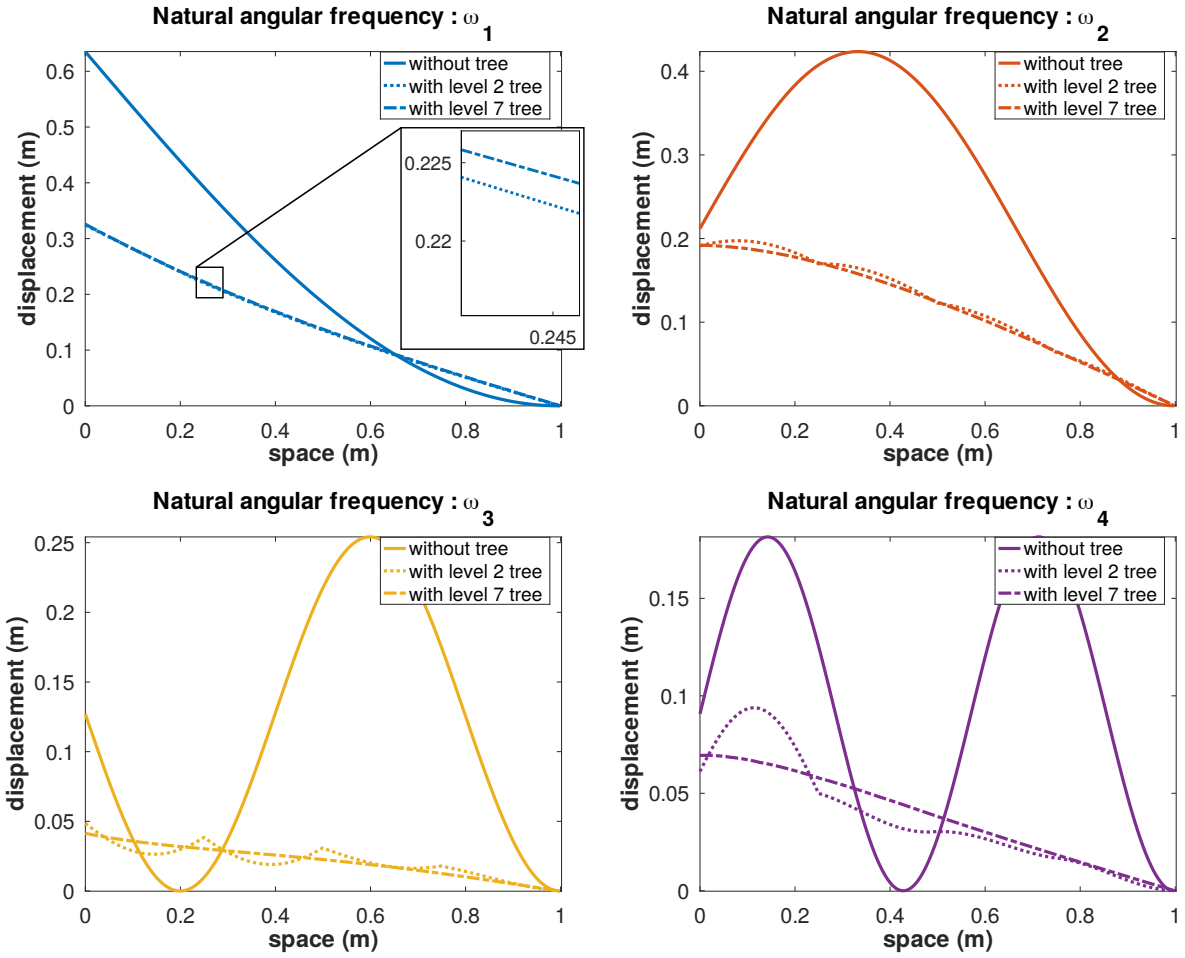

Figure 2.8: Comparison between the material displacements for the non coupled and coupled cases with a three and a eight generations tree at the four first natural modes. The material is stimulated at $x = 0$ by a sinusoidal force whose pulsation varies between the fundamental and the fourth eigen pulsations. The natural pulsations are computed in the absence of three are defined as $\omega_k = \frac{(2k-1)c\pi}{2L}$ for $k \in [\![1, +\infty[\![$. The displacements are displayed at the time when the wave has propagated from $x = 0$ to $x = L = 1$ ($t = 1/c = 1$s).

Description and properties of resonance for a harmonic oscillator with one degree of freedom

A harmonic oscillator is a system that oscillates around a position of equilibrium under the action of a restoring force proportional to the displacement [120, 43]. The motion of a harmonic oscillator is described by a sinusoidal pattern. The comprehension of a system of harmonic oscillator on simple cases can eases the study of more complex systems like our. Harmonic oscillator with one degree of freedom (DoF) is a typical simple case. In our model, the equation ruling our model is not defined for one DoF but for either an infinite number of DoF for the continuous system (2.17) or for a finite number of DoF for the discretized system (2.18). However, we will see that they have similar behaviors. Here, we describe the main properties of a harmonic oscillator with one degree of freedom. We refer the reader to the appendix 2.D and to the references [120, 43] for more details.

The motion of an oscillator can be forced by an external force, and/or damped by a damping influence. Here, we will discuss the case of forced and damped oscillator. For the explanation, we denote by m the mass of the oscillator, c the damping coefficient, k the stiffness coefficient of the oscillator and f a driving force. The evolution in time of the motion of the forced and

damped oscillator designated by $x(t)$ is described by the following equation :

$$\underbrace{\frac{d^2x(t)}{dt^2}}_{\text{acceleration}} + 2\xi\underbrace{\frac{dx(t)}{dt}}_{\text{damping}} + \underbrace{\omega_0^2 x(t)}_{\text{stiffness}} = \underbrace{h(t)}_{\text{driving force}} \tag{2.28}$$

with $\xi = \frac{b}{2m}$ the damping coefficient, $\omega_0 = \sqrt{\frac{k}{m}}$ the natural angular frequency of the oscillator and $h = \frac{1}{m}f$. From the parameter of the system, the Q-factor or quality factor can be derived :

$$Q = \frac{\omega_0}{2\xi}$$

It defines the intensity of the damping. The higher is Q, the lower is the damping. Solutions of (2.28) can be calculated [120, 43]. Particularly, we know that the solution of (2.28) is a combination of the homogeneous solution x_h computed without the forcing term (h) and a particular solution x_p with the forcing term. The homogeneous solution tends to zero when the time goes to infinity. Hence, the solution tends to the particular solution as the time progresses.

$$x(t) = \underbrace{x_h(t)}_{\substack{\longrightarrow 0 \\ t\to+\infty}} + x_p(t) \underset{t\to+\infty}{\longrightarrow} x_p(t)$$

This determines two regimes : the transient phase, for small time, and the steady-state phase when the time is sufficiently large. The transient phase lasts a characteristic time of the order of $1/\xi$ and, consequently, the solution tends quicker to the steady state when the damping is large. In the case of sinusoidal driving force $h(t) = Hcos(\omega t)$, the particular solution is

$$x_p(t) = Xcos(\omega t + \phi_x)$$

where X and ϕ_x are constants determined according to the characteristics of the system and of the stimulation. From an algebraic or a complex method [120, 43], the amplitude X is defined and we deduce that the amplitude X is maximized if $Q > 1/\sqrt{2}$ for pulsation equal to

$$\omega_r = \sqrt{\omega_0^2 - 2\xi^2}$$

The pulsation ω_r is the resonance pulsation of the damped and forced oscillator. We see that the intensity of the damping influences the resonance pulsation of the system that leads to three cases. Without damping, the resonance pulsation is exactly the eigen pulsation of the oscillator. For small damping, the resonance pulsation is slightly less than the natural pulsation and for high damping, it is actually not defined anymore : if the oscillator is too much damped, no more resonance can occur. If the oscillator is continuously forced at the resonance frequency, the amplitude of its motion amplifies through time or reaches a maximum compared to others pulsations, this is called the *displacement-resonance*. Additionally, a similar phenomenon occurs for the velocity. The latter is maximised if the oscillator is forced at the natural pulsation ω_0 and for any value of the damping, this is the *velocity-resonance*.

In the case of harmonic oscillator with one degree of freedom, we define the kinetic energy by $E_k = \frac{1}{2}mv^2(t)$ with $v(t) = \frac{dx(t)}{dt}$ and the potential energy by $E_p = \frac{1}{2}kx^2(t)$. The study of harmonic oscillator also tells us that without damping, the kinetic and potential energies are equal and in anti-phase. With damping, the behaviors of the kinetic and potential energies depend on the intensity of the damping. The kinetic energy, defined with the velocity v, is maximised for pulsation of the driving force equal to the natural pulsation. The potential energy, defined with the displacement x, follows the same pattern as the amplitude X of the particular solution. We recall that a more detailed description of the theory presented in this paragraph can be found in the appendix 2.D.

In our case, the coupled model involves several degrees of freedom with non-local damping terms, hence the solution at each degree of freedom is not easily explicitly defined. However,

thanks to the numerical simulation, we can study the resonance of the material. Particularly, we can study how the coupled system responds to different stimulations (different frequencies) and compare the behaviors of the solutions to those of a simple damped oscillator with one degree of freedom, see above.

Response of the material to different stimulations with and without damping

In order to study the response of the material submitted to different stimulations, we have computed three quantities averaged over the final time T_f for the non-coupled and the coupled system : the total kinetic (E_k) and elastic (E_e) energies and the total quantity of displacements (R_u) averaged over the domain. The unit of the kinetic and elastic energies is the Joule and the one of R_u is the meter. We recall that a sinusoidal pressure $\tau = Asin(\omega t)$ is applied at one boundary ($x = 0$) of the elastic material, with $A = 1$. Here, the pulsation ω is set in the range from $\frac{\omega_1}{10}$ to $\omega_4 + \frac{\omega_1}{2}$. We impose a zero-displacement condition on the other boundary ($x = L$). The quantities E_k, E_e and R_u are defined as

$$E_k = \frac{1}{2}\frac{\rho}{T_f}\int_0^{T_f}\int_0^L \frac{\partial u(x,t)}{\partial t}^2 dxdt$$

$$E_e = \frac{1}{2}\frac{(\lambda+2\mu)}{T_f}\int_0^{T_f}\int_0^L \frac{\partial u(x,t)}{\partial x}^2 dxdt$$

$$R_u = \left(\frac{1}{T_f L}\int_0^{T_f}\int_0^L u^2(x,t)dxdt\right)^{\frac{1}{2}}$$

We set the final time to the time that the wave deformation does six round trips between one boundary ($x = 0$) and the other ($x = L$) in order to get significant results, namely $T_f = 12$ s.

In Figure 2.9, for the non-coupled case, the total displacement reaches a global maximum at the fundamental angular frequency ($\omega = \omega_1$) and local maxima at the angular frequencies $\omega_i,\ i \in [\![2, 4]\!]$, as expected. However, for the coupled case, the total displacement has only a global maximum for a pulsation lesser than the fundamental pulsation ($\omega < \omega_1$). Looking at the kinetic and elastic energies displayed on Figure 2.10, we observe that the maximum of the total displacement for the coupled case is particularly due to the elastic energy which is larger than the kinetic energy for pulsations below the fundamental natural pulsation ($E_e > E_k$ for $\omega < \omega_1$). It is understandable in the sense that as the applied pressure acts with low pulsations here, the material has the time to stretch and to stock energy under the form of elastic energy. While it is true for low pulsation, it is not true for high pulsations as we can observe. The elastic energy decreases as the pulsation increases to the point of being equal to the kinetic energy for pulsations around the fundamental natural pulsation ($E_e \approx E_k$ for $\omega \approx \omega_1$). Then, for higher frequencies, the elastic energy is lower than the kinetic energy. Additionnaly, the kinetic energy is maximal for pulsations close to the natural pulsation. Moreover, as shown in Figure 2.10, the average kinetic and elastic energies are globally equal in the absence of damping and reach global and local maxima at the natural angular frequencies. The results show that the behaviors of the solution of our model are similar to the one of a harmonic oscillator with one DoF. It shows that in the absence of the tree, the amplitude of the displacement amplifies at the natural eigen frequencies and that the kinetic and the elastic energy are equal over a period of the driving force. With the damping of the tree, we observe that the maximum of the amplitude of the displacement is not reached for pulsations around the eigen pulsations but only for the smallest pulsation. According to the theory of harmonic oscillators, the damping is high compared to the elastic properties of the material and prevent resonance.

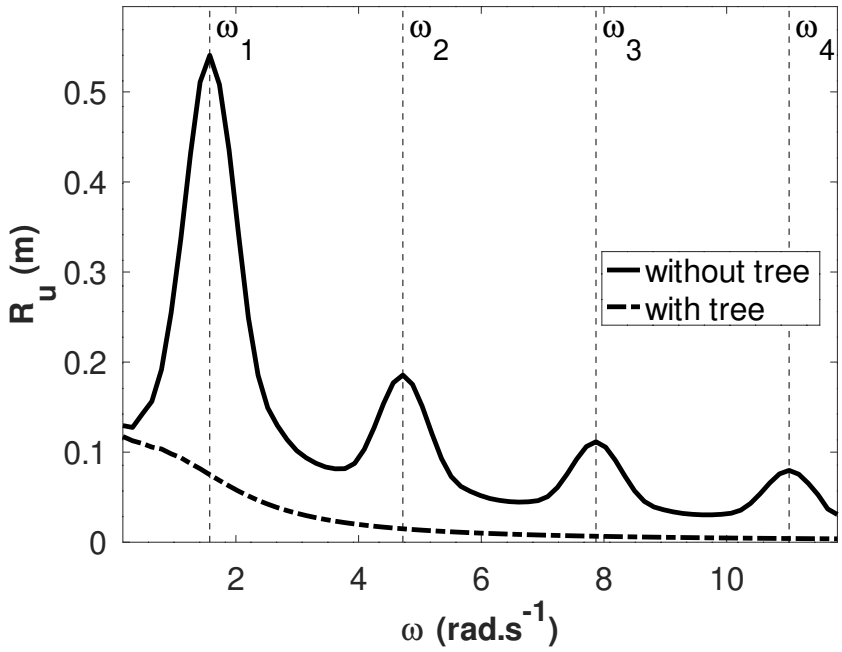

Figure 2.9: Spatial and temporal total displacement of the material (R_u) for the non coupled case and the coupled case with a eight generations tree. The displacement is computed over 12 s. The pulsation of the sinusoidal stimulation varies a range of pulsations $[\frac{\omega_1}{10}, \omega_4 + \frac{\omega_1}{2}]$. The vertical dashed lines display the values of the four first natural angular pulsations computed in the absence of the non coupled case.

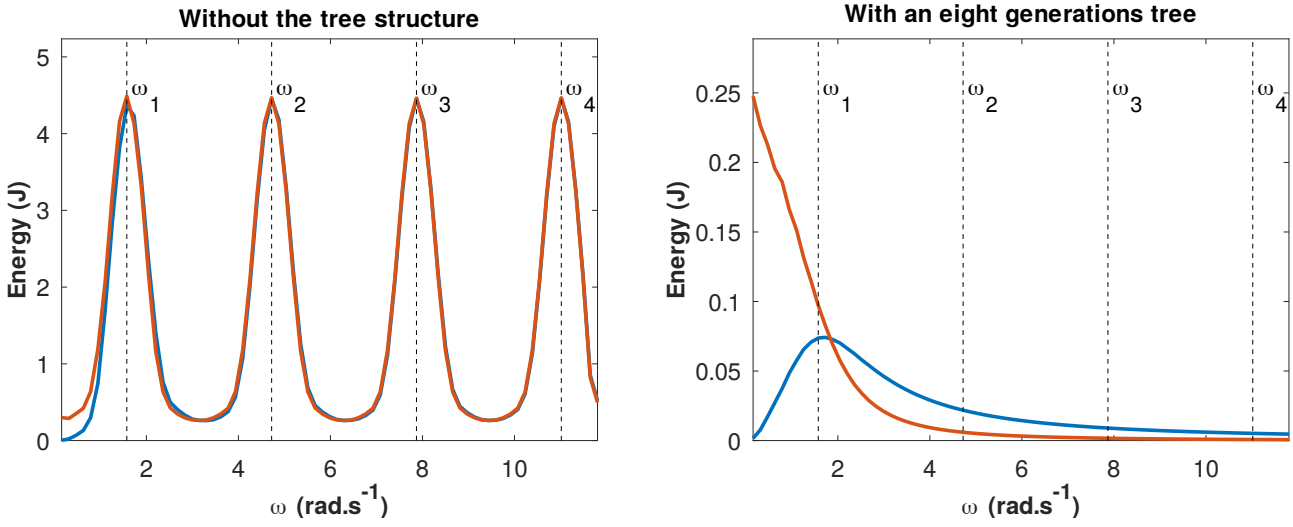

Figure 2.10: Temporal total kinetic E_k and elastic E_e energies for the non-coupled (**left**) and coupled (**right**) system with a eight generations tree structure produced over 12 s by a sinusoidal stimulation for several pulsations varying in $[\frac{\omega_1}{10}, \omega_4 + \frac{\omega_1}{2}]$. The vertical dashed lines display the values of the four first natural angular pulsations computed in the absence of the coupling with the tree.

The comprehension of the resonance phenomenon of the lungs could help on the choice of the configuration of the HFCWO device by suggesting optimal frequencies that could potentially maximize the deformation. The previous results suggest that finding a fundamental pulsation for the lungs in the absence of damping could lead to resonance and would maximize the deformation, the displacement or the velocity. However, from the perspective of harmonic oscillators, the resonance is driven by the intensity of the damping. Hence, we need to characterize the

physical property of the lungs (elastic properties as well as lungs resistance) to study the resonance for physiological lungs model.

With physiological data for the lungs, i.e. size, stiffness and volumetric density (see subsection 2.5.1 and the table in the 2.E), the definition 2.39 brings an estimation of $f_1 = 2\pi\omega_1 = 6.5$ Hz for the fundamental natural frequency of the lungs. Knowing that the numerical simulations of this chapter are dedicated to the ventilation at rest, with a frequency of around 1/5 Hz, much lower than f_1, we will focus on the resonance in the lungs in the frame of HFCWO, that is studied in the next chapter. Before that, we need to calibrate our model for physiological cases. In the next section, we will apply our model on physiological cases to study the ventilation at rest in healthy and non-healthy lungs.

2.5 Rest ventilation of healthy and non-healthy lungs

This section aims at validating and applying the model on human lungs, by mimicking the ventilation at rest. It allows to set the configurations of parameters of the model for physiological simulations and it highlights the influence of the parameters of the model by comparisons between healthy and non-healthy situations. We will first calibrate the model with tidal breathing (subsections 2.5.1 and 2.5.2). Then the model will be applied to cases of non-healthy lungs (subsection 2.5.3). All the configurations of parameters used in this section are gathered in the appendix 2.E and will be used in the next chapter.

2.5.1 Calibration of the model using rest ventilation

We want to use our model to mimic the dynamics of the human lung. However, several parameters need to be adjusted in order for our model to give predictions compatible with the physiology. The ventilation at rest in human is thoroughly documented and studied in the literature [136, 76, 87, 109, 98], hence it is used to calibrate our model. Once calibrated, our model is used to mimic different pathologies of the respiratory system.

This subsection is then dedicated to mimic the pulmonary ventilation at rest for healthy representative adult lungs. We consider the domain $\Omega = [0, L], L \in \mathbb{R}$ composed of an homogeneous material that mimics the lung's tissue. Here, we decompose the domain into 128 subdomains $(A_i)_{i=0,\dots,127}$ which are fed by a tree of eight generations. The size of the tree is chosen so that the calculation time remains tractable. The deepest generations of the lung are mimicked using equivalent resistances added at each terminal branches of the eight generations tree, as explained in subsection 2.2.1.

Our model of the bronchial tree is idealized and does not take into account the oesopharyngeal pathway, the detail of the geometry of the bifurcation and the inertial effects of the air flow [104, 105]. As a consequence, the hydrodynamic resistance of the tree and the resulting damping of the tissue deformation are underestimated if we base its computation on the geometry of our idealized tree only. Hence, the hydrodynamic resistance of the idealized tree needs to be adjusted in order to get pressures and airflows in the terminal branches of the tree compatible with the physiological values. For that purpose, we introduced a corrective factor r_h for the hydrodynamic resistance of each branch of the tree that allows to reach satisfactory orders of magnitudes for both pressures and airflows. The corrective factor is also applied to the virtual subtrees attached to the terminal branches of the tree, see the subsection 2.2.1.2. The equivalent resistance R_{eq} of the tree with the adjusted resistance is then compatible with the physiological data, that estimates the lung's hydrodynamic resistance to range from 0.5 to 4 cmH2O.L^{-1}.s in the case of healthy adults [87].

Parameters values. The material properties are taken from [111].

Since the lung's parenchyma is filled with 10% of tissue and 90% of air, the volumetric mass density ρ of the material is set to 10% of the volumetric density of water, i.e. $\rho = 100$ kg/m^3 [111, 32]. This value for the density is probably not adapted to large volume variations

of the lung, for which the air–tissue ratio could be significantly affected, typically during forced expiratory/inspiratory maneuver. However, for normal ventilation and especially for HFCWO conditions, we can reasonably assume that an air–tissue volume ratio of 90% is a good approximation.

We use the same Young's modulus $E = 1256$ Pa and Poisson's ratio $\nu = 0.4$ as in [111]. From these data, we can compute the quantity $\lambda + 2\mu$ used in our model using the equivalency between (E, ν) and (λ, μ) and the relationships $\lambda = \frac{E\nu}{(1-2\nu)(1+\nu)}$ and $\mu = \frac{E}{2(1+\nu)}$.

The resistance matrix $\mathcal{R}$ is built using physiological data for trachea radius and length : $r_0 = 1$ cm and $l_0 = 6$ cm. The corrective factor is set so as to get the equivalent resistance equal to around 1.5 cmH2O.s.L^{-1} : $r_h = 30$. The corrected resistance matrix is then denoted $\mathcal{R}_h$, mimicking representative healthy lungs resistance. For comparison, without the corrective factor, the equivalent resistance of the tree is about 0.05 cmH2O.s.L^{-1}.

We set the length L to be of the same order of magnitude of adult lungs, namely $L = 20$ cm.

Finally, the amplitude of the boundary constraint $(\sigma(u).n = \tau)$ A is set to 200 Pa. This value for A allows our model to predict values for air flows and pressures in the airway tree that are compatible with the physiology.

For this configuration, the velocity of the deformation wave through the lungs is about 5 m.s^{-1}. The time the wave takes to propagates from one boundary to the other is then 40 ms. Moreover, the corresponding fundamental natural frequency is equal to $f_1 = 6.5$ Hz.

Initial conditions. The initial condition ($t = 0$ s) corresponds to the material being at a rest state, i.e. no initial displacement and no initial velocity.

Boundary conditions. The Neumann condition at $x = 0$ is adjusted to mimic the pressure applied by the diaphragm to the lungs during rest ventilation, $\sigma(u).n = \tau = \frac{A}{2}(cos(\omega t) - 1)$, with $A \in \mathbb{R}$ and $\omega = \frac{2\pi}{5}$ rad.s−1. It mimics a negative pressure that moves back and forth the material, see Figure 2.11 (left). The angular frequency ω is chosen so that the duration of a ventilation cycle is $T = 5$ seconds (2.5 seconds inspiration and 2.5 seconds expiration) mimicking an idealized symmetric ventilation at rest [136]. Moreover, we assume a zero displacement Dirichlet condition at $x = 1$.

To go from computed 1D quantities to interpretable 3D quantities, we involve a section whose surface area is denoted S_L in section 2.2.3. We focus our analysis on the variations of the mouth airflow F_m along time as this quantity is easily measurable in a clinical frame. The mouth airflow F_m is computed as the sum of all the airflows in the terminal branches of the tree,

$$F_m\left[\frac{\partial u}{\partial t}\right] = S_L \sum_{i=1}^{N} \mathcal{F}_i\left[\frac{\partial u}{\partial t}\right] \tag{2.29}$$

Results

At rest, a human ventilates around 6 to 8 L/min [136, 48] and a tidal volume of about 500 mL per respiratory cycle. With the adjusted resistance, our model predicts a tidal volume of 512 mL. These results are shown in Figure 2.11 (right).

For a future use, the configuration of parameters used here is the default configuration of healthy human lungs during ventilation at rest. It is called the healthy lungs model. The next subsections will play with values of parameters and only the difference regarding the healthy lungs model will be denoted. The configurations of parameters mimicking non-healthy lungs are called non-healthy lungs model.

A more realistic respiratory function

We notice that other signals mimicking the action of the diaphragm can be used to model

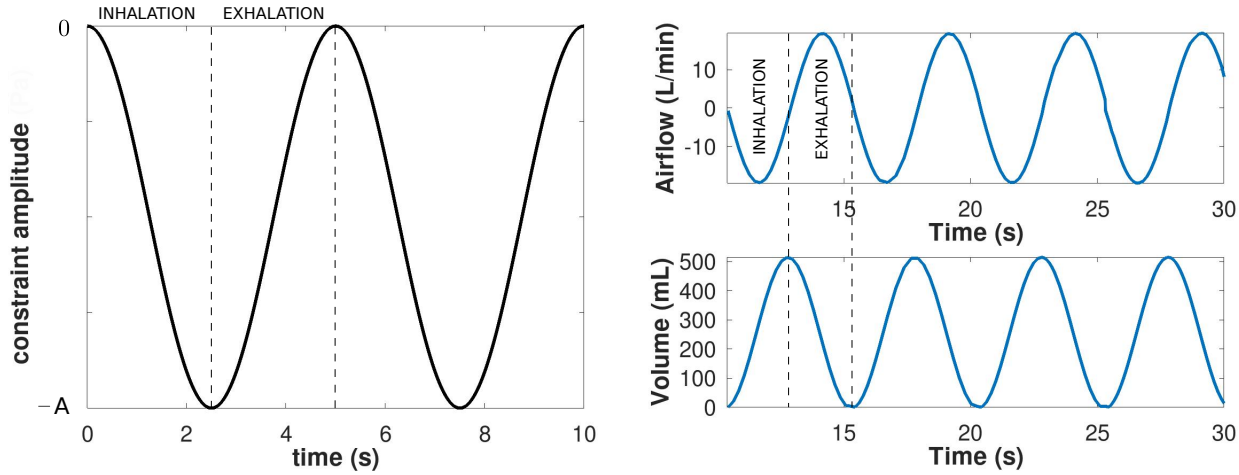

Figure 2.11: **Left:** Pressure applied to simulate the action of the diaphragm (two respiratory cycles are shown). The signal is sinusoidal in time with a period of 5 seconds and an amplitude A. **Right:** Mouth airflow and tidal volume during four respiratory cycles of 5 seconds each with the adjusted hydrodynamic resistance. The airflow and tidal volume data are displayed after they have reached a stationary state ($t \geqslant 10$ s).

more realistic ventilation instead of the sinusoidal one. For example, we can adapt the function proposed in [42] on a five seconds period per respiratory cycle

$$\sigma(u).n = \begin{cases} -A.sin(\frac{\pi t}{2.2}) & 0 \leqslant t < 1.1 \\ -A & 1.1 \leqslant t < 1.3 \\ -A.sin(\frac{\pi(t-1.1)}{0.4}) & 1.3 \leqslant t < 1.5 \\ 0 & 1.5 \leqslant t < 5 \end{cases}$$

In this case, our model predicts a tidal volume of 501 mL, see Figure 2.12. However, as the produced results are quite quantitatively equivalent, we will rather implicitly use the sinusoidal force to save time calculation (20 times faster using the sinusoidal force) and exclude any other functions, except explicitly stated.

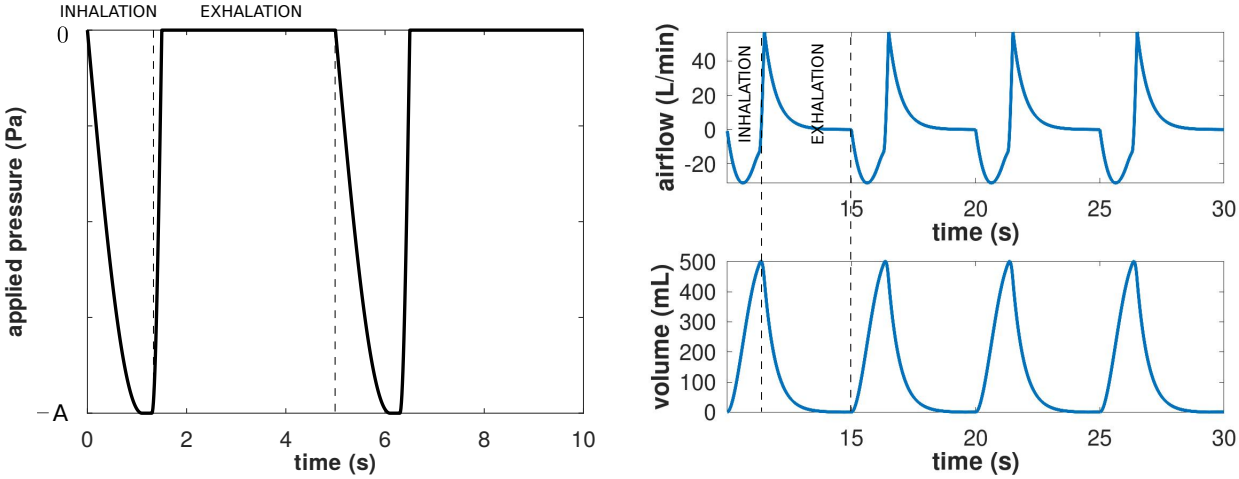

Figure 2.12: **Left:** Pressure applied to simulate a more realistic action of the diaphragm [42] (two respiratory cycles are shown). The function models a five seconds period of a respiratory cycle with 1.5 seconds for inspiration and 3.5 seconds for expiration. **Right:** Mouth airflow and tidal volume during four respiratory cycles of 5 seconds each with the same adjusted hydrodynamic resistance as in Figure 2.11. The airflow and tidal volume data are displayed from the same time $t \geqslant 10$ s as in Figure 2.11.

2.5.2 Tidal breathing between individuals with healthy lungs

The previous subsection mimics the ventilation at rest for healthy adult lungs. For that purpose, we chose the parameters to be in accordance with the data of average lungs. However, for healthy adults, the literature proposes variations on the data between individuals that can induce, in our model, significant differences in lungs behavior for a similar ventilation. This subsection examines the influence of the size and resistance of the lungs as well as the amplitude of the applied force mimicking the action of the diaphragm.

As mentioned in the previous subsection, the lung's hydrodynamic resistance in the case of healthy adults ranges from 0.5 to 4 cmH2O.L^{-1}.s [87]. Actually some report 7 cmH2O.L^{-1}.s [10] or even for infants 50 cmH2O.L^{-1}.s [66]. If we consider two healthy lungs of same volume and of same elastic property but with different resistances, for example if they have differences in their bronchial tree structure, the force needed to inflate a same volume would not have the same amplitudes. For example, for two lungs with resistances of 0.5 cmH2O.L^{-1}.s and of 4 cmH2O.L^{-1}.s, both having the same size and elastic properties, our model predicts that the amplitude of the force mimicking the action of the diaphragm varies respectively from 175 Pa to 325 Pa to ventilate a same tidal volume of 500 mL. That would imply that among individuals, some would force more to ventilate than the others. If we compare with the lungs resistance of infants which reach much stronger value because of the smaller size of their lungs, this argument is even stronger. If we consider that the lungs with higher resistance have a lesser size, let's say $L = 15$ cm and equivalently, the one with a lesser resistance have a bigger size, say $L = 25$ cm, our model predicts that the lesser size lungs would need a force five times bigger in amplitude than the bigger size lungs to ventilate a same tidal volume of 500 mL.

The previous results have to be interpreted with care and in the limit of the model, but they show the influence of the variations of the resistance and the size of the lungs, as well as of the amplitude of the action of the diaphgram, on the ventilation. In reality, there are nuances to be taken into account about these factors. For example, the tidal volume of 500 mL used for the calculation is an average for healthy adult lungs and vary among individuals according to their size, gender, aging or ancestry [122]. For example, it is known that women have lesser lungs volume than men that induce differences in the respiratory properties [88]. Moreover, the lung's hydrodynamic resistance expressed in the data found in the literature is a combination of several resistances that air encounters during all the trip from the ambient air to the exchange surface in the lungs and not of the resistance of the tree only as we use [87]. More specifically, as mentionned in the previous subsection, the lung's resistance is the combination of the resistance of the upper airway (from the nose to the trachea), the resistance of the tree including the role of inertial effects and of bifurcations and the one of the tissue [87]. All of those resistances are more or less involved according to the respiratory behavior, namely the resistance of the upper airway is stronger during nasal breathing or the resistance of the tissue is lower at TLC (total lung capacity, when the volume is maximal) [87]. Finally as presented in the first chapter, the diaphragm is not the only actor during the ventilation, although being the main one at healthy rest ventilation. For example, we can name the intercostal or abdominal muscles.

To be functional and efficient, the respiratory system deals then with numerous variables which interact and induce differences among healthy individuals. As our unidimensional model does not take into account all of those parameters and nuances, our use of lungs data found in the literature has to be understood as a global and average view of the lungs. Typically, the resistance of our tree mimics the overall lungs resistance ; the force modeling the action of the diaphragm includes the action of all respiratory muscles ; or the size of the lungs is an idealized and characteristic size. Our uni-dimensionnal model can then produces qualitative and comparative predictions but cannot be completely quantitative.

2.5.3 Tidal breathing for non-healthy lungs

In the case of non-healthy lungs, the anatomic and physiological properties of the respiratory system change and affect its functioning. This section investigates the impact of those changes on

the ventilation for different respiratory diseases, typically asthma, chronic obstructive pulmonary disease (COPD) and cystic fibrosis (CF). It also shows that our model is able to reproduce known behaviors. It also allows to set the configurations of parameters for non-healthy lungs.

2.5.3.1 Asthma

As described in the chapter 1, one of the main symptom of asthma is the constriction of the bronchial airways due to perturbing stimulations such as the pollution, a emotional stress or a respiratory overactivity, [94, 15, 139]. The constriction of the bronchi leads to an increase of the lung's hydrodynamic resistance that can reach 15 cmH2O.L^{-1}.s [116]. In this study we will consider this value as the lungs resistance of an asthmatic lungs and use the values set in the default configuration of healthy lungs for the other parameters.

In the case of an asthma crisis, the airways of the bronchial tree constrict step by step, that induces a raise of the resistance of the lungs and consequently, perturbs the flow of air in the airways. Hence, the muscles involved in ventilation have to compensate the resistance increase by intensifying their effort. We simulate an asthma attack by increasing step by step the resistance of the 17 generations of the tree with another corrective factor denoted r_{nh}. The corrective factor r_{nh} is used also for the COPD and the CF study. The corrective factor r_{nh} is applied on the healthy lungs resistance $\mathcal{R}_h$ for the airways of the bronchial tree only. We assume that the airways constriction for asthma and COPD or the mucus overproduction for CF affect the bronchial tree only. This allows us to estimate the order of magnitude of the constriction of the bronchial airways when simulating non-healthy lungs. Our model predicts that to reach an equivalent resistance of 15 cmH2O.L^{-1}.s, the radius of the bronchial tree airways has to be reduced by a factor 1.8. In the case when the muscles involved in the ventilation do not intensify their effort, with a resistance of 15 cmH2O.L^{-1}.s, the tidal volume is of 100 mL. Moreover, in order to ventilate a tidal volume of 500 mL, the model suggests that the muscles have to apply a force 5 times stronger which would represent the force needed for moderate activity in case of healthy lungs (around 30 L.min^{-1}). In our model, the quantity of air ventilated is linearly dependant of the amplitude of the applied force, that was expected since our model is linear in A.

The Figure 2.13 shows the effects of the asthma crisis on the ventilation, starting at $t = 20$ s with a lungs resistance increasing progressively from 1.5 cmH2O.L^{-1}.s to 15 cmH2O.L^{-1}.s. Here, the respiratory muscles do not intensify their effort. We observe a progressive decrease of the air flow coming in as well as the air flow coming out. It is understandable in the sense that, as the muscles do not compensate the increase of the resistance, the lungs cannot completely run out and fill up. In reality, during an asthma attack, the energy cost of ventilation is increased : the force exerted by the diaphragm raises during inhalation and the exhalation is no longer done passively but actively, with the help of intercostal and abdominal muscles, as during exercice. Moreover, in addition to the raise of the work of breathing, the time period of the respiratory cycle can also increase to allow the ventilation of a proper volume of air. However, airflow limitation is not always compensated and the phenomenon of pulmonary hyperinflation, that will be discussed in the next subsection (COPD), can occur in acute severe asthma.

In the Figure 2.14, we observe that, in the range of healthy lungs resistances, the amplitude of the applied pressure increases slower than at higher resistances as the resistance increases. The variation of the amplitude is higher from 6 cmH2O.L^{-1}.s (actually linearly according to the resistance). It would suggest that for average lungs in the range of healthy lungs resistances (between 0.5 cmH2O.L^{-1}.s to 4 cmH2O.L^{-1}.s), a small variation in the resistance requires a small variation in the effort amplitude of the respiratory muscles to ventilate a same tidal volume. For higher lungs resistance (for constricted airways), this same small variation requires a higher variation in the amplitude effort of the respiratory muscles. The model suggests, with its limitations, that the structural properties of the lungs, in terms of elasticity and size, would be adapted to authorize the variations of resistance between the individuals with relatively small change in respiratory muscles effort.

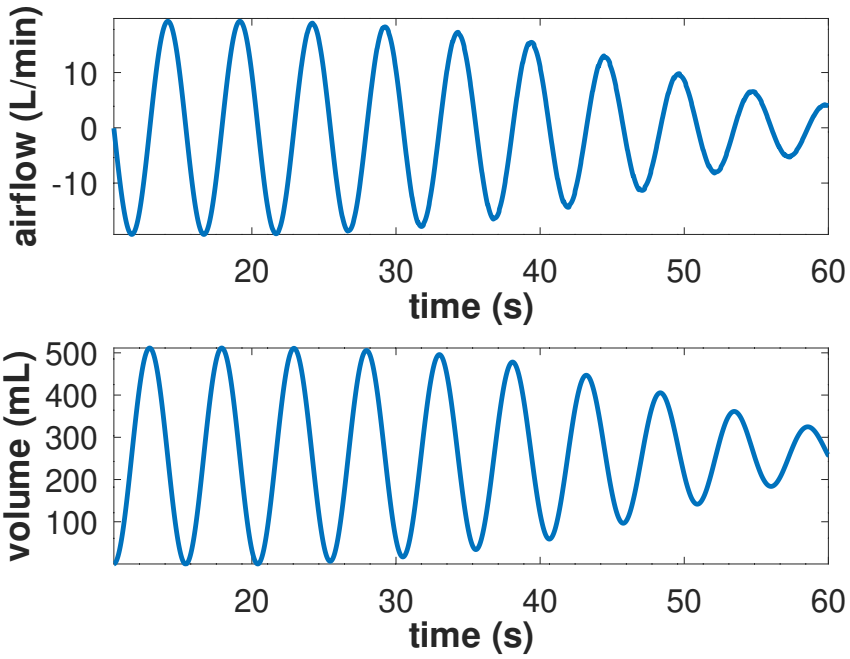

Figure 2.13: Air flow and the associated volume for a ventilation at rest with a progressive increase of the resistance of the tree from 1.5 cmH2O.s.L^{-1}.s to 15 cmH2O.s.L^{-1}.s from time $t = 20$ s, mimicking an asthma crisis. The data are plotted from the time where the solution has adopted a stable equilibrium ($t \geqslant 10$ s). We observe a progressive decrease of the airflow and volume of air at mouth due to the progressive increase of the resistance of the tree. The amplitude of the function mimicking the respiratory muscles is set constant. Hence, the increase of the damping of the tree prevents the deformation of the lungs.

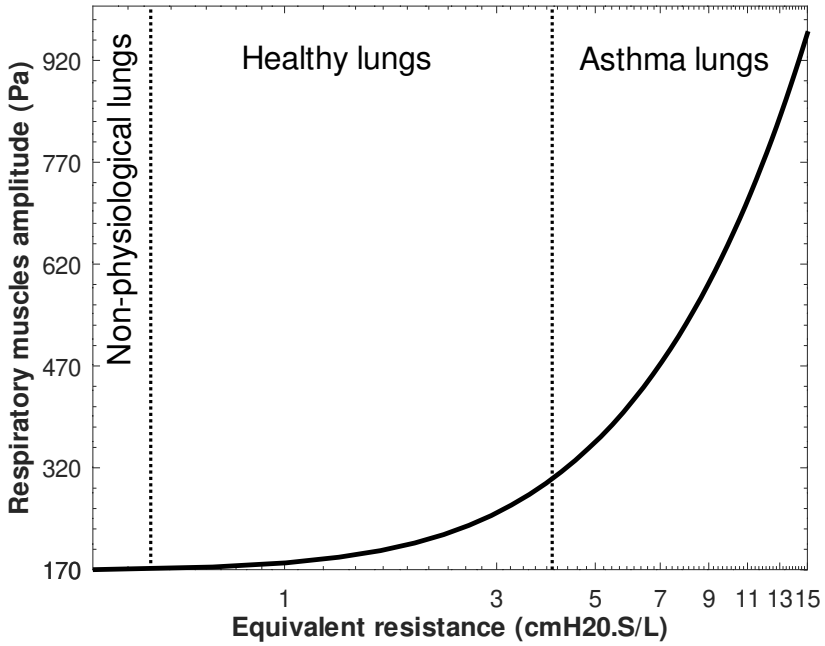

Figure 2.14: Evolution of the amplitude effort of the respiratory muscles according to the increase of the resistance of the lungs in order to ventilate a tidal volume of 500 mL. The axis of the equivalent resistance is displayed in log-scale. This situation simulates the compensatory effort that the respiratory muscles has to produce during an asthma crisis to keep a proper ventilation.

2.5.3.2 Chronic Obstructive Pulmonary Disease

We have seen in the first chapter that the constriction of the first generations of bronchi and bronchioles is one of the main symptom of the COPD. This disease can also lead to the deterioration of the alveoli. Consequently, it induces a decrease of the stiffness of the lungs and the exchange of gas at the acinar level is weaken. The combination of all those factors leads to the phenomenon called pulmonary hyperinflation. The lungs hyperinflation refers to the rise in functional residual capacity (FRC - lung volume at the end of tidal expiration) : the lungs volume is above the volume usually used at rest. It is due to two main factors : the increase of the resistance of the airways and the decrease of the elastic recoil (due to the loss of stiffness). Consequently, as mentioned in the previous paragraph, the time needed to empty the lungs at tidal volume increases and the expiration is not completely ensured. Moreover the degradation of the aveoli increases ventilatory demands which reduces the expiration time and the volume of exhaled air, that induces hyperinflation. Moreover, as the respiratory needs are higher, the muscular work of breathing increases. This phenomena is somewhat compensated by the rise of the lungs volume that enlarges the airways and consequently, decreases the resistance to air flow [121].

We use our model to illustrate and to explore the lungs hyperinflation phenomenon. We use most of the data set in the default configuration of healthy lungs, but change the following ones : the resistance of the tree is manually increased to reach physiological lungs resistance in case of COPD, namely 10 cmH2O.L^{-1}.s [77]. To the best of our knowledge, we do not find any satisfactory values in the literature on the elastic properties of a COPD lungs, then we decide arbitrarily to reduce the Young's modulus by a factor 2, namely $E = 628$ Pa. Finally, for a more realistic visualisation of the elastic recoil, we use the more realistic ventilatory function to mimic the action of the respiratory muscles. We use three different time periods according to the need : three, five and six seconds. Typically, the functions used are respectively :

$$\tau_1(t) = \begin{cases} -A.sin(\frac{\pi t}{1.2}) & 0 \leqslant t < 0.6 \\ -A & 0.6 \leqslant t < 0.8 \\ -A.sin(\frac{\pi(t-0.6)}{0.4}) & 0.8 \leqslant t < 1 \\ 0 & 1 \leqslant t < 3 \end{cases} \quad \tau_2(t) = \begin{cases} -A.sin(\frac{\pi t}{2.2}) & 0 \leqslant t < 1.1 \\ -A & 1.1 \leqslant t < 1.3 \\ -A.sin(\frac{\pi(t-1.1)}{0.4}) & 1.3 \leqslant t < 1.5 \\ 0 & 1.5 \leqslant t < 5 \end{cases}$$

$$\tau_3(t) = \begin{cases} -A.sin(\frac{\pi t}{2.2}) & 0 \leqslant t < 1.1 \\ -A & 1.1 \leqslant t < 1.3 \\ -A.sin(\frac{\pi(t-1.1)}{0.4}) & 1.3 \leqslant t < 1.5 \\ 0 & 1.5 \leqslant t < 6 \end{cases}$$

The Figure 2.15 illustrates the phenomenon of lungs hyperinflation by comparing the air flows and the associated volumes between healthy and COPD lungs, while ventilating a same tidal volume of 500 mL with a same respiratory cycle of five second. Our model predicts that the COPD lungs need a respiratory muscles effort 3.5 times greater than the healthy lungs. We observe that the COPD lungs do not deflate properly the inhaled air during expiration and consequently the lungs progressively works with higher volume. We also see in our model that the FRC increases of about 600 mL for the COPD case. It is not really surprising as the FRC for healthy lungs is about 40% of the TLC (Total Lung Capacity = 3-8 L) whereas it can reach up to 80% of the TLC for COPD lungs [49]. For example for a TLC= 6 L, the FRC increases from 2.4 L to a maximum of 4.8 L for COPD lungs. Additionally, an other consequence of lungs hyperinflation is the increase of the respiratory rate due to the deterioration of the alveoli and less efficient gas exchanges. The Figure 2.16 shows that this increase accentuates the fact that the lungs do not deflate properly and then work with higher volume. Despite the fact that a higher respiratory rate involves higher air flows in average, a higher respiratory rate also involves higher efforts from the respiratory muscles in average. Thus, the muscles need more and more energy, hence the respiratory rate continues to grow and requires more effort from the muscles, etc. The lungs hyperinflation often goes along with fatigue of the respiratory muscles.

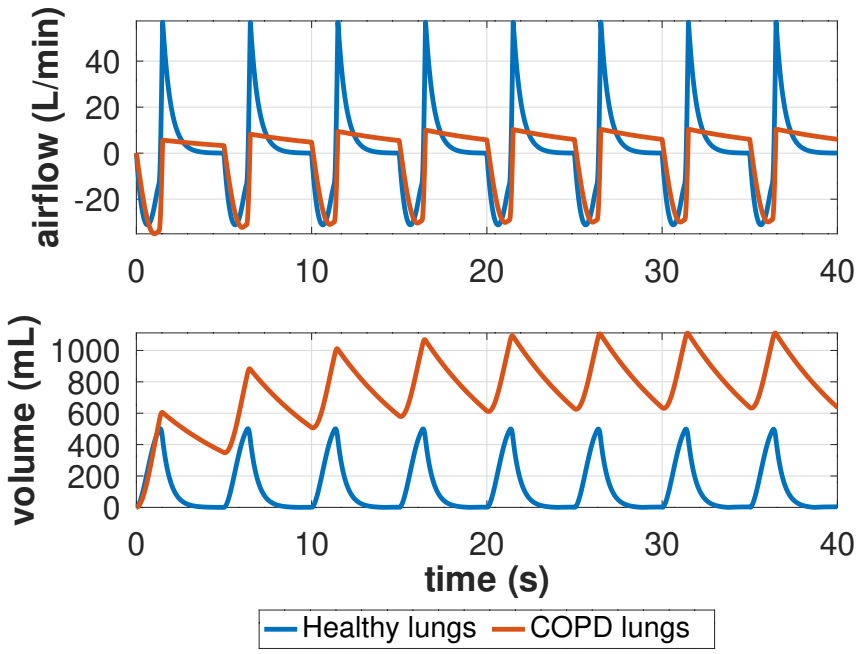

Figure 2.15: Comparison of the airflows and the associated volumes between healthy and COPD lungs during ten respiratory cycles of five seconds. We can see that the increase of the resistance and the reduction of the elastic recoil prevent the lungs to empty properly the air that flows in. Consequently the COPD lungs have to work at higher volumes.

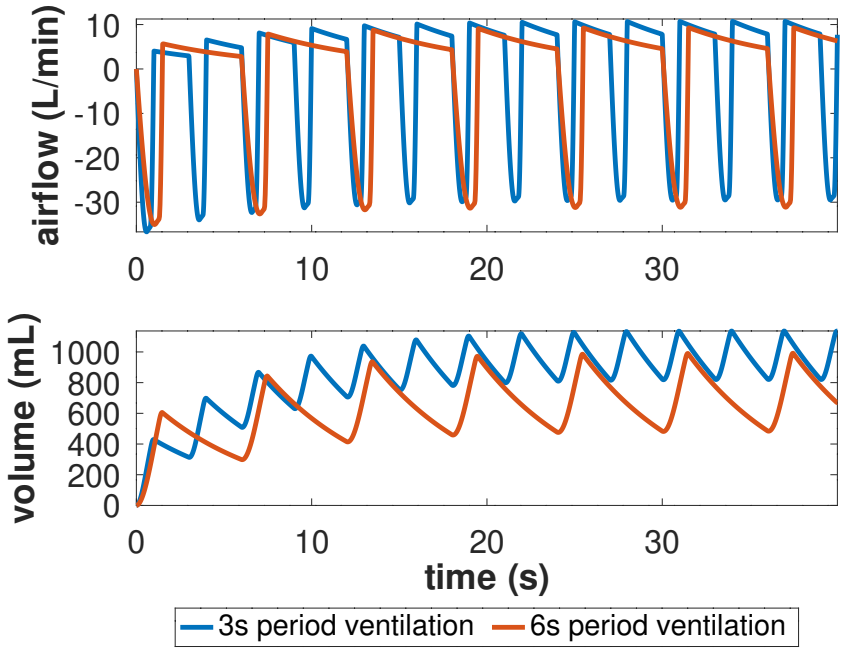

Figure 2.16: Comparison of the airflows and the associated volumes of COPD lungs during ten respiratory cycles of three and five seconds. This figure underlines the fact that the increase of the respiratory rate (reducing the time of the ventilating cycles) due to higher respiratory demands (because of the loss of alveoli in case of emphysema) leads the lungs to work with higher volume. This emphasizes the phenomenon of lungs hyperinflation.

2.5.3.3 Cystic fibrosis

One of the main symptom of the cystic fibrosis (CF) is a bad hydration of the mucus becoming too stick and viscous. This alters its motion and its proper evacuation from the lungs. The mucus is viscoelastic and its inner stress needs to be larger than its yield stress to be able to move. We recall that the order of magnitude of the yield stress σ_0 for an healthy mucus is typically $\sigma_0 \simeq 0.1 - 1$ Pa [70, 83, 84]. For a non-healthy mucus, in case of CF, the order of magnitude for the yield stress is about $\sigma_{cf} \simeq 1 - 10$ Pa [70]. One of the main mechanism to mobilize the mucus is cough. Cough induces strong air flows in the airways. Those air flows apply a stress on the mucus, called shear stress, that mobilizes the mucus and favours its expectoration. In healthy individuals, cough is sufficient to move the mucus toward the trachea and the mouth. The mucus is then either swallowed or expelled. However, in CF individuals, the mucus is overproduced and it is too stick to be shifted. Therapeutic methods are then required, as chest physiotherapy. Here, we will compare the behaviors of the shear stress in the airways between healthy and CF lungs during a maneuver of chest physiotherapy. We choose to model an idealized maneuver of chest physiotherapy and let the next chapter (3) studying the HFCWO. We consider a force that pushes and steers the lungs at low frequency to produce air flow in the pulmonary tree.

To the best of our knowledge, we did not find any satisfactory data about the resistance of adult lungs with CF. However, in [44], the authors propose a mean lungs resistance measured from thirty two patients with CF, aged fourteen on average. Hence our comparison focuses on average healthy adult lungs and average CF young adult lungs.

Then, we consider now the stress due to the air–mucus interaction [83, 84] in the airways, during tidal ventilation. As the mucus layer is in general thin relatively to the diameter of the airways, the stress in the mucus can be approximated by the wall shear stress induced by the air flow in the airways [124, 125]. The amplitude of the applied force is set to the one used for tidal ventilation. Hence, the order of magnitude of the induced air flows will be the same as the ones observed for tidal breathing simulations. We assume that the airflows induced by the ventilation at rest are quite small. Hence, we assume that the air fluid mechanics follows the Poiseuille's regime in the airways. The wall shear stress σ_{a} in an airway with radius r and an airflow ϕ is then [124]

$$\sigma_{\mathrm{a}} = \frac{\mu_a \phi}{\pi r^3}$$

with μ_a the air viscosity, $\mu_a = 1.8\ 10^{-5}$ Pa.s.

The Neumann condition at $x = 0$ mimicking the therapy is set to : $\sigma(u).n = \tau = Asin(\omega t)$, with $A = 100$ and $\omega = 1/5$. The cystic fibrosis reduces the volume of air in the lungs due to to the accumulation of mucus in the airways that reduces their lumen area. As a consequence, the resistance and the stiffness of the lungs are increased [44, 132]. In our model, the CF is modeled by setting the resistance of the tree to 17 cmH2O.L^{-1}.s and the lungs stiffness to $E = 2512$ Pa. The value of the resistance is taken from [44]. In our simulation, setting $R_{eq} = 17$ cmH2O.L^{-1}.s corresponds to reduce the lumen radius of the airways of a healthy bronchial tree by a factor $\simeq 1.9$. This indicates that almost half of the area of all the airways in the bronchial tree is filled by mucus. In reality, the mucus is not necessarily distributed homogeneously in the bronchial tree, some airways are more obstructed than others ; here we choose to keep the symmetrical and fractal properties of our tree by homogenizing the distribution of the mucus along the bronchial tree. Finally, in order to express the increase of the lungs stiffness, we multiply the Young's modulus for healthy tissue by a factor 2 ($E = 2512$ Pa).

Then, we calculate the mean shear stresses over one period of a force cycle of five seconds, for each generation of the tree, that is displayed in the Figure 2.17. Globally, we observe a constant pattern of the mean absolute wall shear stress through the tree with a trumpet-like shape as we sink in the tree. Namely the standard deviation of the wall shear stresses of the bronchi within a same generation grows as the generation index increases. The wall shear stress applied by the air on the mucus is directly related to the size of the airways and to the amount of airflow in the airway. We recall that the size of the branches from one generation to the

next is reduced by a factor $h = \left(\frac{1}{2}\right)^{\frac{1}{3}}$. In these conditions, if the airflows were distributed equally in all the branches of a single generation, the shear stress should decreases from one generation to the next with a factor $\frac{1}{2h^3} = 1$, i.e. the shear stress should be constant through the generations, see [124, 125]. In our case, the airflows are not distributed equally in the airways of a same generation. However, most of the airways feel a wall shear stress of the same magnitude, indicating that the distribution of the airflows in the airways of a same generation remains relatively homogeneous. Moreover the Figure 2.17 reveals that the overall wall shear stresses of the CF young adult lungs is of the same order of magnitude of the one of the healthy adult lungs. It is not surprising with the definition of the shear stress. The air flow is inversely proportional to the resistance, and the resistance is inversely proportional to the radius to the power of four. However, the mucus in case of CF needs to feel a yield stress ten to hundred times bigger than the healthy mucus. The ratio between the wall shear stress and the yield stress is much smaller for CF mucus than for healthy mucus. Consequently, a respiratory therapy is less efficient for CF individual than for healthy individual. It is then needed to understand the effect of such therapies in order to improve their efficiency.

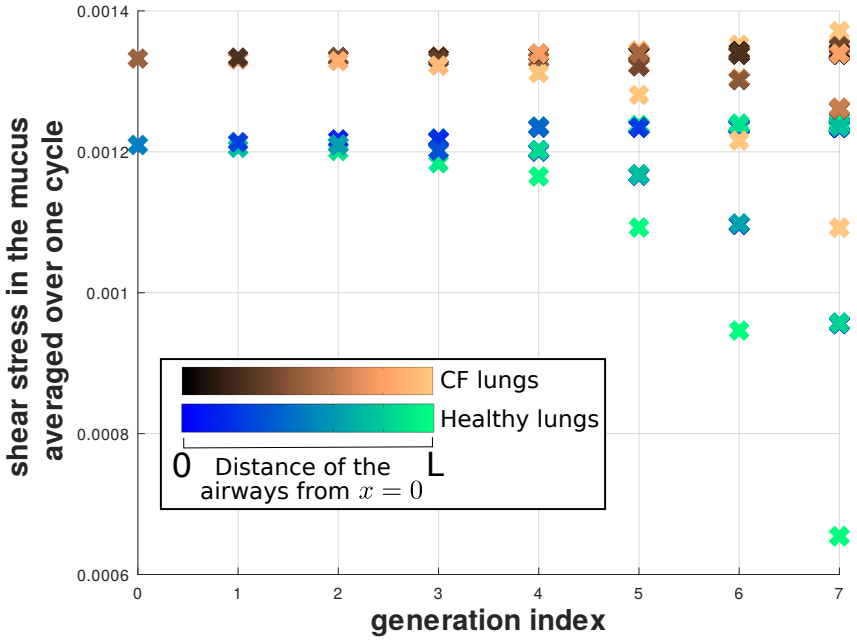

Figure 2.17: Comparison between the mean of the absolute shear stresses of healthy adult lungs and of CF young adult lungs during a sinusoidal maneuver of chest physiotherapy. The mean is computed over the duration of one maneuver cycle for all the bronchi of an eight generations tree. The color reflects the location of the corresponding airway in [0, L], i.e. the mean position of the A_i's fed by the airway. For example, the root of the tree is feeding all the A_i and its mean position is L/2; the two branches of the second generation are located at L/4 and 3L/4, and so on.

2.6 Discussions and conclusion

In this chapter, we propose, in the same spirit as in [137, 110], a mathematical model of the biophysical mechanisms of the lungs in order to study the tidal breathing in healthy and non-healthy lungs. In our model, we accounted for the interaction between two core physical processes involved in the lung's biomechanics: the viscous dissipation of air in the airways and the mechanics of the deformation of the lung's tissues. The tree structure acts on the displacement of the respiratory zone by applying a damping pressure that can even prevent the deformation, if one or several branches are obstructed. Moreover, through the action of the air in the tree, a deformation in the material propagates its influence very quickly –actually instantaneously in our model– everywhere in the material once it has been stimulated.

The unidimensional model suggests that the overall lung's tissue displacements damped by the tree behave similarly as harmonic oscillators whose theory is thoroughly studied in the literature. The general behavior of the coupled model could be described using its similarities with harmonic oscillators that could bring interesting features regarding the resonance.The modelling of the ventilation at rest strengthens the suitability of our model to simulate physiological lungs behaviors. The study of the behaviors of pathological lungs such as in asthma, COPD or CF, provides results in accordance with physiopathology and predicts lungs hyperinflation and its improvement resulting from decreasing breathing frequency. It also shows the influence of each parameter of the model on the response of the system. For example, it shows that the variations of the lung's stiffness plays a role on the elastic capacity of the lungs to return to a steady state, or that the intensity of the lungs deformation is modulated by the resistance of the lungs. However, the model shows the intrinsic influence of the parameters only. The results have to be interpreted within the hypothesis and limitations of the model.

The model is based on a set of simplification hypotheses for the geometry of the lungs, the mechanics of the tissues and the air fluid dynamic. Actually, unlike the real lungs, we consider a tissue that is elastic, isotropic and homogeneous, where the strains are small. We limit the tissue evolution in a single spatial direction, since we use a unidimensional space domain. Hence, we only capture the intrinsic influences of the parameters. The pulmonary tree structure is idealized with symmetric bifurcations and cylindrical airways, it is not accounting for the complex geometry of the bifurcations. Moreover, we assume that the air in this tree follows the Poiseuille's regime, i.e. with low velocities and fully developed axisymmetric profile. This is not well adapted for the upper bronchial airways dynamics. Consequently, the resistance of the tree does not reflect properly the overall resistance that the air encounters on its way from the ambient air to the exchange surface. This is highlighted by the simulation of the human ventilation at rest where a corrective factor for the resistance is needed to catch a realistic behavior. Additionally, although the deformation propagates very quickly in the lungs, we do not account for the the temporal evolution of the circulations of the air inside the tree : the damping of the tree acts instantaneously on the lung's tissue.

Nevertheless, our model is able to successfully mimic the rest ventilation and to capture the interactions between the tissue mechanics and the air flow in the airways. The results are observed for biological and mechanical parameters of a typical average healthy and non-healthy person. Hence, our model hypotheses are a way to get a first clear view of the intrinsic dynamics of the system, and particularly during tidal breathing. Moreover, it suggests the significance of studying the resonance in the lungs that could be an interesting tools for HFCWO. The next chapter takes an interest on this phenomenon through HFCWO simulations and studies the interconnected influences of the parameters with a dimensionless formulation of the system.

Appendices

2.A Details of calculation for the resistance of the tree

Depending on the considered case and on its computational cost, the number of generations $n+1$ in our model can be smaller than the estimated number of generations of the bronchial tree, which is about 17 [136]. Hence, the rest of the generations of the bronchial tree and of the alveolar tracts are mimicked using virtual quasi-fractal subtrees, see subsection 2.2.1.2. We assume that the branches of a virtual subtree are all submitted to the same pressure. Consequently, the hydrodynamic response of these subtrees is based on their equivalent hydrodynamic resistance only. Then, in order to account for these subtrees (bronchial and acinar) in our model of the pulmonary tree, the equivalent hydrodynamic resistance of the subtrees associated to a terminal branch is added to the resistance of that terminal branch. We detail some calculation for that purpose whose results are presented in the subsection 2.2.1.

We set the number of generations of the bronchial tree to $n_t = 17$ [136] and the number of generations of the alveolar tracts to $n_a = 6$ [136]. However, for the calculation, we keep the variable name n_t and n_a if one would like to change their value. The reduction ratios in the bronchial tree and in the respiratory zone (alveolar tracts) are respectively $h_b = \left(\frac{1}{2}\right)^{\frac{1}{3}}$ and $h_{ac} = 1$ [136, 40].

Equivalent resistances. The resistances of the branches at a same generation are considered connected in parallel. Consequently, the equivalent resistance of the generation i of the tree is $R^i_{eq} = (2^{i-1}R^{-1}_{i-1})^{-1}$. Then the equivalent resistances of each generation of the tree are connected in serial. Hence, the theoretical equivalent resistance of the $n+1$ generations tree is

$$R_{th} = R_0 \sum_{i=0}^{n} \left(\frac{1}{2h_b^3}\right)^i$$

In the same way, the equivalent resistance of a single bronchial subtree of $n_t - (n+1)$ generations is

$$R_{st,n} = \frac{R_n}{h_b^3} \sum_{i=0}^{17-n-2} \left(\frac{1}{2h_b^3}\right)^i$$

Similarly, , the equivalent resistance of a single acinar subtree that contains the generations $n_t + 1$ to n_a is

$$R_a = \frac{R_{nt-1}}{h_{ac}} \sum_{i=0}^{n_a-1} \left(\frac{1}{2h_{ac}^3}\right)^i$$

Equivalent resistance of the whole tree. The total resistance of the whole tree is the sum of the equivalent resistances of the $n+1$ tree, the 2^{n+1} bronchial subtrees and the 2^{n_t} acinar subtrees :

$$R_{lung} = R_{th} + \frac{R_{st,n}}{2^{n+1}} + \frac{R_a}{2^{n_t}}$$

Including the contribution of the virtul bronchial and acinar region in the $n+1$ generations tree. We then need to include the contribution of the virtual subtrees in the resistance matrix of the $n+1$ generations tree. For that, we supplement each resistance R_n of the 2^n terminale branches by adding the equivalent resistances of their two bronchial subtrees and their 2^{n_t-n} acinar subtrees. We denote by $\tilde{R}_n$ the adjusted resistance of the airways at the generation $n+1$:

$$\tilde{R}_n = R_n + \frac{R_{st,n}}{2} + \frac{R_a}{2^{n_t-n}}$$

When computing the equivalent resistance of the adjusted resistance matrix $\mathcal{R}$, we obtain as expected

$$R_{eq} = \frac{1}{{}^tJ\mathcal{R}^{-1}J} = R_{lung}$$

2.B Finite element method

The finite element method (FEM) is used to solve the system of equations (2.11). This appendix details the calculus of our use of this numerical method in three dimensions.

We split the domain into n_e identical elements defined with an arbitrarily order basis functions. Let's denote by n_d the number of degrees of freedom in our discretized domain and by n_i the i^{th} degree of freedom, for $0 \leqslant i \leqslant n_d$.

Let's denote $u : \Omega \to \mathbb{R}^3$, $w : \Omega \to \mathbb{R}^3$, $x \in \mathbb{R}^3$ and $t \in \mathbb{R}$, respectively the displacement field, the test function, the spatial variable and the temporal variable. Using the FEM, the displacement field u is approximated by $u(x,t) = \sum_{k=0}^{n_d} u_k(t)\phi_k(x)$ as well as the test function $w(x,t) = \sum_{l=0}^{n_d} w_l(t)\phi_l(x)$. The element $u_k(t)$ stands for the values of the displacement, at time t and at the degree of freedom n_k.

For any smooth function $w : \Omega \to \mathbb{R}^3$ verifying the boundary conditions, the weak formulation of our model is

$$\int_\Omega \left(\rho\frac{\partial^2 u}{\partial t^2}w + \sigma_{elastic}(u) : \epsilon(w)\right) dx - \int_{\Gamma_1} \tau\ w\ dS + \sum_{i=1}^{N} p_i(\mathcal{F}[\dot{u}]) \int_{A_i} \operatorname{div}(w)\, dx = 0 \tag{2.30}$$

with $\sigma_{elastic}(u) = \lambda\ \mathrm{tr}\,(\epsilon(\mathrm{u}))\,\mathrm{I} + 2\mu\ \epsilon(\mathrm{u})$ and $\epsilon(u) = \frac{1}{2}\left(\nabla u + {}^t\nabla u\right)$.

Equation (2.30), which should hold for any w in this finite dimensional space, is written for any element ϕ_l of the basis

$$\begin{aligned}\int_\Omega \left[\rho \sum_{k=0}^{n_d}\sum_{l=0}^{n_d} \frac{\partial^2 u_k(t)}{\partial t^2} w_l(t)\phi_k(x)\phi_l(x) + \sum_{k=0}^{n_d}\sum_{l=0}^{n_d} u_k(t)w_l(t)\sigma_{elastic}(\phi_k(x)) : \epsilon(\phi_l(x))\right] dx + \\ -\int_{\Gamma_1} \tau(t) \sum_{l=0}^{n_d} w_l(t)\phi_l(x) dS + \sum_{i=1}^{N}\sum_{j=1}^{N} \mathcal{R}_{ij} \int_{A_j} \left(\sum_{k=0}^{n_d} \frac{\partial u_k(t)}{\partial t} \operatorname{div}(\phi_k(x))\right) dx \int_{Ai} \sum_{l=0}^{n_d} w_l(t) \operatorname{div}(\phi_l(x)) dx = 0\end{aligned} \tag{2.31}$$

From the previous equation we can compute respectively M, K, h, and G_{ik}, the mass, stiffness and damping matrices as well as dimensionless vector of loads as

$$\begin{cases} M_{kl} = \int_\Omega \rho\phi_k(x)\phi_l(x)dx \\ K_{kl} = \int_\Omega \sigma_{elastic}(\phi_k(x)) : \epsilon(\phi_l(x))dx \\ h_l = \int_{\Gamma_1} \phi_l(x)dS \\ G_{ik} = \int_{A_i} \operatorname{div}(\phi_k)dx \end{cases} \tag{2.32}$$

Note that the formulation above express the matrices and vector without taking the homogeneous boundary condition into account. For example, we can enforce Dirichlet boundary condition by setting $u_{n_i} = 0$ for chosen degrees of freedom i. Then matrices and vector need to be adapted according to. Hence, the last column and/or line associated to the degree of freedom blocked are eliminated in this case. We would rather use $\hat{M}, \hat{K}, \hat{G}$ and $\hat{h}$ to denote

respectively the mass, stiffness and damping matrices and vector of loads where boundary condition are applied. Moreover, for a lumped mass matrix, we notice that the system mass and rigidity matrices are those of vibrating masses linked with springs. The lumped matrix is an approximation of the mass matrix by using a trapezoidal quadrature rule. The point of view of a system of spring-mass may be used as a starting point for an homogenization process, see [39].

With $U = (u_k)_{0 \leqslant k \leqslant n_d}$ the vector of displacement and $D =^t G\mathcal{R}G$, the equation (2.31) is expressed as a linear matrix-vector system :

$$M \frac{d^2U}{dt^2} + K\ U + D\frac{dU}{dt} = \tau(t)\ h \tag{2.33}$$

or applying the Dirichlet condition :

$$\hat{M} \frac{d^2U}{dt^2} + \hat{K}\ U + \hat{D}\frac{dU}{dt} = \tau(t)\ \hat{h} \tag{2.34}$$

with $\hat{D} =^t \hat{G}\mathcal{R}\hat{G}$.

2.B.1 An example of FEM calculation in 1D : the Mass matrix

As an example, here is detailed the calculation of the Mass matrix from (2.32) with one dimension. In one dimension we focus in only one spatial direction, thus $x \in \mathbb{R}$ and the domain is $\Omega = [0, L]$, $L \in \mathbb{R}$. We split the domain Ω into n_x (identical size) segments with 2 nodes. Hence, we note $(x_i)_{0 \leqslant i \leqslant n_x}$, $x_i = i \times \delta x$, $\delta x = \frac{1}{n_x}$.

The coefficients of M are

$$M_{ij} = \int_0^L \rho \phi_i(x)\phi_j(x)dx$$

with ϕ a polynomial of order 1 defined as

$$\phi_i(x) = \begin{cases} \frac{x - x_{i-1}}{\delta x} & if\ x \in [x_{i-1}, x_i] \\ \frac{x_{i+1} - x}{\delta x} & if\ x \in [x_i, x_{i+1}] \\ 0 & otherwise \end{cases} \tag{2.35}$$

Knowing the definition of ϕ, we notice that the product $\phi_i \times \phi_j \quad \forall i, j \in \mathbb{N}$, is different from zero when $i = j$ and when $i = j \pm 1$. Then, we focus the calculation on the interval $[x_{i-1}, x_{i+1}]$ when $i = j$ and $i = j \pm 1$. We also focus on the specific case where $i = j = 0$ and $i = j = n_x$.

- When $i = j$, the coefficients M_{ii} for all i are computed with

$$\int_{x_{i-1}}^{x_{i+1}} \phi_i(x)\phi_i(x)dx = \int_{x_{i-1}}^{x_i} \left(\frac{x - x_{i-1}}{\delta x}\right)^2 dx + \int_{x_i}^{x_{i+1}} \left(\frac{x_{i+1} - x}{\delta x}\right)^2 dx$$

Setting $u = x - x_{i-1}$ and $v = x_{i+1} - x$, the coeffcients M_{ii} are equaled to

$$\int_0^{\delta x} \left(\frac{u}{\delta x}\right)^2 du + \int_0^{\delta x} \left(\frac{v}{\delta x}\right)^2 dv = \frac{2\delta x}{3}$$

- When $i = j \pm 1$, the coefficients $M_{i(i+1)}$ for all i and are calculated with

$$\int_{x_{i-1}}^{x_{i+1}} \phi_i(x)\phi_{i+1}(x)dx = \int_{x_i}^{x_{i+1}} \phi_i(x)\phi_{i+1}(x)dx = \int_{x_i}^{x_{i+1}} \left(\frac{x_{i+1} - x}{\delta x}\right)\left(\frac{x - x_i}{\delta x}\right) dx$$

Setting $u = x - x_i$, previous calculation becomes

$$\int_0^{\delta} x \left(\frac{\delta x - u}{\delta x}\right)\left(\frac{u}{\delta x}\right) dx = \int_0^{\delta} x \left(\frac{u}{\delta x} - \frac{u^2}{\delta x^2}\right) du = \frac{\delta x}{6}$$

The term $M_{i(i+1)}$ is equaled to $M_{(i-1)i}$.

- Moreover

$$M_{00} = M_{n_x n_x} = \frac{\delta x}{3}$$

Therefore the Mass matrix M for the one dimensional case is

$$M = \rho \begin{pmatrix} \frac{\delta x}{3} & \frac{\delta x}{6} & & & \\ \frac{\delta x}{6} & \frac{2\delta x}{3} & \ddots & & 0 \\ & \ddots & \ddots & \ddots & \\ & & \ddots & \frac{2\delta x}{3} & \frac{\delta x}{6} \\ & 0 & & \frac{\delta x}{6} & \frac{\delta x}{3} \end{pmatrix}$$

2.C Angular eigen-frequencies

In this subsection, we describe a specific property of the equation (2.11) written with the finite element method described on the previous subsection for the unidimensional case. Here, we consider the system without taking into account the tree structure, namely $p_i = 0$ for all i. It allows us to study, for materials of fixed size with homogeneous elastic properties, the propagation of deformation wave and the natural frequencies of the material.

The unidimensional domain is $\Omega = [0, L]$, $L \in \mathbb{R}$. We use the unidimensional linear matrix-vector relation (2.18) presented in the subsection 2.3.2. Without considering the coupling with the tree, the matrix of damping D is not taking into account. Hence the relation is

$$M \frac{d^2U}{dt^2} + K\,U = \tau(t)\,h \tag{2.36}$$

The matrices M, K stand for the matrices of Mass and Stiffness. The vector of load is denoted by h.

We decompose the matrix M as $M = L^t L$ using Cholesky factorization. Setting $\mathcal{S} = {}^tLU$, $\overline{K} = L^{-1}K^tL^{-1}$ and $G(t) = \tau(t)L^{-1}h$, the equation becomes

$$\frac{d^2\mathcal{S}}{dt^2} + \overline{K}\,\mathcal{S} = G(t)$$

$\overline{K}$ is symmetrical and invertible so it can be diagonalised using its eigenvectors q_i associated to its eigenvalues $\overline{k}_i$. With $Q = (q_i)_{1 \leqslant i \leqslant n_x}$, $\mathcal{U} = Q^{-1}\mathcal{S}$ and $H(t) = Q^{-1}G(t)$, we finally have :

$$\frac{d^2\mathcal{U}}{dt^2} + \mathcal{D}\mathcal{U} = H(t) \tag{2.37}$$

where the vector unknowns is $\mathcal{U}$. As presented in 2.B, the equation (2.37) is adapted in the case of Dirichlet boundary condition and the same calculation process used is applied to $\hat{M}$ and $\hat{K}$. The diagonal matrix $\mathcal{D}$ contains the square of the natural angular frequencies (called $(\omega_i)_{1 \leqslant i \leqslant n_x}$). For example, to obtain the two first angular eigen-frequencies ω_1 (fundamental) and ω_2 used in our numerical simulations, we compute the square root of $\mathcal{D}$ and take the two smallest values ; the smallest between the two is the fundamental natural angular frequency ω_1. The relation between the frequency and the angular frequency is $f = 2\pi\omega$. We note that there are as much natural angular frequencies as there are degrees of freedom and that the accuracy of their values is improved when the number of degrees of freedom increases. Actually, the natural angular frequencies ω_n are such that

$$|K - \omega_n^2 M| = 0 \quad \text{or} \quad |\hat{K} - \omega_n^2 \hat{M}| = 0 \quad \text{(Dirichlet)} \tag{2.38}$$

It is interesting to get natural frequencies of our system to get an idea about the resonance and to link the frequencies used with HFCWO devices with the theoretical eigen angular frequencies.

Analytical definition of the natural angular frequencies

The natural frequencies are computed with the discrete system without tree. However, they can be computed directly from the continuous system in a classical way [114, 41, 69]. The natural angular frequencies are linked to the boundary conditions. For example, considering the case of axial vibrations of elastic bars with one end fixed and the other end free similar to our case, the natural angular frequencies are defined as :

$$\omega_k = \frac{(2k-1)c\pi}{2L} \quad ; \quad 1 \leqslant k \leqslant +\infty \tag{2.39}$$

with $c = \sqrt{\frac{(\lambda+2\mu)}{\rho}}$ the velocity of the wave deformation. For our numerical cases we do not change the boundary conditions : a Neumann condition on the boundary $x = 0$ (τ) and a Dirichlet condition on $x = L$ ($u = 0$). Consequently, we do not need to compute the natural frequencies from others boundary conditions.

Through simulations, we display the four first natural modes in Figure 2.18. We set the values of the parameters of the model to those used in the non-physiological configuration in subsection 2.4.1. We use $\mathcal{R}_{norm} = \frac{\mathcal{R}}{\mathcal{R}_{eq}}$ with $\mathcal{R}$ the resistance matrix computed from $l_0 = 6$cm and $r_0 = 1$cm, and c and all other variables are equal to one. The natural pulsations computed with the experimental definition (2.38) are similar to those computed with the theoretical definition (2.39).

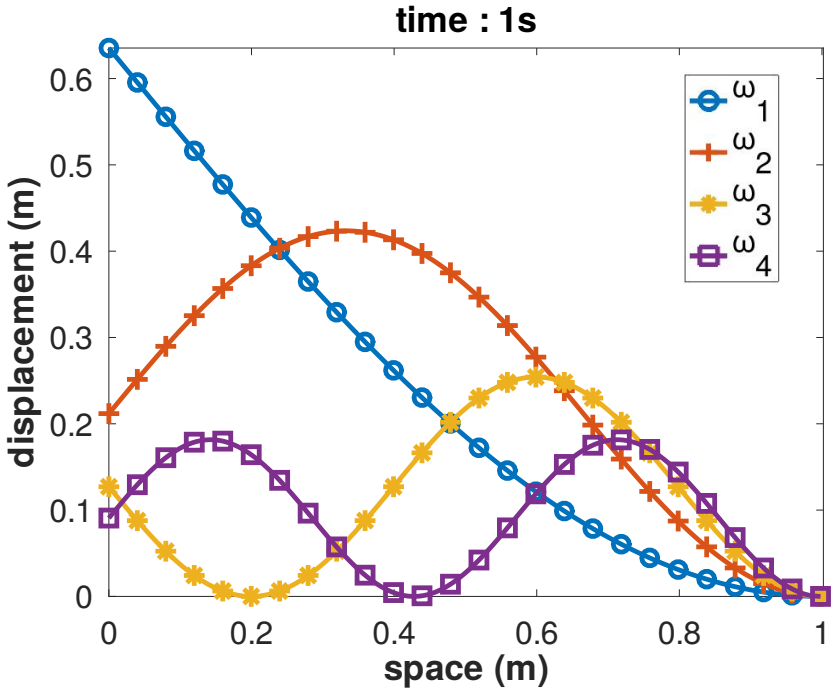

Figure 2.18: Material displacements along the domain at time $t = \frac{1}{c} = 1$ (i.e. the time the wave takes to propagate from one boundary to the other with a velocity of $c = 1$). The material is fixed at one boundary ($u(L,t) = 0$) and stimulated at the other ($x = 0$) by a sinusoidal force whose pulsation varies between the four first eigen pulsation (ω_1 to ω_4).

2.D A case of damped harmonic oscillator with one degree of freedom

This appendix details the theory behind the damped and forced harmonic oscillator with one degree of freedom on which we base some of the results.

With one degree of freedom (DoF), an oscillatory system describes for example the oscillations of a mass tied to a spring, of a pendulum or of an electronic circuit. Taking the case of a pendulum system, the motion of the mass can be damped by a damping influence or/and can be stimulated by an exciting force. In the absence of damping or exciting influences, the oscillation is considered as free and the motion of the mass is only due to its initial conditions on position or velocity. The contents of this appendix are classic and can be found in the litterature [120, 43].

The general equation describing the motion of a forced damped harmonic oscillator designated by $x(t)$ with one DoF is :

$$m\frac{d^2x(t)}{dt^2} + b\frac{dx(t)}{dt} + kx(t) = f(t) \tag{2.40}$$

with m the mass, c the damping coefficient, k the stiffness coefficient and $f(t)$ a driving force. The equation (2.40) can be written

$$\underbrace{\frac{d^2x(t)}{dt^2}}_{\text{acceleration}} + 2\xi\underbrace{\frac{dx(t)}{dt}}_{\text{damping}} + \underbrace{\omega_0^2 x(t)}_{\text{stiffness}} = \underbrace{h(t)}_{\text{driving force}} \tag{2.41}$$

with $\xi = \frac{b}{2m}$ the damping coefficient, $\omega_0 = \sqrt{\frac{k}{m}}$ the natural angular frequency of the oscillator and $h = \frac{1}{m}f$. We concentrate on periodic driving force. The solution of the equation (2.41), that can be explicitly computed, relies on the value of the damping coefficient, of the amplitude and of the pulsation of the driving force.

Free oscillations

In the case of free oscillation ($b = 0$ and $f(t) = 0\ \forall t$), the solution of the equation (2.41) is a combination of sines and cosines depending on the initial conditions on position and velocity :

$$x(t) = x(0)cos(\omega_0 t) + \frac{v(0)}{\omega_0}sin(\omega_0 t)$$

Then the mass oscillates at the natural pulsation. The potential and kinetic energies produced during the movement follow this oscillating pattern with a 180° difference of phase. The kinetic energy is defined by $E_k = \frac{1}{2}mv^2(t)$ with $v(t) = \frac{dx(t)}{dt}$ and the potential energy by $E_p = \frac{1}{2}kx^2(t)$. At the equilibrium position, the velocity of the mass is maximal, then the kinetic energy is maximal. Then, the more the mass deviates from its equilibrium position, the more the potential energy, and the less the kinetic energy. Finally, the mass returns to the equilibrium position once the kinetic energy is equal to zero, see Figure 2.19.

Damped and forced oscillations

When the motion of the mass is damped, for example if it is plunged into a viscous fluid, and forced by an external action, the solution of the equation 2.41 is a combination of a homogeneous and a particular solutions :

$$x(t) = x_h(t) + x_p(t)$$

The homogeneous solution tends to zero as time goes to infinity, leading the general solution to tend to the particular solution. Consequently, the general solution follows two regimes : a transient and a steady-state regime.

The homogeneous solution x_h**.** The homogeneous solution x_h follows one of the three types of behavior, defined in table 2.2, according to the value of the reduced discriminant $\Delta' = \xi^2 - \omega_0^2$.

For each of the three types of behavior, the decreasing exponential term ($e^{-\xi t}$) leads the homogeneous solution to be damped and to tend to zero as time goes to infinity ($x_h(t) \underset{t\to+\infty}{\longrightarrow} 0$).

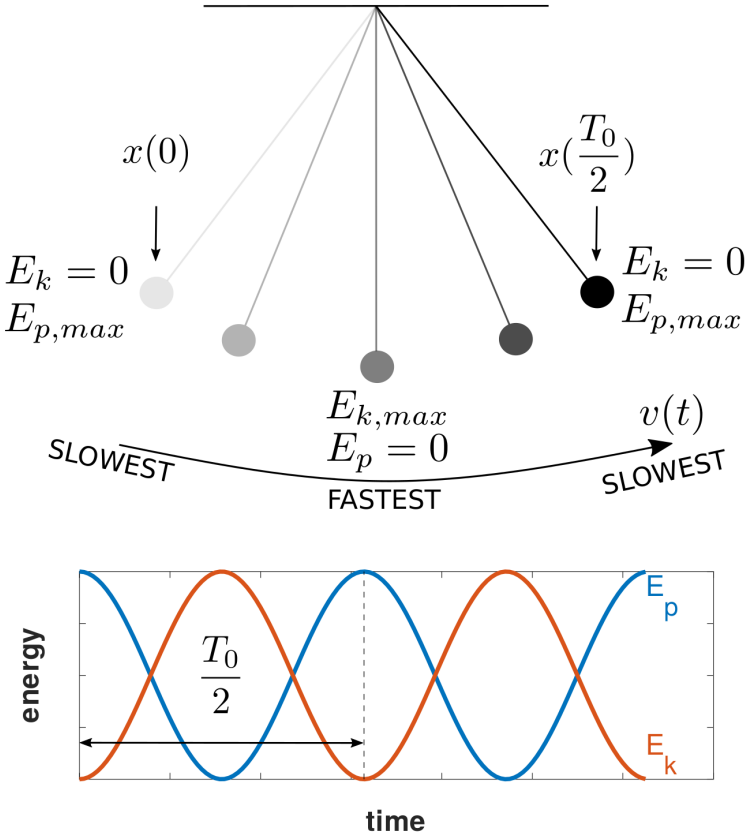

Figure 2.19: Schematic of the free oscillations of a pendulum released from the initial position ($x(0)$) over half a period ($\frac{T_0}{2}$) without any damping or driving force. It displays the evolution of the kinetic and potential energies where $E_{k,max}$ and $E_{p,max}$ are the maximal values of respectively the kinetic and the potential energies. Particularly we observe that the average of the kinetic and potential energies over one period is equal.

$\Delta' > 0$	$x_h(t) = e^{-\xi t}\left(A_a e^{\sqrt{\Delta' t}} + B_a e^{-\sqrt{\Delta' t}}\right)$	over damping
$\Delta' = 0$	$e^{-\xi t}(A_c t + B_c)$	critical damping
$\Delta' < 0$	$(A_p cos(\omega_d t) + B_p sin(\omega_d t))\, e^{-\xi t}$	under damping

Table 2.2: The tree types of behavior of the homogeneous solution depending on the intensity of the damping. The couples (A_a, B_a), (A_c, B_c) and (A_p, B_p) are constant values computed from initial conditions and $\omega_d = \sqrt{\omega_0^2 - \xi^2}$ the damped pulsation. In case of small damping and without external force, we notice that the motion of the mass oscillates at pulsation slightly lower than the fundamental natural pulsation.

Hence, the transient regime is determined by the homogeneous solution.

The particular solution x_p**.** The steady-state regime occurs for large times t when the homogeneous solution is close to zero. Hence, the solution $x(t)$ is only depending on the particular solution ($x(t) \underset{t\to+\infty}{\longrightarrow} x_p(t)$). The particular solution is of the form of the external force. For a periodic driving force of the type $h(t) = Hcos(\omega t)$, the particular solution is

$$x_p(t) = Xcos(\omega t + \phi_x)$$

where X and ϕ_x are constants determined according to the characteristics of the system and

of the stimulation. The constant X is the magnitude of the oscillations in the steady state and ϕ_x is the phase difference of those oscillations according to the stimulation. The two constants can be determined through two ways : an algebraic and a complex method. We will not detail the methods here and give directly the expression of X and ϕ_x :

$$X = \frac{H}{\sqrt{(\omega_0^2 - \omega^2)^2 + (2\xi\omega)^2}} \qquad \text{and} \qquad tan(\phi_x) = \frac{-2\xi\omega}{\omega_0^2 - \omega^2}$$

We can also study the magnitude of the oscillations with the Q-factor or quality factor which characterizes the intensity of the damping :

$$Q = \frac{\omega_0}{2\xi}$$

Hence, the higher is Q, the lower is the damping.

Resonance for the displacement. The study of denominator of X expression shows that there exists a maximum for X if $\xi < \frac{\omega_0}{\sqrt{2}}$. This maximum is reached at the angular frequency

$$\omega_r = \sqrt{\omega_0^2 - 2\xi^2}$$

The angular pulsation ω_r is the resonance pulsation of the oscillator at steady-state for damping satisfying $Q > \frac{1}{\sqrt{2}}$ ($\xi < \frac{\omega_0}{\sqrt{2}}$). Particularly, if the driving force stimulates the mass at this particular angular frequency, the resulting displacement is maximal and tends to increase through time. It appears that for the pulsation ω_0, the smaller the damping is, the closer the resonance angular frequency is to the fundamental angular frequency ($\omega_r \approx \omega_0$).

For sufficiently high damping such as $Q \leqslant \frac{1}{\sqrt{2}}$ ($\xi \geqslant \frac{\omega_0}{\sqrt{2}}$), the amplitude of the steady solution reaches its maximum for $\omega = 0$, see the Figure 2.20.

Resonance for the velocity. The phenomena of resonance appears also for the velocity $\frac{dx(t)}{dt}$. We can deduce the amplitude of the velocity :

$$V = \frac{\omega H}{\sqrt{(\omega_0^2 - \omega^2)^2 + (2\xi\omega)^2}}$$

which reaches its maximum for angular frequency equal to the fundamental angular frequency. It also indicates that the phenomena of resonance for the velocity occurs for any values of damping, see the Figure 2.20.

2.E Configurations of parameters for the numerical simulations

For a clear distinction, this appendix gathers all the values of the configurations of parameters used in the numerical simulations of this manuscript. One of the configuration is of non-physiological lungs where all the variables are standardized. The others configurations of parameters model averaged healthy and non-healthy lungs. Specifically, the non-heatlhy lungs mimic asthma, chronic obstructive pulmonary disease (COPD) and cystic fibrosis (CF) diseases. Most of the variables are taken from [111] for physiological lungs, if not the reference is stated.

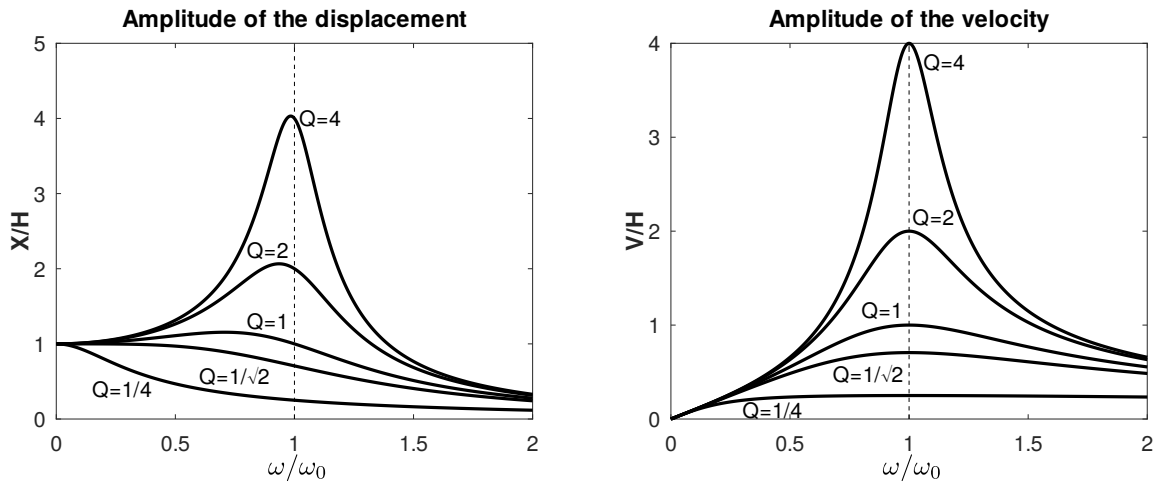

Figure 2.20: **Left:** Evolution of the magnitude of the oscillations (X/H) according to the pulsation (ω/ω_0). If the damping is small ($Q > \frac{1}{\sqrt{2}}$), the maximum of the amplitude of the oscillation is reached for a pulsation close to the resonance pulsation ($\omega \approx \omega_r = \sqrt{\omega_0^2 - 2\xi^2}$), and for a pulsation close to zero otherwise $\omega \approx 0$. The smaller the damping is (i.e. the bigger the Q-factor is $Q >> 1$), the closer the resonance pulsation is to the natural pulsation ($\omega_r \approx \omega_0$). **Right:** Evolution of the magnitude of the velocity (V/H) according to the pulsation (ω/ω_0). The maximum of the amplitude is always reached for a pulsation equal to the natural pulsation ($\omega = \omega_0$) independently of the intensity of the damping. However, for high damping ($Q < \frac{1}{\sqrt{2}}$), the amplitude of the velocity is small and in a plateau, i.e. it does not vary too much as the pulsation ω varies.

Model input parameters modeling the applied pressure		
Non-physiological force		
Physical quantity	**Parameter name**	**Value**
Frequency of the applied pressure	f	1 Hz
Amplitude of the applied pressure	A	1 Pa
Respiratory muscles effort for the ventilation at rest in healthy lungs (tidal volume of 500 mL)		
Frequency of the applied pressure	f	$\frac{1}{5}$ Hz *1
Amplitude of the applied pressure	A	200 Pa *2
Pressure applied by the HFCWO therapy		
Frequency of the applied pressure	f	1 to 20 Hz
Amplitude of the applied pressure	A	200 Pa

Table 2.3: Input parameters of the model for the applied pressure. *1We make the frequency varying in the case of COPD lungs to $\frac{1}{3}$Hz and $\frac{1}{6}$Hz, see subsection 2.5.3.2. *2The amplitude varies in the cases of non-healthy lungs in order to ventilate a tidal volume of 500mL ; it is detailed in the subsection 2.5.3. The amplitude is computed in order to get physiological value of tidal breathing.

Lungs model input parameters		
Non-physiological lungs		
Physical quantity	**Parameter name**	**Value**
Lung volumetric density	ρ	1 kg.m^{-3}
Characteristic lungs size	L	1 m
Lamé parameters	$\lambda + 2\mu$	1 Pa
Tree root radius (trachea radius)	r_0	0.01 m
Tree root length (reduced trachea length)	l_0	0.06 m
Number of generations in the tree	n	2 to 5
Hydrodynamic resistance of the airway tree	$R_{eq} = \frac{1}{{}^tJ\mathcal{R}^{-1}J}$	8.10^{-3} cmH$_2$O.s.L^{-1}
Resistance matrix of the airway tree	$\mathcal{R}_{np} = \frac{\mathcal{R}}{R_{eq}}$	see *
Healthy lungs		
Lung volumetric density	ρ	100 kg.m^{-3}
Characteristic lungs size	L	0.2 m
Poisson's ratio	ν	0.4
Young's modulus	E	1256 Pa
Lamé parameters	$\lambda + 2\mu$	2691 Pa
Tree root radius (trachea radius)	r_0	0.01 m
Tree root length (reduced trachea length)	l_0	0.06 m
Number of generations in the tree	n	8
Corrective factor for the resistance of the tree	r_h	30
Resistance matrix of the airway tree	$\mathcal{R}_h = r_h\mathcal{R}$	see * *[1]
Hydrodynamic resistance of the airway tree	$R_{eq} = \frac{1}{{}^tJ\mathcal{R}_h^{-1}J}$	1.5 cmH$_2$O.s.L^{-1} [87]

Table 2.4: Input parameters of the model for the non-physiological and healthy lungs. *The resistance matrix $\mathcal{R}$ is defined from r_0 and l_0, see the subsection 2.2.1 and [25] for the definition. *[1]The corrective factor r_h is applied on each airway of the tree, even the ones of the bronchial and acinar subtrees that are added to the terminal branches of the tree, as detailed in the appendix 2.A.

Lungs model input parameters		
Shared parameters		
Physical quantity	**Parameter name**	**Value**
Lung volumetric density	ρ	100 kg.m^{-3}
Characteristic lungs size	L	0.2 m
Poisson's ratio	ν	0.4
Tree root radius (trachea radius)	r_0	0.01 m
Tree root length (reduced trachea length)	l_0	0.06 m
Number of generations in the tree	n	8
Asthma lungs		
Young's modulus	E	1256 Pa
Lamé parameters	$\lambda + 2\mu$	2691 Pa
Corrective factor for the resistance of the tree	r_{nh}	11
Resistance matrix of the airway tree	$\mathcal{R}_a = r_{nh}\mathcal{R}_h$	see *
Hydrodynamic resistance of the airway tree	$R_{eq} = \frac{1}{{}^tJ\mathcal{R}_a^{-1}J}$	15 cmH$_2$O.s.L^{-1} [116]
COPD lungs		
Young's modulus	E	628 Pa
Lamé parameters	$\lambda + 2\mu$	1346 Pa
Corrective factor for the resistance of the tree	r_{nh}	7
Resistance matrix of the airway tree	$\mathcal{R}_{copd} = r_{nh}\mathcal{R}_h$	see *
Hydrodynamic resistance of the airway tree	$R_{eq} = \frac{1}{{}^tJ\mathcal{R}_{copd}^{-1}J}$	10 cmH$_2$O.s.L^{-1} [77]
CF lungs		
Young's modulus	E	2512 Pa
Lamé parameters	$\lambda + 2\mu$	5383 Pa
Corrective factor for the resistance of the tree	r_{nh}	12
Resistance matrix of the airway tree	$\mathcal{R}_{cf} = r_{nh}\mathcal{R}_h$	see *
Hydrodynamic resistance of the airway tree	$R_{eq} = \frac{1}{{}^tJ\mathcal{R}_{cf}^{-1}J}$	17 cmH$_2$O.s.L^{-1} [44]

Table 2.5: Input parameters of the model for the non-healthy lungs. *The resistance matrix $\mathcal{R}_h$, mimicking the resistance matrix associated to a healthy lungs, is defined in the previous page. The corrective factor r_{nh} in case of non-healthy lungs is applied only on the airways of the bronchial tree and not for the ones of the acinar region when adding the contribution of the generations that the tree structure does not take into account to the terminal branches of this same tree, as detailed in the appendix 2.A. Consequently the equivalent resistances of the acinar region for the healthy and non-healthy lungs are equal ; only differ the equivalent resistance of the bronchial tree (hence the equivalent resistance of the whole tree).

Chapter 3

Mechanics of the lungs and optimization of HFCWO

"Ubi stimulus, ibi fluxus humorum."

-

"Where the stimulation is, there is a flow of fluid."

Well known medical axiom of 19$^{\text{th}}$ century [107].

From *Résumé historique des principales découvertes sur la structure et les fonctions des poumons*, Léonard-Fulcrand Gasté, 1832, p.15.

Contents

3.1 Introduction

In the previous chapter, we propose a mathematical and numerical model of the biomechanics of the lungs to analyze the isolated phenomenon acting during tidal breathing in healthy and non-healthy human lungs. It proposes the interest of studying the resonance of the lungs which can be an interesting feature for the HFCWO. The previous chapter also allows to calibrate the set of parameters of the model to get model predictions compatible with the physiology of the lungs. In this chapter, we use the unidimensional model to study the effect of the HFCWO therapy on the lungs isolated from the ventilation.

We have seen in the frame of forced and damped harmonic oscillator, that the natural pulsation of the oscillator could maximize the displacement and velocity amplitudes of the oscillator and that those amplitudes are dependent of the intensity of the damping. Moreover, we have observed some similar behaviors between our coupled model and the harmonic oscillator such as the balance of energies of the system. Hence, we take an interest on studying the resonance in our model.

Analyzing the velocity of the deformation in our model amounts to study the air flows in the tree induced by the material deformation. Hence, this study aims at determining optimal operating parameters for HFCWO, in the sense of maximizing the resulting amount of air flow in the bronchi, and potentially maximizing the stress applied on the mucus in the airways. For that purpose, we propose a dimensionless formulation of the model in order to understand the intrinsic and interconnected influences of the parameters of the model. The dimensionless formulation is used to explain the induced phenomena that occur during HFCWO maneuvers such as resonance. This formulation raises two dimensionless parameters. We also determine from an idealized perspective, another dimensionless parameter which indicates the influence of the intensity of the damping of the tree on the material deformation. The way those dimensionless parameters are calculated and the physical analysis of the model are presented in section 3.2. Then, we apply our model to idealized HFCWO. The model suggests that a frequency can maximize the air flows in the tree induced by the deformation of the material during a HFCWO therapy. The frequency is related to the natural frequency of the material. Moreover, we propose a way to model the stress felt by the mucus in the tree. We define two types of stress felt by the mucus in the pulmonary airways from the deformation of the lung's parenchyma : one originates from the air-mucus interaction and one from the mechanical vibration of the airway's wall. Finally we propose the use of HFCWO as a non-invasise tool to asses the resistance and the compliance of the lungs. The application of HFCWO in our model, modelling the mucus and the way to assess idealized lung's physical properties are presented in the section 3.3.

3.1.1 Recall of the equations of the coupled model

The model is based on the coupling between two idealized models : one of a quasi-fractal tree mimicking the pulmonary tree and one of an elastic medium mimicking the lung's parenchyma tissue. The model is described in the previous chapter 2. Here, we recall the equations of the model, see chapter 2 for more details.

The deformation of the latter is then submitted to the dissipative action of the tree. The number of generations in the tree is $n+1$ and the number of terminal branches is $N = 2^n$. The domain representing the spatial occupation of the elastic material is defined as $\Omega = \cup_{i=1}^{N} A_i$. Each subregion A_i is fed (and feeds) with air by one of the terminal branch of the tree. The equations that rule the biomechanics of the tissue region are defined for any dimension $m = \{1, 2, 3\}$

$$\begin{cases} \rho \frac{\partial^2 u}{\partial t^2} - \mathrm{div}(\sigma(u, \mathcal{F}[\dot{u}]))) = 0 & x \in \Omega \\ \sigma(u, \mathcal{F}[\dot{u}]) = \lambda \mathrm{Tr}(\epsilon(u)) I + 2\mu\epsilon(u) - \ p_{\mathrm{tree}}(\mathcal{F}[\dot{u}]) I & x \in \Omega \\ \sigma(u, \mathcal{F}[\dot{u}])).n = \tau(t) & x \in \Gamma_1 \\ u(x,t) = 0 & x \in \Gamma_2 \\ u(x,0) = u_0(x) & \text{for } x \in \Omega \end{cases} \tag{3.1}$$

where u is the displacement of the lung's parenchyma tissue, and σ is the viscoelastic stress-strain relationship. A Neumann boundary condition (τ) is applied on the boundary Γ_1 and no displacement $u = 0$ is imposed in the boundary Γ_2. We denote by $\mathcal{F}[\dot{u}] = (\mathcal{F}_i[\dot{u}])_{1\leqslant i\leqslant N}$ the vector of the flows at the N terminal branches and $P = (p_i)_{1\leqslant i\leqslant N}$, the vector of the pressures at those same branches. The pressure p_{tree} is a piecewise continuous function that depends on the hydrodynamic resistances of the airways tree :

$$p_{tree}(\mathcal{F}[\dot{u}]) = \sum_{i=1}^{N} p_i(\mathcal{F}[\dot{u}])\chi_i \tag{3.2}$$

with

$$\text{with } \chi_i(x) = \begin{cases} 1, & \text{if } x \in A_i \\ 0, & \text{otherwise} \end{cases}$$

The linear relationship between the pressures and flows vectors is written using the resistance matrix $\mathcal{R}$ of the airway tree [37, 25],

$$P = \mathcal{R}\mathcal{F}[\dot{u}] \tag{3.3}$$

This chapter numerically studies the model in one dimension. An analytical solution of (3.1) can be computed on a particular case, see 2.3.3. Otherwise, more generally, we apply the finite element with the weak formulation. The system of equations (3.1) can be written using the weak formulation with one dimension

$$\begin{cases} \int_0^L \rho\frac{\partial^2 u}{\partial t^2}w + (\lambda+2\mu)\frac{\partial u}{\partial x}\frac{\partial w}{\partial x}\ dx - \sum_{i=1}^{N} p_i(\mathcal{F}[\dot{u}])\int_{A_i}\frac{\partial w}{\partial x}\ dx - \tau(t)w(t,0) = 0 \\ u(0,x) = u_0(x) \\ u(t,L) = u_b(L) \quad \textbf{and} \quad w(L) = 0 \\ p_i(F[\dot{u}]) = -S_L\left(\sum_{j=1}^{N}\mathcal{R}_{ij}\left(\frac{\partial u}{\partial t}(x_{j+1},t) - \frac{\partial u}{\partial t}(x_j,t)\right)\right) \quad i = 1,\dots N \end{cases} \tag{3.4}$$

The first equation in (3.4) is written with the discretized approach of the finite element method that leads to solve the following ordinary differential equation :

$$M\frac{d^2}{dt^2}U(t) \ + \ D\frac{dU(t)}{dt} \ + \ KU(t) \ = \ \tau(t)h \tag{3.5}$$

with $U = (u_i(t))_{0\leqslant i\leqslant n_x}$ the unknown vector of displacements composed of n_x+1 displacement elements. The spatial position of the u_i are called degree of freedom (DoF). We refer the reader to the section 2.2 in the previous chapter for more details.

3.2 Physical analysis of the parameters of the model with a dimensionless formulation

To reach a better understanding of the equations and to determine the intrinsic parameters of the problem, we rewrite the equation (2.11) into a dimensionless formulation, see section 3.2.1. This formulation is very convenient to relate the influence of the parameters of the model and to extract the dimensionless numbers that drive the behaviors of the system. These parameters will be then used to correlate the behaviors of our model with the ones of harmonic oscillator presented in the previous chapter 2. For that, we propose an idealized formulation of the model which is represented with only one degree of freedom, see section 3.2.2. Then, in section 3.2.3, we propose an analysis of the dimensionless parameters for the configurations of healthy lungs and non-healthy lungs model. The configurations of parameters are detailed in the appendix 2.E.

3.2.1 Determination of the dimensionless parameters

The space, the time and the amplitude of the solution are adimensionalized as follows

$$\begin{aligned} &y = x/L \\ &s = t/T \\ &u(x,t) = \Upsilon\tilde{u}(y,s) = \Upsilon\tilde{u}(\tfrac{x}{L}, \tfrac{t}{T}) \\ &p_i(\mathcal{F}[\dot{u}]) = \mathcal{P}\tilde{p}_i(\tilde{\mathcal{F}}[\tfrac{\partial\tilde{u}}{\partial s}]) \end{aligned} \tag{3.6}$$

The quantities L and T represent respectively the characteristic length of the system and its characteristic time. The quantity Υ represents the characteristic displacement of the structure and $\mathcal{P}$ the characteristic pressure. The rate of volume change is now

$$\tilde{\mathcal{F}}[\frac{d\tilde{u}}{ds}] = \left(-\int_{\tilde{A}_i} \frac{\partial}{\partial y}(\frac{\partial\tilde{u}}{\partial s})dy\right)_{1\leqslant i\leqslant N} = -\left(\frac{\partial\tilde{u}}{\partial t}(y_{j+1},s) - \frac{\partial\tilde{u}}{\partial t}(y_j,s)\right)_{1\leqslant i\leqslant N}$$

The space domain becomes $\tilde{\Omega} = [0,1]$. $\tilde{\Omega}$ is decomposed into N subsets $\tilde{A}_i$, which are the transformations by the adimensionalization of the corresponding A_i in the original space. Hence the projection of $\tilde{A}_i$ on the axis y is the segment $[y_j, y_{j+1}]$. We define the characteristic velocity v of the system by $v = L/T$.

Characteristic quantities

Physical quantity	**Variable name**	**Expression**
Time	T	$\frac{1}{f}$
Velocity	v	$\frac{L}{T}$
Wave velocity	c	$\sqrt{\frac{(\lambda+2\mu)}{\rho}}$
Displacement	Υ	$\frac{AL}{(\lambda+2\mu)}$
Equivalent resistance of the tree	R_{eq}	$\frac{1}{{}^tJ\mathcal{R}J}$
Air pressure in the tree	p_L	$R_{eq}S_Lv$
Effective air pressure in the tree	$\mathcal{P}$	$\frac{A}{(\lambda+2\mu)}p_L$
Tissue inertia	–	ρv^2

Dimensionless numbers

Name	**Variable name**	**Expression**
Euler number	$\mathcal{E}$	$\frac{p_L}{\rho v^2}$
Inverse of Cauchy number	$\mathcal{B} = \frac{1}{\mathcal{C}}$	$\left(\frac{c}{v}\right)^2$
Lung Mechanics number	$\mathcal{L}_M$	$\frac{p_L}{(\lambda+2\mu)}$

Table 3.1: Characteristic quantities and dimensionless numbers used in this chapter. All the characteristic quantities and dimensionless numbers are defined with the input parameters of the model. Notice that $\mathcal{E} = \mathcal{L}_M\mathcal{B}$.

The characteristic pressure $\mathcal{P}$ is obtained by

$$p_{tree}(\mathcal{F}[\frac{\partial u}{\partial t}]) = \mathcal{R}\mathcal{F}[\frac{\partial u}{\partial t}] = \mathcal{P}\tilde{p}_{tree}(\tilde{\mathcal{F}}[\frac{\partial\tilde{u}}{\partial s}]) = \underbrace{R_{eq}\frac{S_L\Upsilon}{T}}_{\mathcal{P}}\underbrace{\frac{\mathcal{R}}{R_{eq}}\tilde{\mathcal{F}}[\frac{\partial\tilde{u}}{\partial s}]}_{\tilde{p}_{tree}(\tilde{\mathcal{F}}[\frac{\partial\tilde{u}}{\partial s}])}$$

where we recall that $R_{eq} = 1/({}^tJ\mathcal{R}J)$ is the equivalent resistance of the tree, i.e. how it responds to an homogeneous distribution of pressures in its branches, see the subsection 2.2.1.2. The vector J is defined as $J = {}^t(1, ..., 1) \in \mathbb{R}^N$. Hence, we can now define $\mathcal{P} = R_{eq}\frac{S_L\Upsilon}{T}$. The quantity $\frac{S_L\Upsilon}{T}$ represents a characteristic air flow in the system.

The stress–strain relationship becomes,

$$\tilde{\sigma}(\tilde{u}, \tilde{\mathcal{F}}[\frac{\partial\tilde{u}}{\partial s}]) = \frac{\partial\tilde{u}}{\partial y} - \frac{\mathcal{P}L}{(\lambda+2\mu)\Upsilon}\ \tilde{p}_{tree}(\tilde{\mathcal{F}}[\frac{\partial\tilde{u}}{\partial s}]) = \frac{\partial\tilde{u}}{\partial y} - \frac{R_{eq}S_LL}{(\lambda+2\mu)T}\ \tilde{p}_{tree}(\tilde{\mathcal{F}}[\frac{\partial\tilde{u}}{\partial s}])$$

and consequently, $\sigma(u, \mathcal{F}[\dot{u}]) = \frac{\Upsilon(\lambda+2\mu)}{L}\tilde{\sigma}(\tilde{u}, \tilde{\mathcal{F}}[\frac{\partial\tilde{u}}{\partial s}])$. We call the number $\mathcal{L}_M = \frac{R_{eq}S_Lv}{(\lambda+2\mu)}$ the Lung Mechanics number, it compares the characteristic pressure in the terminal branches $p_L = R_{eq}S_Lv$ induced by the viscous dissipation of the air flow in the tree to the the elastic response of the material, here represented by $(\lambda + 2\mu)$.

At the boundary $y = 0$, $\tilde{\sigma}(\tilde{u}, \tilde{\mathcal{F}}[\frac{\partial\tilde{u}}{\partial s}]).n = \frac{AL}{(\lambda+2\mu)\Upsilon}\tilde{\tau}(s)$, with A the characteristic amplitude of pressure applied on the boundary and $\tilde{\tau}(s) = \frac{\tau(Ts)}{A}$ the applied stress. In order to get a dimensionless stress at the boundary, we set the characteristic displacement to $\Upsilon = \frac{AL}{(\lambda+2\mu)}$. It is the result of the trade-off between the applied boundary stress and the elastic response of the material, scaled by the size of the object. Typically, the applied stress τ on the boundary is a sinusoidal signal with frequency ω, $\tau(t) = A\sin(\omega t)$, hence unless stated differently, $T = 2\pi/\omega$ is the characteristic time of the system.

Substituting these dimensionless quantities in the weak formulation of the system brings a new dimensionless weak formulation, for any smooth function w such as $w(1) = 0$,

$$\int_{\tilde{\Omega}} \frac{\partial^2\tilde{u}}{\partial s^2}w + \left(\mathcal{B}\frac{\partial\tilde{u}}{\partial y} - \mathcal{E}\tilde{p}_{tree}\left(\tilde{\mathcal{F}}\left[\frac{\partial\tilde{u}}{\partial s}\right]\right)\right)\frac{\partial w}{\partial y}\ dy - \mathcal{B}\underbrace{\int_{\tilde{\Gamma}_1}\tilde{\tau}(s)w\ dy}_{=\tilde{\tau}(s)w(0)\ \text{(1D case)}} = 0 \tag{3.7}$$

with $\mathcal{B}$ the inverse of the Cauchy number of the system $\mathcal{B} = (\lambda + 2\mu)/\rho v^2$ that compares the elastic forces in the material with the inertial forces. The number $\mathcal{E} = \mathcal{L}_M\mathcal{B}$ is actually the Euler number of the system since it can be rewritten in the form $\mathcal{E} = \frac{p_L}{\rho v^2}$. It compares the pressures forces induced by the viscous dissipation of the air flow in the tree with the inertial forces in the material.

Finally, the system is characterized by two dimensionless numbers: $\mathcal{B} = (\lambda + 2\mu)/\rho v^2$ and $\mathcal{E} = p_L/\rho v^2 = R_{eq}S_L/\rho v$. The pressure p_L represents the non-coupled characteristic pressure in the terminal branches of the tree, i.e. in the absence of the coupling with the respiratory zone; the pressure $\mathcal{P}$ represents the efficace characteristic pressure resulting from the coupling, it is equal to the non-coupled characteristic pressure weighted by the ratio between the applied force A and the elastic response $(\lambda + 2\mu)$. As a verification, we express the balance of energy of the system.

Energy of the system. Taking w in equation as the velocity of the material, i.e. $w = \frac{\partial\tilde{u}}{\partial s}$, we can determine the time variation of the energy of the system.

$$\underbrace{\frac{d}{ds}\left(\frac{1}{2}\int_0^1\left(\frac{\partial\tilde{u}}{\partial s}(y,s)\right)^2 dy + \mathcal{B}\frac{1}{2}\int_0^1\left(\frac{\partial\tilde{u}}{\partial y}(y,s)\right)^2 dy\right)}_{\text{Total energy of the system}} = \underbrace{\mathcal{B}\tilde{\tau}(s)\frac{\partial\tilde{u}}{\partial s}(0,s)}_{\text{input power}} + \underbrace{\mathcal{E}\ \sum_{i=1}^{N}\tilde{p}_i(\tilde{\mathcal{F}}[\frac{\partial\tilde{u}}{\partial s}])\tilde{\mathcal{F}}_i[\frac{\partial\tilde{u}}{\partial s}]}_{\text{viscous power dissipated}} \tag{3.8}$$

Since the pressure $\tilde{p}_i(\tilde{\mathcal{F}}[\frac{\partial\tilde{u}}{\partial s}])$ in an A_i is of the opposite sign than the corresponding flow $\mathcal{F}_i[\frac{\partial\tilde{u}}{\partial s}]$, then the term in $\mathcal{E}$ corresponds to a damping of the tissue, as expected.

In the dimensionless equation (3.7), each term plays a part on the shape of the solution and is weighted and compared with the other terms by the value of its respective prefactor. The prefactors are either 1 or one of the two dimensionless parameters $\mathcal{B}$ or $\mathcal{E}$. The dimensionless

equation (3.7) can be decomposed according to the physical role of its different terms:

$$\int_0^1 \underbrace{\frac{\partial^2 \tilde{u}}{\partial s^2}}_{\text{acceleration}} w + \left(\underbrace{\mathcal{B}\frac{\partial \tilde{u}}{\partial y}}_{\text{elasticity}} - \underbrace{\mathcal{E}\tilde{p}_{tree}\left(\tilde{\mathcal{F}}\left[\frac{\partial \tilde{u}}{\partial s}\right]\right)}_{\text{damping}} \right) \frac{\partial w}{\partial y}\, dy - \underbrace{\mathcal{B}\,\tilde{\tau}(s)}_{\text{boundary force}} w(0) = 0 \tag{3.9}$$

The study of the role of each dimensionless parameter singled out allows to determine characteristic behaviors of the system. These behaviors could be interpreted in terms of the physiology as highly pathological situations, such as strong constrictions of the bronchi. An analysis is proposed in the appendix 3.A to study the behaviors of the system for asymptotic values of the dimensionless parameters.

The next section proposes an idealized formulation for our coupled model with one degree of freedom. This formulation is then assimilated to an equation ruling the motion of an harmonic oscillator with one degree of freedom.

3.2.2 The coupled model reduced to one degree of freedom

The section 2.4 in the previous chapter shows some similarities between the response of our coupled model and the harmonic oscillator. Moreover, the appendix 2.D presents the properties and characteristics of the motion of a damped and forced harmonic oscillator with one degree of freedom (DoF) ruled by the equation :

$$\frac{d^2x(t)}{dt^2} + 2\xi\frac{dx(t)}{dt} + \omega_0^2 x(t) = h(t) \tag{3.10}$$

with ξ the damping coefficient, ω_0 the natural angular frequency of the oscillator and h a driving force. The appendix 2.D details how the amplitudes of the motion and of the velocity of the oscillations evolve according to the pulsation of the forced component and to the intensity of the damping coefficient. It raises two behaviors that can be predicted from the value of the quality factor (the Q-factor) defined by $Q = \frac{\omega_0}{2\xi}$. The Q-factor, which is determined from the natural frequency (ω_0) and the damping coefficient (ξ), characterizes the influence of the damping and determines the intensity of the phenomenon of resonance. More precisely, we have seen that if the Q-factor is strictly above a specific value ($Q > \frac{1}{\sqrt{2}}$), the amplitude of the motion of the oscillator is maximized when the oscillator is forced at a pulsation equal to the resonance frequency ($\omega \approx \omega_r = \sqrt{\omega_0^2 - 2\xi^2}$). Additionally, for $Q > \frac{1}{\sqrt{2}}$, the amplitude of the velocity is maximised at the the natural frequency of the oscillator ($\omega = \omega_0$). Below this specific value ($Q \leqslant \frac{1}{\sqrt{2}}$), no resonance occurs, the oscillator is too damped, see Appendix 2.D for more details.

The Q-factor is then a relevant variable indicating if the oscillating system can reach resonance that could maximize its motion while forced. In this subsection, we focus on expressing the equation of our model with an idealised one DoF formulation in order to draw a quality factor that can inform on the resonance of the lungs. We will use the discretized equation (3.5) of the dimensionless model obtained with the finite element method :

$$M\frac{d^2}{dt^2}U(t) \;+\; D\frac{dU(t)}{dt} \;+\; KU(t) \;=\; \tau(t)h \tag{3.11}$$

with $U = (u_i(t))_{0\leqslant i\leqslant n_x}$ the displacement vector containing displacement element u_i computed at the $n_x + 1$ degrees of freedom. For this subsection, we use the term "coupled model" to refer to the equations (3.11) defined for several degrees of freedom. The idealised one DoF model is named "the single DoF model" and it will be defined from the dimensionless formulation of (3.11). The equation of the single DoF model can be assimilated to the equation of the motion of a damped and forced harmonic oscillator with one degree of freedom. Hence, the single DoF model is a qualitative expression built to study the Q-factor and potentially to propose insight on the resonance of the lungs. Then, to ensure the significance of this quality factor, we compare the results obtained from the response of the coupled model with those of the single DoF model.

3.2.2.1 Hypothesis

We consider the unidimensional and discretized equation (3.5) written with the dimensionless formulation (3.7). We assume that the spatial occupation of the lung's parenchyma is expressed with only two positions (or degrees of freedom). In our case, the two degrees of freedom are the positions $x = 0$ and $x = L$. Moreover, in the subsections 2.4.1 we saw that the damping influence of an idealised symmetric tree with a large number of generations behave quite the same as the one with a small number of generations. Hence, we assume that the lung's tissue is subjected to only one homogeneous pressure. This can be simulated by considering only one A_i. Finally, we apply a homogeneous Dirichlet condition ($u(L,t) = 0\ ,\forall t$) in $x = L$ and a sinusoidal Neumann condition in $x = 0$ $\left(\frac{\partial u(0,t)}{\partial x}.n = \tau(t)\ ,\forall t\right)$.

3.2.2.2 Formulation of the single DoF model

We recall that the discretized equation of the dimensionless coupled model can be computed using the finite element method described in the appendix 2.B. It is written :

$$\tilde{M}\ddot{\tilde{U}} \ + \ \mathcal{E}\tilde{D}\dot{\tilde{U}} \ + \ \mathcal{B}\tilde{K}\tilde{U} \ = \ \mathcal{B}\tilde{h}\tilde{\tau}$$

with $\ddot{\tilde{U}} = \frac{d\dot{\tilde{U}}}{dt} = \frac{d^2\tilde{U}}{dt^2}$, and with $\tilde{M}$, $\tilde{D}$ and $\tilde{K}$ respectively the dimensionless mass, damping and stiffness matrices and $\tilde{h}$ the dimensionless vector of loads. The vector $\tilde{U}$ is the dimensionless vector displacement. The dimensionless damping matrix $\tilde{D}$ is defined as $\tilde{D} = S\ {}^t\tilde{G}\frac{\mathcal{R}}{R_{eq}}\tilde{G}$, with S a characteristic surface. For two degrees of freedom this equation becomes

$$\begin{pmatrix}\tilde{M}_{11} & \tilde{M}_{12}\\ \tilde{M}_{21} & \tilde{M}_{22}\end{pmatrix}\begin{pmatrix}\ddot{\tilde{U}}_1\\ \ddot{\tilde{U}}_2\end{pmatrix} + \mathcal{E}\begin{pmatrix}\tilde{D}_{11} & \tilde{D}_{12}\\ \tilde{D}_{21} & \tilde{D}_{22}\end{pmatrix}\begin{pmatrix}\dot{\tilde{U}}_1\\ \dot{\tilde{U}}_2\end{pmatrix} + \mathcal{B}\begin{pmatrix}\tilde{K}_{11} & \tilde{K}_{12}\\ \tilde{K}_{21} & \tilde{K}_{22}\end{pmatrix}\begin{pmatrix}\tilde{U}_1\\ \tilde{U}_2\end{pmatrix} = \tilde{\tau}\begin{pmatrix}\tilde{h}_1\\ 0\end{pmatrix}$$

Particularly, the damping matrix $\tilde{D}$ is written :

$$\begin{pmatrix}\tilde{D}_{11} & \tilde{D}_{12}\\ \tilde{D}_{21} & \tilde{D}_{22}\end{pmatrix} = S\begin{pmatrix}\tilde{G}_1 & \tilde{G}_2\end{pmatrix}\frac{1}{R_{eq}}\begin{pmatrix}\mathcal{R}_{11} & \mathcal{R}_{12}\\ \mathcal{R}_{21} & \mathcal{R}_{22}\end{pmatrix}\begin{pmatrix}\tilde{G}_1\\ \tilde{G}_2\end{pmatrix}$$

Actually, as considering only one generation for the tree, the elements of the resistance matrix are equal to R_0 as well as the equivalent resistance R_{eq}. With the homogeneous Dirichlet condition in $x = L$, the second element of the vector $\tilde{U}$ is null ($\tilde{U}_2 = 0$). We got :

$$\tilde{M}_{11}\ddot{\tilde{U}}_1 \ + \ \mathcal{E}\tilde{D}_{11}\dot{\tilde{U}}_1 \ + \ \mathcal{B}\tilde{K}_{11}\tilde{U}_1 \ = \ \mathcal{B}\tilde{h}_1\tilde{\tau} \tag{3.12}$$

With the dimensionless formulation and with two degrees of freedom, the elements of the matrices and of the vector are equal to

$$\begin{cases} \tilde{M}_{11} = \frac{1}{3} \\ \tilde{K}_{11} = 1 \\ \tilde{h}_1 = 1 \\ \tilde{D}_{11} = S\ \tilde{G}_1\ \frac{\mathcal{R}_{11}}{R_{eq}}\ \tilde{G}_1 = S\ (-1)\frac{\mathcal{R}_{11}}{R_{eq}}(-1) = S\ \frac{\mathcal{R}_{11}}{R_{eq}} = 1 \end{cases}$$

With $\mathcal{E} = \frac{R_{eq}TL}{\rho}$, $\mathcal{B} = \left(\frac{c}{v}\right)^2$ and setting $\tilde{u} = \tilde{U}_1$, equation (3.12) can then be written :

$$\ddot{\tilde{u}} \ + \ \frac{3R_{eq}TL}{\rho}\dot{\tilde{u}} \ + \ 3\left(\frac{c}{v}\right)^2\tilde{u} \ = \ 3\left(\frac{c}{v}\right)^2\tilde{\tau} \tag{3.13}$$

The previous equation is a typical equation describing the motion of a damped and forced harmonic oscillator, see (3.10) and Appendix 2.D. This is the expression of the single DoF model. By analogy, we conclude that

$$2\xi = \frac{3R_{eq}TL}{\rho} \qquad \text{and} \qquad \omega_0^2 = 3\left(\frac{c}{v}\right)^2$$

and that the Q-factor is :

$$Q = \frac{\omega_0}{2\xi} = \frac{c\rho\sqrt{3}}{3R_{eq}L^2}$$

In the case of a one generation tree, the equivalent resistance, as stated above, is equal to the resistance of the only airway (R_0). However, to reach a physiological value for the resistance of the tree, the value of R_0 can be modulated with a corrective factor as used in the previous chapter. Consequently the variable R_{eq} can characterize the overall resistance that the air encounters from the ambient air to the exchange surface in the lungs.

The Q-factor is then computed from the properties of the tissue and of the tree. By extension, it can be written with the dimensionless parameters as :

$$Q = \frac{1}{\sqrt{3}}\frac{\sqrt{\mathcal{B}}}{\mathcal{E}} \tag{3.14}$$

We recall that the higher the Q-factor is, the lesser is the damping. We also notice that, considering the dimensional discretized equation, we obtain the same definition for the quality factor, see the appendix 3.C.

3.2.2.3 Numerical simulations

We want to verify the significance of the definition of the Q-factor found above with numerical simulations. More specifically, we want to check if this quality factor has similar predictions properties for resonance with the single DoF model and the coupled model. We run comparative numerical simulations. On one hand, we compute the amplitudes of the motion and of the velocity of the solution of the single DoF model (3.13) whose definitions is deduced from the theory of harmonic oscillator, see Appendix 2.D. On the other hand, we compute the averaged displacement over the domain and the time and the averaged kinetic energy over the time computed from our coupled model.

Input data. We use the set of parameters from the non-physiological lungs (see the appendix 2.E) in which the value of the resistance of the tree varies in order to have different values of the Q-factors. For the single DoF model, we adjust the resistance R_{eq} to 1, 1/3, or 1/7, resulting in a Q-factor equal to respectively, 0.6, 1.7 or 4. For the coupled model, we adjust the non-physiological matrix $\mathcal{R}_{np}$ using the same values 1, 1/3, or 1/7 as multiplying factors that leads to Q-factors equal respectively to 0.5, 1.6 or 3.7. Typically, for the coupled model, the equivalent resistance R_{eq} is equal to $k/({}^tJ\mathcal{R}_{np}^{-1}J)$, with k set to 1, 1/3, or 1/7. For numerical visualisation purpose, the natural pulsation of the single DoF model is called ω_0 and the fundamental pulsation (the smallest natural frequencies) of the coupled model is written ω_1.

Output data. On one hand, we compute the amplitudes of the motion and of the velocity of the oscillation (divided by the amplitude of the forcing term) from the equation (3.13) and from the values of the Q-factors, see the appendix 2.D for the definitions. On the other hand, we compute the quantity R_u and E_k defined in section 2.4.2 for the coupled model : $E_k = \frac{1}{2}\frac{\rho}{T_f}\int_0^{T_f}\int_0^L \frac{\partial u(x,t)}{\partial t}^2 dxdt$ and $R_u = \left(\frac{1}{T_f L}\int_0^{T_f}\int_0^L u^2(x,t)dxdt\right)^{\frac{1}{2}}$.

Results. In the figure 3.1, we observe that the amplitudes of displacement and the velocity of the deformation behave similarly in the single DoF model and in our coupled model. Typically, the respective maxima are reached for the closely same pulsations according to the natural pulsations (ω_0 and ω_1 for respectively the single DoF and coupled models). We also notice that the averaged kinetic energy and the averaged displacement for the highest quality

factor ($Q = 3.9$) has a local maximum located at pulsations equal to the second eigen pulsation. For that case, that explains that the damping is low and allows resonance phenomenon for the other natural pulsations. The amplitudes of the curves are not equivalent as we compute different quantities. The results have to be understood for qualitative and comparative purposes and not quantitative ones. The results raises the fact that the quality factor of the single DoF model can be used to predict resonance phenomenon of the coupled model while saving drastically time computation.

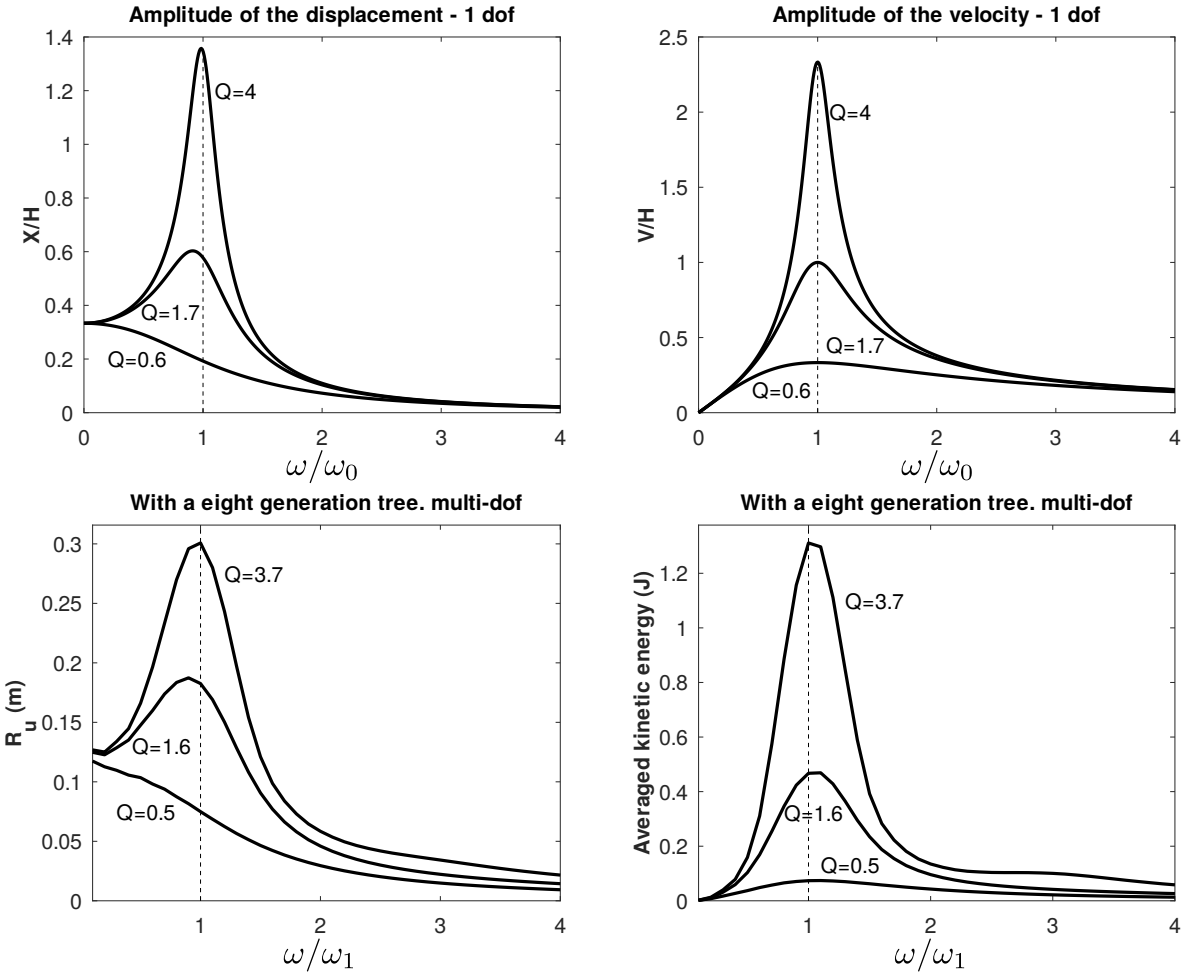

Figure 3.1: **Top :** Evolution of the amplitude of the oscillation (**left**) and of the velocity of the oscillations (**right**) according to the pulsation of the external force for different Q-factors (by varying the damping of the tree) with the single degree of freedom model (1 DoF). **Bottom :** Evolution of the kinetic energy averaged in time (**left**) and of the total displacement averaged in time and in space (**right**) according to the pulsation of the applied pressure for different Q-factors (by varying the damping of the tree) with the coupled model (multi-DoF). **Note :** The single DoF model is ruled by the equation (3.13). The coupled model is ruled by the equation (2.18). For both models, the quality factor is defined by (3.14). For the single DoF model, R_{eq} is set to 1, 1/3, or 1/7. For the coupled model, R_{eq} is equal to $k/({}^tJ\mathcal{R}_{np}^{-1}J)$, with k set to 1, 1/3, or 1/7.

3.2.2.4 Application of the Q-factor to the HFCWO

The previous results show that the Q-factor allows to determine if the resonance occurs in our coupled model of the lungs. The value of the quality factor, which is computed directly from the dimensionless parameters, informs on the influence of the damping on the motion of the lungs' tissue. The major advantage is that the computation of the Q-factor avoids computing the response of the lungs for different pulsations, which might lead to a heavy computational

cost.

3.2.3 Predicted behaviors of healthy and non-heatlhy lungs with the dimensionless parameters

In this subsection, we propose an analyze of the dimensionless parameters in the case of healthy and non-healthy lungs models. For this cases, we also investigate the values of the Q-factor that we determine in the previous subsection. The dimensionless parameters propose indications on the potential behaviors of the model. The Q-factor informs on the influence of the damping of the tree on the elastic material. The quality factor can be an indicator for resonance phenomenon. The parameters of healthy and non-healthy are taken from averaged values found in the literature. The results have to be understood in the limits of the model.

We compute the values of the dimensionless parameters for healthy and non-healthy (asthma, COPD, CF[1]) lungs, during the tidal breathing and during a HFCWO therapy, see the section 2.5 and the appendix 2.E. For HFCWO, we set the frequency to a relatively high frequency (20 Hz) which is usually used in the treatment [96] in order to have an indicated comparison between the therapy and the ventilation at rest which works with lower frequency (1/5 Hz). Moreover, we compute the values of the Q-factor (definition (3.14)). As it is independent of the frequency, the quality factor has the same value for the ventilation at rest and for HFCWO.

Ventilation at rest

For the ventilation at rest for healthy lungs, the Euler number $\mathcal{E}$, which represents the damping, is about 10 times lower than the inverse Cauchy number $\mathcal{B}$ that represents the relative role of the elasticity. This indicates that the system tends to dissipate slowly the elastic energy injected by the diaphragm. The damping of the tree is not high enough to stop the elastic recoil of the lungs that allows the expiration to be passive. However, the damping is also not negligible as the small value of the Q-factor indicates. It prevents any amplification of the deformation of the lungs, i.e. any kind of resonance that could lead to an excessive deformation of the system. Moreover, both $\mathcal{E}$ and $\mathcal{B}$ are larger than 1, indicating that the acceleration plays a small role on the dynamics and that most of the energy is stored as elastic energy. Hence, the elastic recoil is preponderant during rest ventilation for healthy lungs.

For the non-healthy lungs at tidal breathing, the euler number $\mathcal{E}$ is about 10 times higher than for healthy lungs. It is close to the parameter $\mathcal{B}$ for asthma, exceeds $\mathcal{B}$ for COPD (about 20% higher) and represents half $\mathcal{B}$ for CF. This shows that the stored energy is less dissipated by the tree for CF than for asthma and COPD. Globally, it shows that for non-healthy lungs, the stored energy is more dissipated by the tree than for healthy lungs. This indicates that the respiratory muscles have to increase their work in order to compensate the dissipation of the tree and to ensure a proper ventilation. Moreover, the reduction of the parameter $\mathcal{B}$ in COPD corresponds to a reduction of the elastic recoil that leads to lungs hyperinflation because of the reduction of the efficiency of the passive expiration. This is a typical symptom of the COPD disease that implies severe respiratory muscles fatigue due to the increase of their work. While lungs hyperinflation is also true for the asthma because of the increase of the dissipation, study shows that severe respiratory muscles weakness was not often seen in CF patients [26] which is in agreement with the values of the dimensionless parameters in the case of CF lungs. Specifically, the increase of $\mathcal{B}$ because of the increase in lung's tissue stiffness in CF favours a better elastic recoil for CF than for asthma or COPD. As a consequence, a better elastic recoil reduces the work of breathing, for expiration at least. Interestingly, the authors of [26] have measured, in a population of 27 CF adolescent and adult patients, that the respiratory muscles strength during expiration remains within the range of healthy lungs whereas during inspiration, it is higher than for healthy lungs. This suggests that the respiratory muscles do not have to compensate a lack of elastic recoil, as our dimensionless parameters suggest.

[1]COPD : Chronic Obstructive Pulmonary Disease, CF = Cystic Fibrosis

HFCWO (20 Hz)
With higher frequency than ventilation at rest, typically 20Hz of HFCWO, we observe that the prefactor in front of the kinetic (1) and the elastic terms ($\mathcal{B}$) are of the same order of magnitude for both healthy and non-healthy lungs. The parameter $\mathcal{B}$ is always lower than $\mathcal{E}$. The ratio between $\mathcal{B}$ and $\mathcal{E}$ is about 1% and 10% for respectively healthy and non-healthy lungs. For all cases, the parameter $\mathcal{B}$ is of the same order of magnitude as the prefactor 1. This indicates that the kinetic and the elastic components are of the same order of magnitude. We have seen previously that the kinetic and the elastic components are of the same order of magnitude around the fundamental natural frequency. Typically, at this frequency, the kinetic and the elastic components compensate and cancel each other out, leading to a system that is driven only by the remaining components, i.e. the damping and the driving force according to the type of system. This frequency favours resonance. Then, the intensity of the damping modulates the intensity of the resulting displacement which can be maximum at frequencies lower than the natural frequency. For a small damping, the resonance frequency is close to the natural pulsation. For a higher damping the resonance frequency is lower to the natural pulsation, see the appendix 2.D in the previous chapter.

Actually, in our model, for both healthy and non-healthy cases, the Q-factor is lower than the critical value of $\frac{1}{\sqrt{2}}$ (see Appendix 2.D). This indicates that the intensity of the damping of the tree is large compared to the physical properties of the lung's tissue. This prevents resonance. However, we recall that the values used to mimic the resistance, the size and the elastic properties of the lungs are taken in the literature from average healthy lungs. Those data is not valid for all individuals. Moreover, the dimensionless parameters of the model and the Q-factor are determined from a model of the lungs based on idealized assumptions. The result have to be interpreted in the limitations of the model. Nevertheless, we have seen that the model is able to reproduce qualitative physiological behavior of the lungs such as tidal breathing or pathological breathing. We have seen that the dimensionless parameters can corroborate those behaviors, for example : lungs hyperinflation. Hence, the quality factor could be used as an indicative parameter. Here, the Q-factor indicates that the damping influence is too high to prevent resonance. However, we have seen for harmonic oscillator, that the velocity is always maximised when the oscillator is forced at pulsation equal to the natural pulsation. The damping acts on the amplitude of the maximum of the velocity. In the next section we will investigate the influence of the damping on the velocity of the elastic deformation with numerical simulations. Precisely, we will study how the lungs respond to a range of pulsations compatible with HFCWO. We will focus on the air flows in the tree, computed from the air velocities, and analyze the behaviors of the lungs using the quality factor.

		Healthy lungs model	**Non-healthy lungs model**		
			Asthma	COPD	CF
Ventilation at rest	$\mathcal{E}$	1565	14765	10806	17314
	$\mathcal{B}$	16821	16821	8411	33643
HFCWO (20Hz)	$\mathcal{E}$	15.650	147.66	108	173.14
	$\mathcal{B}$	1.6821	1.6821	0.84	3.3643
Quality factor	Q	0.048	0.0051	0.0050	0.0061

Table 3.2: Values of the dimensionless parameters to mimic healthy and non-healthy lungs models for tidal breathing and HFCWO (20 Hz). The values of the Q-factor are computed from the definition (3.14). The term COPD is for Chronic Obstructive Pulmonary Disease and CF is for Cystic fibrosis.

3.2.4 Conclusion

The dimensionless formulation raises two specific dimensionless parameters defined from the parameters of the model. The dimensionless parameters propose indications on the behaviors of the lungs. For example, they can suggest if the elastic recoil of the lungs is sufficient relatively to the damping of the tree to allow a passive expiration. Moreover the dimensionless parameters indicate how the dimensional parameters are interacting together. Last but not least, a quality factor can be computed from the dimensionless parameters. It indicates the capability of the lungs model to resonate. The Q-factor is defined from the fundamental pulsation of the material (without damping) and from the resistance and the size of the lungs. In the table 3.2, we have computed the values of the Q-factor for the healthy and non-healthy lungs models. The quality factor is smaller than the critical values $\frac{1}{\sqrt{2}}$, see Appendix 2.D. This indicates that no phenomenon of resonance can occur. However, from the study of a harmonic oscillator (Appendix 2.D), we have seen that the amplitude of the velocity is always maximised at the natural frequency of the oscillator and that this amplitude is modulated by the damping. In our model, the velocity of the deformation is directly related to the air flow induced by the displacement of the lung's parenchyma. In the next section, we investigate the impact of the damping on the mouth air flows at mouth in the case of an idealized a HFCWO.

3.3 Modelling the High Frequency Chest Wall Oscillation in healthy and non-healthy lungs

The values of the quality factor computed in the previous section 3.2 for the healthy and non-healthy cases suggest that no phenomenon of resonance can occur for the lungs : if the lungs are continuously stimulated by a periodic force, its motion will not amplify through time. However, the study of the harmonic oscillator shows that the amplitude of the velocity of the deformation is always maximised at the natural frequency of the material. The damping acts on the intensity of this maximum. We want to determine the influence of the damping on the amplitude of the velocity. In our model, it amounts to observe the airflows induced by HFCWO. With the hypothesis that a HFCWO device is more efficient if the airflows are larger, we compare its efficiency by applying periodic pressures on the model of the lungs with different frequencies. The study is performed for the healthy lungs model in the subsection 3.3.2. Moreover, we study the stress felt by the mucus inside the tree during a HFCWO manipulation. First, to be able to compute those stresses, we propose an idealised model for the mucus, see subsection 3.3.1. Then, we propose perspectives of use for the model. We investigate the influence of the damping for non-healthy lungs (subsection 3.3.4) and we propose a way to use the HFCWO as a non-invasis tool (subsection 3.3.5).

The parameters used for the modelling of HFCWO are based on the configuration of parameters mimicking healthy and non-healthy lungs, see the section 2.5 of the previous chapter, and also the tables of the appendix 2.E for more details. We notice that due to the linearity of the equations relatively to the Neumann boundary condition at $x = 0$ (where the periodic pressure is applied), mixing the rest ventilation and HFCWO would bring an amount of airflow that would be the sum of the airflows induced by the ventilation and by the HFCWO computed separately. Hence, in order to isolate the effects of HFCWO in our simulations, we do not account here for the lung's ventilation as discussed in the introduction.

3.3.1 Modeling the stress in the mucus

During HFCWO manipulations, the mucus is submitted to two types of stress that deform the mucus layer : one arising from the air–mucus interactions and one from the oscillations of the airways walls. The mucus is viscoelastic and its inner stress needs to be larger than its yield stress to be able to move. These stress add together and can either overcome directly the mucus yield stress and make it flow, or represent a buffer of stress, de facto reducing the quantity of

stress to apply to overcome the mucus yield stress.

Air–mucus interaction

The first stress is the one induced by the air–mucus interaction [83, 84]. As the mucus layer is in general thin relatively to the diameter of the airways, this stress can be approximated by the wall shear stress induced by the air flow in the airways [124, 125]. As the airflows induced by HFCWO are small, we assume that the air fluid mechanics follows the Poiseuille's regime in the airways. Hence, the wall shear stress σ_{a} in an airway with radius r and an airflow ϕ is [124]

$$\sigma_{\mathrm{a}} = \frac{\mu_a \phi}{\pi r^3}$$

with μ_a the air viscosity, $\mu_a = 1.8\ 10^{-5}$ Pa.s. Globally, the wall shear stress in the tree is maximal when the air flow in the tree is maximal.

Airways wall oscillations

The tissue oscillations regularly compress and relax the airways, with the consequence of periodically affecting the geometry of the airways walls. To evaluate the resulting stress applied to the mucus, we assume as a first approximation that a deformed airway remains a cylinder with the same length, that only its radius is affected and that no strain occurs along the axis of the airway. With these hypotheses, the displacements of the wall of an airway with rest radius r_0 induce a change of the perimeter of their section from the rest length, $2\pi r_0$, to the deformed length, $2\pi r(t)$ with $t \to r(t)$ representing the radius of the airway as a function of the time. The airways deformations are small and, for determining the radius evolution with time, we can use the same model as in [85] that considers the airway walls as springs. We can then relate the time evolution of the radius of an airway to the elastic properties of its wall and to the variations of the pressures in the tissue p_t and of the pressure of the air in the airways p_a. In this first approximation model, we assume that the Young's modulus E_b of the walls of the airways is the same for all the airways and that $E_b = 6250$ Pa [85]. Details about the derivation of the dynamics of the airways radii are given in Appendix 3.D. The pressure p_a is taken as the mean air pressure in the airway and is computed using the pressure–flow relationships in the airways, see equation (3.3) and Appendix 3.D. The pressure p_t is an estimation of the mechanical pressure surrounding the airway. In our model, the airways have no spatial occupation, hence p_t is estimated using the mean mechanical pressure over the region $\mathcal{Q}$ of the respiratory zone fed by the airway studied. More precisely, if we consider all the paths from the terminal branches to the root of the tree, the set $\mathcal{Q}$ is the union of the A_i's that are coupled to a terminal branch whose associated path includes the airway studied. Finally,

$$p_t(t) = \frac{\int_{\mathcal{Q}} \frac{1}{n}\mathrm{Tr}(\sigma(u)(t,x))\ dx}{\int_{\mathcal{Q}} 1\ dx}$$

See details in Appendix 3.D. In the unidimensional in space, $n = 1$ and

$$p_t(t) = \int_{\mathcal{Q}} (\lambda + 2\mu)\frac{du}{dx} - p_{tree}(\mathcal{F}[\dot{u}])\ dx / \int_{\mathcal{Q}} 1\ dx$$

The way the radius evolves with time induces a tangential strain on the interface between the mucus and the airway wall, $\epsilon_\theta(r_0, \theta, z) = \frac{r(t)-r_0}{r_0}$. Under the hypothesis that the pressure difference felt by the airway is small relatively to E_b, the resulting absolute stress in the mucus can then be estimated to,

$$\sigma(t) \simeq \frac{5}{4}\frac{E_m}{E_b}\,|p_a(t) - p_t(t)| \tag{3.15}$$

with E_m is the Young's modulus of the mucus, see Appendix 3.D.

3.3.2 Effects of the HFCWO on the healthy lungs model

3.3.2.1 Modeling HFCWO with our model

In our unidimensional model of the lungs, we recall that a Neumann boundary condition is applied on one boundary (τ on $x = 0$) and no displacement is set to the other boundary ($u = 0$ on $x = L$). The amplitude A and the pulsation ω of the boundary condition at $x = 0$ are adjusted to mimic an idealised HFCWO maneuver. We consider HFCWO to work as a thrust and a traction at each cycle, with a boundary normal constraint (pressure) $\tau(t) = Asin(\omega t)$, with $\omega = 2\pi f$ and f the frequency. The typical frequencies used in HFCWO devices are in the range 1Hz to 20Hz. To the best of our knowledge, the amplitude of the force felt by the lungs due to the pressure on the thorax is not documented as of today. Since our model is linear in A, we can easily determine the solution for any value of A from a single computation once the other parameters, such as the frequency, have been fixed. Our goal is to compare the efficiency of the different frequencies by observing the airflow induced by HFCWO.

3.3.2.2 Influence of the amplitude A of the applied pressure

HFCWO devices are used to help the draining of the mucus but not for assisting ventilation. The volume of air moved at each cycle, called V_p, is small relatively to the tidal volume of normal ventilation. At rest, the tidal volume is around 500 mL including the dead space, $V_d = 150$ mL, that does not take part in the gas exchanges. We assume that the device does not ventilate more than half the dead space ($V_p \leqslant \frac{V_d}{2} = 75$ ml). With this hypothesis, setting $f = 10$Hz, the amplitude A of the applied pressure in our model, in order to ventilate half the dead space, is $A = 247$ Pa. We assume that this value of A is the maximal possible pressure applied by HFCWO in our model. For the next, we set $A = 200$ Pa.

3.3.2.3 An optimal range of frequencies

HFCWO is known to help the mucus movement by affecting its rheology, out of the scope of this study, and by applying airflows that interact with the mucus by inducing shear stress at the air–mucus interface [83, 84, 125]. The air volume V_p exchanged with the ambiant air and the airflows created by HFCWO are dependant on its working frequency, whose recommended values are based on empirical knowledge. Hence, we study with our model the influence of the HFCWO frequencies on the inhaled air volume and on the tracheal airflow (flow in the first generation of the tree). We assume that the amplitude of the applied pressure A at the boundary $x = 0$ is fixed to $A = 200$ Pa and make the frequency of HFCWO range between 1 Hz and 20 Hz.

The model predicts that V_p decreases as the frequency increases, with a decreasing slope, as shown on figure 3.2 (left). Also, the average airflow increases for frequencies lower than 6.6 Hz and then decreases, hence the maximal airflow is reached at an optimal frequency $f_o = 6.6$ Hz, see figure 3.2 (right). As our model is linear in the amplitude of the boundary constraint A, A affects only the amplitude of the volumes and of the airflows, but not the location of the maximum. Near the optimal frequency f_o, the airflow is actually on a plateau. In the range of frequencies from 3 Hz to almost 20 Hz, the amount of airflow remains within 1% of the maximum. By maximizing the airflow in the tree, this range of frequencies also maximizes the air–mucus interactions during HFCWO maneuvers. It appears that the optimal frequency $f_o = 6.6$ Hz that maximizes the airflow in the tree corresponds to the fundamental natural frequency (Appendix 2.C) of the material $f_1 = \sqrt{\frac{(\lambda+2\mu)}{\rho}}\frac{1}{4L} = 6.5$ Hz that relies on the properties of the material (rigidity, density and size). Then, this maximum corroborates the properties of a harmonic oscillator. Indeed, we have seen that the velocity of the motion of a harmonic oscillator is always maximised for the natural frequency.

Actually, resonance frequencies (i.e. eigen frequencies) of the respiratory system have been estimated in the litterature to 6 Hz for healthy adults [91] and to 18Hz for infants lungs with respiratory distress syndrome (in average over 18 infants) [75]. Those estimations are quite

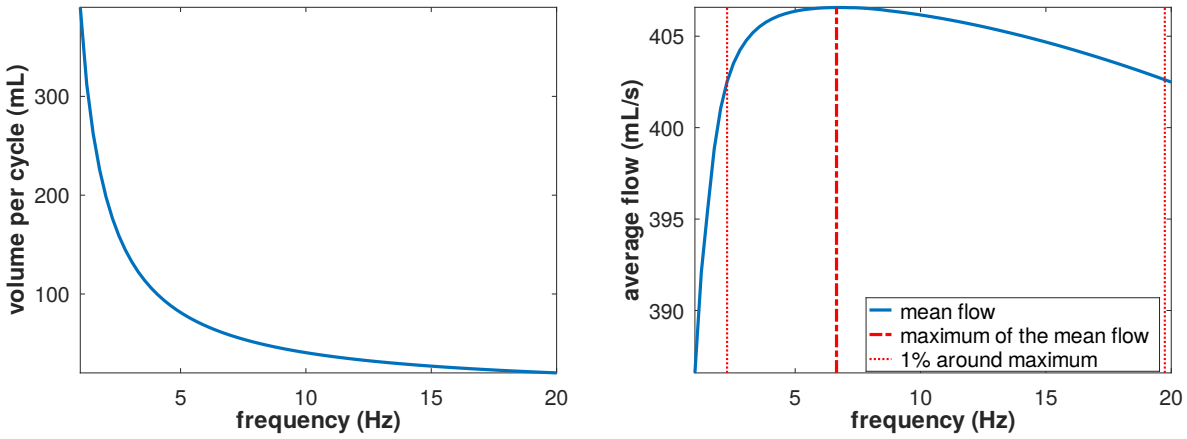

Figure 3.2: **Left:** Volume of air (mL) ventilated at each cycle of the applied constraint according to the frequency of the applied constraint from 1Hz to 18Hz. **Right:** Mean air flow according to the frequency of the applied constraint (from 1Hz to 20Hz) with a maximum of mean flow for $\simeq 6.6$Hz (long red-dashed line) and a range of frequencies for a mean flow within a range of 1% of the maximum (small red-dashed line).

equivalent with our fundamental eigenfrequency $f_1 = 6.5$ Hz obtained by considering a characteristic length of $L = 20$ cm for average adult lungs. Particularly, if we assume approximately a characteristic length of 7 cm for infants lungs, we obtain a fundamental eigenfrequency of $f_1 = 18.5$ Hz.

The wide range of frequencies from 3 Hz to 20 Hz that remains in 1 % of the maximum describes the fact that the intensity of the damping is pretty strong compared to the elastic properties of the the material, as shown by the value of the Q-factor ($Q = 0.048$). If we study the displacement averaged over space and time for different pulsations, we observe that the maximum is reached for the smallest frequency. This is a result that occurs also for harmonic oscillator. Indeed, for harmonic oscillator, the maximum of the motion amplitude is reached for the smallest frequency if the damping is too high compared to the stiffness of the oscillator. However, the resistance of the tree controls the intensity of the resonance in the value of the Q-factor. Hence, different lungs resistances involve different intensity resonance. The next subsection 3.3.3 studies the intensity of the mouth air flows for different resistances in the range of healthy lungs resistances (from 0.5 $\mathrm{cmH_2O.s.L^{-1}}$ to 4 $\mathrm{cmH_2O.s.L^{-1}}$ [87]). Prior to that, we will investigate the distribution of the stress inside the generations of the tree.

3.3.2.4 Stress in the mucus in the optimal configuration.

At the optimal frequency, we computed the two types of stress (defined in 3.3.1), averaged over one HFCWO cycle per unit of stress applied at the boundary. We estimate the order of magnitude of the stresses in the different airways of the tree, see figure 3.3.

The stress due to the vibrations of the walls is larger than the stress induced by the air flow in the proximal[2] part of the tree, but becomes smaller deeper in the tree. This effect is related to the air pressure in the airways. In the proximal part of the tree, the air pressure is small and the airways mechanics is mainly driven by the tissue pressure. Hence, we can deduce from equation (3.15) that in the distal airways, $\sigma(t) \simeq \frac{5}{4}\frac{E_m}{E_b}|p_t(t)|$. Since the amplitude of p_t is directly related to the applied sinusoidal stress of amplitude A, we can derive an estimation of the maximal possible mean stress due to the wall vibrations of about $\sigma \sim \frac{5}{4}\frac{E_m}{E_b}\frac{A}{2} = 0.02$ Pa when $A = 200$ Pa. The estimation is of the same order of magnitude than the results found by our numerical simulations. In the distal parts of the tree, the air pressure increases and compensates

[2]The proximal airways are located in the generations close to the trachea. Inversely, the distal airways are located in the generations far from the trachea.

more strongly the tissue pressures around the airways. As a consequence, the amplitudes of the oscillations of the airways walls decrease with the generations.

Regarding the wall shear stress, globally, we observe a constant pattern of the mean absolute wall shear stress through the tree. We observe a trumpet-like shape as we sink in the tree similar to the ones studied in the previous chapter. We recall that the wall shear stress applied by the air on the mucus is related to the size of the airways and to the amount of airflow in the airway. Moreover, the size of the branches from one generation to the next is reduced by a factor $h = \left(\frac{1}{2}\right)^{\frac{1}{3}}$. Hence, with those assumptions, if the airflows were distributed equally in all the branches of a single generation, the shear stress should decreases from one generation to the next with a factor $\frac{1}{2h^3} = 1$, i.e. the shear stress should be constant through the generations, see [124, 125]. In our case, the airflows are not distributed equally in the airways of a same generation. However, the pressures jumps between the A_i regions are small relatively to the pressure itself. That indicates that the amplitude pressures in the terminal bronchi are quite similar.

Nevertheless, the airways that are closer to the boundary $x = 0$, where the stress is applied, feel a stronger tissue pressure than the other airways, hence, they are submitted to larger stresses than the airways near $x = L$.

Considering the two stresses, our model predicts that the idealized HFCWO therapy submits the mucus to a stress of about a hundredth of pascal, namely one to ten percent of the yield stress necessary for the mucus to move. However, our model produces more qualitative results than quantitative. The amount of stresses here have to be taken in the limitations of the model. Moreover, this suggests that once the mucus located in distal bronchi starts to move, the larger stress in the proximal airways should facilitate its flow to the outside.

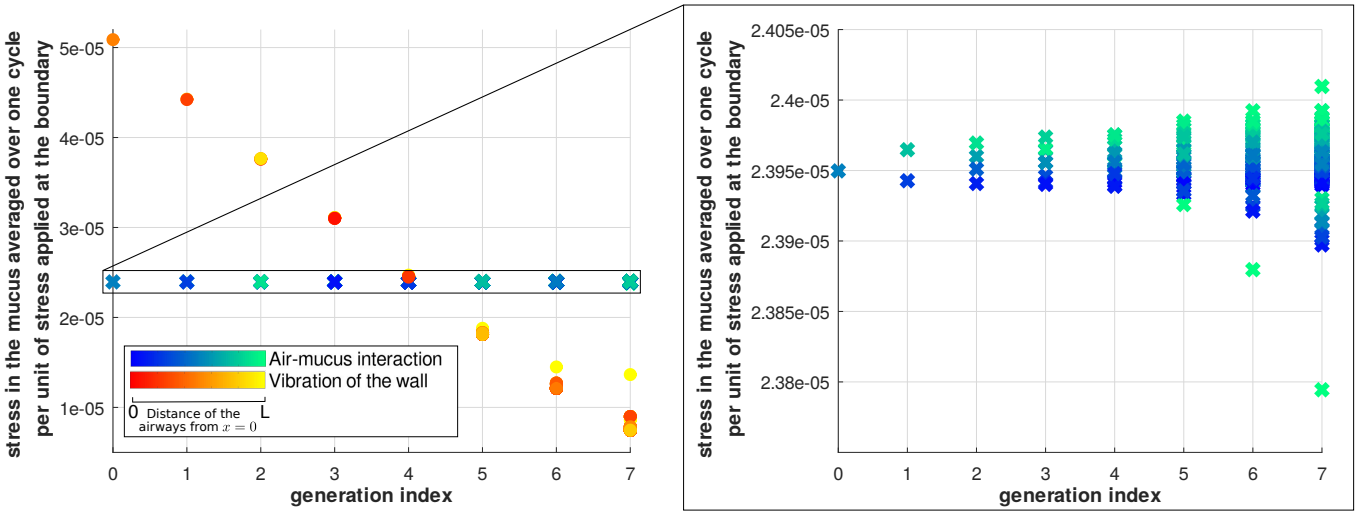

Figure 3.3: Absolute mean of the air wall shear stress (cross-shaped cold-color points) and of the stress due to airways wall oscillations (circle-shaped hot-color points). The mean is computed over the duration of one HFCWO cycle at the optimal frequency $f_o = 6.6$Hz, for all the bronchi of the eight generations tree. We display the stress per unit of the pressure applied by HFCWO (A). The color corresponds to the location of the corresponding airway in $[0, L]$. This location is computed as the mean position of the A_i fed by the airway. For example, the root of the tree is feeding all the A_i and its mean position is $L/2$; the two branches of the second generation are located at $L/4$ and $3L/4$, and so on.

3.3.3 Airflows at mouth induced by HFCWO for the range of healthy lungs resistances

In our model, the quality factor for the healthy lungs model is too low to allow resonance. Nevertheless, we have seen that the fundamental pulsation of the material that mimics the

lung's parenchyma still maximizes the airflows at mouth in the idealized HFCWO. However, we observed that a wide range of frequencies from 3 to 20 Hz around the fundamental frequency (6.5 Hz) is within 1 % of the maximum. Hence, the damping is high but not high enough to prevent the existence of a maximum. We wonder here what happens to the airflows at mouth for healthy lungs with different resistances, from 0.5 $cmH_2O.s.L^{-1}$ to 4 $cmH_2O.s.L^{-1}$. This range represents the range of healthy lungs resistance [87]. We use the same configuration of parameters than in the previous subsections and we change only the corrective factor for the resistance of the tree. We use three equivalent resistances : 0.5, 1.5 or 4 $cmH_2O.s.L^{-1}$.

First of all, the figure 3.4 shows that for all cases the mean air flows are maximised at the fundamental natural frequencies. However, we clearly distinguish that the higher the damping, the lesser is the amplitude of the air flow. In addition, we observe that the width of the optimal range of frequencies within 1% of the maximum increases as the dissipating action of the tree increases. This indicates that the greater the damping, the more homogeneous are the amplitudes of the mean air flow for the different frequencies. If the resistance is high enough, the mean air flows are very close whatever the working frequency of the HFCWO pressures.

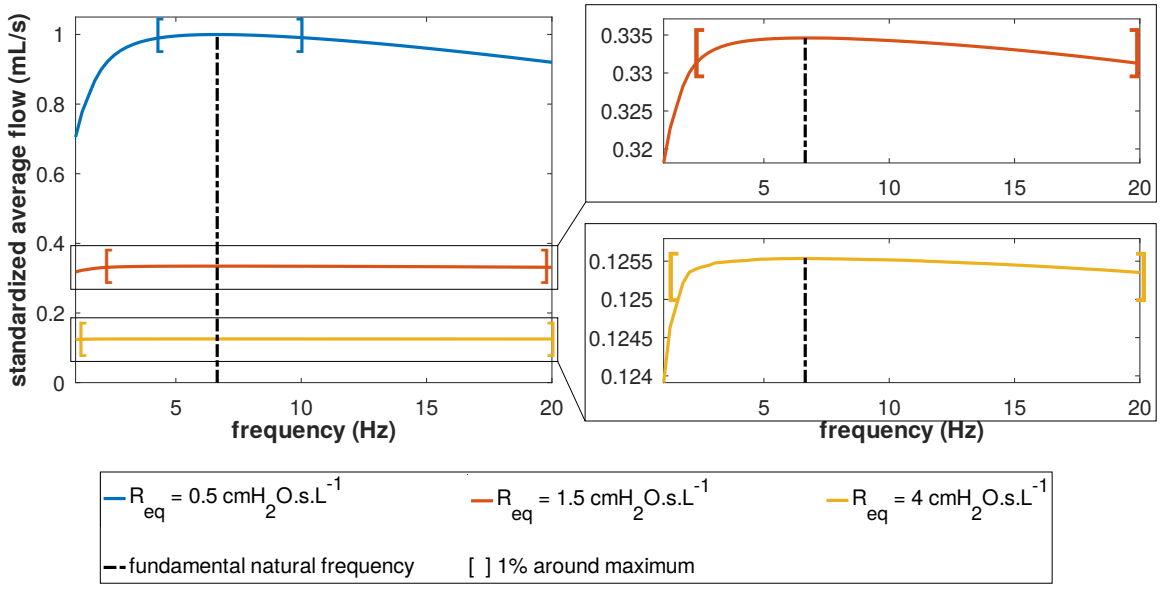

Figure 3.4: Mean air flow according to the frequency of the applied constraint (from 1Hz to 20Hz) for different resistances of the lungs in the range of healthy lungs resistance (0.5, 1.5 and 4 $cmH_2O.s.L^{-1}$) with detailed plots (**right**). The mean air flow are divided by the maximum mean air flow produced with the smallest resistance of the lungs (0.5 $cmH_2O.s.L^{-1}$). The black-dashed line displays the fundamental natural frequency ($\simeq$ 6.6Hz) and the colored square brackets show the respective range of frequencies for a mean flow within a range of 1% of the maximum.

3.3.4 Idealized HFCWO for non-healthy lungs models

The previous subsections show that for equivalent resistances of the lungs above 1.5 $cmH_2O.s.L^{-1}$, the airflows at mouth induced by the idealized HFCWO are too damped to be significantly maximised at a given frequency. This threshold value of the resistance corresponds to the critical quality factor of $Q = 0.048$. The table 3.2 shows that the computed values of the Q-factor for the non-healthy lungs model is strictly above this critical quality factor. In the limits of the hypothesis of our model, the quality factor applied to the lungs suggests that the induced air flows in the airways have a tendency to be constant for any frequency of HFCWO. We will see in the next section that the HFCWO device could be used as an non-invasive tool to measure resistance and compliance of the lungs.

However, we recall that the data used in the numerical simulations are either taken or inspired

from the literature and they constitute averaged values. For example the resistance of the lungs we used to mimick lungs resistance of CF patients is taken from a population of 32 people aged fourteen in average or the Young's modulus of the lung's parenchyma of non-healthy lungs is set arbitrarily and comparatively from the literature and from the value of the Young's modulus of healthy lungs. Nevertheless, the limitations of the model does not allow us to conclude that no frequency can maximize the effect of the HFCWO. The fundamental frequency might still be an interesting data for HFCWO, even for non-healthy lungs. In that way, from the data given in the appendix 2.E, we gather, in table 3.3, resonance frequencies for the healthy and non-healthy lungs suggested by the model.

		Healthy lungs model	**Non-healthy lungs model**		
			Asthma	COPD	CF
Resonance frequency (Hz)	f_o	6.5	6.5	4.6	9.1

Table 3.3: Values of the resonance frequency of the healthy and non-healthy lungs model from the set of parameters displayed in the appendix 2.E, in the limit of our model.

3.3.5 Estimation of the operational hydrodynamic resistance of the airway tree from HFCWO mouth airflow

Actually, with the model, we can derive the measurements of the resistance and the compliance of the lungs from HFCWO. This subsection propose the way to assess, in the limits of the model, the resistance of the lungs. The next subsection 3.3.6 proposes the way to assess the compliance of the lungs.

We define the operational hydrodynamic resistance R_{op} of the airway tree according to a distribution of the air flows at the terminal branches given by $\mathcal{F}[\dot{u}]$ and to the total air flow in the tree root (mouth air flow) given by $F_m = {}^tJ\mathcal{F}[\dot{u}]$,

$$R_{op} = \int_0^T {}^t\mathcal{F}[\dot{u}]\mathcal{R}\mathcal{F}[\dot{u}]dt \Big/ \int_0^T F_m^2(t)dt \tag{3.16}$$

The operational resistance reflects the resistance of the regions of the airway tree where there is an actual air flow. Moreover, the influence of the regions is weighted according to the relative amount of airflows that they receive. The regions where no airflow occurs are not accounted for in that resistance. Hence, R_{op} is in general an overestimation of the equivalent hydrodynamic resistance of the whole tree. In the case where the pressures at each terminal branches of the tree are similar, then the operational resistance is close to the equivalent hydrodynamic resistance R_{eq} of the tree.

Coming back to our model of the lung, if we consider the balance of energy of the system of equations (3.8) over a cycle when the periodic regime is reached, then the energy dissipated during one cycle is equal to the amount of energy put in the system by the boundary $x = 0$. This balance is detailed in the appendix 3.E and can be summarized as

$$\int_0^T \tau(t)F_m(t) \;\; dt = \int_0^T {}^t\mathcal{F}[\dot{u}]\mathcal{R}\mathcal{F}[\dot{u}] \; dt \tag{3.17}$$

The relationship (3.17) allows to estimate the operational resistance of a HFCWO maneuver if the applied signal $\tau(t)$ is known, if the total air flow $F_m(t)$ through the tree (i.e. the mouth airflow) is measured and if a periodic ventilation regime has been reached:

$$R_{op} = \int_0^T \tau(t)F_m(t)dt \Big/ \int_0^T F_m^2(t)dt \tag{3.18}$$

We showed earlier that in our idealised HFCWO maneuvers, the pressure jumps between the A_i compartments are small relatively to the pressure itself, indicating that the pressures at

the terminal branches are almost similar in amplitude. Hence, the operational resistance is a good approximation of the equivalent resistance of the tree in the case of the idealised HFCWO maneuvers. Our numerical simulations confirms that during idealised HFCWO maneuvers, we have $R_{op} \simeq R_{eq}$.

Hence, the operational resistance might have interesting applications for evaluating the actual resistance of the parts of the lung accessible to air flow, for evaluating the performance of a HFCWO maneuver and for estimating the equivalent hydrodynamic resistance of the lung using HFCWO.

3.3.6 Estimation of the compliance using the fundamental frequency

The results about the optimal frequency and its similarity with the fundamental frequency suggest that HFCWO could be used to estimate the compliance of the lung of a patient by searching for the device frequency that maximizes the air flow at mouth level. Since HFCWO applies small and quick deformations on the lung, the lung's response can reasonably be considered as mainly elastic and linear. Then, using the fact that the frequency found should be close to the fundamental natural frequency of the lung in this elastic framework, we can derive the elastic properties of the lung and determine the quantity $(\lambda + 2\mu)$ from which we can estimate its compliance. Since our model is unidimensional, we can relate the compliance to the elastic parameters by $C \simeq V/(\lambda + 2\mu)$ with $V = S_L L = L^3$ the volume of our model of the lung. From the expression of the fundamental frequency, we can then deduce that

$$C \simeq \frac{V^{\frac{1}{3}}}{16\rho f_o^2} \tag{3.19}$$

with V the volume of the lung, ρ its density and $f_o \simeq f_1$ the frequency that maximizes the air flow at mouth level. This formula is derived from a unidimensional model and should be considered with care and/or be validated with clinical data. However, this demonstrates that HFCWO might be a potential tool for estimating the lung's compliance based on the analysis of the air flows at mouth level.

3.4 Discussions and conclusion

This chapter uses the coupled model developed in the previous chapter in order to suggest new insights on the operating choices of HFCWO. Moreover it proposes models to evaluate the stress felt by the mucus during our idealized HFCWO manipulations.

Particularly, our model gives for the first time a physical estimation of the optimal range of frequencies to be used by HFCWO, which is in scope of the working frequencies usually applied to the patient during HFCWO maneuvers [96]. More specifically, we show that in the range of optimal frequencies, the fundamental natural frequency of the lungs deduced from its physical characteristic maximizes the efficiency of the HFCWO in term of mouth air flows. From the data of the literature, our computed optimal frequency is similar to the resonance frequency of the lungs observed in clinical studies that optimizes volume delivery [91, 75]. Moreover, as the natural frequencies are defined from the characteristic of the lungs (size, density, stiffness), the optimal frequency differs between individuals, particularly in the case of respiratory diseases. In the frame of HFCWO, it underlines the significance of determining properly the properties of the lungs in order to apply pressures on the patient's thorax with frequency that could potentially optimize the efficiency of the therapy. Moreover we observe that in this optimal range, HFCWO can apply stress to healthy mucus to about one to ten percent of the estimated yield stress that has to be overcome for the mucus to flow. Last but not least, in our model, the analysis of the mouth air flow during idealized HFCWO allows to estimate the hydrodynamic resistance and the compliance of our model of the lung. This suggests that HFCWO might be a powerful non invasive tool for helping the diagnosis of lung pathologies in the frame of personalized medicine.

However, we have seen that the efficiency of the HFCWO is driven by the intensity of the damping of the tree and we proposed a way to deduce it.

We propose a dimensionless formulation of the model ruled by two dimensionless variables defined from the parameters of the model : $\mathcal{E}$, the Euler number and $\mathcal{B}$ the inverse of the Cauchy number. The Euler number compares the pressures forces induced by the viscous dissipation of the air flow in the tree with inertial forces in the material while the inverse of the Cauchy number compares the elastic forces in the material with the inertial forces. Through the equation of the energies, we show that $\mathcal{E}$ and $\mathcal{B}$ mainly drive respectively the dissipating and the elastic energies. We suggest, using a simplification of the model, the existence of a quality factor (Q-factor) for the lungs, defined from the dimensionless parameters. The Q-factor indicates the capacity of the lungs to resonate with external stimulations. More specifically, according to the value of the Q-factor, the deformation of the lungs can be either maximized at a frequency smaller or equal to the natural frequency for small damping, or not maximized at all, i.e. no phenomenon of resonance occurs. Moreover, we observe that the air flows induced by HFCWO are always maximized at the natural frequency whatever the damping. However, the intensity of the damping drives quantitatively the produced air flow and the width of the range of optimal frequencies around the optimal. Precisely, below a specific value of the quality factor, all the operating frequencies of HFCWO induce similar mean air flows in the tree. In our case, this corresponds to non-healthy lungs with resistances higher than usual.

Our model predictions have to be interpreted in the limit of of the model hypotheses. Actually, as discussed in the previous chapter, it is based on a set of simplification hypotheses for the geometry of the lung, the mechanics of the tissues and the air fluid dynamics. Typically, to get correct flows and pressures when mimicking rest ventilation, a corrective factor for the resistance was needed. Hence, our model can only represent the lung behavior in a qualitative way. Moreover, the predictions of our model are based on averaged biological and mechanical parameters. Those variables are submitted to inter-individual variations, typically for the pulmonary resistance or the compliance, they are affected by the age, the gender, etc. Such variability should be accounted for in future works.

In addition, a simplification was made concerning the physics of the system, for the sake of tractability. Actually, the dimensionless parameter $\mathcal{E}$ is built from the equivalent hydrodynamic resistance of the tree. Hence, it captures only the global influence of the dissipation of the energy by viscous effects in the tree. Thus some changes in the tree configuration can be missed as soon as the equivalent hydrodynamic resistance is not affected by the geometrical change. To get a more fine description of the dynamics linked to the viscous dissipation in the tree, we can consider one dimensionless parameter per generation of the tree (symmetric bifurcating) or per branch of the tree (asymmetric bifurcating), see the appendix 3.B. This improvement would allow to catch any influence of local changes in the tree, such as localized constrictions. However, this would lead to a large number of dimensionless parameters, more than a hundred thousand for a 17^{th} generation tree, and would break the tractability of the model and its potential applicability to medicine.

Finally, the definition of the quality factor has used carefully. Indeed, it is deduced from an idealized and simplified formulation of our continuous coupled model. It does not take into consideration all the full spatial occupation of the lungs. Hence, it has to be interpreted qualitatively, and comparatively from averaged data.

Nevertheless, our model is able to successfully mimic physiological behaviors of the lungs, as the rest ventilation, and to capture the interactions between the tissue mechanics and the air flow in the airways.The two dimensionless parameters $\mathcal{B}$ and $\mathcal{E}$ allow to highlight the relative influence of the elasticity and of the dissipation, depending on the physiological parameters and on how the idealised lung is ventilated. In its limits, the model proposes different tools to suggest optimal working parameters to be used by HFCWO devices. The results predicted by our model have to be validated by clinical data.

Appendices

3.A Behaviors of the solution according to the dimensionless parameters

The dimensionless equation (3.7) can be decomposed according to the physical role of its different terms:

$$\int_0^1 \underbrace{\frac{\partial^2 \tilde{u}}{\partial s^2}}_{\text{acceleration}} w + \left(\underbrace{\mathcal{B}\frac{\partial \tilde{u}}{\partial y}}_{\text{elasticity}} - \underbrace{\mathcal{E}\tilde{p}_{tree}\left(\tilde{\mathcal{F}}\left[\frac{\partial \tilde{u}}{\partial s}\right]\right)}_{\text{damping}} \right) \frac{\partial w}{\partial y}\, dy - \underbrace{\mathcal{B}\,\tilde{\tau}(s)}_{\text{boundary force}} w(0) = 0 \tag{3.20}$$

All of the following possibilities have been simulated numerically, the results agree with the theory.

High frequencies. The system is driven only through the acceleration term, namely the parameters $\mathcal{B}$ and $\mathcal{E}$ are negligible compared to the prefactor 1. This situation occurs if the system works with high enough frequencies : the characteristic time is then low. It could also appear for a very dense and soft material associated to a poor resistive tree. The equation (3.7) can be expressed as

$$\int_{\tilde{\Omega}} \frac{\partial^2 \tilde{u}}{\partial s^2} w dy = 0$$

The solutions of the previous equation is, with c_1 and c_2, two space-dependant constants in time :

$$\tilde{u}(y,s) = c_1(y)s + c_2(y)$$

The two constants are determined with the initial conditions.

- With zero initial condition on displacement or velocity, the solution is equal to zero.
- The constant c_2 is obtained with the initial condition on the displacements. The solution stays constant through time if the initial condition on the velocity is zero.
- The constant c_1 is calculated with the initial condition on the velocity and the solution converges to plus or minus infinity according to c_1 values.

Low frequencies. In this case, the elastic term and the driving force are the only acting terms in the system, i.e the parameter $\mathcal{B}$ is dominant compared to $\mathcal{E}$ and the prefactor 1 which drives the acceleration term. This situation particularly happens when the characteristic time is high (low characteristic frequency). It could also occurs for very stiff material or if the characteristic length is small. The associated equation is :

$$\int_{\tilde{\Omega}} \mathcal{B}\frac{\partial \tilde{u}}{\partial y}\frac{\partial w}{\partial y}\, dy - \mathcal{B} \underbrace{\int_{\tilde{\Gamma}_1} \tilde{\tau}(s) w\, dy}_{=\tilde{\tau}(s)w(0) \text{ (1D case)}} = 0$$

The velocity of propagation of the deformation in this case is very high as well as the angular eigenfrequencies. The amplitude of displacement is linear in space as we put a zero-displacement on the frontier Γ_2. The equation can be assimilated to the Poisson's equation with one dimension.

A highly resistive tree. In this case, the values of $\mathcal{E}$ is large compared to $\mathcal{B}$ and the prefactor 1. This situation is related to a highly resistive tree or a very long material ($L >> 1$). In that case, the terms of stiffness, mass and boundary force can be neglected and the equation (3.7) is written :

$$\int_{\tilde{\Omega}} \mathcal{E}\,\tilde{p}_{tree}\left(\tilde{\mathcal{F}}\left[\frac{\partial \tilde{u}}{\partial s}\right]\right)\frac{\partial w}{\partial y}\, dy = 0$$

This situation implies that either the solution is constant in time or that the mean flows are nulls. If zero-initial condition on the displacement or the velocity is applied, the solution stays null. Otherwise, this is the the mean flow due to the displacement that is equal to zero.

A low resistive tree. The variable $\mathcal{E}$ is considered small relatively to $\mathcal{B}$ and the prefactor 1. This situation occurs for a low resistive tree. The equation (3.7) is rewritten as :

$$\int_{\tilde{\Omega}} \left(\frac{\partial^2 \tilde{u}}{\partial s^2} w + \frac{1}{C} \frac{\partial \tilde{u}}{\partial y} \right) \frac{\partial w}{\partial y} \, dy - \frac{1}{C} \, \tilde{\tau}(s) w(0) = 0$$

As explained in the appendix 2.C, solving equation (3.7) comes down to solve the wave equation with a system of ordinary differential equation.

The material reacts to the boundary conditions and to the initial condition. With the Neumann boundary condition on $y = 0$ and the zero initial condition on displacement (and velocity), we observe a typical deformation wave propagating trough the material presented, see figure 2.3. Without any boundary conditions, the solution is zero unless there is an initial condition on the displacement or on the velocity. Then, the material deformation only responds to elastic properties (there is not damping effect), the deformation propagates endlessly with a velocity associated to the material stiffness.

A soft material.

The parameter $\mathcal{B}$ is considered negligible compared to the other terms of the equation. This corresponds to a very soft material (for example a foam or a fluid). The equation (3.7) becomes:

$$\int_{\tilde{\Omega}} \frac{\partial^2 \tilde{u}}{\partial s^2} w + \left(\mathcal{E} \tilde{p}_{tree} \left(\tilde{\mathcal{F}} \left[\frac{\partial \tilde{u}}{\partial s} \right] \right) \right) \frac{\partial w}{\partial y} \, dy = 0$$

Without the term of elasticity, the material is not deformed at all space points, but only at the frontier of the A_i depending on the initial and boundary conditions.

A very stiff material with a very resistive tree.

It is equivalent to a low density material. Both parameters $\mathcal{B}$ and $\mathcal{E}$ are considered dominant in the equation.

$$\int_{\tilde{\Omega}} \left(\mathcal{B} \frac{\partial \tilde{u}}{\partial y} + \mathcal{E} \tilde{p}_{tree} \left(\tilde{\mathcal{F}} \left[\frac{\partial \tilde{u}}{\partial s} \right] \right) \right) \frac{\partial w}{\partial y} \, dy - \mathcal{B} \underbrace{\int_{\tilde{\Gamma}_1} \tilde{\tau}(s) w \, dy}_{= \tilde{\tau}(s) w(0) \text{ (1D case)}} = 0$$

The term of the first derivative in time of the displacement is only defined locally on the boundaries of the subareas A_i. We analyse this case with a numerical simulation. It shows that for zero-initial condition on displacement and velocity and with the boundary conditions used in the non-physiological case 2.4.1 of the previous chapter , the solution is piecewise-continuous, in particular it is discontinuous at the boundaries of the A_i. Moreover the amplitude of the solution is close to zero.

3.B Extension of the definition of the dimensionless parameter $\mathcal{E}$

3.B.1 Numerical simulation

The dimensionless parameter $\mathcal{E}$ is not able to discriminate between all the trees, as two different trees can have the same hydrodynamic resistance but not the same branches. To illustrate this phenomenon, we run two similar numerical simulations with the same $\mathcal{E}$, but with two different trees. We chose the resistance matrices $\mathcal{R}$ so that they are different but with the same equivalent resistance and consequently the same $\mathcal{B}$ and $\mathcal{E}$. Hence, one tree branches symmetrically, i.e. a mother branch divides into two daughters branches of same size. The

other tree branches asymmetrically, i.e. the size of the daughters branches have not the same size. We call R_{11} and R_{12} the hydrodynamic resistance of the two airways in the generation 2. The airway with resistance R_{1i} feeds the set A_i $(i = 1, 2)$. The asymmetric bifurcating tree is related to the symmetric tree by a decrease by a factor 100 of the hydrodynamic resistance of one of the branch of generation 2, i.e. $R_{11} = R_1/100$, and an increase by the same factor of the hydrodynamic resistance of the other branch, i.e. $R_{12} = 100\, R_1-$, see Figure 3.4. We keep $r_0 = 1$ cm and $l_0 = 6$ cm to define the hydrodynamic resistance R_0 of the root branch. The values of the dimensionless parameters are $\mathcal{B} = 1$ and $\mathcal{E} = 1$. We use the same boundary conditions as the section 2.4 and a zero initial condition on displacement and velocity.

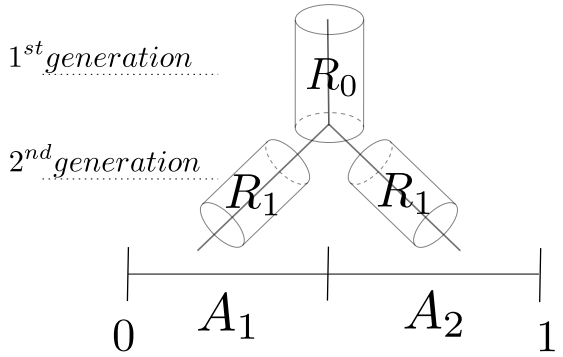

(a) 2 generations tree structure with symmetric bifurcations. We set $R_1 = 2R_0$.

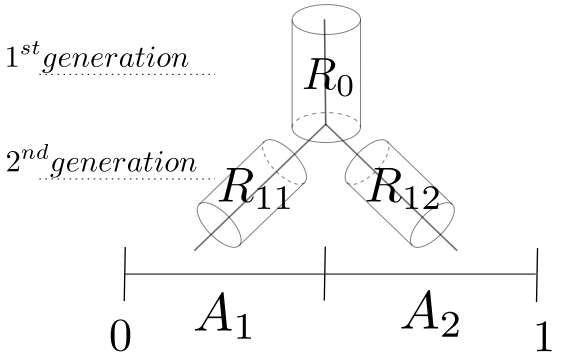

(b) 2 generations tree structure with asymmetric bifurcations. We set $R_{11} = R_1/100$ and $R_{12} = 100R_1$.

$$\mathcal{R} = \begin{pmatrix} \underbrace{R_0 + R_1}_{3R_0} & R_0 \\ R_0 & \underbrace{R_0 + R_1}_{3R_0} \end{pmatrix}$$

(c) Resistance matrix for the 2 generations tree structure with symmetric bifurcations

$$\mathcal{R} = \begin{pmatrix} \underbrace{R_0 + R_{11}}_{(1.02)R_0} & R_0 \\ R_0 & \underbrace{R_0 + R_{12}}_{201R_0} \end{pmatrix}$$

(d) Resistance matrix for the 2 generations tree structure with asymmetric bifurcations : $R_{11} = R_1/100$ and $R_{12} = 100R_1$.

Table 3.4: Two different tree structures with the same equivalent resistance and parameters $\mathcal{B}$ and $\mathcal{E}$, but with different resistance matrices. On the left is displayed a symmetric bifurcations tree structure (a) with the corresponding resistance matrix (c). On the right, is displayed a asymmetric bifurcating tree structure (b) with the corresponding resistance matrix (d).

The Figure 3.5 shows the material displacement for the two cases. Since A_2 is connected to the more resistive branch in the asymmetric case, the displacements in A_2 are lower in the asymmetric case than in the symmetric case. This example shows that the local contribution of the resistance of each branch of the tree is not accounted for in the dimensionless formulation based on $\mathcal{E}$ and $\mathcal{B}$. This choice allows however to keep the physics of the system tractable and to connect more easily with clinical measures which often reflect global behaviors of the pulmonary system.

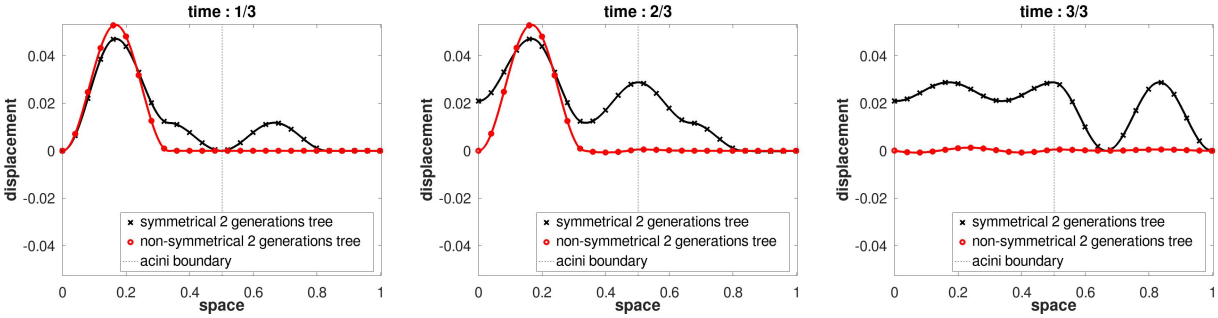

Figure 3.5: Propagation of wave deformation of a two generations symmetric bifurcating tree (black cross) and a two generations asymmetric bifurcating (red circle) tree at time $s = \frac{1}{3}$ (a), $s = \frac{1}{2}$ (b), $s = \frac{2}{3}$ (c). For the two cases above, the parameters $\mathcal{B}$ and $\mathcal{E}$ are equal.

3.B.2 Alternative definition of the dimensionless parameter $\mathcal{E}$

The definitions of the dimensionless parameter $\mathcal{E} = \frac{R_{eq} S_L}{\rho v}$ in Table 3.1 is based on the equivalent hydrodynamic resistance of the tree R_{eq} only. This approach is not able to distinguish the dynamics induced by two different trees with the same hydrodynamic resistance. Hence, we propose alternative definitions of the dimensionless parameters.

In the case of a symmetric bifurcating tree, one dimensionless variable $\mathcal{E}_i$ can be defined for each generation i of the tree. In this case, all the branches belonging to the generation i have the same hydrodynamic resistance R_i. The dimensionless weak formulation is then

$$\int_0^1 \frac{\partial^2 \tilde{u}}{\partial s^2} w + \left(\mathcal{B} \frac{\partial \tilde{u}}{\partial y} + \mathcal{E}^n \, \tilde{F}_T \right) \frac{\partial w}{\partial y} \, dy - \mathcal{B} \underbrace{\int_{\tilde{\Gamma}_1} \tilde{\tau}(s) w \, dy}_{=\tilde{\tau}(s) w(0) \text{ (1D case)}} = 0 \tag{3.21}$$

with $\mathcal{E}^n = \sum_{i=0}^{n} \mathcal{E}_i$, $\tilde{F}_T = \sum_{i=1}^{N} \tilde{\mathcal{F}}_i \left[\frac{\partial \tilde{u}}{\partial s} \right]$ and for $i = 0, \ldots, n$,

$$\mathcal{E}_i = 2^{n-i} \frac{R_i}{R_{eq}} \mathcal{E}$$

Similarly, in the case of a tree with non symmetric bifurcations, all the branches of the tree can be different and one dimensionless number $\mathcal{E}$ can be defined for each branch. Hence, the number of dimensionless parameters $\mathcal{E}$ would equal the number of branches in the tree, i.e. $2^{n+1} - 1$ if the tree has $n + 1$ generations. The dimensionless number $\mathcal{E}_b$ associated to a branch b belonging to the generation i and with a hydrodynamic resistance R_b would then be

$$\mathcal{E}_b = 2^{n-i} \frac{R_b}{R_{eq}} \mathcal{E}$$

It is important to adapt the number of dimensionless parameters to the problem in order to keep some tractability in the study.

3.C A one degree of freedom equation.

This appendix deals with the one degree of freedom simplification of the equation of the coupled model using the dimensional and discretized expression (2.18). It allows to verify the definition of the Q-factor obtained in the subsection 3.2.2 using the dimensionless equation.

The dimensional and discretized equation of our coupled model, obtained with the finite element method in 2.B, is :

$$M \frac{d^2}{dt^2} U(t) \; + \; D \frac{dU(t)}{dt} \; + \; KU(t) \; = \; \tau(t) h$$

with $\ddot{U} = \frac{d\dot{U}}{dt} = \frac{d^2U}{dt^2}$, and with M, D and K respectively the mass, the damping and the stiffness matrices and with h the vector of loads. The damping D is defined as $D = S\ {}^tG\mathcal{R}G$, with S a characteristic surface. For two degrees of freedom this equation becomes

$$\begin{pmatrix} M_{11} & M_{12} \\ M_{21} & M_{22} \end{pmatrix} \begin{pmatrix} \ddot{U}_1 \\ \ddot{U}_2 \end{pmatrix} + \begin{pmatrix} D_{11} & D_{12} \\ D_{21} & D_{22} \end{pmatrix} \begin{pmatrix} \dot{U}_1 \\ \dot{U}_2 \end{pmatrix} + \begin{pmatrix} K_{11} & K_{12} \\ K_{21} & K_{22} \end{pmatrix} \begin{pmatrix} U_1 \\ U_2 \end{pmatrix} = \tau \begin{pmatrix} h_1 \\ 0 \end{pmatrix}$$

Particularly, the damping matrix D is written as

$$\begin{pmatrix} D_{11} & D_{12} \\ D_{21} & D_{22} \end{pmatrix} = S \begin{pmatrix} G_1 & G_2 \end{pmatrix} \begin{pmatrix} \mathcal{R}_{11} & \mathcal{R}_{12} \\ \mathcal{R}_{21} & \mathcal{R}_{22} \end{pmatrix} \begin{pmatrix} G_1 \\ G_2 \end{pmatrix}$$

Considering only a one generation tree, the coefficients of the resistance matrix are equal to r_0 as well as the equivalent resistance R_{eq}. With the homogeneous Dirichlet condition in $x = L$, the second element of the vector U is null ($U_2 = 0$). Finally we have :

$$M_{11}\ddot{U}_1 \ + \ D_{11}\dot{U}_1 \ + \ K_{11}U_1 \ = \ h_1\tau \tag{3.22}$$

With the dimensional formulation and with two degrees of freedom, the elements of the matrices and of the vector are equal to

$$\begin{cases} M_{11} = \frac{\rho L}{3} \\ K_{11} = \frac{(\lambda+2\mu)}{L} \\ h_1 = 1 \\ D_{11} = S\ G_1\ \mathcal{R}_{11}\ G_1 = S\ (-1)\mathcal{R}_{11}(-1) = S\ \mathcal{R}_{11} \end{cases}$$

Setting $u = U_1$, $S = L^2$, and with $R_{eq} = r_0$, the equation (3.22) becomes :

$$\ddot{u} \ + \ \frac{3R_{eq}L}{\rho}\dot{u} \ + \ \frac{3(\lambda+2\mu)}{\rho L^2}u \ = \ \frac{3}{\rho L}\tau$$

We relate on parameters with those of the harmonic oscillator :

$$2\xi = \frac{3R_{eq}L}{\rho} \qquad \text{and} \qquad \omega_0^2 = \frac{3(\lambda+2\mu)}{\rho L^2}$$

Finally the Q-factor is, with $c = \sqrt{\frac{(\lambda+2\mu)}{\rho}}$:

$$Q = \frac{\omega_0}{2\xi} = \frac{c\rho\sqrt{3}}{3R_{eq}L^2}$$

3.D Estimation of the stress in the mucus layer induced by the airway walls oscillations

The airway walls are oscillating due to the oscillation of their transmural pressure. In order to estimate the stress applied on the mucus by the oscillations of the airway walls, we have first to determine the response of the airways radius to the changes in transmural pressure. We assume that the airways wall behaves as a circular spring [85]. Then, we compute the stress in the mucus assuming that the mucus remains solid and behaves as a linear elastic material. The hypotheses of linear elasticity are justified by the small amplitudes of the oscillations applied by HFCWO.

3.D.1 Estimation of the evolution of the airways radii

As HFCWO devices apply small deformations to the lung, we model the walls of the airways in the same way as in [85]. Hence, we assume that the airway wall reacts as a spring that remains circular. We consider an airway with a rest radius r_0 and with a constant length l_0. As in [113, 85], we assume the airway wall to have a thickness $w_0 = \frac{2}{5}r_0$, a Young's modulus $E_b = 6250$ Pa, a Poisson ratio $\nu_b = 0.5$ (incompressible material) and a density $\rho_b = 1000$ kg.m^{-3}. We consider cylindrical coordinates (r, θ, z) adjusted to the cylindrical geometry of the airway: r corresponds to the radial position, θ to the angular position and z to the axial position. The corresponding basis vectors are denoted e_r, e_θ and e_z. Assuming that the cylindrical airway has a radius r, we consider a part of its wall with an angular width of $d\theta$ located at the angular position θ. Applying the Newton's second law to that segment leads to

$$\underbrace{r\,d\theta\,w_0\,l_0\,\rho_b}_{\text{mass}}\underbrace{\frac{d^2r}{dt^2}\mathbf{e_r}(\theta)}_{\text{acceleration}} = \underbrace{t(r)\,l_0\,\mathbf{e}_\theta(\theta) - t(r)\,l_0\,\mathbf{e}_\theta(\theta+d\theta)}_{\text{elastic force}} + \underbrace{r\,d\theta\,l_0\,(p_a(t)-p_t(t))\,\mathbf{e_r}(\theta)}_{\text{pressures forces}} \tag{3.23}$$

where:

- The function $r \to t(r)$ is the lineic tension due to the elongation of the wall, $t(r) = -\frac{E_b}{1-\nu_b^2}w_0\frac{r-r_0}{r_0}$, see more details in [85].
- The pressure in the tissue $p_t(t)$ is computed using the trace of the stress tensor $\sigma(u)$ in the respiratory zone, see equation (2.8),

  $$p_t(t) = \frac{\int_{\mathcal{Q}} \frac{1}{n}\mathrm{Tr}(\sigma(u)(t,x))\;dx}{\int_{\mathcal{Q}} 1\;dx}$$

  with n the spatial dimension and Q the set defined as the union of the A_i fed by the airway studied. For example, the tissue pressure in the first generation airway is the mean of the tissue pressures computed on all the A_i as this airway is feeding all the tissue, i.e. $Q = \Omega$. With $n = 1$, we can rewrite the pressure in the tissue as

  $$p_t(t) = \frac{\int_{\mathcal{Q}}(\lambda+2\mu)\frac{du}{dx} - p_{\text{tree}}(\mathcal{F}[\dot{u}])\;dx}{\int_{\mathcal{Q}} 1\;dx}$$

- The air pressure in the airway $p_a(t)$ results from the air fluid dynamics in the tree. It is approximated by the mean air pressure in the airway, which is computed using the linear relationships between the air flows and pressures in the tree, see equation (2.1). More precisely, we define the set I of the indexes of the airways that are on the path starting from the root of the tree and ending at the airway studied. For $i \in I$, we denote R_i is the hydrodynamic resistance of the airway with index i and ϕ_i the airflow in that same airway; the quantity $R_i\phi_i$ is the pressure drop in the airway i. Finally, denoting R_b the hydrodynamic resistance of the airway studied and ϕ_b the airflow in that same airway, we have

  $$p_a(t) = -\left(\sum_{i\in I} R_i\phi_i(t)\right) + \frac{R_b}{2}\phi_b(t)$$

  where the first term computes the pressure at the end of the airway studied and the second term is a correction to get the pressure in the middle of that airway.

Using the relationship $\mathbf{e}_\theta(\theta) - \mathbf{e}_\theta(\theta+d\theta) = \mathbf{e_r}(\theta)d\theta$, projecting the equation (3.23) on $\mathbf{e_r}$ and simplifying, we obtain

$$w_0\rho_b\frac{d^2r}{dt^2} = -\frac{w_0}{r_0}\frac{E_b}{1-\nu_b^2}\frac{r-r_0}{r} + (p_a(t)-p_t(t)) \tag{3.24}$$

Then, rewriting the equation (3.24) in a dimensionless form allows to compare the different influences of acceleration, elasticity and pressures:

$$\underbrace{\frac{\rho_b r_0^2(1-\nu_b^2)}{E_b T^2}}_{N}\frac{d^2\tilde{r}}{ds^2} = -1 \times \frac{1}{\tilde{r}}(\tilde{r}-1) + \underbrace{\frac{r_0}{w_0}\frac{P(1-\nu_b^2)}{E_b}}_{M}(\tilde{p}_a(s)-\tilde{p}_t(s))$$

using $s = t/T$, $\tilde{r}(s) = r(sT)/r_0$, $\tilde{p}_*(s) = p_*(sT)/P$ with $* = a$ or t. T is the characteristic time of the oscillations, i.e. their period; at the optimal configuration (see figure 3.2), $T = 0.05$ s. P is the order of magnitude of the pressure, typically the pressure applied on the boundary, reflected by the variable A, hence we chose $P = A = 200$ Pa. Finally, we can estimate the dimensionless numbers $N = \frac{\rho_b r_0^2(1-\nu_b^2)}{E_b T^2}$ and $M = \frac{r_0}{w_0}\frac{P(1-\nu_b^2)}{E_b}$ at the optimal configuration,

$$N \leqslant N_{|r_0=1\text{cm}} = 5.1\ 10^{-4} \text{ and } M = 6.0\ 10^{-2}$$

Consequently, the acceleration is small relatively to the elastic term ($N << 1$) and we can assume at first approximation a static equilibrium between the elastic forces and the pressure forces. Notice that N decreases when the generation index increases since the radii of the airways are decreasing with the generation index. Hence, the approximation $N << 1$ is better for the small airways. The number M is also quite small relatively to 1, indicating that the displacements due to the pressures are also small, in agreement with the linear elasticity approximation.

Solving the static equation leads to $\tilde{r}(s) = (1 - M(\tilde{p}_a(s) - \tilde{p}_t(s))^{-1}$. Considering $M << 1$, we can go further in the approximation, and $\tilde{r}(s) \simeq 1 + M(\tilde{p}_a(s) - \tilde{p}_t(s))$. Equivalently, using dimensional variables and replacing ν_b with 1/2, we can finally reach an expression for $r(t)$:

$$r(t) = \frac{r_0}{1 - \frac{3}{4}\frac{r_0}{w_0}\frac{p_a(t)-p_t(t)}{E_b}} \simeq r_0\left(1 + \frac{3}{4}\frac{r_0}{w_0}\frac{p_a(t)-p_t(t)}{E_b}\right)$$

The determination of the evolution of the radius relatively to that of the transmural pressure $p_a(t) - p_t(t)$ allows to compute in the next section the resulting stress in the mucus.

3.D.2 Estimation of the stress in the mucus layer

The way the radius evolves with time induces a tangential strain on the interface between the mucus and the airway wall, $\epsilon_\theta(r^0, \theta, z) = \frac{r(t)-r_0}{r_0}$. This tangential strain propagates into the mucus at a characteristic velocity $c = \sqrt{E_m/\rho_m}$ where E_m is the Young's modulus of the mucus and ρ_m its density. In an healthy mucus layer, $E_m \simeq 1$ Pa and $\rho_m \simeq 1000$ kg.m^{-3} [70] and we can estimate that $c \simeq 3$ cm.s^{-1}. Since the typical thickness of the mucus layer is about 10 μm [59], the wave propagates through the depth of the mucus in less than 0.5 ms. Hence, the strain on the mucus wall represents well the strain inside the mucus layer at the time scale of HFCWO. At the position (r, θ, z) the strain in the mucus layer is then $\epsilon_\theta(r, \theta, z) = \frac{r(t)-r_0}{r_0}$. The mucus is an incompressible material, hence the trace of the strain operator is zero and $\epsilon_\theta = -\epsilon_r$ since we assume $\epsilon_z = 0$. Finally, based on these hypotheses and on the linear elasticity in cylindrical coordinates states that

$$\begin{aligned}\epsilon_r &= (1+\nu_m)\left((1-\nu_m)\sigma_r - \nu_m\sigma_\theta\right)/E_m \\ \epsilon_\theta &= (1+\nu_m)\left((1-\nu_m)\sigma_\theta - \nu\sigma_r\right)/E_m\end{aligned}$$

Then, using $\epsilon_r = -\epsilon_\theta$, we have $\sigma_* = \frac{E_m}{1+\nu_m}\epsilon_*$ with $* = r$ or θ. Making the mucus Poisson's ratio ν_m going to 0.5 since the mucus is incompressible, the norm of the stress in the thin layer of mucus on the wall of the airway can be estimated with

$$\sigma(t) = \frac{2}{3}E_m\left|\frac{r(t)-r_0}{r_0}\right| \simeq \frac{1}{2}\frac{r_0}{w_0}\frac{E_m}{E_b}\left|p_a(t)-p_t(t)\right|$$

The stress induced in the mucus by airways wall oscillations is then compared to the yield stress of the mucus, see main text.

3.E Operational resistance

We consider the dimensionless energy conservation in our model, see equation (3.8). and use the fact that the total air flow through the tree is $\tilde{F}_m(s) = {}^tJ\tilde{F} = \sum_{i=1}^N \tilde{\mathcal{F}}_i[\frac{\partial\tilde{u}}{\partial s}] = -\int_0^1 \frac{\partial^2\tilde{u}}{\partial y\partial s}(y,s)dy = \frac{\partial\tilde{u}}{\partial s}(0,s) - \frac{\partial\tilde{u}}{\partial s}(1,s) = \frac{\partial\tilde{u}}{\partial s}(0,s)$. Hence, we can rewrite the dimensionless energy conservation,

$$\frac{d}{ds}\left(\frac{1}{2}\int_0^1\left(\frac{\partial\tilde{u}}{\partial s}(y,s)\right)^2 dy + \mathcal{B}\frac{1}{2}\int_0^1\left(\frac{\partial\tilde{u}}{\partial y}(y,s)\right)^2 dy\right) = \mathcal{B}\tilde{\tau}(s)\tilde{F}_m(s) - \mathcal{E}\ {}^t\tilde{F}\frac{\mathcal{R}}{\mathcal{R}_{eq}}\tilde{F} \tag{3.25}$$

since ${}^t\tilde{\mathcal{F}}[\frac{\partial\tilde{u}}{\partial s}]\frac{\mathcal{R}}{\mathcal{R}_{eq}}\tilde{\mathcal{F}}[\frac{\partial\tilde{u}}{\partial s}] = -\sum_{i=1}^N \tilde{p}_i(\tilde{\mathcal{F}}[\frac{\partial\tilde{u}}{\partial s}])\tilde{\mathcal{F}}_i[\frac{\partial\tilde{u}}{\partial s}]$. Now, if we assume that the system is periodic with a period 1, then integrating the previous equation over a cycle and going back to dimensional variables lead to

$$\int_0^1 \tilde{\tau}(s)\tilde{F}_m(s)\ \ ds = \frac{\mathcal{L}_M}{R_{eq}}\int_0^1 {}^t\tilde{\mathcal{F}}[\frac{\partial\tilde{u}}{\partial s}]\mathcal{R}\tilde{\mathcal{F}}[\frac{\partial\tilde{u}}{\partial s}]\ ds\ \rightarrow\ \int_0^T \tau(t)F_m(t)\ \ dt = \int_0^T {}^t\mathcal{F}[\dot{u}]\mathcal{R}\mathcal{F}[\dot{u}]\ dt \tag{3.26}$$

We define now the operational hydrodynamic resistance of the airway tree

$$R_{op} = \frac{\int_0^T {}^t\mathcal{F}[\dot{u}]\mathcal{R}\mathcal{F}[\dot{u}]dt}{\int_0^T F_m^2(t)dt} \tag{3.27}$$

When the pressures are all identical in the terminal branches of the tree, then we have ${}^t\mathcal{F}[\dot{u}]\mathcal{R}\mathcal{F}[\dot{u}]dt = R_{eq}F_m^2$. In that case, $R_{op} = R_{eq}$. More generally, R_{op} is the equivalent resistance of the parts of the tree where the air flows occur, weighted by the relative values of the airflows. Hence, the value of R_{op} ranges from the value of the equivalent resistance of the most resistive path between the root of the tree and the terminal branches, and the value of the equivalent resistance of the tree. In the quasi-fractal model with $n+1$ generations, R_{op} ranges from $R_0 + R_1 + ... + R_n$ (hydrodynamic resistance of a path from generation 0 and n, all identical) and $R_{eq} = \sum_{i=0}^n \frac{R_i}{2^i}$.

Chapter 4

Towards the improvement of the model of the lungs

"[...] ; ce qui ne demande point de preuve, c'est-à-dire, que l'air est la cause de tous les mouvements des animaux, [...] de sorte que l'air est le premier mobile dans les animaux, & qu'on peut l'appeler le principe de la vie, & qu'on peut dire avec fondement que c'est dans ce sens, que l'Ecriture l'a appelé l'air de la vie."

Joseph-Etienne Bertier,
Dissertation sur cette question si l'air de la respiration passe dans le sang, 1739, p.95.

Contents

4.1 Introduction

The study of the model proposed in the previous chapters has been performed from an idealized perspective with several hypothesis. The hypotheses simplify the model and its solving to mimic the conductive pulmonary tree. We use for example an idealized tree geometry which is dichotomous and symmetric. The flow of air inside the tree are also considered low to allow the use of Poiseuille's regime. Additionally, the composition of the lung's parenchyma is mimicked by an homogeneous media, although it is known that it is heteregeneous and composed of numerous of air-filled alveoli. In parallel, we analyze mostly the one-dimensional formulation of the model that produces mainly qualitative and comparative results. In this chapter, we discuss the different hypotheses of the model and investigate the potential ways to improve it. Moreover, we present the different methods leading to efficient multi-dimensional numerical simulations. Finally, the setup of a clinical study to estimate experimentally the efficiency of a HFCWO device is proposed and detailed.

4.2 Hypotheses of the model

With the aim of respecting the balance between precision and computational time, our model of the lungs is based on several assumptions. The model is based on hypotheses for the dissipating action of the tree structure mimicking the pulmonary tree, see subsection 4.2.1, and for the physical properties of the lung's parenchyma, see subsection 4.2.2. In addition, the 0D model of the mucus used in the chapter 3 produces only comparative outputs and further adjustments can be proposed to reach better estimations of the stress felt by the pulmonary secretions, see subsection 4.2.3.

4.2.1 Assumptions of the tree region

It has been discussed that our model of the pulmonary tree is idealized and does not take into account the oesopharyngeal pathway, the details of the geometry of the bifurcations, the inertial effects of the air flow and the asymmetric branching [104, 105, 87]. That is the reason why, to model real lungs behaviors, we used a corrective factor for the resistance of our tree structure to get it closer to the physiological values of real resistances of the lungs. We notice that the overall resistance of the lungs measured experimentally takes all those effects into account [87]. Actually, the resistance of the lungs corresponds to the resistance of the air pathway from the ambient air to the exchange surface in the acinar region, and not the one of the tracheo-bronchial tree only. Hence, in order to reduce the value of the corrective factor, i.e. to have a model of the pulmonary tree which is closer to the reality, several hypotheses can be improved.

4.2.1.1 Considering circulation of air in the pulmonary tree

We model the pulmonary airways as rigid cylinders where the circulation of air follows the steady-state Poiseuille's regime. This type of flow is valid for low flow and when neglecting the inertial effects in the fluid. Moreover, we do not take into account the complex geometry of the bifurcations between the generations. Actually, as evoked in [109], the respiratory airways are not longitudinal circular tracts, their section can vary. This can increase the overall resistance of the pulmonary tree. In addition, while Poiseuille's flow is a valid approximation for low flow in cylindrical airways, i.e. HFCWO manipulation, it does not allow to determine properly the air fluid dynamics in complex geometries (for example bifurcations [60]), non-cylindrical airways constrictions or high flow breathing. Hence, the resistance can be flow dependant and account for complex geometrical features. Inertial effects can appear, particularly in the upper airways [134]. In that case, the hydrodynamic resistance is higher than Poiseuille's : $R = Z\, R_{pois}$, $Z \geqslant 1$ [123]. We denote by R_{pois} the resistance of Poiseuille's regime. We recall that it is defined in a three-dimensional cylinder as $R_{pois} = \frac{8\pi\eta l}{\pi r^4}$, where η is the dynamic viscosity, and r and l the respective radius and length of the pipe.

HFCWO induces relatively low amplitude air flows compared to tidal breathing. The inertial effects due to high flow may be limited to highly constricted airways, not in the scope of this thesis. However, we could consider the non-linear resistance due to the geometry of the bifurcations. The author in [123] describes different models found in the literature to determine the prefactor Z. In [104], it is proposed a model for the resistance based on experimental measurement for symmetric bifurcations. The prefactor is denoted

$$Z_{Pedley} = C\sqrt{\frac{R_e}{l}2r}$$

where $C = 0.327$ and R_e is the Reynolds number defined by $R_e = \frac{2\rho|\phi|}{\nu\pi r}$ which denotes the regime of the fluid. The higher the Reynolds number is, the higher are the inertial effects. The model has been designed to inspiratory air flow as in [16] where asymmetric branching is considered. Typically, in [16], they consider that, at a bifurcation, the mother branch opens on one bigger and one smaller daugther branches. Hence, they defined two prefactors Z_+ (for the bigger) and Z_- (for the smaller) to describe the resistances. In [130], the model is built for high Reynolds number in cylinders. Particularly for $R_e \leqslant 300$, the prefactor is one and the resistance is defined as that of Poiseuille. Otherwise for $R_e > 300$, the resistance is defined as

$$R = (\frac{1}{2} + \frac{R_e}{600})R_{pois}$$

Notice that other models of airways resistance could also be discussed [60, 134], see [109].

The model of resistance should be considered according to the situation, if one assumes asymmetric/symmetric branching or low/high flows. At a first try, the models proposed by [104] should be considered to take into account the inertial effects of the bifurcations in the tree.

4.2.1.2 Towards more realistic geometries of the respiratory tree

Our 0D model of the pulmonary tree used in the previous chapters is based on the homogeneous model of Weibel [135]. Typically, the tree is considered as a dichotomous symmetrical branching system, namely all the branches of a given generation have the same size. Actually, studies show that, despite being quasi dichotomous, the tree rather adopts asymmetric structure [82]. More specifically, this asymmetry can be defined by two distinct aspects : the asymmetry of branching and the asymmetry of topology [123]. The branching is asymmetric when a mother airway divides into two daughter airways with different sizes. The asymmetry of topology defines the fact that the pathways from trachea through the acini do not encounter the same number of generations. This results on air pathways from the trachea to the acini composed of about nine generations up to thirty generations [47].

We have seen, through the study of the wall shear stress induced by the air flow in the tree in the section 3.3, that with the hypothesis of a dichotomous and symmetrical branching tree, the wall shear stress due to the air–mucus interaction in the airways rather spread homogeneously. Considering the tree asymmetry would be a benefit approach to study more realistic distributions of the air flow dynamics in the airways of the tree. That would also allow to better understand the behaviors of the mucus inside the airways. Several models have been proposed for that purposes [72, 138, 47, 16]. The asymmetric properties of the lung would be taken into account in the matrix of resistance defining the resistances of paths and sub-paths of the considered tree. In the case of asymmetrical branching, the properties of the matrix remain verified [37]. For the asymmetric topology, a new matricial formulation has to be derived [123].

4.2.2 Assumptions about the lung's parenchyma

We consider the lung's parenchyma as a homogeneous linear elastic medium. Typically, we do not account for the spatial heterogeneity of the physical properties of the lung's parenchyma and we remain only in the frame of small deformation. The chapter 1 shows the complexity of the

lung's parenchyma and show the difficulties of a detailed modeling. However, some refinements can be proposed insired from literature.

4.2.2.1 On the heterogeneity of the lung's parenchyma

We have seen in the chapter 1 that the lung's parenchyma is filled with acini and is composed of millions of alveoli, i.e. little cavities filled with air. It is then formed of successions of tissue and air space, whose physical properties are different. In our model of the lung's parenchyma, we do not account for this spatial heterogeneity. Actually, remembering that the size of the alveoli and the thickness of their surface are small compared to the spatial occupation of the lung's parenchyma, the hypothesis of homogeneity regarding the physical property of the elastic medium can be quite relevant. In fact, several studies have already discussed about the justification of this hypothesis [71]. For example, as stated in [109], the heterogeneity of the alveoli micro-structure can be considered at a macroscopic level by way of a homogenization method proposed in [19, 3]. However, the way those physical properties are considered can be discussed. In particular, the stiffness of the lung's parenchyma is one of the main data in our model. It determines the capability of the lungs to recoil from a stimulation. Moreover, the stiffness of the lung affects the velocity of the wave deformation. Estimating the bio-mechanical properties of the lung's parenchyma is then important for our model. Several studies propose different approaches for that purpose. The estimations are done by mixing mathematical models and clinical measurements (in dogs) [74, 71] or using hypo-elastic model [31]. Moreover, different factors can modify the physical properties of the lungs, as the age or the health condition. Hence, assessing personalized data could be beneficial to our HFCWO model. For example, this is done in [119], which uses an inverse non-invasive method from four-dimensional computed tomography. Moreover, as suggested in the chapter 3, the HFCWO therapy could be also used as a non-invasive measurement tool to measure the resistance and the compliance of the lungs. Nevertheless, those properties should be adapted for any individuals and complete lungs data should be reviewed and compiled from literature.

4.2.2.2 Spatial composition of the thorax

We do not model the deformation induced by HFCWO in all the physical components of the thorax. In reality, the action of the HFCWO pressures propagates through the skin tissue, muscles, bones, pleural liquid and tissues, before acting on the lungs. The physical properties of those layers are different and affect the deformation. For example, bones are known to be much stiffer than tissue [106, 12]. One arising question would then be : does some locations of the applied pressures on the thorax's patient induce more efficient deformation than others? Those considerations should be taken into account in future works. The study of those features would be relevant only in multidimensional model of the lungs.

The consideration of the spatial heterogeneity of the thorax could be integrated directly into the stress-strain law of our elastic medium. With the weak formulation for our continuous system, integrating the different layers composing the thorax would resume to add a spatial dependence for the Lamé parameters. The linear stress (2.6) would become

$$\sigma_{elastic}(u) = \lambda(x)\ \mathrm{tr}\left(\epsilon(u)\right) I + 2\mu(x)\ \epsilon(u)$$

with $u(x,t) \in \mathbb{R}^m$, m the spatial dimension, and $t \in \mathbb{R}_+$.

The heterogeneity of the thorax could be also considered by using different equations, connected with boundary conditions or interaction forces, each one ruling a specific region of the thoraco-pulmonary region as in [32]. Typically, using our discretized system (2.18) and in the same spirit as [32], we would have the following illustrative system of dynamics equations to

solve

$$\begin{cases} M^l\ddot{U}^l + D^l\dot{U}^l + K^lU^l = h^{l\to r} + h^{r\to l} \\ M^r\ddot{U}^r + D^r\dot{U}^r + K^rU^r = h^{l\to r} + h^{\text{HFCWO}} \end{cases}$$

if considering the ribs and the lungs regions and their interacting forces h. The deformation of the rib is represented by the ^{r} index and the one of the lungs by the ^{l} index. The right arrow in index represents the interacting forces and the $^{\text{HFCWO}}$ index expresses the action of the HFCWO therapy, as an example.

As a first study, one could consider an idealized 2D model of the thoraco-pulmonary region mimicking cuts as shown on figure 4.1. The different physical layers of the thorax could be defined from the Lamé parameters and the volumetric density. The tissue areas (the A_i in our model) submitted to the pressures of the tree region should be defined from the sub-domain mimicking the interior of the lungs only (see 4.1). From both horizontal and vertical cuts, positions of the pressures on the external surface could be tested measuring the induced airflow at mouth as a first try, with similar purposes as in the chapter 3. By extension, idealized 3D model of the thoraco-region could be studied. Ultimately, 3D geometry of the thoraco-pulmonary model could be used which is discussed in the subsection 4.3.1.

4.2.3 To an enhanced model of the mucus

The model of the mucus used in the chapter 3 is based on several assumptions. We propose here ways to improve these assumptions to reach a better estimation of the stress felt by the mucus during HFCWO manipulations.

For the computation of the stress due to the air-mucus interaction in the airways, we consider low flows and neglect the inertial effects. In order to compute the stress arising from the vibration of the airways wall, we relate the change of their radius with the transmural pressure in the airways. However, we do not account for the spatial occupation of the airways. Hence the pressure in the airways tissue is estimated for all generations of the tree only from the tissue pressures induced by the deformation of the regions of the lung's parenchyma that feed the terminal bronchi of the tree. Additionally, we do not consider neither the spatial occupation of the mucus inside the airways nor its displacement through the tree.

Ways to estimate those stresses have been studied in the literature. First of all, as discussed in the subsection 4.2.1, one could consider different approaches to mimic the flows of air in the airways. Typically, for example, we could consider either the effects of symmetric bifurcations on the flow of air [104], or the effects of asymmetric branching [16], see the subsection 4.2.1. Then, as in [125], we could consider that the airways are not rigid. For that, the authors of [125] use the static relationship proposed by [72] that relates the surface area of the airways lumen and the transmural pressure they are submitted to for the seventeen generations of the tree. The radii of the airways change according to their transmural pressure. This relationship is based on experimental data, hence, in [72] estimations of the lengths and radii of the airways at functional residual volume (FRC) are proposed. Realistic data for the airways could be also interesting for our purposes. The pressure-surface area relation of [72] could be included in our model for estimating the mucus stress by computing the transmural pressure in the airways from the deformation of the lung's parenchyma, as detailed in the subsection 3.3.1. The relationships of [72] is also used in [84] where the authors develop a quasi-static model to study the behaviors of the lungs and of the mucus during Chest Physiotherapy (CP). While [125] do not, the authors of [84] consider also the mechanics of the airways from the volume–pressure relationship of [2]. Moreover, they model the spatial occupation and the mechanics of the mucus in the airways and its displacement through the generations. However, they consider only the stress coming from the air-mucus interaction. Nevertheless, this consideration is interesting for our purpose and could be adapted. Further studies are necessary.

With the improvements proposed above, the unidimensional model of the lung's parenchyma could already produce better estimations of the stress felt by the mucus. However, considering

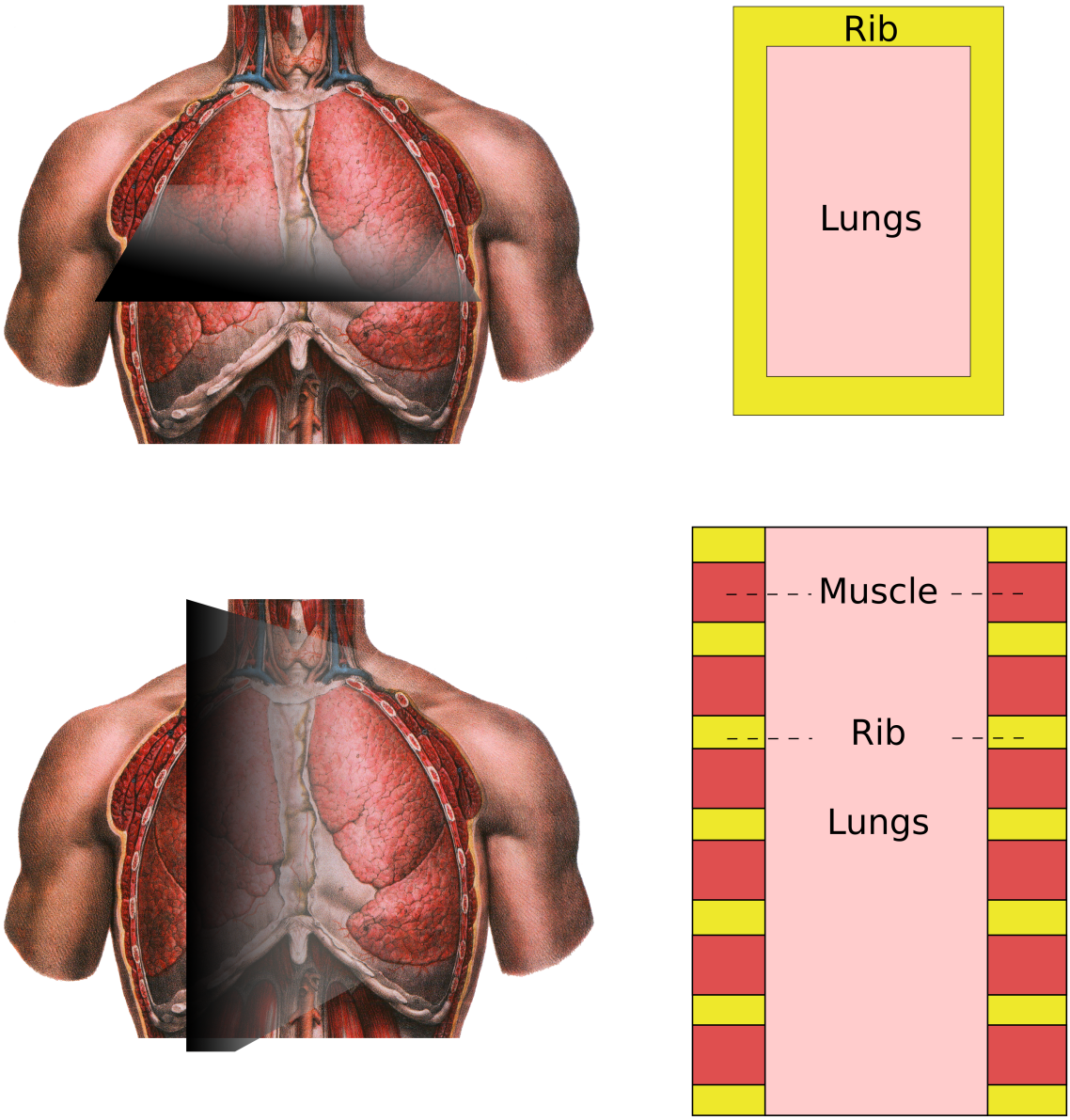

Figure 4.1: **Top:** Schematic of a horizontal cut-view of the thorax (left) with an idealized associated geometry (right). **Bottom:** Schematic of a vertical cut-view of the thorax (left) with an idealized associated geometry (right). The black-shaded surfaces expresses the cut-view.

3D geometry of the lungs could bring far better predictions. Three dimensional geometry of the bronchial tree brings realistic estimation of the size of the airways which is different to each individual. Moreover, being able to locate the bronchial tree in the lungs volume could allow to estimate properly the difference in tissue pressures along the tree. Additionally, the shape of the different regions corresponding to the terminal bronchi of our tree would be more realistic. That would allow a better estimation of the pressure inside and outside the airways.

4.3 Towards the modeling of the lungs with 3D geometries

In the previous chapters, we have tested and validated our model with the unidimensional formulation and idealized geometry of the lungs. These results can be only discussed in a qualitative and comparative way. In order to reach more quantitative results, still in the limits of the model, the use of 3D geometry of the lungs is necessary. In this section, we propose ways to obtain 3D geometry of the lungs (subsection 4.3.1), to solve our model with 3D geometry

(subsection 4.3.2) and to optimize the resolution of the numerical method (subsection 4.3.3).

4.3.1 Three dimensional geometries of the lungs

One relevant way to assess 3D lungs geometry is medical imaging associated to segmentation techniques[1]. Nevertheless, as of today, the use of medical imaging and segmentation techniques does not allow to reproduce entirely the spatial geometry of the lungs [38, 118]. Typically, CT-scan (Computerized Tomography scan) or HRCT-scan (High Resolution Computerized Tomography scan) reach spatial precision of around respectively few millimeters and few tenth of millimeters [57, 36, 109]. Hence, generally, segmentation techniques allow to detect the first 5 or 6 generations of the pulmonary tree only [38, 76]. Consequently, the 3D geometries provided by medical imaging, can be segmented into two parts : the first generations of the bronchial tree (from the trachea to the generations 5 or 6) and the lung parenchyma (the remaining volume of the lungs). For example, in figure 4.2, from a CT-scan and using the segmentation software ITK-SNAP [54, 141], we display those two geometries. Consequently, we can either work with those geometries at this scale as in [140, 118, 129], or we can use algorithms to generate idealized tree geometries as in [64, 131]. Specifically, the algorithm proposed in [64] allows to generate an idealized bronchial tree from trachea to terminal bronchioles that homogeneously fills all the space inside a given lungs geometry. It is based on several deterministic rules. It would appear that the algorithm of [64] is quite sensitive to geometrical changes and produces more asymmetry than in reality [131]. In the tree generating algorithm proposed in [131], the rules seem more adapted to reproduce realistic airways dimension, see figure 4.3 (left).

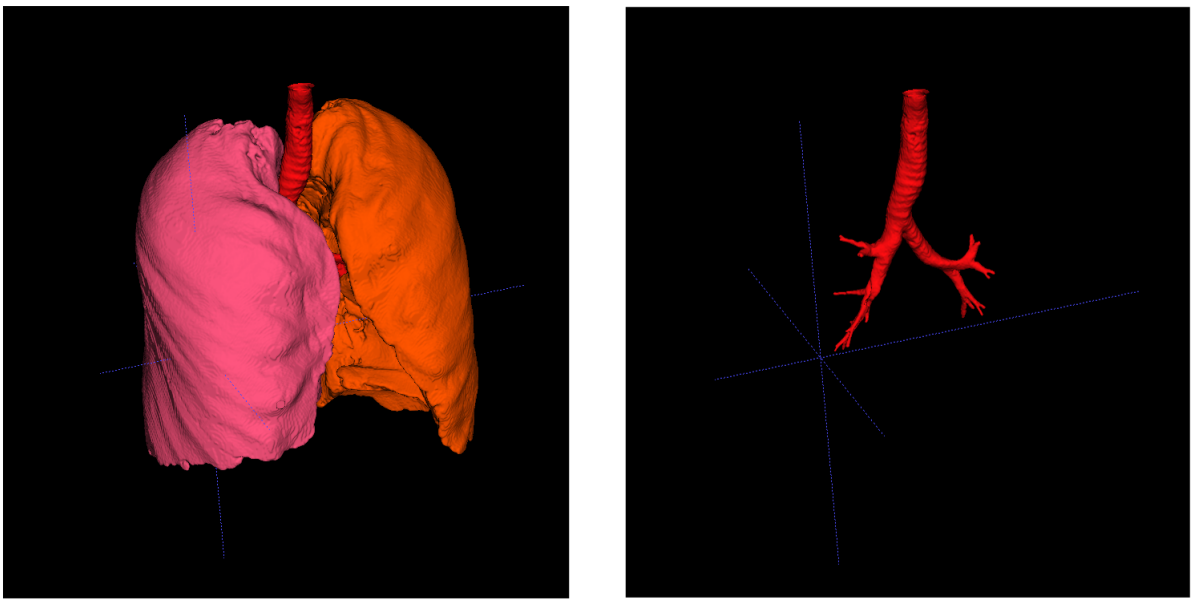

Figure 4.2: **Left:** Geometries of the lung's parenchyma with the first generations of the tracheobronchial tree (red). The colors correspond to the right (pink) and left (orange) lungs. **Right:** Geometry of the first generations of the bronchial tree (around 4 and 5). Geometries are constructed from CT-scan images with the segmentation software ITK-SNAP [54, 141].

Then, the two 3D geometries, i.e the first generations of the bronchial and the lung parenchyma, can be coupled. In [109], the pulmonary tree is modeled using the coupling between the HRCT-scan of the first generations of the tree and the tree generating algorithm proposed in [131]. The results is illustrated in figure 4.3 (right). Then, the lung parenchyma is segmented into several regions fed by the terminal bronchi of the tree. Hence, in the same spirit as [109], as with our 1D model displayed in the previous chapters, we can relate the dissipation of the bronchial tree to the deformation of the lung's parenchyma with 3D geometries. Additionally, as in the previous

[1]Segmentation techniques consist in dividing and dissociating several specific areas of an image.

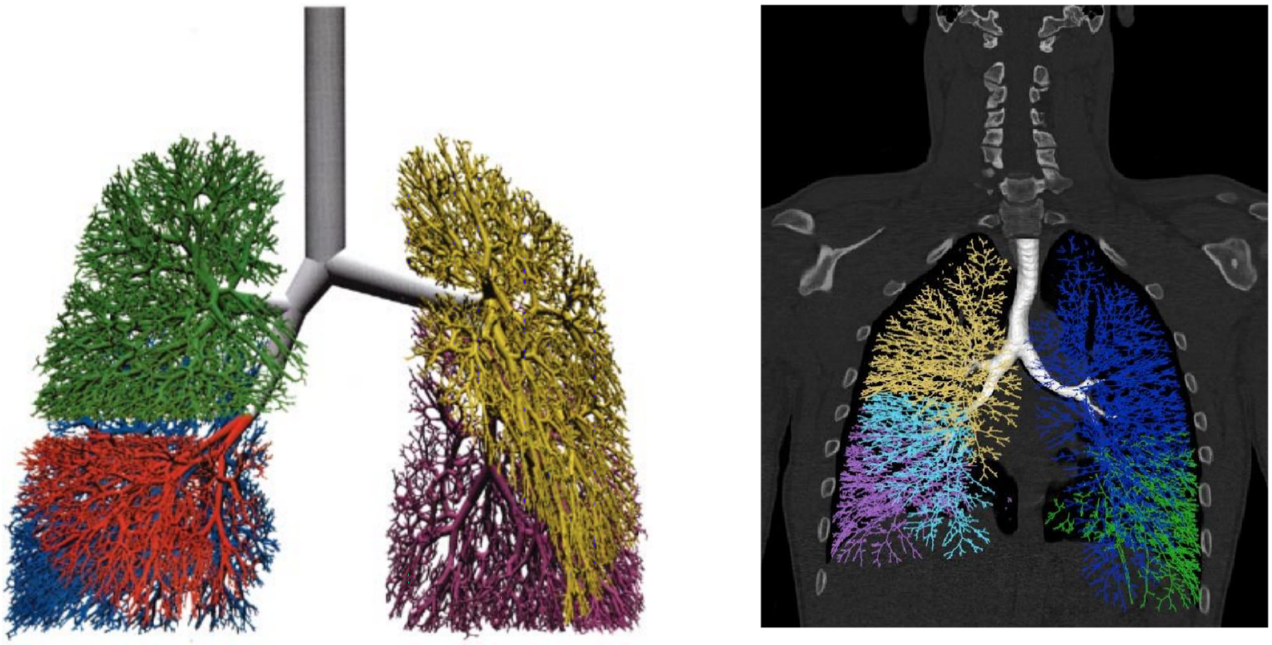

Figure 4.3: **Left:** Idealized geometry of the tracheo-bronchial tree generated by a tree generation algorithm. The colors correspond to the different lobes of the lungs where the airways are contained. Taken from [131]. **Right:** Geometry of the tracheo-bronchial tree coupling HRCT-scan images (white region) and tree generation algorithm (colored regions). Taken from [109].

chapters, virtual sub-trees can be added to the terminal branches in order to get a more realistic resistance for the lungs.

Finally, in the aim of applying our model in such 3D geometry of the lungs, the geometry has to be meshed. Generating a mesh from a geometry allows to transform a continuous domain into a discrete one in order to be used by numerical method such as the finite element method. Different mesh generator are available such as Gmsh [33] or *snappyHexMesh* proposed by the software OpenFOAM [101].

4.3.2 Solving the 3D model using the finite element library deal.II

The application of the model proposed in the chapter 2 in a multi-dimensional framework is under process. We implement a dimension-independent resolution of the system of equations using the finite element method (FEM) with the finite element library deal.II [5, 6]. The numerical results computed with deal.II have been validated in one dimension by comparing the results from deal.II with those presented in the previous chapters. For multi-dimensional cases, the calculated results have not been validated yet. Nevertheless, as a perspective, we will present the approach.

4.3.2.1 Quick presentation of the library deal.II

The library deal.II is a C++ [53] open-source software designed for programming finite element codes. It provides tools for each step in the FEM method, except for the mesh generation of complex geometries. The documentation offers a wealth of information and goes along with more than 75 tutorials and 70 video lectures.

4.3.2.2 Multi-dimensional formulation

The three-dimensional equation of the model is described in the chapter 2 as well as the application of the finite element (subsection 2.2.4). We recall here only the main equations.

The deformation of the lung's tissue at time t and at position $x \in \mathbb{R}^3$, 3 the spatial dimension, is given by $u(x,t) \in \mathbb{R}^m$. For any proper smooth function $w : \Omega \to \mathbb{R}^m$, the weak formulation of our model is

$$\int_\Omega \left(\rho \frac{\partial^2 u}{\partial t^2} w + \sigma_{elastic}(u) : \epsilon w \right) dx - \int_{\Gamma_1} \tau.\ w\ dS - \sum_{i=1}^{N} p_i(\mathcal{F}[\dot{u}]) \int_{A_i} \operatorname{div}(w)\, dx = 0 \tag{4.1}$$

As displayed in the chapter 2, the continuous equation (4.1) is turned discrete by using the finite element method. Consequently, the equation (4.1) is written as a linear matrix-vector equation :

$$M \frac{d^2}{dt^2} U(t) \ + \ D \frac{dU(t)}{dt} \ + \ KU(t) \ = \ \tau(t) h \tag{4.2}$$

The matrix M and K stand for the mass and the stiffness matrix. The matrix D is the damping matrix arising from the coupling with the tree structure. It is defined as $D =^t G\mathcal{R}G$ whose coefficients are defined above. The vector h is the vector of loads. With $x \in \mathbb{R}^3$, those objects are defined as

$$\begin{cases} M_{kl} = \int_\Omega \rho \phi_k(x) \phi_l(x) dx \\ K_{kl} = \int_\Omega \sigma_{elastic}(\phi_k(x)) : \epsilon(\phi_l(x)) dx \\ h_l = \int_\Omega \phi_l(x) dx \\ G_{ik} = \int_{A_i} \operatorname{div}(\phi_k) dx \end{cases} \tag{4.3}$$

with $\epsilon(u) = \frac{1}{2}\left(\nabla u + {}^t\nabla u\right)$ the strain tensor. More specifically, the components of the stiffness matrix are computed as

$$K_{kl} = \int_\Omega \left[\lambda\ \operatorname{div}(\phi_k(x)) \operatorname{div}(\phi_l(x)) + \mu\ \epsilon(\phi_k(x)) : \epsilon(\phi_l(x)) \right] dx$$

4.3.2.3 Numerical scheme

In order to solve the linear system (4.2), we need to use a numerical scheme to discretize the time. To apply the time stepping scheme, we reduce the time derivative order of the equation. Typically we set

$$v(x,t) = \frac{\partial u(x,t)}{\partial t}$$

Its variational form, for any smooth test function $w : \Omega \to \mathbb{R}^m$ is

$$\int_\Omega v w dx = \int_\Omega \frac{\partial u(x,t)}{\partial t} w dx$$

Using the finite element method, the previous equation becomes

$$M \frac{dU}{dt} - MV = 0$$

Finally, as the mass matrix is invertible, we have

$$\frac{dU}{dt} - V = 0$$

The linear system to solve is then

$$\begin{cases} \frac{dU}{dt} - V = 0 \\ M\frac{dV}{dt} = -D\frac{dU(t)}{dt} - KU(t) + \tau(t)h \end{cases} \tag{4.4}$$

In the second equation of (4.4), we keep the term $\frac{dU(t)}{dt}$ instead of V to facilitate the resolution of the system, see below.

We use the Crank-Nicholson numerical scheme to discretize the time with $(t_i)_{0 \leqslant i \leqslant n_t}$, $t_i = i \times \delta t$. Using the subscript ^{n} to denote the time step, and applying the Crank-Nicholson scheme with the θ leads to write (4.4) as

$$\begin{cases} \frac{U^n - U^{n-1}}{\delta t} - \theta V^n - (1-\theta)V^{n-1} = 0 \\ M\frac{V^n - V^{n-1}}{\delta t} = -D\frac{U^n - U^{n-1}}{\delta t} - K\theta U^n - K(1-\theta)U^n + \theta\tau^n h + (1-\theta)\tau^{n-1}h \end{cases} \tag{4.5}$$

In order to cancel the term V^n in the first line of (4.5), we add the second line multiplied by $\delta t\theta$ to the first line. It leads to

$$\begin{cases} U^n(M + \delta t^2\theta^2 K + \delta t\theta D) = U^{n-1}(M + \delta t^2\theta(1-\theta)K + \delta t\theta D) + \delta t M V^{n-1} + \delta t^2\theta^2\tau^n h + \delta t^2\theta(1-\theta)\tau^{n-1}h \\ MV^n = U^n(-\delta t\theta K - D) + U^{n-1}(D - \delta t(1-\theta)K) + MV^{n-1} + \delta t\theta\tau^n h + \delta t(1-\theta)\tau^{n-1} \end{cases} \tag{4.6}$$

The system (4.6) is then solved using the deal.II library. A quick explanation of how it is implemented in deal.II is given in the following subsection.

4.3.2.4 Overview of the implementation of the finite element method in deal.II

The resolution of the equations governing our multi-D model of the lungs has been tested for idealized geometry of the lung's tissue only, typically a square and a cube. The validation of the implementation has been validated in 1D only and is in progress for the multi-D. We will detail the main steps of the implementation using the library deal.II. The following explanation is inspired from the steps of the deal.II documentation [6, 5].

The first step consists in either importing a meshed geometry or creating a geometry and meshing it with the desired number of cells. Then, in order to associate the number of degrees of freedom (DoF, i.e. the spatial position where the solution will be expressed) to the cells, we need to choose the type of finite element. For example, if we use 1^{st} order elements, the degrees of freedom will be associated to the nodes of the mesh. For higher order elements, the degrees of freedom can be associated also to faces, edges, etc. Once the geometry is meshed in deal.II, we need to prepare the matrices before they evaluate the integrals of the shape functions depending on the weak formulation. Typically, as the matrices are frequently sparse, it consists in locating the non-zero coefficients in the matrices. We can then assemble the matrices and evaluate their elements. Then, we create a loop over the cells and over the DoFs of the cells. We evaluate the value of the specific integral of shapes functions for one cell. Then we add the contribution of this cell in the global matrices. Once the loop is finished, we apply the homogeneous boundaries conditions. The linear matrix-vector equation is then solved using a solver among the range of solvers in deal.II.

4.3.3 The splitting method

This section has been investigated in collaboration with Bernard Rousselet, emerita professor, Université Côte d'Azur, CNRS, LJAD.

The coupling between the elastic material and the tree structure involves a non-usual differential operator. As we have seen in the previous chapters, the effect of the dissipation of the tree on the elastic deformation is non-local. Then, in the finite element framework, the damping of the tree is represented by the matrix $D = {}^tG\mathcal{R}G$ applied to the velocity. The matrix $\mathcal{R}$ is the resistance matrix [25] of the considered tree and contains the resistances of paths and subpaths from the trachea to the terminal branches. The matrix G is the operator that computes the air flow with $G_{ik} = \int_{A_i} \mathrm{div}(\phi_k)dx$. Hence, in the finite element framework, the matrix D has a specific matrix patterns which is different from the usual ones appearing in the mass or stiffness matrices. While the mass and stiffness matrices are sparse, the damping matrix D is not. Numerically, it induces higher computational time when solving the matrix-vector system. Moreover, if one would consider inertial effects for the first generations of the tree, the matrix D has to be reconstructed at each time step during the numerical resolution, as performed in [109]. Hence, in the aim of studying complex 3D geometries of the lungs with sufficient numerical precision, finding a way to optimize the calculation time is important.

In [109], to reduce time calculation due to the consideration of inertial effects, they decompose the product $D\dot{U}$ into three distinct products. That results in smaller computational time. In our case, we do not take the inertial effects into account yet. However, in order to reduce the calculation time, we used a method easily adaptable. In that sense, in the spirit of "divide and conquer" [46], the approach of the splitting method is well adapted.

The method of splitting is a method that allows to simplify the resolution of Ordinary and Partial Differential Equations (ODEs and PDEs) by dividing the ODE or PDE into a system of ODEs and PDEs [46]. Specifically, each equation of the system takes into consideration only one or several differential operators. Then, the equations are linked together using specific conditions on the discretization step, see above.

The splitting method is also named *operator splitting*, *dimensional splitting* or also *fractional step*. It was mainly introduced in the early 1950s but since 1990s, with the technological progress, the method is now recognized as an important numerical tool. The splitting method has been applied on several fields with typical ODEs or PDEs, see [90] for more details.

The splitting method has several advantages. Sometimes, some complex equations exhibit different behaviors which do not work at the same scale. For example, it could be used to couple the spatial deformation of the trachea with the one of an alveolus, which do not have the same order of magnitude in size. Another application could be to link the human ventilation with the high frequency pressure induce by HFCWO, which do not work at the same time scale. Hence, the coupled equations would deal with operators which are not defined at the same scale. The splitting method allows to consider the different operators influences while solving a set of different equations. This splitting also allows to work with different solving algorithm or stepping scheme, adapted to each equation. Consequently, it can reduce the numerical calculation memory, favours multi-processing, and improve the stability of the scheme [46]. However, the implementation of the method is not straightforward. The choice in the operator splitting and numerical scheme has to be thoroughly studied carefully to satisfy efficient numerical resolution. Moreover, it can be less efficient if the operators are common.

Our implementation of the splitting method is not validated yet. However, we can already give some indications on its implementation and present potential applications for the model of the lungs. Before discussing the implementation of the method in our case (subsection 4.3.3.1), we present the method from a general perspective (subsection 4.3.3.2). Then, we propose some numerical results in subsection 4.3.3.3.

4.3.3.1 The splitting method

This subsection is inspired from [90, 46, 34]. Let's consider the following Cauchy problem, with $U,\ U_0 \in \mathbb{R}^n$, A and B two $n \times n$ matrix operators and $\dot{U} = dU/dt$:

$$\dot{U} = (A + B)U, \qquad U(0) = U_0 \tag{4.7}$$

whose typical solution is

$$U = e^{(A+B)t}U_0$$

For large matrices and specific operators, it may be more efficient to solve the differential equation with one matrix at a time. Namely, conceptually, it would be easier to compute, with $\Delta t > 0$ the time step and $U^n = U(n\Delta t) = U(t^n)$,

$$U^{n+1/2} = e^{\Delta tA}U^n$$

and

$$U^{n+1} = e^{\Delta tB}U^{n+1/2} \equiv e^{\Delta tB}e^{\Delta tA}U^n$$

This is an aproximation particularly due to the Lie product formula, which states that $\lim_{n\to\infty}\left(e^{A\frac{t}{n}}e^{B\frac{t}{n}}\right)^n = e^{(A+B)t}$. It is equivalent to solve iteratively in $[t^n, t^{n+1}]$

$$\begin{cases} \dot{U}_a - AU_a = 0 \\ U_a(n\Delta t) = U^n \end{cases} \tag{4.8}$$

$$\begin{cases} \dot{U}_b - BU_b = 0 \\ U_b(t^n) = U^{n+1/2} \end{cases} \tag{4.9}$$

by setting $U^{n+1/2} = U_a(t^{n+1})$. And finally, the solution at time $(n+1)\Delta t$ is $U^{n+1} = U_b(t^{n+1})$.

Since the equation (4.7) can be approximated by the iterative resolution of equations (4.8) and (4.9) with specific stepping conditions, the method encourages the use of adapted algorithms and it can reduce the numerical calculation time. However, the method does not provide neither the numerical algorithms nor the way the splitted equations are coupled ($u^{n+1/2}$ and u^{n+1}).

4.3.3.2 The splitting method for the model of the lungs

Our model of the lungs couples the deformations of an elastic material with the dissipation of air in a tree structure. In the finite element framework, two specific differential operators act for that purpose : the stiffness matrix and the damping matrix. The stiffness matrix is common. However, as discussed above, the damping matrix has a specific pattern. It is then quite natural to use the splitting method to decompose the equations based on those two operators in our model of the lungs. In the continuous formulation, it amounts to separate the two terms in the stress–strain relationship :

$$\sigma(u, \mathcal{F}[\dot{u}]) = \underbrace{\lambda \mathrm{Tr}(\epsilon(\mathrm{u}))\mathrm{I} + 2\mu\epsilon(\mathrm{u})}_{\sigma_{elastic}(u)} \underbrace{-p_{tree}(\mathcal{F}[\dot{u}])I}_{\sigma_{tree}(\dot{u})}$$

The following equations are a proposition for the use of the splitting method. The validation of this approach in terms of numerical computation and stability, is in process.

From the continuous weak formulation

The equation of the model will be solved using the Crank-Nicolson scheme in the discrete form of the finite element method. Hence, we use the weak formulation and we set $\partial u(x,t)/\partial t = v(x,t)$. We recall that the deformation of the lung's tissue at time t and at position $x \in \mathbb{R}^m$, m the spatial dimension, is given by $u(x,t) \in \mathbb{R}^m$. Then, we recall that the biomechanics of the tissue in our model is ruled by the following system of equations : for any proper smooth function $w : \Omega \to \mathbb{R}^m$ which cancels in Γ_2,

$$\int_\Omega \left(\rho \frac{\partial^2 u}{\partial t^2} w + \sigma_{elastic}(u) : \epsilon w \right) dx - \int_{\Gamma_1} \tau.\ w\ dS - \sum_{i=1}^{N} p_i(\mathcal{F}[\dot{u}]) \int_{A_i} \mathrm{div}\,(w)\, dx = 0 \tag{4.10}$$

with Γ_1 and Γ_2 the parts of the boundary of the domain Ω where the Neumann and the Dirichlet condition are applied respectively.

To split (4.10) in the spirit of the splitting method, we set the two couples of stepping unknowns $\Theta = [\theta, \chi]^T$ and $Z = [y, z]^T$ with $\chi = \partial\theta/\partial t$ and $z = \partial y/\partial t$; $\theta, \chi, y, z \in \mathbb{R}^m$. Consequently, equation (4.10) can be solved alternatively with

$$\begin{cases} \int_\Omega \rho \frac{\partial \theta}{\partial t} w dx = \int_\Omega \chi w dx \\ \int_\Omega \frac{\partial \chi}{\partial t} w dx = -\int_\Omega \sigma_{elastic}(\theta) : \epsilon(w) dx + \int_{\Gamma_1} \sigma(u).n w dx \\ \theta(x,0) = u(x,0) \\ \chi(x,0) = v(x,0) \end{cases} \tag{4.11}$$

$$\begin{cases} \int_\Omega \frac{\partial y}{\partial t} w dx = 0 \\ \int_\Omega \frac{\partial z}{\partial t} w dx = -\sum_{i=1}^{N} p_i(\mathcal{F}[\dot{u}]) \int_{A_i} \mathrm{div}\,(w)\, dx \\ y(x,0) = \theta(x, \Delta t) \\ z(x,0) = \chi(x, \Delta t) \end{cases} \tag{4.12}$$

for a small time increment Δt. For this increment Δt, the solutions are $y(x, \Delta t)$ and $z(x, \Delta t)$. Then, the systems are solved successively for all time step. Finally, the solution u of the equation (4.10) at a time t is $y(x,t)$.

From the finite element discret formulation

The splitted equations presented above in the continuous formulation, are discretized into the following equations in the finite element framework (see (4.4)) :

$$\begin{cases} \frac{dU}{dt} - V = 0 \\ M \frac{dV}{dt} = -D \frac{dU}{dt} - KU + \tau h \end{cases} \tag{4.13}$$

or

$$\frac{d\mathcal{U}}{dt} = \mathcal{A}\mathcal{U} + H$$

with

$$\mathcal{U} = [U, V]^T, H = [0, \tau h]^T \text{ and } \mathcal{A} = \begin{pmatrix} 0, 1 \\ -M^{-1}K, -M^{-1}D \end{pmatrix} \tag{4.14}$$

We can split the matrix $\mathcal{A}$ into two matrices as $\mathcal{A} = \mathcal{A}_1 + \mathcal{A}_2$ with

$$\mathcal{A}_1 = \begin{pmatrix} 0, 1 \\ -M^{-1}K, 0 \end{pmatrix} \text{ and } \mathcal{A}_2 = \begin{pmatrix} 0, 0 \\ 0, -M^{-1}D \end{pmatrix} \tag{4.15}$$

With the vector functions $\Theta = [\theta, \chi]^T, Z = [y, z]^T$, we solve successively with Δt a small time increment

$$\frac{d\Theta}{dt} = \mathcal{A}_1\Theta + H \tag{4.16}$$

and

$$\frac{dZ}{dt} = \mathcal{A}_2 Z \tag{4.17}$$

The system (4.16) takes into account the elastic deformation of the material and the system (4.17) the dissipation of the tree. The initial conditions are $\Theta(0) = U(0)$ and $Z(0) = \Theta(\Delta t)$. Then for a given time $t^n = n\Delta t$, the stepping time conditions are $\Theta(n\Delta t) = Z(n\Delta t)$ and $Z(n\Delta t) = \Theta((n+1)\Delta t)$.

4.3.3.3 Some preliminary feedback on the use of the splitting method

We implement the splitting method in the library deal.II [6] using the discrete formulation described above. We use the Crank-Nicolson scheme to discretize the time for both the equation of the elasticity (4.16) and the equations for the damping of the tree (4.17). In future works we would like to study which scheme is the best adapted for each resolution. For example, we suggest that an explicit scheme (semi-implicit Euler scheme) would be more adapted, in terms of reducing the time calculation, to solve the system that rules the elastic deformation.

Although the implementation of the resolution of the multi-D model has not been validated yet, using the splitting method described above leads to the same results as the ones by solving directly the original system (4.4). We gather in the following table the calculation times for 2D and 3D numerical simulations for different spatial and time precisions. In 2D, the geometry is a square with a side length of 2. In 3D, we consider a cube with the same side length. We consider a 9 generations tree feeding 64 areas in the elastic medium. The Lamé parameters, the density, the amplitude and the frequency of the applied pressure and the final time of the simulations are set to 1. For the 2D simulations, we apply a zero displacement condition at one side of the square and the Neumann boundary condition τ at the opposite side of the square. We apply the same strategy for the 3D simulations. Zero displacement is applied at one face of the cube and the Neumann boundary condition τ is applied to the opposite face. The Neumann boundary condition is set to $\tau = sin(2\pi t)$. The parameter of the Crank-Nicolson scheme is set to $\theta = 1/2$. In that way, the scheme is second order accurate and conserve energy in the solution. We use the conjugate gradient solver with no preconditioner. We do not compare the efficiency of different preconditioners or solvers. In our case, the conjugate gradient solver with no preconditioner works and allows us to make comparative results. The numerical simulations are performed with a Intel® Core™ i7-8650U CPU@1.90 GHz × 8 processors. The computations are performed with one processor only.

From the table 4.1, we suggest that the use of the splitting method could be interesting in reducing calculation time. For both two and three dimensions, for a same parameters configuration, the splitting method needs about half the time than with the original method. The results are proposed in the limits of the validation of the computing implementation. Further investigations are required.

	Number of degrees of freedom	Time step Δt (s)	**Calculation time (s)**	
			Original system	Splitting system
2D	2178	0.1	11.44	6.31
	8450	0.05	240.15	92.28
3D	2187	0.1	18.25	12.22
	14739	0.05	1105.29	465.10

Table 4.1: Computation times comparison between the original resolution and the solving using the splitting method for different spatial and time discretizations.

4.4 Investigation of the efficiency of a HFCWO device through a clinical study

This section has been worked in collaboration with Valentin Mons, PhD student, Université Côte d'Azur, LJAD, LAMHESS.

The chapter 3 shows that a change in lungs mechanical parameters induces a more or less significant change in lungs deformation and in the induced airflow inside the pulmonary tree. Particularly, we suggest that it might exist an optimal stimulating frequency that can maximize lungs deformation and/or induced airflows in the tree. This frequency is related to the fundamental natural frequency of the lungs and to the intensity of the dissipative action of the tree. We propose a mathematical formula to compute natural frequencies of the lungs that depends on the characteristic stiffness, density and size of the lungs. The HFCWO technique applies pressures on the patient's chest to stimulate lungs deformation. Its efficiency is only modulated by the intensity and the frequency of those pressures which are empirically chosen parameters. Consequently, finding the natural frequencies of the lungs could be an interesting tool for the determination of the operating parameters of HFCWO.

In this section, we introduce the setup of a clinical study that aims at helping to determine of HFCWO operating parameters. Specifically, the study examines if some frequencies and/or intensity levels could be optimal for HFCWO.

Several studies investigate the efficiency of the technique by comparing with other airway clearance techniques [95, 96, 35]. They measure various indicators such as pulmonary function (FVC, FEV_1 or PEF[2]), mucus sputum expectoration or quality of life score. To the best of our knowledge, only a few take an interest on studying the influence of the values of the HFCWO operating parameters. In [61], the authors investigate the impact of three types of combination of intensity–frequency pressure on the quantity of expectorated mucus with a High Frequency Chest Wall Compression (HFCWC) device. The study is performed on 16 young adults with chronic mucus production. As best as we know, the HFCWC device used in [61] and the HFCWO device that we will study produce comparable therapy. The only difference is that HFCWC applies an added homogeneous pressure on the patient's chest [50]. In [61], the pressures intensity are expressed in the arbitrarily device unit taken from a $1-10$ scale. The evaluated combinations in [61] are : 1) intensity 10 with 8, 9 and 10 Hz frequency ; 2) intensity 6 with 18, 19 and 20 Hz frequency ; 3) intensity 5 with 12 Hz frequency. The conclusions of [61] suggest that the combinations 1) and 2) result in higher quantity of expectorated mucus than the combination 3). The combination 1) and 2) are not compared. Those measures are interesting but, from our perspective, do not seem sufficient to infer which of the intensity or of the frequency has a preponderant impact on the mucus expectoration. The influence of the frequency of the HFCWC pressure is studied in [92] for the same HFCWC device, through a 100 patients study. They

[2]FVC : Forced Vital Capacity, FEV_1 : Forced Expiratory Volume in 1 second, PEF : Peak Expiratory Flow, see [126]

measure the average mouth volume of air moved and the average induced airflow. In [92], the HFCWC device applies pressures with a sine wave-forms as in [61] and as our HFCWO device. The authors of [92] concludes that, on average, with sine wave-form pressures, highest mean volumes and highest mean airflows are measured from frequencies respectively between 6 and 10 Hz and between 13 and 20 Hz. From an other perspective, as the HFCWO technique acts first on the patient's chest, one could also study the response of the chest to HFCWO stimulation. This is actually investigated in [67] with a HFCWC device. However, the name of the device used is not specified but the functions described seem similar to the previous one. Moreover, the operating frequency of this device can range from 0 to 50 Hz, which is not applicable in typical HFCWO devices (usually 1 to 25 Hz) [121, 96]. The authors of [67] measure the acceleration response of the chest versus the force applied on the patient's chest, i.e. they measure the inertance. On average over 21 healthy adults, they find out that the maximal inertance is obtained with a frequency equal to 26 Hz. This frequency could represent the resonance frequency of the chest. They also suggest that, in average, HFCWC device should work in a range of frequencies between 18 and 34 Hz. In parallel, they infer that there is a negative linear correlation between the patient's chest size and the resonance frequency. Typically, the wider the chest size is, the lesser the resonance frequency. This relationship is in accordance with the natural frequencies definition (2.39), inversely proportional to the characteristic size. Indeed, it can be applied to any elastic media, as muscles and bones that compose the chest.

Consequently, it looks like no study investigates the influence of the operating parameters for a HFCWO device. In that way, in this section, we propose a clinical study with some preliminary insights. The HFCWO technique acts on the mobilization of the mucus by submitting two types of stress : from the air flowing along the mucus inside the airways and from the vibrations of the airways wall that deform the mucus. In this clinical study, we focus only on the shear stress arising from the air–mucus interaction. To estimate this influence, we propose to measure the airflow at mouth induced by the HFCWO therapy. In order to eliminate the ventilation, the patient holds her/his breath times to times during the therapy, while keeping her/his glottis aperture open to let air flows in and out. The data would be then post-processed to keep only the times when ventilation is on hold.

The study will be performed in healthy non-smoking young adults. The volume of air will be measured at mouth with a calibrated pneumotachograph (spirometry device). Four configurations of parameters in the intensity–frequency range will be tested. Then, statistical analysis will be performed according to the results. We will focus on significance test as a first approach to compare the efficiency of the different combinations, see next subsection. The protocol of this clinical study has been tested on two individuals. We started to analyze the measurements from one record. The following subsections detail the method and the protocol proposed for this study, as well as the first preliminary insights.

We also propose the use of flexible force sensors to measure the pressure that is applied by the HFCWO device on the patient's chest. The quantity could be related to the scale of the HFCWO device. Moreover, we take the opportunity of this study to measure Maximal Flow Volume Loop (MFVL). Before and after the therapy, maneuvers of MFVL are performed and data acquired. This kind of curve can inform on the ventilatory lungs function [9] and could inform on the effect of a potential bronchodilator (personnal communication with HFCWO manufacturer).

We also propose that, alternatively to significance test, parametric tests could be considered. However, although being more powerful than significance test, they are considered less robust [112]. Parametric tests need an initial assumption on the parameters of the data distribution. As this assumption is quite difficult to determine in our case, we would rather focus on significance tests.

4.4.1 Method and protocol

As stated above, a significance test would be an interesting tool to analyse the data of the study. Before going deeper in the details of the experimentation, we introduce the concept of this statistical test.

Introduction to significance test. A significance test or statistical hypothesis testing is based on the principle of accepting an assumption, called the null hypothesis, or rejecting it in favor of an other assumption, called the alternative hypothesis, based on statistical data [28]. The test is used either to suggest that something interesting is happening (the alternative hypothesis is favored) or to suggest that two assumptions can be considered as similar (hypothesis null accepted). However, such statistical test is subject to errors, and particularly two types of error : the error of type I and of type II. The error of type I occurs if the null hypothesis is rejected whereas it is true. The probability of this error is called the significance level and is denoted α. Usually, it is set to $\alpha = 0.05$, which let 5% of chance to incorrectly reject the null hypothesis. The error of type II occurs when the null hypothesis is accepted whereas it is false. The probability of this error is denoted β and we rather consider the inverse probability $(1 - \beta)$ to specify the power of the test. It is usually set to $1 - \beta = 0.8$, saying that there is 80% of chance that the null hypothesis is correctly rejected. In such test, the power is a significant figure that has to be properly chosen in order to justify the relevance of the results. An other important criteria is the sample size that is discussed in the next paragraph.

Participants criteria. First, subjects are asked to be healthy non-smoker young adults (< 30 years old) who are free of any acute and chronic respiratory disease. Then, as stated above, the required number of participants is an important parameter that has to be justified carefully. As the subjects represent a sample for a global population, a larger numbers of subjects leads to more truthful results. However, clinical researches also have to deal with experimental cost, work time and patient ethic [23, 112]. Consequently, a clinical study generally tends to minimize sample size while maximizing results confidence (power). With significance test, it amounts to examine mainly the significance level (α), the power $(1 - \beta)$ and the standard deviation of the distribution obtained with the data [23]. We will not discuss here how to deal with those quantities for that purpose. A specific study has to be performed in the future and during the clinical trial to propose a justified sample size.

Material. The HFCWO device is called RespIn 11 (RespInnovation SAS, Seillans, France). It is composed of a jacket containing lines of flexible pistons (two at the front and three at the back) and of an electronic device containing a blower which fed with air the pistons through medical tubes, see Figure 4.4. The device controls the frequency and the intensity of the expansion of the pistons. The technology is also called *focused pulses techniques* because it applies pressures on the patient's chest and back only on specific regions, i.e. where the pistons are acting. The ventilation function is measured using a pneumotachograph (model 3813, Hans Rudolph, Kansas, USA). The pneumotachograph is calibrated with a 3L-syringe (model 5530, Hans Rudolph, Kansas, USA) at three varying flow rates for six volumes from $0,5$ L to 3 L. We would like to measure also the force applied by the HFCWO device on the patient's chest. For example, we propose the use of flexible sensor in the range FlexiForce™ (Tekscan Inc., Boston, MA, US). During the whole session, raw flow and volume data were continuously recorded at a sample rate of 4000 Hz using a 16-channel analog-to-digital data acquisition system (Powerlab 16/35, Model XX, ADInstrument, USA) and stored on a lab computer via adapted software (Labchart v.7, ADInstrument).

Spirometry measurement protocol. During the therapy, which lasts 18 minutes, 4 combinations of intensity–frequency in the scope of HFCWO are applied for 4 minutes each. We denote by I the intensity unit of the HFCWO applied pressures, which is expressed in the arbritrarily scale of HFCWO device 1 to 10. The four intensity–frequency combinations are {6 I, 12 Hz}, {10 I, 12 Hz}, {6 I, 20 Hz} and {10 I, 20 Hz}. The four combinations are chosen to get insights on the influences of both the intensity and the frequency of HFCWO pressures. The combinations of parameters have to be randomly chosen. Different experimental designs

Figure 4.4: Mechanical device of chest physiotherapy called RespIn 11 using High Frequency Chest Wall Oscillation technique. It is developed and commercialized by RespInnovation SAS, Seillans, France. **Left:** The jacket called Wrap (blue) with the controller unit (orange and white). **Right:** Line of pistons contained in the Wrap. The front part of the jacket contains two lines and the back part contains three lines. The pictures have been provided by RespInnovation SAS.

exist and have to be studied. For example, we propose the block randomisation method [7]. The method seems convenient to distribute several groups of test, such as our four HFCWO configurations, amongst several patients. For each combination, the participant holds his breath during at least 10 seconds while keeping its glottis aperture open. Before and after the therapy, the participant performs at least 3 maneuvers of Maximal Flow Volume Loop (MFVL). The post-therapy maneuvers should be performed directly after the therapy with a 30 s to 60 s interval between the maneuvers. Before the therapy, the participant gets accustomed to both 'holding breath–open glottis' and MFVL maneuvers, following the experimentators instructions. The sensors of the pneumotachograph can be wet due to the participant ventilation and can disturb the data acquisition. Moreover, even if it is usually not observed for healthy individual (personal communication with HFCWO manufacturer), the participants could need to expectorate during the therapy. Consequently, the therapy does not stop unless the sensors needs to be cleanead or dried or if the participant needs to expectorate.

Data post-processing. Raw data are analysed using the computing environment MATLAB [79]. The volume of air at mouth is computed by the numerical integration of the flow of air signal. Each holding-breath recording is dissociated from the rest of the signal and is studied independently. From the obtained periodic signal, the volume of air ventilated at each cycle of the HFCWO pressures is computed, see the subsection 4.4.2. We can also deduce the frequency of the HFCWO pressures and compare it to the frequency declared by the manufacturer.

4.4.2 Preliminary results

The study protocol has been performed on two individuals. The data post-processing has been realised for one individual. This subsection details the post-processing process and presents the first preliminary results.

Focusing on the holding breath signal

The overall signal of the spirometry session is displayed in the figure 4.5 (left). In the same figure (right), we display a zoom on one of the holding-breath recording (combination {6 I, 20 Hz}). We dissociate the latter from the overall signal in order to analyse the flow of air during a holding-breath maneuver only.

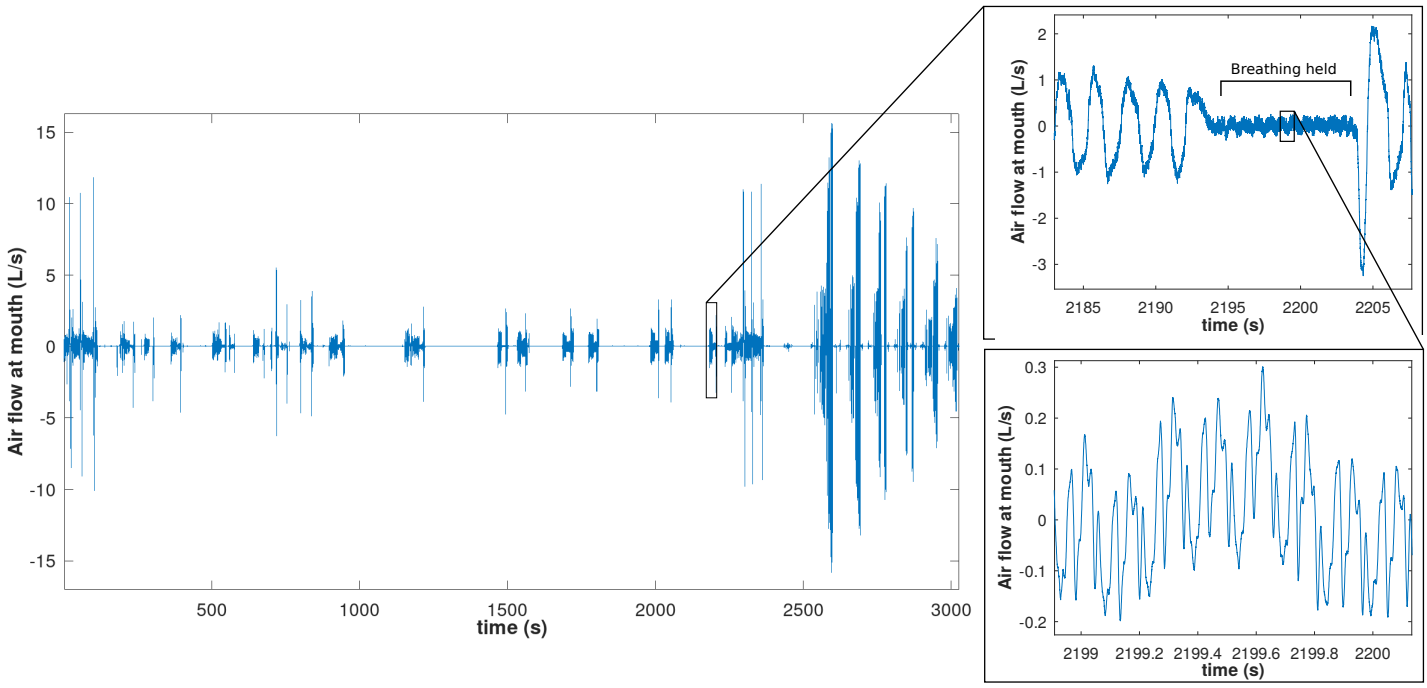

Figure 4.5: **Left:** Overall spirometry signal during the entire protocol. **Right:** Zoom of the signal around (top) and of (bottom) a holding-breath session for the intensity–frequency combination {6 I, 20 Hz}.

Computing the volume of air exchanged during one HFCWO cycle

The volume of air is then computed by integration of the flow. To compute the volume of air exchanged at each cycle, we need to find the local extrema of the volume curve. Then, we consider that the amplitude difference between one local maximum and the next local minimum represents the volume that goes in the lungs. Equivalently, we consider that the amplitude difference between one local minimum and the next local maximum represents the volume of air that goes out of the lungs. The total of those two volumes is the volume exchanged during one cycle of the HFCWO pressure, see figure 4.6 (right).

Correcting the spirometer shift

Due to several factors, such as temperature or humidity, the recorded signal of flow suffers what we called a "shift". Specifically, this shift leads the signal amplitude to continuously increase or decrease little by little during the therapy. In our case, we observe mostly an increasing amplitude pattern. Consequently, the volume integrated from the flow also suffers from this shift, see figure 4.6 (left). Two computing techniques are proposed and compared to correct the shift. Both of the techniques consist in computing a spline of the volume curve and subtracting it to the original volume curve. The first technique computes a spline passing through the local maxima of the original curve. The second technique computes a spline passing through the average value between one local maximum and the next local minimum of the original curve. The volume of air exchanged is then computed from the original curve of the corrected curves. The volumes obtained from the two spline methods are compared with each others and are compared with the volume computed without spline methods. We display in figure 4.7 the splines of the curve of volume. In figure 4.8 are displayed the corrected curves, i.e. curves obtained from subtracting the spline to the original curve.

Data validation

The amplitude of the HFCWO pressures are small and one could doubt on the capability of the pneumotachograph to capture the low signals. For that purpose, two measurements recorded during the HFCWO therapy are compared : one with a closed glottis aperture and one with

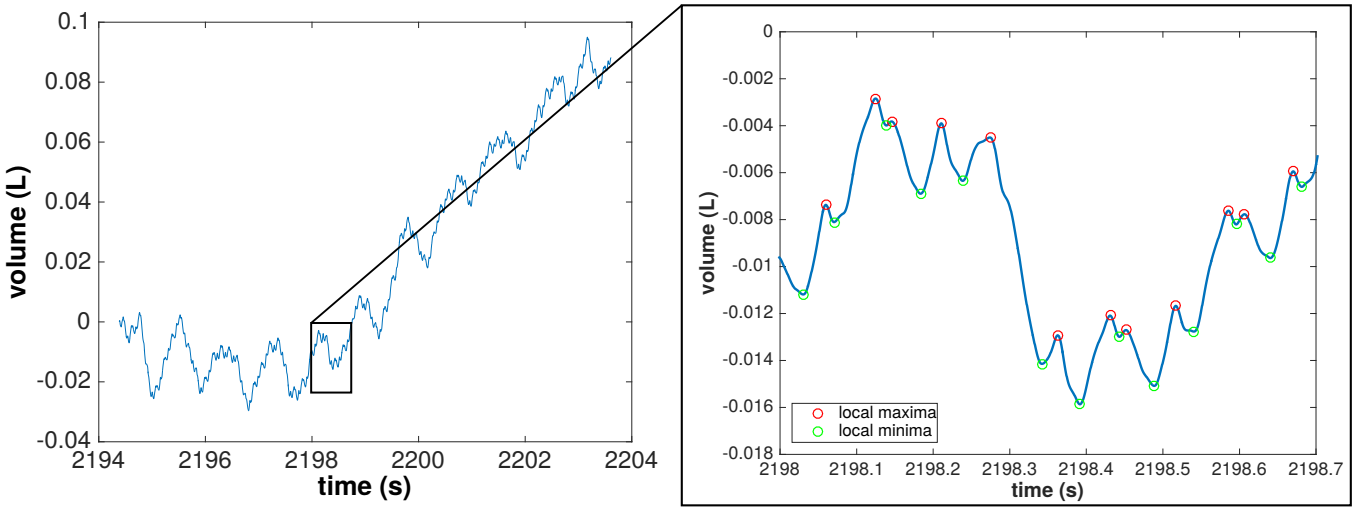

Figure 4.6: **Left:** Volume of air during a holding breath recording. Due to the pneumotacograph sensibility, a "shift" of the amplitude occurs. **Right:** Volume of air during a held breathing recording with local extrema.

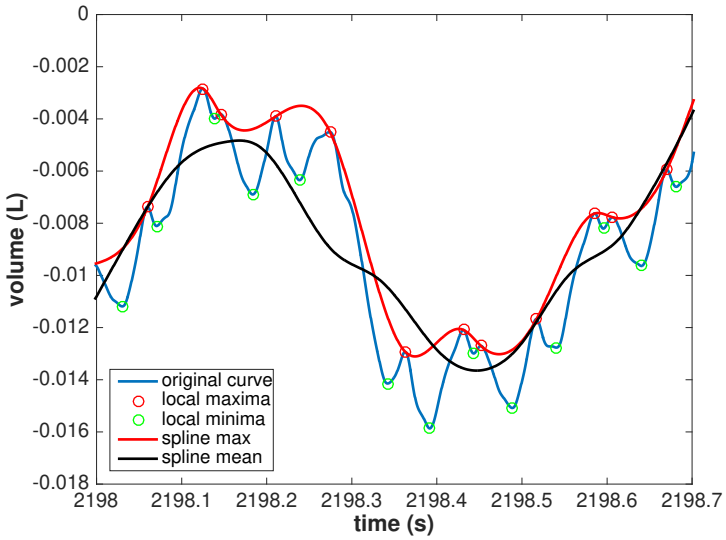

Figure 4.7: Original volume curve with two interpolating splines. One spline (red) goes through the local maxima. The other spline (black) goes through the mean between one local maximum and the next local minimum.

an opened glottis aperture, see figure 4.9. We can distinguish small oscillating airflows with opened glottis aperture. We deduce that the amplitude precision of the pneumotachograph is high enough. Moreover, to verify that the oscillations correspond to HFCWO, we compared the measured frequency with the HFCWO frequency, with and without the correction of the shift, see table 4.2. We computed the frequency from the time period between two consecutive maxima or between two consecutive minima. As those time periods may differ on each consecutive maxima/minima, we computed the average frequency of all the time periods. We also computed the average frequency from the two types of average frequencies obtained (from the maxima and from the minima). For higher frequency (20 Hz) the computed frequency is quite similar to the declared frequency. However, for lower frequency (12 Hz), frequencies differences can be observed. Those differences lead us to verify the actual frequency applied by the HFCWO. For that purpose, we used a 120 images per second camera to record the pressures frequencies delivered by the HFCWO device. We filmed directly the inflatable pistons contained inside the HFCWO jacket. Then, with the video editing software Adobe Premiere Pro® [52], we determined

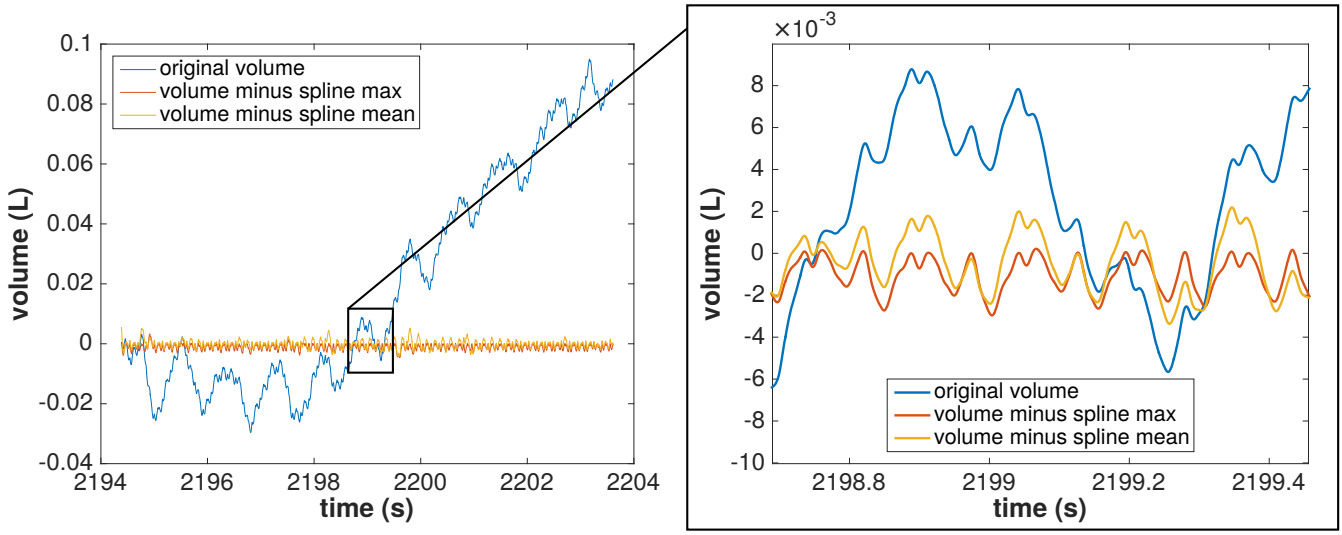

Figure 4.8: **Left:** Original volume curve and two volume curve correcting the shift with the splines method. **Right:** Zoom of the original volume curve and the two volume curve correcting the shift with the splines method. **Note:** The corrected curves are computed by subtracting the spline with the maxima and the spline with the mean between two consecutive extrema to the original volume curve.

the period of the oscillations of the HFCWO pressures. With 120 recorded images per second, the precision of the computed period is $\approx$ 0.01s. We found out that the HFCWO pressure frequencies declared by the manufacturer correspond to the frequencies of the combined lines of the pistons but not of each line of pistons. Typically, when expecting 20 Hz, each line of piston actually applies pressures at frequency $\approx$ 6.5 Hz. However, on the back of the patient, three lines of pistons are acting in a asynchronous way. Hence, at each HFCWO cycle, three pressures are applied successively. Consequently, the actual HFCWO frequency is, in this case, three times the frequency of one line of pistons. For example, when expecting 20 Hz, the HFCWO device applies $3 \times 6.5 = 19.5$ Hz. We verify this for all the frequencies delivered by the HFCWO device and, the same same observation is made. However, the HFCWO device also applies pressures on the patient's chest through two lines of pistons, which are independent from the back pistons. Consequently, the action of the back and front pistons can interfere on the measured frequency. This could explain the difference between the measured frequencies and the one declared by the manufacturer.

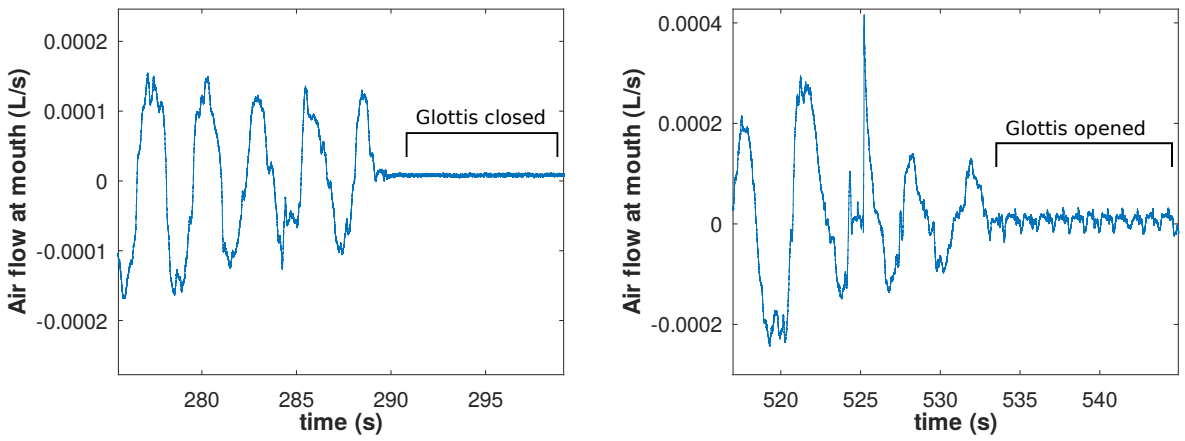

Figure 4.9: **Left:** Holding breath recording while closing the glottis aperture. **Right:** Holding breath recording while opening the glottis aperture.

	Method	Average frequency from the maxima (Hz)	Average frequency from the minima (Hz)	Average frequency from the maxima and the minima (Hz)
6 I, 20 Hz	without spline	22.42	18.79	20.60
	spline max	25.42	20.63	23.03
	spline mean	23.79	19.36	21.58
10 I, 12 Hz	without spline	7.64	8.14	7.89
	spline max	12.04	7.68	9.86
	spline mean	9.54	7.88	8.71

Table 4.2: Comparison of the frequency declared by the HFCWO device and the ones measured by the pneumotachograph and computed by numerical analysis. We computed the frequency from the volume curve without shift correction and with shift correction. The two spline methods correcting the shift are also compared.

Results and comparison

We are interested in computing the volume of air ventilated per cycle of the HFCWO pressures as well as the average air flow. To do so, we calculated the volume of air for each HFCWO cycle during the holding–breath maneuver. Then, we computed the mean between all the volume cycles. The average flow is computed by multiplying the mean volume to the average frequency presented before. We performed the calculation for one individual, with and without the corrections of the shift. We display the results for two combinations of intensity–pressure ({ 6 I, 20 Hz} and {10 I, 12 Hz}). They are gathered in the table 4.3. First, we observe that the average volumes over a HFCWO are quite similar with or without the correction of the shift. Then, from the two intensity–pressure combinations, we can distinguish that the average volumes are higher for higher HFCWO intensity pressures. However, we can not see the influence of the frequency from these two combinations. Moreover, force measurement is needed to determine the intensity unit of the HFCWO device. Additionally, we need to compute those quantities for several subjects in order to have confidence in the results. Further analysis are then required.

	Method	Average volume over a cycle (L)	Average flow ($\frac{L}{s}$)
6 I, 20 Hz	without spline	0.0027	0.055
	spline max	0.0018	0.042
	spline mean	0.0022	0.048
10 I, 12 Hz	without spline	0.015	0.12
	spline max	0.016	0.15
	spline mean	0.015	0.13

Table 4.3: Comparison of the average volume over a HFCWO cycle and the average flow induced by a HFCWO device for different combinations of HFCWO intensity–frequency. The data computed from the corrected volume (with spline method) are also compared to the original volume.

4.4.3 On the perspectives of the clinical study

The study presented in this subsection is only a preliminary insight on the clinical study proposed. The data have not been analyzed for all combinations of HFCWO intensity–pressure and for several participants. However, the way the clinical study should be performed has been prepared and studied. We raised the fundamental elements needed to justify the relevance of the study, such as the statistical power and the participants sample size for example. We propose different ways to post-process the recorded data with a first comparison about their suitability. We suggest the use of a significance test to analyze the data when we would have the record from a sufficient number of subjects. This kind of test can suggest which intensity–pressure combinations is more efficient than the others, with a level of confidence. Moreover, the use of force sensors can also be important to determine the quantity of pressure applied by the HFCWO device. Determining the pressure amplitude is an important step in order to interpret properly the results of our study.

Chapter 5

Conclusion

This thesis proposes, studies and validates a model of the biophysical mechanisms of the lungs. The model goal is to propose new insights for High Frequency Chest Wall Oscillation (HFCWO).

For that purpose, the model, inspired from the literature, is built in the chapter 2. It is based on the coupling between an idealized tree structure mimicking the pulmonary tree and an elastic medium mimicking the lung's parenchyma. The tree is based on 0D assumptions and the equations ruling the elastic material are written for three dimensions. We considered linear isotropic elasticity with small deformations adapted to HFCWO. A numerical method to solve the equations of the model is presented. Regarding the coupling hypotheses, we considered that the deformation of the elastic material feeds the tree with air. Particularly, each one of the terminal branches of the tree is fed by one specific region in the material. As air is viscous, the tree resists to the air flow inside. Hence, the influence of the tree plays the role of a damping on the material deformation. The tree induces dissipative pressures in the material regions connected to its terminal branches and these pressures affect the material deformation. The resulting stress–strain law of the material is that of a viscoelastic material, with a non-local viscous behavior. To study the behaviors of the coupled model, we analyzed the unidimensional formulation of the model. First, we studied the damping influence of the tree on the material deformation in a non-physiological framework. Actually, in our model, we saw that we can compute the natural pulsations of the elastic material in the absence of the influence of the tree. Those pulsations present interesting features for HFCWO as they are related to the resonance. The resonance of a vibrating system occurs when the system is submitted to a force oscillating at the natural pulsations of the system. Then, the motion amplitude of the system amplifies. Consequently, we studied the resonance in non-physiological cases. We observed that the tree structure affects the natural modes of vibration of the material. We linked these behaviors with those of harmonic oscillators, using the energies of the systems. The analysis of the resonance of our coupled model is extended in the chapter 3 in the frame of HFCWO application. The rest of the chapter 2 aimed at validating and calibrating the model to produce numerical estimations compatible with the physiology. Different set of parameters are determined to mimic healthy and non-healthy lungs (asthma, chronic obstructive disease and cystic fibrosis).

The chapter 3 studies the physical influence of the parameters of the unidimensional model in the frame of HFCWO. It proposes a dimensionless formulation that raises two dimensionless parameters. Actually, those parameters are the Euler number and the inverse of the Cauchy number. We also propose a simplification of the coupled model inspired from the harmonic oscillators with one degree of freedom. This brings another dimensionless parameter known as the quality factor (Q-factor). This Q-factor evaluates the influence of the damping of the tree on the material deformation. It allows to predict the existence or absence of resonance in the coupled material. The three dimensionless parameters (Euler, Cauchy and the Q-factor) are used to highlight the model predictions for idealized healthy and non-healthy lungs during the ventilation at rest and during HFCWO. In the limits of the model, the Q-factor indicates that no resonance can occur for the deformation of the coupled material when mimicking the lungs.

However, we saw that, for harmonic oscillators, the velocity of the material deformation is always maximised at the fundamental natural frequency of the material. In our model, the flows of air in the tree arise from the velocity of the material deformation. Hence, we studied the air flows at mouth. From lungs data found in the literature, we showed that the averaged air flows at mouth are maximized at a frequency of around 6.5 Hz. We found out that similar velocity resonance frequencies of the respiratory system have been estimated in the literature from clinical experimentation. Nevertheless, in the limits of the model, we showed that the resistance of non-healthy lungs might be too high to allow any kind of resonance. For pathological lungs with increased resistance, the model predicts that for different frequencies, the air flows at mouth are similar. The chapter 3 also proposes a way to model the stress felt by the mucus inside the tree. This model mimics the stress due to the vibration of the airway wall and the stress due to the air–mucus interaction inside the tree. We show that during HFCWO, the stress arising from the air–mucus interaction is of the same order of magnitude for all generations of the tree. We also show that the stress due to the vibration of the airways wall follows a negative linear pattern as we sink in the tree. Moreover, in our model, for generations deeper than the fourth, this stress becomes smaller than the stress due to the air–mucus interaction. Finally, the chapter 3 proposes in the limits of the model, that HFCWO could be used as a non-invasive tool to assess the resistance and compliance of the lungs.

The results have to be interpreted in the limitations of the model. Our model is based on hypotheses that simplify the complexity of the geometry of the lungs and of its biomechanical behaviors. Ways to improve the model are proposed and discussed in the chapter 4. We propose improvements for the physics of the air flow in the tree, for the geometry of the tree, for the geometry of the lung's parenchyma as well as for the mucus distribution in the airways and for its movement through the generations of the tree. We also propose a splitting method that aims at reducing the computational time for the multi-dimensional numerical resolution of the model. Finally, the chapter 4 also proposes the setup of a clinical study that will investigate the efficiency of a HFCWO device based on our model predictions.

Hence, in the limits of the model hypotheses, this thesis proposes new insights on what happens in the lung during HFCWO using mathematical modelling. This work focus on the core phenomena involved in the lungs during HFCWO to extract and explain characteristic behaviors compatible with the physiology of that complex organ. These new insights could help at developing new features for HFCWO. The mathematical model has been designed to be easily adaptable and is able to include higher complexity modelling. This thesis also paves the ways toward these future improvements. This work shows the significance of mathematical modelling at understanding the behaviors in the lungs for which in-vivo and in-vitro approaches are not so easily realisable. By extension, this is applicable for any other human organ.

Bibliography

[1] Paula Agostini and Nicola Knowles. Autogenic drainage: the technique, physiological basis and evidence. *Physiotherapy*, 93(2):157–163, June 2007.

[2] Emilio Agostoni and Robert E. Hyatt. *Static Behavior of the Respiratory System*, pages 113–130. American Cancer Society, 2011.

[3] Grégoire Allaire. Homogenization and two-scale convergence. *SIAM Journal on Mathematical Analysis*, 23(6):1482–1518, 1992.

[4] S. P. Ambesh, N. Singh, D. Gupta, P. K. Singh, and U. Singh. A huffing manoeuvre, immediately before induction of anaesthesia, prevents fentanyl-induced coughing: a prospective, randomized, and controlled study. *BJA: British Journal of Anaesthesia*, 104(1):40–43, 11 2009.

[5] Daniel Arndt, Wolfgang Bangerth, Bruno Blais, Marc Fehling, Rene Gassmöller, Timo Heister, Luca Heltai, Uwe Köcher, Martin Kronbichler, Matthias Maier, Peter Munch, Jean-Paul Pelteret, Sebastian Proell, Konrad Simon, Bruno Turcksin, David Wells, and Jiaqi Zhang. The `deal.II` library, version 9.3. *Journal of Numerical Mathematics*, 2021, accepted for publication.

[6] Daniel Arndt, Wolfgang Bangerth, Denis Davydov, Timo Heister, Luca Heltai, Martin Kronbichler, Matthias Maier, Jean-Paul Pelteret, Bruno Turcksin, and David Wells. The deal.II finite element library: Design, features, and insights. *Computers & Mathematics with Applications*, 81:407–422, 2021.

[7] Mohammad Asghari-Jafarabadi and Homayoun Sadeghi-Bazargani. Randomization: Techniques and Software-aided Implementation in Medical Studies. *Journal of Clinical Research & Governance*, 4(2), October 2015.

[8] Peter J. Barnes. Pharmacology of Airway Smooth Muscle. *American Journal of Respiratory and Critical Care Medicine*, 158(supplement_2):S123–S132, November 1998. Publisher: American Thoracic Society - AJRCCM.

[9] Harry Bass. The Flow Volume Loop: Normal Standards and Abnormalities in Chronic Obstructive Pulmonary Disease. *Chest*, 63(2):171–176, 1973.

[10] Jason H. T. Bates. *Lung Mechanics: An Inverse Modeling Approach*. Cambridge University Press, 2009.

[11] Klaus-Jürgen Bathe. *Finite Element Procedures - Second edition*. K.J. Bathe, Watertown, MA, 2014.

[12] Sabine Bensamoun, Marie-Christine Ho Ba Tho, Son Luu, Jean-Marc Gherbezza, and Jean-François de Belleval. Spatial distribution of acoustic and elastic properties of human femoral cortical bone. *Journal of Biomechanics*, 37(4):503–510, April 2004.

[13] Lorenz Berger, David Kay, Kelly Burrowes, Vicente Grau, Simon Tavener, and Rafel Bordas. A poroelastic model coupled to a fluid network with applications in lung modelling. *arXiv:1411.1491 [physics, q-bio]*, April 2015. arXiv: 1411.1491.

[14] J. L. Black and P. R. Johnson. Airway smooth muscle in asthma. *Respirology (Carlton, Vic.)*, 1(3):153–158, September 1996.

[15] Larry Borish and Jeffrey A. Culp. Asthma: a syndrome composed of heterogeneous diseases. *Annals of Allergy, Asthma & Immunology: Official Publication of the American College of Allergy, Asthma, & Immunology*, 101(1):1–8; quiz 8–11, 50, July 2008.

[16] Alexandra Buess, Benjamin Sobac, Benjamin Mauroy, and Benoit haut. Energy dissipation in an asymmetric tracheobronchial tree: a CFD analysis. In *27th Canadian Congress of Applied Mechanics*, Sherbrooke, Canada, May 2019.

[17] Ximena M. Bustamante-Marin and Lawrence E. Ostrowski. Cilia and Mucociliary Clearance. *Cold Spring Harbor Perspectives in Biology*, 9(4):a028241, April 2017.

[18] Brian Button and Richard C. Boucher. Role of mechanical stress in regulating airway surface hydration and mucus clearance rates. *Respiratory Physiology & Neurobiology*, 163(1):189–201, 2008. Respiratory Biomechanics.

[19] Paul Cazeaux and Céline Grandmont. Homogenization of a Multiscale Viscoelastic Model with Nonlocal Damping, Application to the Human Lungs. *Mathematical Models and Methods in Applied Sciences*, 25(6):1125, February 2015.

[20] E. Alberdi Celaya, J. J. Anza Aguirrezabala, and P. Chatzipantelidis. Implementation of an Adaptive BDF2 Formula and Comparison with the MATLAB Ode15s. *Procedia Computer Science*, 29:1014–1026, January 2014.

[21] Michelle Chatwin, Michel Toussaint, Miguel R. Gonçalves, Nicole Sheers, Uwe Mellies, Jesus Gonzales-Bermejo, Jesus Sancho, Brigitte Fauroux, Tiina Andersen, Brit Hov, Malin Nygren-Bonnier, Matthieu Lacombe, Kurt Pernet, Mike Kampelmacher, Christian Devaux, Kathy Kinnett, Daniel Sheehan, Fabrizio Rao, Marcello Villanova, David Berlowitz, and Brenda M. Morrow. Airway clearance techniques in neuromuscular disorders: A state of the art review. *Respiratory Medicine*, 136:98–110, March 2018. Publisher: Elsevier.

[22] L.Y.M. Chin, Y. Bossé, Y. Jiao, D. Solomon, T.L. Hackett, P.D. Paré, and C.Y. Seow. Human airway smooth muscle is structurally and mechanically similar to that of other species. *European Respiratory Journal*, 36(1):170–177, 2010.

[23] MO Columb and MS Atkinson. Statistical analysis: sample size and power estimations. *BJA Education*, 16(5):159–161, 08 2015.

[24] Cara F. Dosman and Richard L. Jones. High-Frequency Chest Compression: A Summary of the Literature, 2005.

[25] Xavier Dubois de La Sablonière, Benjamin Mauroy, and Yannick Privat. Shape minimization of the dissipated energy in dyadic trees. *Discrete and Continuous Dynamical Systems - Series B*, 16(3):767–799, June 2011.

[26] M. A. Dunnink, W. R. Doeleman, J. C. A. Trappenburg, and W. R. de Vries. Respiratory muscle strength in stable adolescent and adult patients with cystic fibrosis. *Journal of Cystic Fibrosis*, 8(1):31–36, 2009.

[27] John W. Eaton, David Bateman, Søren Hauberg, and Rik Wehbring. *GNU Octave version 5.1.0 manual: a high-level interactive language for numerical computations*. 2019.

[28] Frank Emmert-Streib and Matthias Dehmer. Understanding statistical hypothesis testing: The logic of statistical inference. *Machine Learning and Knowledge Extraction*, 1(3):945–961, 2019.

[29] Monika Fagevik Olsén, Louise Lannefors, and Elisabeth Westerdahl. Positive expiratory pressure – Common clinical applications and physiological effects. *Respiratory Medicine*, 109(3):297–307, March 2015.

[30] E. Fornasa, M. Ajčević, and A. Accardo. Characterization of the mechanical behavior of intrapulmonary percussive ventilation. *Physiol. Meas.*, 34(12):1583, 2013.

[31] Alan D. Freed and Daniel R. Einstein. Hypo-elastic model for lung parenchyma. *Biomechanics and Modeling in Mechanobiology*, 11(3):557–573, March 2012.

[32] B. Fuerst, T. Mansi, Jianwen Zhang, P. Khurd, J. Declerck, T. Boettger, Nassir Navab, J. Bayouth, Dorin Comaniciu, and A. Kamen. A Personalized Biomechanical Model for Respiratory Motion Prediction. *Medical image computing and computer-assisted intervention : MICCAI International Conference on Medical Image Computing and Computer-Assisted Intervention*, 15(0 3):566–573, 2012.

[33] Christophe Geuzaine and Jean-François Remacle. Gmsh: A 3-d finite element mesh generator with built-in pre- and post-processing facilities. *International Journal for Numerical Methods in Engineering*, 79(11):1309–1331, 2009.

[34] Roland Glowinski, Stanley J. Osher, and Wotao Yin, editors. *Splitting Methods in Communication, Imaging, Science, and Engineering*. Scientific Computation. Springer International Publishing, 2016.

[35] Yasemin Gokdemir, Evrim Karadag-Saygi, Ela Erdem, Ozun Bayindir, Refika Ersu, Bulent Karadag, Nimet Sekban, Gulseren Akyuz, and Fazilet Karakoc. Comparison of conventional pulmonary rehabilitation and high-frequency chest wall oscillation in primary ciliary dyskinesia. *Pediatric Pulmonology*, 49(6):611–616, 2014.

[36] Lee W. Goldman. Principles of CT: Multislice CT. *Journal of Nuclear Medicine Technology*, 36(2):57–68, June 2008. Publisher: Society of Nuclear Medicine Section: CONTINUING EDUCATION.

[37] Céline Grandmont, Bertrand Maury, and Nicolas Meunier. A viscoelastic model with non-local damping application to the human lungs. *ESAIM: Mathematical Modelling and Numerical Analysis*, 40(01):201–224, January 2006.

[38] Philippe A. Grenier, Catalin I. Fetita, and Pierre-Yves Brillet. Quantitative computed tomography imaging of airway remodeling in severe asthma. *Quantitative Imaging in Medicine and Surgery*, 6(1):76–83, February 2016.

[39] Jean Luc Guermond and Richard Pasquetti. A correction technique for the dispersive effects of mass lumping for transport problems. *Computer Methods in Applied Mechanics and Engineering*, 253:186–198, 2012. Publisher: Elsevier.

[40] Beatrice Haefeli-Bleuer and Ewald R. Weibel. Morphometry of the human pulmonary acinus. *The Anatomical Record*, 220(4):401–414, 1988.

[41] Peter Hagedorn and Anirvan DasGupta. Vibration of string and bars. In *Vibrations and Waves in Continuous Mechanical Systems*, chapter 1, pages 1–67. John Wiley & Sons, Ltd, 2007.

[42] Liming Hao, Yan Shi, Maolin Cai, Shuai Ren, Yixuan Wang, Hao Zhang, and Qihui Yu. Dynamic characteristics of a mechanical ventilation system with spontaneous breathing. *IEEE Access*, 7:172847–172859, 2019.

[43] Cyril M. Harris and Allan G. Piersol, editors. *Harris' shock and vibration handbook*. McGraw-Hill handbooks. McGraw-Hill, New York, 5th ed edition, 2002.

[44] Nicholas Hart, Michael I. Polkey, Annick Clément, Michèle Boulé, John Moxham, Frédéric Lofaso, and Brigitte Fauroux. Changes in Pulmonary Mechanics with Increasing Disease Severity in Children and Young Adults with Cystic Fibrosis. *American Journal of Respiratory and Critical Care Medicine*, 166(1):61–66, July 2002. Publisher: American Thoracic Society - AJRCCM.

[45] DR Hess. The evidence for secretion clearance techniques. *Respiratory care*, 46(11):1276—1293, November 2001.

[46] Helge Holden, Kenneth H. Karlsen, Knut-andreas Lie, and Nils Henrik Risebro. *Splitting Methods for Partial Differential Equations With Rough Solutions: Analysis and Matlabr Programs*. European Mathematical Society, Zürich : Providence, R.I, April 2010.

[47] K. Horsfield. Diameters, generations, and orders of branches in the bronchial tree. *Journal of Applied Physiology*, 68(2):457–461, 1990. PMID: 2318756.

[48] F. Horwat and J.P. Meyer. Débit ventilatoire de travail - Elaboration et validation de méthodes indirectes d'évaluation au moyen de la fréquence cardiaque et de l'observation de l'activité. *INRS, numero 76, 4eme trimestre*, 1998.

[49] Alexandra Hough. Physiotherapy in respiratory care : an evidence-based approach to respiratory and cardiac management. *Physiotherapy Research International*, pages 56–57, 2001. Third edition.

[50] A Hristara-Papadopoulou, J Tsanakas, G Diomou, and O Papadopoulou. Current devices of respiratory physiotherapy. *Hippokratia*, 12(4):211–220, 2008.

[51] J. Hussey and S.A. Prasad. *Paediatric Respiratory Care: A guide for physiotherapists and health professionals*. Springer US, 2013.

[52] Adobe Inc. Adobe premiere pro®. Video editing software.

[53] ISO. *ISO/IEC 14882:1998: Programming languages — C++*. sep 1998.

[54] ITK-SNAP, 2019. Medical image segmentation software, www.itksnap.org.

[55] N.H. Jacob J.M. Bourgery. *The Atlas of Human Anatomy and Surgery*. 2021. TASCHEN, Bibliotheca Universalis, republication of the 19th century book.

[56] Luis C. (Luis Carlos Ucha) Junqueira and Anthony L. 20319 Mescher. *Junqueira's basic histology : text & atlas / Anthony L. Mescher*. New York [etc.] : McGraw-Hill Medical„ 2013. Accepted: 2018-11-04T14:22:52Z Journal Abbreviation: Basic histology.

[57] Ryutaro Kakinuma, Noriyuki Moriyama, Yukio Muramatsu, Shiho Gomi, Masahiro Suzuki, Hirobumi Nagasawa, Masahiko Kusumoto, Tomohiko Aso, Yoshihisa Muramatsu, Takaaki Tsuchida, Koji Tsuta, Akiko Miyagi Maeshima, Naobumi Tochigi, Shun-ichi Watanabe, Naoki Sugihara, Shinsuke Tsukagoshi, Yasuo Saito, Masahiro Kazama, Kazuto Ashizawa, Kazuo Awai, Osamu Honda, Hiroyuki Ishikawa, Naoya Koizumi, Daisuke Komoto, Hiroshi Moriya, Seitaro Oda, Yasuji Oshiro, Masahiro Yanagawa, Noriyuki Tomiyama, and Hisao Asamura. Ultra-High-Resolution Computed Tomography of the Lung: Image Quality of a Prototype Scanner. *PLoS ONE*, 10(9):e0137165, September 2015.

[58] Cyril Karamaoun. *Mathematical modeling of nitric oxide and mucus dynamics in the human lungs, using a phenomenological approach, to provide new insights into asthma and cystic fibrosis*. PhD thesis, 10 2017.

[59] Cyril Karamaoun, Benjamin Sobac, Benjamin Mauroy, Alain Van Muylem, and Benoît Haut. New insights into the mechanisms controlling the bronchial mucus balance. *PLOS ONE*, 13(6):e0199319, June 2018.

[60] Ira M Katz, Andrew R Martin, Pierre-Antoine Muller, Karine Terzibachi, Chia-Hsiang Feng, Georges Caillibotte, Julien Sandeau, and Joëlle Texereau. The ventilation distribution of helium-oxygen mixtures and the role of inertial losses in the presence of heterogeneous airway obstructions. *Journal of biomechanics*, 44(6):1137—1143, April 2011.

[61] Robert R Kempainen, Carlos Milla, Jordan Dunitz, Kay Savik, Ann Hazelwood, Cynthia Williams, Bruce K Rubin, and Joanne L Billings. Comparison of settings used for high-frequency chest-wall compression in cystic fibrosis. *Respiratory Care*, 55(6):695–701, 2010.

[62] R. J. King. Pulmonary surfactant. *Journal of Applied Physiology*, 53(1):1–8, 1982. PMID: 6749772.

[63] H. Kitaoka, R. Takaki, and B. Suki. A three-dimensional model of the human airway tree. *Journal of Applied Physiology (Bethesda, Md.: 1985)*, 87(6):2207–2217, December 1999.

[64] Hiroko Kitaoka, Ryuji Takaki, and Béla Suki. A three-dimensional model of the human airway tree. *Journal of Applied Physiology*, 87(6):2207–2217, 1999. PMID: 10601169.

[65] Janet Kluft, Leila Beker, Maria Castagnino, Judith Gaiser, Holly Chaney, and Robert J. Fink. A comparison of bronchial drainage treatments in cystic fibrosis. *Pediatric Pulmonology*, 22(4), 1996.

[66] Martin Kneyber, Marc Heerde, Jos Twisk, Frans Plötz, and Dick Markhorst. Heliox reduces respiratory system resistance in respiratory syncytial virus induced respiratory failure. *Critical care (London, England)*, 13:R71, 06 2009.

[67] V. Kulish. Human Respiration: Anatomy and Physiology, Mathematical Modeling, Numerical Simulation and Aplications. *Shock*, 26(6):637–638, December 2006. Chapter 8.

[68] Ufuk Kuyrukluyildiz, Orhan Binici, İlke Kupeli, Nurel Erturk, Barış Gulhan, Fethi Akyol, Adalet Ozcicek, Didem Onk, and Guldane Karabakan. What Is the Best Pulmonary Physiotherapy Method in ICU? *Canadian Respiratory Journal*, 2016, 2016.

[69] San Andrés L. Vibrations of continuous systems. *MEEN 617 - HD#14*, 2008.

[70] Samuel K. Lai, Ying-Ying Wang, Denis Wirtz, and Justin Hanes. Micro- and macrorheology of mucus. *Advanced Drug Delivery Reviews*, 61(2):86–100, February 2009.

[71] Stephen J. Lai-Fook. Elastic properties of lung parenchyma: The effect of pressure-volume hysteresis on the behavior of large blood vessels. *Journal of Biomechanics*, 12(10):757–764, 1979.

[72] R. K. Lambert, T. A. Wilson, R. E. Hyatt, and J. R. Rodarte. A computational model for expiratory flow. *J Appl Physiol Respir Environ Exerc Physiol*, 52(1):44–56, January 1982.

[73] Sandrine Launois-Rollinat. *Ventilation pulmonaire (4) Propriétés élastiques de l'appareil respiratoire.* 2010.

[74] GC Lee and A Frankus. Elasticity properties of lung parenchyma derived from experimental distortion data. *Biophysical journal*, 15(5):481—493, May 1975.

[75] S Lee, J Alexander, R Blowes, D Ingram, and A Milner. Determination of resonance frequency of the respiratory system in respiratory distress syndrome. *Archives of Disease in Childhood. Fetal and Neonatal Edition*, 80(3):F198–F202, May 1999.

[76] M.G. Levitzky. *Pulmonary Physiology, Seventh Edition.* LANGE Physiology Series. McGraw-Hill Education, 2007.

[77] Stephen H. Loring, Mauricio Garcia-Jacques, and Atul Malhotra. Pulmonary characteristics in copd and mechanisms of increased work of breathing. *Journal of Applied Physiology*, 107(1):309–314, 2009. PMID: 19359620.

[78] C. J. Martin, S. Das, and A. C. Young. Measurements of the dead space volume. *Journal of Applied Physiology: Respiratory, Environmental and Exercise Physiology*, 47(2):319–324, August 1979.

[79] MATLAB. *version 7.10.0 (R2010a).* The MathWorks Inc., Natick, Massachusetts, 2010.

[80] B. Mauroy, M. Filoche, E. R. Weibel, and B. Sapoval. An optimal bronchial tree may be dangerous. *Nature*, 427(6975):633–636, February 2004.

[81] Benjamin Mauroy and Plamen Bokov. The influence of variability on the optimal shape of an airway tree branching asymmetrically. *Phys Biol*, 7(1):16007, 2010.

[82] Benjamin Mauroy and Plamen Bokov. The influence of variability on the optimal shape of an airway tree branching asymmetrically. *Physical Biology*, 7(1):016007, jan 2010.

[83] Benjamin Mauroy, Christian Fausser, Dominique Pelca, Jacques Merckx, and Patrice Flaud. Toward the modeling of mucus draining from the human lung: role of the geometry of the airway tree. *Physical Biology*, 8(5):056006, October 2011.

[84] Benjamin Mauroy, Patrice Flaud, Dominique Pelca, Christian Fausser, Jacques Merckx, and Barrett R. Mitchell. Toward the modeling of mucus draining from human lung: role of airways deformation on air-mucus interaction. *Frontiers in Physiology*, 6, August 2015.

[85] Benjamin Mauroy and Nicolas Meunier. Optimal Poiseuille flow in a finite elastic dyadic tree. *ESAIM: Mathematical Modelling and Numerical Analysis*, 42(4):507–533, July 2008.

[86] Benjamin Mauroy and Nicolas Meunier. Optimal poiseuille flow in a finite elastic dyadic tree. *ESAIM: Mathematical Modelling and Numerical Analysis - Modélisation Mathématique et Analyse Numérique*, 42(4):507–533, 2008.

[87] Bertrand Maury. *The Respiratory System in Equations.* MS&A. Springer-Verlag, Mailand, 2013.

[88] Steven R. McClaran, Craig A. Harms, David F. Pegelow, and Jerome A. Dempsey. Smaller lungs in women affect exercise hyperpnea. *Journal of Applied Physiology*, 84(6):1872–1881, 1998. PMID: 9609779.

[89] Maggie Patricia McIlwaine, Nancy Alarie, George F. Davidson, Larry C. Lands, Felix Ratjen, Ruth Milner, Blythe Owen, and Jennifer L. Agnew. Long-term multicentre randomised controlled study of high frequency chest wall oscillation versus positive expiratory pressure mask in cystic fibrosis. *Thorax*, 68(8):746–751, August 2013. Publisher: BMJ Publishing Group Ltd Section: Cystic fibrosis.

[90] Robert I. McLachlan and G. Reinout W. Quispel. Splitting methods. *Acta Numerica*, 11:341–434, 2002.

[91] Jere Mead. Measurement of Inertia of the Lungs at Increased Ambient Pressure. *Journal of Applied Physiology*, sep 1956.

[92] Carlos E. Milla, Leland G. Hansen, and Warren J. Warwick. Different frequencies should be prescribed for different high frequency chest compression machines. *Biomedical Instrumentation & Technology*, 40(4):319–324, 07 2006.

[93] B.R. Mitchell, F. Lupi, P. Gianangeli, G. Poldi, G. Malerba, and M. Pontesilli. Hfcwo vest, May 2013. US Patent App. 13/521,495.

[94] Hiroyuki Nakamura and Kazutetsu Aoshiba, editors. *Chronic Obstructive Pulmonary Disease: A Systemic Inflammatory Disease*. Respiratory Disease Series: Diagnostic Tools and Disease Managements. Springer Singapore, 2017.

[95] Antonello Nicolini, Federica Cardini, Norma Landucci, Sergio Lanata, Maura Ferrari-Bravo, and Cornelius Barlascini. Effectiveness of treatment with high-frequency chest wall oscillation in patients with bronchiectasis. *BMC Pulmonary Medicine*, 13(1):21, April 2013.

[96] Antonello Nicolini, Bruna Grecchi, and Paolo Banfi. Effectiveness of two high frequency chest wall oscillation techniques in patients with bronchiectasis: a randomized controlled preliminary study. *Panminerva Medica*, March 2020.

[97] Antonello Nicolini, Bruna Grecchi, Maura Ferrari-Bravo, and Cornelius Barlascini. Safety and effectiveness of the high-frequency chest wall oscillation vs intrapulmonary percussive ventilation in patients with severe COPD. *International Journal of Chronic Obstructive Pulmonary Disease*, 13:617–625, February 2018.

[98] Frédérique Noël. *Influence of the ventilation on the transport properties in the healthy and inflamed lung*. Theses, Université Côte d'Azur, February 2021.

[99] Frédérique Noël, Cyril Karamaoun, Jerome A. Dempsey, and Benjamin Mauroy. The origin of the allometric scaling of lung's ventilation in mammals, 2021.

[100] C. M. Oermann, P. R. Swank, and M. M. Sockrider. Validation of an instrument measuring patient satisfaction with chest physiotherapy techniques in cystic fibrosis. *Chest*, 118(1):92–97, July 2000.

[101] OpenFOAM. OpenFOAM Foundation Ltd., OpenCFD Ltd., Computational Fluid Dynamics simulation software, www.openfoam.com/documentation/overview.

[102] Paola Paone and Patrice D. Cani. Mucus barrier, mucins and gut microbiota: the expected slimy partners? *Gut*, 69(12):2232–2243, December 2020. Publisher: BMJ Publishing Group Section: Recent advances in basic science.

[103] S. Paramothayan. *Essential Respiratory Medicine*. Essentials. Wiley, 2019.

[104] T. J. Pedley, R. C. Schroter, and M. F. Sudlow. Energy losses and pressure drop in models of human airways. *Respiration Physiology*, 9(3):371–386, June 1970.

[105] T. J. Pedley, R. C. Schroter, and M. F. Sudlow. Flow and pressure drop in systems of repeatedly branching tubes. *Journal of Fluid Mechanics*, 46(02):365–383, March 1971.

[106] Celina Pezowicz and Maciej Głowacki. The mechanical properties of human ribs in young adult. *Acta of Bioengineering and Biomechanics*, 14(2):53–60, 2012.

[107] Roland Pfister, Katharina A. Schwarz, and Markus Janczyk. Ubi irritatio, ibi affluxus: a 19th century perspective on haemodynamic brain activity. *Cortex; a Journal Devoted to the Study of the Nervous System and Behavior*, 48(8):1061–1063, September 2012.

[108] Agence Nationle pour le Développement de l'Evaluation Médicale. Recommandations de la 1ère conférence de consensus en kinésithérapie respiratoire, 1995.

[109] Nicolas Pozin. *Multiscale lung ventilation modeling in health and disease*. Phd thesis, Paris 6, October 2017.

[110] Nicolas Pozin, Spyridon Montesantos, Ira Katz, Marine Pichelin, Irene Vignon-Clementel, and Céline Grandmont. Predicted airway obstruction distribution based on dynamical lung ventilation data: A coupled modeling-machine learning methodology. *International Journal for Numerical Methods in Biomedical Engineering*, 34(9):e3108, 2018.

[111] Nicolas Pozin, Spyridon Montesantos, Ira Katz, Marine Pichelin, Irene E. Vignon-Clementel, and Céline Grandmont. A tree-parenchyma coupled model for lung ventilation simulation. *International Journal for Numerical Methods in Biomedical Engineering*, February 2017. Publisher: John Wiley and Sons.

[112] Bhavna Prajapati, Mark C. M. Dunne, and Richard A. Armstrong. Sample size estimation and statistical power analyses. *Optometry Today*, 2010(July), July 2010.

[113] Françoise Prêteux, Catalin Fetita, Andre Capderou, and Philippe Grenier M.d. Modeling, segmentation, and caliber estimation of bronchi in high resolution computerized tomography. *Journal of Electronic Imaging*, 8(1):36, January 1999. Publisher: International Society for Optics and Photonics.

[114] Singiresu S. Rao. Longitudinal vibration of bars. In *Vibration of Continuous Systems*, chapter 9, pages 234–270. John Wiley & Sons, Ltd, 2006.

[115] Gregory Reychler, Emilie Debier, Olivier Contal, and Nicolas Audag. Intrapulmonary Percussive Ventilation as an Airway Clearance Technique in Subjects With Chronic Obstructive Airway Diseases. *Respiratory Care*, 63(5):620–631, May 2018. Publisher: Respiratory Care Section: Systematic Review.

[116] Thomas Ritz, Bernhard Dahme, Arthur B. Dubois, Hans Folgering, Gregory K. Fritz, Andrew Harver, Harry Kotses, Paul M. Lehrer, Christopher Ring, Andrew Steptoe, and et al. Guidelines for mechanical lung function measurements in psychophysiology. *Psychophysiology*, 39(5):546–567, 2002.

[117] Duncan F. Rogers. Airway mucus hypersecretion in asthma: an undervalued pathology? *Current Opinion in Pharmacology*, 4(3):241–250, 2004.

[118] Jan Rosell and Paolo Cabras. A three-stage method for the 3D reconstruction of the tracheobronchial tree from CT scans. *Computerized Medical Imaging and Graphics: The Official Journal of the Computerized Medical Imaging Society*, 37(7-8):430–437, December 2013.

[119] Behnaz Seyfi, Anand P. Santhanam, and Olusegun J. Ilegbusi. A Biomechanical Model of Human Lung Deformation Utilizing Patient-Specific Elastic Property. *Journal of Cancer Therapy*, 07(06):402, 2016. Number: 06 Publisher: Scientific Research Publishing.

[120] Ahmed Shabana. *Theory of Vibration: An Introduction*. Mechanical Engineering Series. Springer International Publishing, 3 edition, 2019.

[121] Peter D. Sly and Rachel A. Collins. Chapter 7 - applied clinical respiratory physiology. In Lynn M. Taussig and Louis I. Landau, editors, *Pediatric Respiratory Medicine (Second Edition)*, pages 73–88. Mosby, Philadelphia, second edition edition, 2008.

[122] American Thoracic Society Statement. Lung function testing: selection of reference values and interpretative strategies. american thoracic society. *The American review of respiratory disease*, 144(5):1202—1218, November 1991.

[123] Jonathan Stephano. *Conséquences de l'asymétrie et de la compliance des bronches sur les propriétés hydrodynamiques du poumon, applications à la kinésithérapie respiratoire*. Theses, Université Côte D'Azur ; École doctorale Sciences fondamentales et appliquées (Nice), May 2021.

[124] Jonathan Stephano and Benjamin Mauroy. Modeling shear stress distribution in a deformable airway tree. In *27th Canadian Congress of Applied Mechanics*, Sherbrooke, Canada, June 2019.

[125] Jonathan Stéphano and Benjamin Mauroy. Wall shear stress distribution in a compliant airway tree. *Physics of Fluids*, 33(3):031907, Mar 2021.

[126] Karl Peter Sylvester, Nigel Clayton, Ian Cliff, Michael Hepple, Adrian Kendrick, Jane Kirkby, Martin Miller, Alan Moore, Gerrard Francis Rafferty, Liam O'Reilly, Joanna Shakespeare, Laurie Smith, Trefor Watts, Martyn Bucknall, and Keith Butterfield. ARTP statement on pulmonary function testing 2020. *BMJ Open Respiratory Research*, 7(1), 2020. Publisher: Archives of Disease in childhood _eprint: https://bmjopenrespres.bmj.com/content/7/1/e000575.full.pdf.

[127] Josué Sznitman. Respiratory microflows in the pulmonary acinus. *Journal of biomechanics*, 46(2):284—298, January 2013.

[128] Lynn Taussig and Lynn Landau. *Pediatric Respiratory Medicine - 2nd Edition.* Mosby, Philadelphia, 2008.

[129] Merryn H. Tawhai, Peter Hunter, Juerg Tschirren, Joseph Reinhardt, Geoffrey McLennan, and Eric A. Hoffman. CT-based geometry analysis and finite element models of the human and ovine bronchial tree. *Journal of Applied Physiology*, 97(6):2310–2321, December 2004. Publisher: American Physiological Society.

[130] Merryn H Tawhai and Peter J Hunter. Modeling water vapor and heat transfer in the normal and the intubated airways. *Annals of biomedical engineering*, 32(4):609—622, April 2004.

[131] Merryn H. Tawhai, A. J. Pullan, and P. J. Hunter. Generation of an anatomically based three-dimensional model of the conducting airways. *Ann Biomed Eng*, 28(7):793–802, July 2000.

[132] HA Tiddens, LP Koopman, RK Lambert, WM Elliott, WC Hop, TW van der Mark, WJ de Boer, and JC de Jongste. Cartilaginous airway wall dimensions and airway resistance in cystic fibrosis lungs. *European Respiratory Journal*, 15(4):735–742, 2000. Publisher: European Respiratory Society _eprint: https://erj.ersjournals.com/content/15/4/735.full.pdf.

[133] Umolo, 2021. Calligraphic designer, Köln, Germany.

[134] Caroline van Ertbruggen, Charles Hirsch, and Manuel Paiva. Anatomically based three-dimensional model of airways to simulate flow and particle transport using computational fluid dynamics. *Journal of Applied Physiology*, 98(3):970–980, 2005. PMID: 15501925.

[135] Ewald R. Weibel. *Morphometry of the Human Lung.* Springer-Verlag, Berlin Heidelberg, 1963.

[136] Ewald R. Weibel. *The Pathway for Oxygen: Structure and Function in the Mammalian Respiratory System.* Harvard University Press, 1984.

[137] René Werner, Jan Ehrhardt, Rainer Schmidt, and Heinz Handels. Patient-specific finite element modeling of respiratory lung motion using 4D CT image data. *Medical Physics*, 36(5):1500–1511, May 2009.

[138] B. J. West, V. Bhargava, and A. L. Goldberger. Beyond the principle of similitude: renormalization in the bronchial tree. *Journal of Applied Physiology*, 60(3):1089–1097, 1986. PMID: 3957825.

[139] S. Whittemore and D.A. Cooley. *The Respiratory System.* Human body, how it works. Chelsea House, 2009.

[140] Lena Yoshihara, Christian J. Roth, and Wolfgang A. Wall. Fluid-structure interaction including volumetric coupling with homogenised subdomains for modeling respiratory mechanics. *International Journal for Numerical Methods in Biomedical Engineering*, 33(4):e2812, 2017. e2812 cnm.2812.

[141] Paul A. Yushkevich, Joseph Piven, Heather Cody Hazlett, Rachel Gimpel Smith, Sean Ho, James C. Gee, and Guido Gerig. User-guided 3D active contour segmentation of anatomical structures: significantly improved efficiency and reliability. *NeuroImage*, 31(3):1116–1128, July 2006.